Equations of State, Sound Velocities, and Thermoelasticity of Iron-Nickel-Silicon Alloys in the Earth's Inner Core

Thesis by
Rachel A. Morrison

In Partial Fulfillment of the Requirements for the
Degree of
Doctor of Philosophy

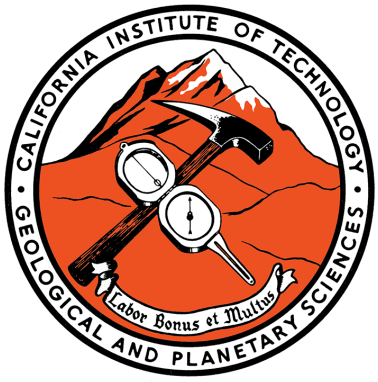

CALIFORNIA INSTITUTE OF TECHNOLOGY
Pasadena, California

2019
Defended August 6, 2018

Rachel A. Morrison
ORCID: 0000-0003-3585-827X

ACKNOWLEDGEMENTS

First and foremost, I would like to thank my thesis committee. Paul, thank you for advising me on my second research project. I am excited to see that my abandoned project has once again been adopted, and I look forward to seeing where Olivia takes it. I am particularly grateful for the time and dedication you gave to help me study for my qualifying exams. You have a unique dedication to improving the quality of student life in our division, which I greatly admire. Victor, thank you for being my academic advisor for all these years, and thank you for letting me TA your data analysis course. The knowledge you shared was so incredibly useful in my research. Mike, thank you for helping keep the Seismolab afloat, and thank you for reminding me that even problems with spherical harmonics can be tackled with some patience and book work.

Jennifer, you welcomed me into your research group with open arms. Thank you for your endless support, motivation, enthusiasm, and careful attention to detail. You are such a great advocate for your students. I've always admired that about you. Thank you for your patience and understanding as I navigated through some of life's hardships, and thank you for your even greater patience as I navigated through research. I am so grateful to have spent the past six years in your lab.

Wolfgang, thank you for your for sharing your expertise about nuclear resonant scattering, and thank you for your extensive help with PHOENIX and MINUTI. I am also very grateful for your enthusiasm in updating and improving the software as our research evolved. And, of course, thank you for your help developing the theory in Section 3.3 of this thesis. Synchrotron experiments are frequently a many person operation, and much of this research would be impossible without the help of my those from our research group who helped run the experiments: Jennifer, Wolfgang, Caitlin, June, Dongzhou, Natalia, and Greg. Thank you! I would like to acknowledge Lisa and Caitlin, who synthesized nearly all of the samples used in this thesis. Caitlin, I wish we had overlapped at Caltech. Thank you for paving the way for my NRIXS research. June, you provided so much mentorship and support early on. Thank you for sharing your sample prep wisdom. Dongzhou, thank you for being such an incredible teacher during beamtime. Aaron, thank you for sharing your enthusiasm for Bayesian statistics. Natalia, you are one of the most careful

and thorough researchers I know. There's no one else I'd rather share beamtime with. Greg, the department is both quieter and lonelier now that you've moved to Hawaii. Thank you for the foodie adventures and the discussions about uncertainty ellipses. Tyler, thank you for the opportunity to help mentor you. Have a wonderful time working with June! I'm excited to hear about your graduate school adventures. Olivia, Vasilije, you've got this. Feel free to reach out to me whenever you feel stuck.

A very special thank you is reserved for the beamline scientists at the Advanced Phonon Source Sectors 3 and 13 and the Advanced Light Source beamline 12.2.2: Jiyong, Ahmet, Ercan, Wenli, Thomas, Michael, Eran, Vitali, Mark, Sergey, Dongzhou, Martin, Christine, and those I have surely forgotten. Without your seemingly endless dedication, time, and expertise, none of these experiments would be possible. A second important thank you goes to the Seismolab and GPS staff who manage to make things function seamlessly on a day to day basis. I don't know how you do it.

A huge thank you is in order for my mentors and colleagues at ExxonMobil, who welcomed me into their family during my internship last fall. I'm very much looking forward to returning to Houston.

Thank you to all my friends in the Seismolab and GPS department. I'll miss the lunches, dinners, social hours, whiskey nights, and adventures. I have chosen to not list you all out of a deep fear of leaving someone out. To my current and former office mates Zhongwen, Yingdi, Chris, Celeste, Ethan, thank you in particular for helping me stay sane during graduate school, especially these last few years. Seriously, thanks. To everyone still working on their PhD, you've got this. Remember to look out for each other. It matters more than you may realize.

Lisa and Kevin, after being together through high school, undergrad, and grad school, I'm excited to see where the next adventure takes us. Justin and Bérénice, I am so glad we overlapped in the same town, if only for a short time. Marta and Christopher, thank you for being amazing friends, and thank you for keeping our cats alive. To my physics friends Nicole, David, Anna, Christopher, thanks for pretending I'm cool, even when I get lost in the conversation. Annélise, thanks for being the friend who always understands. I'd like to add a special note for my friend Monica Rice, who didn't get the opportunity to defend her PhD thesis on Parkinson's research at UNR. You

brought so much light into the world. You will be missed.

Jem, thank you for sharing your enthusiasm. Betina, thank you for your help editing. You both have so much patience and warmth. (These are not attributes typically ascribed to cats.) Stay *purr*-fect.

Laura, my dear mother-in-law, thank you so much for letting me kidnap you into my crazy family. Your unending support and friendship (and patience!) mean so much to me. Grandma, I don't think you have any idea how awesome you are. Thank you so much for your support and enthusiasm.

Mom, while I was growing up, you always said you were happy for me, never that you were proud of me. You gave me the chance to take ownership of my own pride, and for that I am so very thankful. Thank you for giving me your strength, especially during the times when our whole world changed around us. And thank you for all of your help with math when I was in school; it wasn't until I was older that I realized men could also be good at math. I am so grateful to women like you and Laura who pursued math and science before it was cool. You dealt with so much criticism so that I didn't have to. Thanks.

Thank you Dad, for always being proud of me, even when I forgot how to be proud of myself. You were always my biggest cheerleader, and you would be so proud today. I finally read your favorite book, *Zen and the Art of Motorcycle Maintenance*, which told me, "Assembly of Japanese bicycle require great peace of mind." It turns out a graduate degree also requires great peace of mind. Thank you for helping me find that.

Muir, it would be insulting to say you are my rock, especially in a geophysics department. So instead, I'll say you are my craton. I could spend the entire length of this thesis listing my gratitudes for everything you have given, but I hope it will suffice to say just thanks. You know what for.

Finally, I would like to thank the funding sources which have supported this research, including NSF-EAR-1727020 and 1316362, the W. M. Keck Institute for Space Studies, Caltech, and NDSEG. Portions of this work were performed at GeoSoilEnviroCARS Sector 13 (funded by NSF-EAR-1634415 and DOE - GeoSciences DE-FG02-94ER14466) and Sector 3 at the Advanced Photon Source (APS) at Argonne National Laboratory. The use of APS is supported by the U.S. DOE, Office of Science DE-AC02-06CH11357. Portions of this

work were also performed at beamline 12.2.2 (supported in part by COMPRES under NSF Cooperative Agreement EAR 10-43050) at the Advanced Light Source (ALS) at Lawrence Berkeley National Laboratory. The use of ALS is supported by the U.S. DOE, Office of Science DE-AC02-05CH11231. Microprobe analyses were carried out at the Caltech GPS Division Analytical Facility (funded in part by the MRSEC Program of the NSF under DMR-0080065).

ABSTRACT

The core of the Earth is predominately iron alloyed with approximately 5 wt% nickel along with some amount of light elements, e.g., Si, O, S, C, H, Mg. Mineral physics studies, in conjunction with seismological and cosmochemical observations, provide an opportunity to improve constraints on the composition of the core. In this thesis, we investigate the thermoelastic and vibrational properties of bcc- and hcp-structured $Fe_{0.91}Ni_{0.09}$ and $Fe_{0.8}Ni_{0.1}Si_{0.1}$ (atomic percent) at high pressures.

We present powder x-ray diffraction data on bcc- and hcp-structured $Fe_{0.91}Ni_{0.09}$ and $Fe_{0.8}Ni_{0.1}Si_{0.1}$ at 300 K up to 167 GPa and 175 GPa, respectively. The alloys were compressed in diamond anvil cells, and their equations of state and axial ratios were measured with high statistical quality. These equations of state are combined with thermal parameters from previous reports to improve the extrapolation of the density, adiabatic bulk modulus, and bulk sound speed to the pressures and temperatures of Earth's inner core. We place constraints on the composition of Earth's inner core by combining these results with seismic observations and available data on other light-element alloys of iron. We find the addition of 4.3 to 5.3 wt% silicon to $Fe_{0.95}Ni_{0.05}$ alone can explain geophysical observations of density, adiabatic bulk modulus, and bulk sound speed at the inner core boundary, as can up to 7.5 wt% sulfur with negligible amounts of silicon and oxygen. Our findings favor an inner core with less than $\sim$2 wt% oxygen and less than $\sim$1 wt% carbon, although uncertainties in electronic and anharmonic contributions to the equations of state may shift these values.

Seismic studies provide evidence for an anisotropic inner core, which is suggested to be related to the ratio of the c- to a-unit cell parameters of hcp-structured materials. We demonstrate hcp-$Fe_{0.91}Ni_{0.09}$ and $Fe_{0.8}Ni_{0.1}Si_{0.1}$ have measurably greater c/a axial ratios than those of hcp-Fe over the measured pressure range. We further investigate the relationship between the axial ratios, their pressure derivatives, and elastic anisotropy of hcp-structured materials.

Next, we present high pressure NRIXS data on bcc- and hcp-$Fe_{0.91}Ni_{0.09}$ and $Fe_{0.8}Ni_{0.1}Si_{0.1}$ at 300 K with in situ x-ray diffraction. From these data, we

determine the partial phonon density of states for each composition, and we systematically compare our results to iron. We constrain the Debye sound velocity from the low energy region of the phonon density of states. Using our previously determined equations of state for the same compositions, we constrain the compressional and shear sound velocities and shear moduli. At 300 K, we find that 9 at% nickel decreases the shear velocity of hcp-iron by ∼6% and that silicon has a minimal effect on the shear velocity of hcp-$Fe_{0.91}Ni_{0.09}$. Thermal effects likely play a large role in the sound velocities of iron alloys at core conditions, so constraining these effects is critical to further constrain the composition of the core.

From the volume scaling of the phonon DOS, we find the 300 K vibrational components of the Grüneisen parameter for hcp-$Fe_{0.91}Ni_{0.09}$ and $Fe_{0.8}Ni_{0.1}Si_{0.1}$ are very similar to that of hcp-Fe within uncertainties. We also constrain vibrational thermal pressure from the volume dependence of vibrational free energy, and we find negligible differences within uncertainty between the vibrational thermal pressures of hcp-Fe, $Fe_{0.91}Ni_{0.09}$, and $Fe_{0.8}Ni_{0.1}Si_{0.1}$. By combining the vibrational component of thermal pressure with theoretical estimates of the anharmonic and electronic contributions, we provide an estimate for the total thermal pressure. We constrain a variety of additional parameters from the NRIXS data and phonon density of states, including the vibrational component of entropy, the vibrational thermal expansion, the vibrational kinetic energy, the Lamb-Mössbauer factor, and the vibrational specific heat.

PUBLISHED CONTENT AND CONTRIBUTIONS

Morrison, R. A., J. M. Jackson, W. Sturhahn, D. Zhang, and E. Greenberg (2018), Equations of state and anisotropy of Fe-Ni-Si alloys, *Journal of Geophysical Research: Solid Earth*, 122, doi:10.1029/2017JB015343. R.A.M. conducted the synchrotron experiments, performed the data analysis, and wrote the manuscript.

TABLE OF CONTENTS

LIST OF FIGURES

LIST OF TABLES

NOMENCLATURE

Acronyms

ALS Advanced Light Source

APD Avalanche photodiode

APS Advanced Photon Source

bcc Body centered cubic

DAC Diamond anvil cell

DOS Density of states

EOS Equation of state

fcc Face centered cubic

FWHM Full width at half maximum

hcp Hexagonal close packed

ICB Inner core boundary

IXS Inelastic X-ray scattering

NRIXS Nuclear resonant inelastic X-ray scattering

PREM Preliminary reference Earth model

SMS Synchrotron Mössbauer spectroscopy

XRD X-ray diffraction

Variables

2θ Angular dispersion in XRD (degrees)

α_{vib} Vibrational component of thermal expansion (K^{-1})

χ^2 Reduced goodness of fit (unitless)

γ Grüneisen parameter (unitless)

$\langle u^2 \rangle$ Mean square atomic displacement ($Å^2$)

μ	Shear modulus (GPa)
ρ	Density (g/cm^3)
Θ	Debye temperature (K)
ξ	Phonon DOS scaling parameter (unitless)
c/a	Unit cell axial ratio for hcp lattice (unitless)
C_{vib}	Vibrational component of specific heat (k_B/atom)
d	Distance between planes of atoms (Å)
$D(E,V)$	Density of states as a function of energy and volume (1/eV)
E	Energy, frequently in reference to NRIXS measurements (meV)
E_K	Vibrational kinetic energy per ^{57}Fe atom (meV/atom)
f_{LM}	Lamb-Mössbauer factor (unitless)
F_{vib}	Vibrational free energy (meV/atom)
K_S	Isentropic bulk modulus (GPa)
K_T	Isothermal bulk modulus (GPa)
K'_T	Pressure derivative of isothermal bulk modulus (unitless)
P	Pressure (GPa)
P_{anh}	Anharmonic contribution to thermal pressure (GPa)
P_{el}	Electronic contribution to thermal pressure (GPa)
P_{th}	Thermal pressure (GPa)
q	Constant used in Grüneisen parameter approximation (unitless)
S_{vib}	Vibrational component of entropy per ^{57}Fe atom (k_B/atom)
T	Temperature (K)
U_{vib}	Vibrational internal energy per ^{57}Fe atom (meV/atom)
V	Volume (Å^3)
v_ϕ	Bulk sound speed (km/s)
v_P	Compressional sound velocity (km/s)
v_S	Shear sound velocity (km/s)

Chapter 1

INTRODUCTION

1.1 The Earth's core

At the center of the Earth lies the Earth's core, which is composed of an iron-rich liquid outer core surrounding a small solid inner core which has grown over time from the outer core. The convection of the outer core generates the Earth's magnetic field, and the heat from the core contributes to the convection of the mantle, which in turn drives plate tectonics on the surface of the Earth. Despite the core's influence on life on Earth's surface, direct samples of the core are inaccessible. Therefore, much of our knowledge of the Earth's core comes from indirect methods, including cosmochemical and seismic observations, experimental mineral physics studies, and theoretical calculations. Cosmochemical observations of chondritic meteorites, the sun, and the Earth's crust and mantle suggest iron and nickel are preferentially sequestered within the deep interior of the Earth. These findings indicate the core is predominately iron alloyed with ∼5 wt% nickel (*Allègre et al.*, 1995; *McDonough and Sun*, 1995; *McDonough*, 2003).

Seismic observations of free oscillations and body wave travel times, combined with knowledge of the Earth's mass, radius, and moment of inertia, place constraints on the density and sound velocities of the inner and outer core as a function of radius. Two of the most commonly referenced models are the one-dimensional radial models AK135-F (*Kennett et al.*, 1995; *Montagner and Kennett*, 1996) and the Preliminary Reference Earth Model (PREM) (*Dziewonski and Anderson*, 1981) (See Figure 1.1). While these two models are generally in close agreement, neither reports uncertainty on density (ρ), compressional velocity (v_P), or shear velocity (v_S) in the core. Constraints on the uncertainties of ρ, v_P, and v_S come from more recent free oscillation studies. For instance, *Deuss* (2008) report average inner core velocities of $v_P = 11.15 \pm 0.05$ km/s and $v_S = 3.55 \pm 0.05$ km/s, and a study by *Masters and Gubbins* (2003) reports the density jump at the inner core boundary to be 0.82 ± 0.18 g/cm^3. More recently, body waves and free oscillations have also provided evidence for complex structure and anisotropy in the inner core

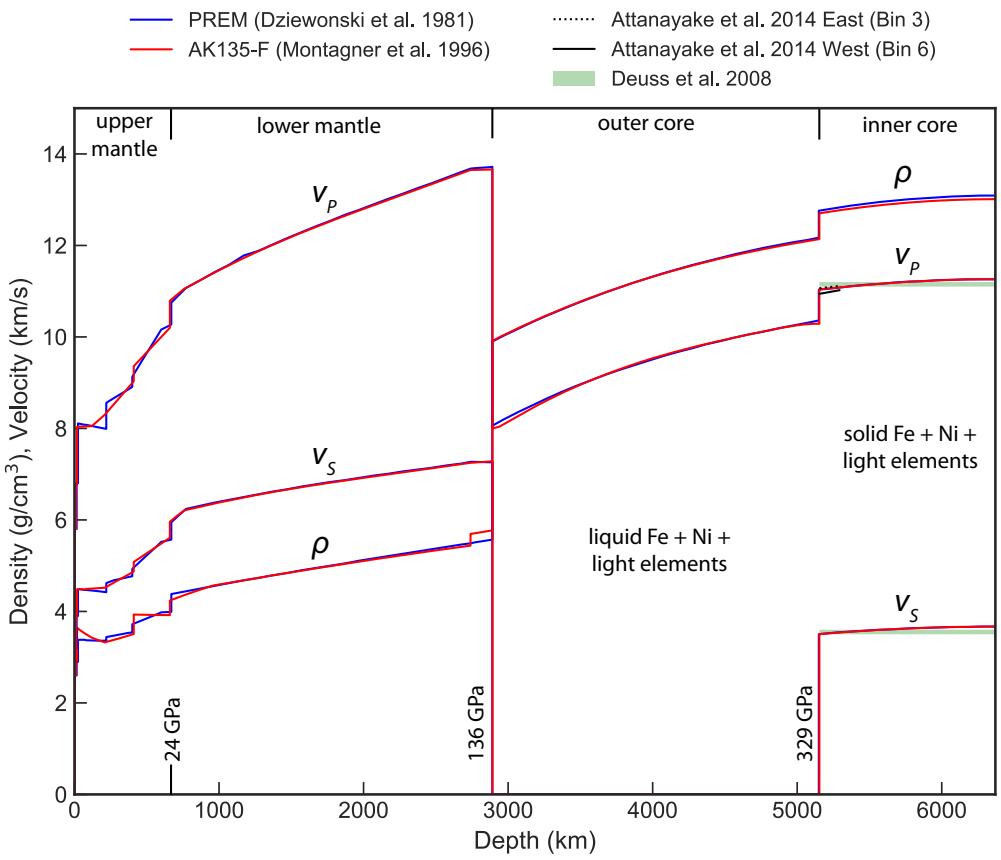

Figure 1.1: Seismic constraints on density (ρ) and compressional (v_P) and shear (v_S) sound velocities: one-dimensional seismic models AK135-F (*Kennett et al.*, 1995; *Montagner and Kennett*, 1996) and PREM (*Dziewonski and Anderson*, 1981), two lateral bins from *Attanayake et al.* (2014), and average inner core sound velocities from *Deuss* (2008).

(reviewed in *Deuss*, 2014). For instance, the hemispherical variation of v_P at the top of the inner core has been investigated by *Attanayake et al.* (2014). We compare two v_P bins from opposite hemispheres from their study in Figure 1.1.

The composition of the core can be further constrained by comparing seismic constraints of ρ, v_P, v_S, isentropic bulk modulus K_S, and bulk sound speed v_ϕ to mineral physics experiments and ab initio calculations of various iron alloys. At inner core conditions, the density of the outer core is ~10% lighter than liquid iron (reviewed in *Poirier*, 1994), and the density of the inner core is ~3–5% lighter than hcp-iron (reviewed in *Li and Fei*, 2014), which supports the presence of light elements (e.g., Si, O, S, C, H, Mg) in the core (*Li and Fei*, 2014; *Litasov and Shatskiy*, 2016; *O'Rourke and Stevenson*, 2016; *Vočadlo*,

2015). This evidence indicates a greater concentration of light elements in the outer core than in the inner core. A plausible core composition must also match the compressional and shear velocities of the core. The v_P and v_S of the inner core are reported to be respectively ∼4–10% slower (e.g., *Sakamaki et al.*, 2016) and >30% slower than hcp-iron (e.g., *Martorell et al.*, 2013a). A detailed understanding of the effect of composition on the sound velocities and densities of iron alloys at core pressures and temperatures is necessary to constrain the outer and inner core compositions and the melting temperature at the inner core boundary. Additionally, constraints on core composition would aid our understanding of the nature of anisotropy and heterogeneity in the inner core. Furthermore, an understanding of the thermoelastic properties of these alloys at core conditions can constrain geodynamical simulations of the evolution and ongoing processes of the core.

1.2 Phases of iron-nickel-silicon alloys

The phase diagrams of iron and $Fe_{0.91}Ni_{0.09}$ are illustrated in Figure 1.2. The portion of the phase diagram from 0–25 GPa and up to 1000 K is after *Huang et al.* (1988), and the portion from ∼25–330 GPa is after *Zhang et al.* (2016). We note that the $Fe_{0.91}Ni_{0.09}$ samples used in *Zhang et al.* (2016) were synthesized from the same batch of $Fe_{0.91}Ni_{0.09}$ used throughout this thesis. At ambient pressure and temperature, iron is in the body-centered cubic (bcc) structure. With increasing temperature at ambient pressure, iron transitions into the face-centered cubic (fcc) phase, then briefly into another bcc phase, before melting around 1800 K (*Strong et al.*, 1973). With increasing pressure at 300 K, iron transitions into the hexagonal close packed (hcp) structure via a sluggish transition nominally around 8.3 GPa, although the bcc phase has been observed up to 25 GPa on compression, and the hcp phase has been observed down to 2 GPa on decompression (*Zarkevich and Johnson*, 2015). According to *Huang et al.* (1988) and *Zhang et al.* (2016), nickel stabilizes the fcc phase and slightly decreases the melting temperature of hcp-iron. Several studies have proposed iron or iron-nickel may assume a bcc phase at inner core conditions (e.g., *Belonoshko et al.*, 2008; *Dubrovinsky et al.*, 2007). However, recent experimental studies at pressures and temperatures close to the inner core have found iron and $Fe_{0.9}Ni_{0.1}$ in the hcp structure (*Sakai et al.*, 2011; *Tateno et al.*, 2010, 2012). Much of this thesis, therefore, focuses on the hcp phases of iron alloys. The melting temperature of iron-alloys at pressures cor-

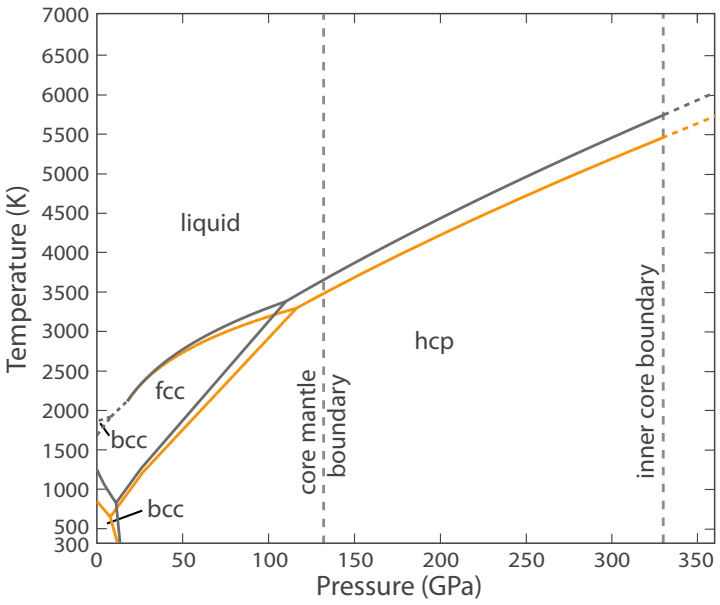

Figure 1.2: Phase diagram of Fe (gray) and $Fe_{0.9}Ni_{0.1}$ (orange). The phase diagrams from 0–25 GPa and up to 1000 K are after *Huang et al.* (1988). The phase diagrams from ∼25–330 GPa are after *Zhang et al.* (2016).

responding to the inner core boundary is of particular interest, as this phase transition is a key constraint on the geotherm of the core. *Zhang et al.* (2016) propose a melting temperature at the inner core boundary of 5700 ± 200 K for hcp-iron and of 5500 ± 200 K for hcp-$Fe_{0.91}Ni_{0.09}$, although the range of reported melting temperatures for hcp-iron and iron-nickel is wide. For instance, *Anzellini et al.* (2013) report an inner core boundary temperature of 6230 ± 500 K for hcp-iron.

Silicon is a favored light element in the inner core for a variety of reasons. First, the high magnesium to silicon ratio in the crust and mantle of Earth compared to chondritic meteorites suggests silicon may be sequestered in the core (*Allègre et al.*, 2001, 1995). Second, silicate-iron partitioning experiments conducted at high pressure and high temperature observe that silicon preferentially partitions into iron (*Fischer and Campbell*, 2015; *Ricolleau et al.*, 2011). Lastly, ab initio and experimental results demonstrate silicon partitions roughly equally between liquid and solid iron at high pressure (*Alfè et al.*, 2002, 2007). The phase diagram of $Fe_{0.84}Si_{0.16}$ (*Fischer et al.*, 2013, converted to atomic units) is compared to the phase diagram of iron (*Huang et al.*, 1988; *Zhang et al.*, 2016) in Figure 1.3. Near ambient conditions, the phase dia-

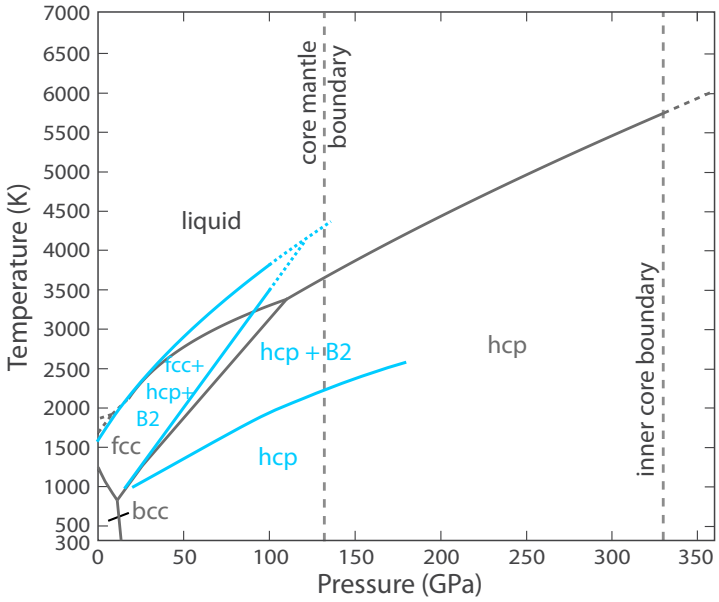

Figure 1.3: Phase diagram of Fe (gray) and $Fe_{0.84}Si_{0.16}$ (blue). The phase diagram of Fe from 0–25 GPa and up to 1000 K is after *Huang et al.* (1988). The phase diagram from ∼25–330 GPa of Fe is after *Zhang et al.* (2016). The phase diagram $Fe_{0.84}Si_{0.16}$ is after (*Fischer et al.*, 2013). Gray labels refer to Fe phases; blue labels refer to $Fe_{0.84}Si_{0.16}$ phases.

gram of $Fe_{0.84}Si_{0.16}$ is similar to that of Fe, with $Fe_{0.84}Si_{0.16}$ taking on a bcc structure. With increasing pressure, $Fe_{0.84}Si_{0.16}$ transitions to an hcp structure, with silicon stabilizing the bcc phase to higher pressures. For instance, we found in this thesis that the bcc-hcp transition of $Fe_{0.8}Ni_{0.1}Si_{0.1}$ occurred ∼6 GPa above that of $Fe_{0.91}Ni_{0.09}$, in agreement with *Zhang and Guyot* (1999) and *Lin* (2003). With the addition of silicon, the fcc phase of iron takes on a metastable coexistence with the hcp and B2 phase, and, at higher temperatures, the hcp phase of iron becomes coexistent with the B2 phase. It is thought that the addition of light elements depresses the melting temperature of iron. For instance, silicon is estimated to decrease the temperature at the inner core boundary by 0–400 K (as reviewed in *Fischer*, 2016). Figure 1.3 appears to show a higher melting temperature of $Fe_{0.84}Si_{0.16}$ compared to iron because the $Fe_{0.84}Si_{0.16}$ melting temperature reported in *Fischer et al.* (2013) is based upon the iron melting temperature of *Ma et al.* (2004), which reports a higher iron melting temperature than *Zhang et al.* (2016).

The iron-silicon composition investigated in this thesis, $Fe_{0.8}Ni_{0.1}Si_{0.1}$, likely has a phase diagram which lies somewhere between the phase diagrams of Fe,

Table 1.1: Summary of synchrotron experiments presented in this thesis

Composition	Experimental Methods	DAC Run	Beamline	Dates (mo/yr)	Pressure (GPa)	Chapter
Fe	NRIXS, XRD		APS 3-ID-B	03/15	0	4
$Fe_{0.91}Ni_{0.09}$	NRIXS, XRD		APS 3-ID-B	03/15	0	4
$Fe_{0.91}Ni_{0.09}$	NRIXS, XRD	FeNi-Run#1	APS 3-ID-B	04/12, 06/12, 10/12	3.8–104	4
$Fe_{0.91}Ni_{0.09}$	NRIXS, XRD	FeNi-Run#2	APS 3-ID-B	02/13	1.7–4.5	4
$Fe_{0.91}Ni_{0.09}$	NRIXS, XRD		APS 3-ID-B	03/15	0	4
$Fe_{0.8}Ni_{0.1}Si_{0.1}$	NRIXS, XRD	FeNiSi-Run#1	APS 3-ID-B	11/13	7.1	4
$Fe_{0.8}Ni_{0.1}Si_{0.1}$	NRIXS, XRD	FeNiSi-Run#2	APS 3-ID-B	02/14	6.5	4
$Fe_{0.8}Ni_{0.1}Si_{0.1}$	NRIXS, XRD	FeNiSi-Run#3	APS 3-ID-B	02/14 03/15	27.9–86	4
$Fe_{0.91}Ni_{0.09}$	XRD		APS 13-BM-C	02/15	0	2, 3
$Fe_{0.91}Ni_{0.09}$	XRD	FeNi-Run#1	APS 13-BM-C	02/15	0–104	2, 3
$Fe_{0.91}Ni_{0.09}$	XRD	FeNi-Run#2	ALS 12.2.2	04/16	1.4–104	2, 3
$Fe_{0.91}Ni_{0.09}$	XRD	FeNi-Run#3	APS 13-ID-D	06/16	14.6–167	2, 3
$Fe_{0.8}Ni_{0.1}Si_{0.1}$	XRD		ALS 12.2.2	05/15	0	2, 3
$Fe_{0.8}Ni_{0.1}Si_{0.1}$	XRD	FeNiSi-Run#1	ALS 12.2.2	05/15	0–88.1	2, 3
$Fe_{0.8}Ni_{0.1}Si_{0.1}$	XRD	FeNiSi-Run#2	APS 13-ID-D	06/16	31.6–175	2, 3

$Fe_{0.9}Ni_{0.1}$, and $Fe_{0.84}Si_{0.16}$. $Fe_{0.8}Ni_{0.1}Si_{0.1}$ at inner core conditions is thought to adopt an hcp-structure or a mixture of hcp and B2 phases (*Fischer and Campbell*, 2015; *Fischer et al.*, 2013; *Sakai et al.*, 2011; *Tateno et al.*, 2015), where the B2 phase of Fe-Si and Fe-Ni-Si becomes more favorable as Si content or temperature is increased.

1.3 Overview of thesis

Throughout this thesis, we investigate the thermoelastic properties of bcc- and hcp-$Fe_{0.91}Ni_{0.09}$ and $Fe_{0.8}Ni_{0.1}Si_{0.1}$, and we compare systematically to the thermoelastic properties of bcc- and hcp-Fe whenever possible. While we make an effort to compare our measured and derived quantities to other iron-light-element alloys, systematic comparisons are frequently hindered by the scarcity of existing experimental data. The greater portion of this work was collected in a high pressure environment via the use of diamond anvil cells (DACs) at 300 K. Data presented in this thesis rely on synchrotron x-ray diffraction (XRD) and nuclear resonant inelastic x-ray scattering (NRIXS) experiments. We outline the synchrotron experiments from which this thesis draws in Table 1.1.

In Chapter 2, we present high-quality 300 K pressure-volume relations of bcc- and hcp-$Fe_{0.91}Ni_{0.09}$ and $Fe_{0.8}Ni_{0.1}Si_{0.1}$ measured with XRD up to 167 GPa and 175 GPa, respectively. These measurements were conducted in a helium pressure medium, which ensures a more hydrostatic compressional environment than other commonly selected pressure media, and with a tungsten pressure calibrant. Quantities derived from these x-ray diffraction results are tabulated in Appendix A. We fit equations of state (EOS) to the presented pressure-volume data, and we present uncertainties and correlations on the EOS fit parameters, which is necessary for uncertainty calculations when comparing and extrapolating EOSs. We systematically compare our findings to an EOS study on iron conducted with the same pressure media and pressure calibrant (*Dewaele et al.*, 2006).

In the later half of Chapter 2, we extrapolate our 300 K hcp-$Fe_{0.91}Ni_{0.09}$ and $Fe_{0.8}Ni_{0.1}Si_{0.1}$ EOSs to inner core conditions to determine the effect of nickel and silicon on density, bulk modulus, and bulk sound speed. These quantities are of particular interest, as they can be directly compared to seismic observations of the inner core. To estimate the allowable nickel and silicon content in the inner core, we apply a linear and bulk aggregate mixing model to the thermal EOSs. We find that for a fixed nickel content of 5 wt%, the density, bulk modulus, and bulk sound speed of the inner core can accommodate 4.3–5.3 wt% silicon. We then expand our compositional space search using existing thermal EOSs for FeO, FeS_2, and Fe_7C_3, and we propose a variety of inner core compositions consistent with seismic observations of density, bulk modulus, and bulk sound speed. For example, we find the inner core can accommodate up to 7.5 wt% sulfur, up to ∼2 wt% oxygen, and less than 1 wt% carbon, although uncertainties in electronic and anharmonic contributions to the equations of state may shift these values.

In Chapter 3, we apply our experimental data from Chapter 2 and Appendix A to investigate the relationship between the hcp-phase c/a axial ratio and elastic anisotropy. Due to experimental difficulties in synthesizing large single crystals of hcp-iron alloys, the elastic anisotropy of hcp-iron alloys is poorly constrained and currently debated. The elastic anisotropy of an hcp-structured material is suggested to be related to its c/a axial ratio. Our measurements in a helium pressure medium provide a tight constraint on the c/a axial ratio of hcp-$Fe_{0.91}Ni_{0.09}$ and $Fe_{0.8}Ni_{0.1}Si_{0.1}$. We investigate the relationship between c/a

and elastic anisotropy and then apply our findings to hcp-cobalt and helium, whose elastic anisotropy can be directly measured with single crystals. We then apply our findings to hcp-$Fe_{0.91}Ni_{0.09}$ and $Fe_{0.8}Ni_{0.1}Si_{0.1}$ and compare with experimental predictions.

In Chapter 4, we present high pressure NRIXS data on bcc- and hcp-$Fe_{0.91}Ni_{0.09}$ and $Fe_{0.8}Ni_{0.1}Si_{0.1}$ at 300 K. The sample volume is constrained in situ by XRD collected immediately before and after each NRIXS measurement. From these data, we determine the partial phonon density of states (DOS) for each composition, and we systematically compare our results to iron by re-analyzing previously collected hcp-iron NRIXS data (*Murphy et al.*, 2011a,b, 2013). A wide variety of thermoelastic quantities can be determined either directly from NRIXS data or from the partial phonon DOS.

We demonstrate a new method of determining the Debye sound velocity from the low energy region of the phonon DOS which provides an improved estimate on the Debye sound velocity uncertainty. From this, we present Debye sound velocities for bcc- and hcp-$Fe_{0.91}Ni_{0.09}$ and $Fe_{0.8}Ni_{0.1}Si_{0.1}$. Using our previously determined equations of state for the same compositions, we constrain the compressional and shear sound velocities and shear moduli of bcc- and hcp-$Fe_{0.91}Ni_{0.09}$ and $Fe_{0.8}Ni_{0.1}Si_{0.1}$. At 300 K, we find that 9 at% nickel decreases the shear velocity of hcp-iron by ~6%, and that silicon has a minimal effect on the shear velocity of hcp-$Fe_{0.91}Ni_{0.09}$. We conclude that thermal effects likely play a large role in the sound velocities of iron alloys at core conditions, so constraining these effects is critical to further constrain the composition of the core.

From the volume scaling of the phonon DOS, we constrain the 300 K vibrational component of the Grüneisen parameter for hcp-$Fe_{0.91}Ni_{0.09}$ and $Fe_{0.8}Ni_{0.1}Si_{0.1}$. The phonon DOS also provides constraints on the volume dependence of vibrational free energy, which is directly related to the harmonic vibrational component of thermal pressure. By combining the harmonic vibrational component with theoretical estimates of the anharmonic and electronic contributions, we provide an estimate for the total thermal pressure of hcp-$Fe_{0.91}Ni_{0.09}$ and $Fe_{0.8}Ni_{0.1}Si_{0.1}$. The phonon DOS provides access to the harmonic vibrational component of entropy per ^{57}Fe atom, the volume derivative of which is directly related to the product of isothermal bulk modulus and thermal expansion. Therefore, we can apply the isothermal bulk modulus constrained

in Chapter 2 to determine the harmonic vibrational component of thermal expansion for hcp-$Fe_{0.91}Ni_{0.09}$ and $Fe_{0.8}Ni_{0.1}Si_{0.1}$. From the NRIXS data and from the phonon DOS, we present constraints on the kinetic energy per ^{57}Fe atom and on the Lamb-Mössbauer factor, which is related to the mean square displacement. The phonon DOS also provides information on the vibrational component of specific heat, which we present at the end of Chapter 4. In summary, this thesis provides improved constraints on the effects of nickel and silicon on the thermoelastic and vibrational properties of iron, which will aid our community's progress in constraining core composition, the thermal profile of the Earth, and the thermodynamic properties of the core.

Chapter 2

EQUATIONS OF STATE OF IRON-NICKEL-SILICON ALLOYS[1]

2.1 Introduction

Earth models, such as the Preliminary Reference Earth Model (PREM) (*Dziewonski and Anderson*, 1981) and AK135-F (*Kennett et al.*, 1995), provide one-dimensional radial models of the compressional, shear, and bulk sound velocities down to the center of Earth. Combined with a model for the density distribution within Earth, these models provide the adiabatic bulk and shear moduli along this 1-D profile. Cosmochemical studies suggest the Earth is composed primarily of iron alloyed with approximately 5 wt% nickel (*Allègre et al.*, 1995; *McDonough*, 2003). The presence of some amount of light elements (e.g., Si, O, S, C, H) inside the core has been suggested based upon the properties of pure iron and their deviation from these seismically inferred values (e.g., *Allègre et al.*, 1995; *Campbell*, 2016; *Hirose et al.*, 2013; *Li and Fei*, 2014; *McDonough*, 2003; *Ohtani*, 2013).

The equation of state (EOS) and c/a axial ratio of pure hexagonal close packed (hcp)-iron have been well constrained by a powder x-ray diffraction (XRD) study at 300 K, which used tungsten as a pressure marker and helium as a pressure medium (*Dewaele et al.*, 2006). Helium is considered to provide more uniform stress conditions inside the sample chamber compared to other commonly selected pressure media, especially under extreme conditions (*Klotz et al.*, 2009; *Zarochentsev et al.*, 2004). While an iron-nickel diamond anvil cell (DAC) study up to 255 GPa suggested the pressure-volume relation of iron is indistinguishable from that of iron alloyed with 20 at% nickel (*Mao et al.*, 1990), a systematic study evaluating the effect of alloying iron with nickel in a helium pressure medium has not yet been conducted. The *Mao et al.* (1990) study was conducted without the use of a pressure medium and with the platinum pressure calibrant of *Holmes et al.* (1989). Subsequent EOS experiments

[1]This chapter contains material previously published as part of Morrison, R. A., J. M. Jackson, W. Sturhahn, D. Zhang, and E. Greenberg (2018), Equations of state and anisotropy of Fe-Ni-Si alloys, *Journal of Geophysical Research: Solid Earth*, 122, doi:10.1029/2017JB015343.

have predominantly neglected nickel and focused on iron alloyed with various light elements (*Hirose et al.*, 2013; *Poirier*, 1994). However, the presence of non-hydrostatic stress conditions could blur such compositional effects, as it is known that the lattice parameters and resulting unit-cell volumes can be highly sensitive to stress conditions (e.g., *Zhao and Ross*, 2015). The stress conditions inside Earth's core are thought to be hydrostatic, so achieving experimental conditions that are as close to hydrostatic as possible is critical. Determination of these quantities for a suite of iron alloys under low deviatoric stress conditions can provide important constraints on compositional effects.

We present high-precision pressure-volume data for $Fe_{0.91}Ni_{0.09}$ and $Fe_{0.8}Ni_{0.1}Si_{0.1}$ using powder x-ray diffraction at 300 K up to 167 GPa and 175 GPa, respectively. By using tungsten powder as pressure calibrant and helium as a pressure transmitting medium, we minimize error in determination of compositional effects due to pressure calibration and non-hydrostatic stresses. The results are a suite of high fidelity data sets fit with equations of state. By systematically comparing our findings to those of pure iron (*Dewaele et al.*, 2006), we constrain the effect of nickel and silicon on the density, bulk modulus, and bulk sound speed of iron alloys, which is a critical step in constraining the inner core's composition. We find that for iron alloys, constraining the equation of state at 300 K significantly reduces the uncertainty of high-temperature equations of state extrapolated to inner core conditions. After extrapolating our hcp-$Fe_{0.91}Ni_{0.09}$ and hcp-$Fe_{0.8}Ni_{0.1}Si_{0.1}$ equations of state to inner core conditions, we estimate the allowable inner core composition in Fe-Ni-Si composition space and then extrapolate to the Fe-Ni-Si-O-C-S composition space.

2.2 Experimental methods

The samples were synthesized from individual pieces of Ni, Si, and 95%-enriched ^{57}Fe to produce iron containing ∼10 wt% nickel and iron containing ∼10 wt% nickel and ∼5 wt% silicon. The Fe, Ni, and Si pieces were arc-melted in an argon atmosphere and then cold rolled to ∼10 μm. Sample compositions were confirmed with scanning electron microscopy (SEM) measurements to be $Fe_{0.91(1)}Ni_{0.09(1)}$ and $Fe_{0.80(1)}Ni_{0.10(1)}Si_{0.10(1)}$ (atomic units), and sample homogeneity was observed at a scale of 1 μm. The unit-cell volume is insensitive to the ^{57}Fe-enrichment of our samples. We remove the effect of the enrichment of our sample by using the natural isotopic abundances of iron to compute the density.

Table 2.1: Conditions for each x-ray diffraction experimental run

Run	Phase	Composition	P range (GPa)	Diamond culet diameter (μm)	Sample size (μm^2)	Experimental Facility	X-ray focus size (μm^2, FWHM)
FeNi-Run#1	bcc	$Fe_{0.91}Ni_{0.09}$	0–15.2	250	20x20	APS 13-BM-C	15x15
	hcp	$Fe_{0.91}Ni_{0.09}$	15.2–104				
FeNi-Run#2	bcc	$Fe_{0.91}Ni_{0.09}$	1.4–13.1	250	20x35	ALS 12.2.2	20x20
	hcp	$Fe_{0.91}Ni_{0.09}$	15.1–104				
FeNi-Run#3	hcp	$Fe_{0.91}Ni_{0.09}$	14.6–167	100	10x10	APS 13-ID-D	3x3
FeNiSi-Run#1	bcc	$Fe_{0.8}Ni_{0.1}Si_{0.1}$	0–21.6	250	20x20	ALS 12.2.2	20x20
	hcp	$Fe_{0.8}Ni_{0.1}Si_{0.1}$	21.6–88.1				
FeNiSi-Run#2	hcp	$Fe_{0.8}Ni_{0.1}Si_{0.1}$	31.6–175	100	10x10	APS 13-ID-D	3x3

To achieve high pressures, the iron alloys were cut to a range of lateral dimensions and placed in the center of the sample chamber of symmetric DACs with diamond culet diameters of 100 or 250 μm and bevels extending to 300 μm. Rhenium gaskets were used to maintain sample-chamber integrity. Each gasket was indented to a thickness of 20–40 μm and then drilled with a 65–130 μm diameter hole using electric discharge machining. A cubic boron nitride seat on the downstream side of the DAC maximized the accessible 2θ range for x-ray diffraction measurements. We placed tungsten powder proximal to the sample in the sample chamber to act as a pressure calibrant. Tungsten was selected as a pressure calibrant for its high x-ray scattering coefficient, its well-known equation of state (e.g., *Dewaele et al.*, 2004; *Dorogokupets and Oganov*, 2006), and its use as a pressure calibrant in a study on pure iron (*Dewaele et al.*, 2006). The sample chamber was filled with compressed helium at 25,000 PSI as a pressure transmitting medium with the gas loading facility located at Caltech. Helium's remarkably low shear modulus (*Zarochentsev et al.*, 2004) enables the measurement of highly accurate data, including the c/a axial ratios of the hcp-structured phases. The x-ray powder diffraction study on iron by *Dewaele et al.* (2006) also used helium as a pressure medium. Thus, the similarity in sample environments permits a more precise comparison of the iron alloys investigated in this study to those of iron.

Powder x-ray diffraction experiments were conducted at GSECARS' beamlines 13-BM-C and 13-ID-D at the Advanced Photon Source (APS) near Chicago and at beamline 12.2.2 at the Advanced Light Source (ALS) in Berkeley. Each beamline delivered slightly different characteristics of the x-rays for the $Fe_{0.91}Ni_{0.09}$ and $Fe_{0.8}Ni_{0.1}Si_{0.1}$ experimental runs (hereafter referred to as FeNi-Run#1, FeNi-Run#2, FeNi-Run#3, FeNiSi-Run#1, and FeNiSi-Run#2). Specifically, a beam size of $\sim$15 $\times$ 15 μm^2 full-width at half maximum (FWHM) and an energy of 28.57 keV was used at APS sector 13-BM-C for FeNi-Run#1. A beam size of $\sim$20 $\times$ 20 μm^2 FWHM and energies of 30 and 35 keV were used at beamline 12.2.2 at the ALS for FeNiSi-Run#1 and for FeNi-Run#2. A beam size of $\sim$3 $\times$ 3 μm^2 FWHM and an energy of 37.08 keV was used at APS sector 13-ID-D for FeNi-Run#3 and FeNiSi-Run#2. Pressure was increased manually offline for FeNi-Run#1, FeNi-Run#2, and FeNiSi-Run#1. For FeNiSi-Run#2 and FeNi-Run#3 at APS sector 13-ID-D, pressure was increased in situ using a membrane DAC (*Sinogeikin et al.*, 2015). The standard LaB_6 was used to calibrate x-ray diffraction images for all runs except FeNi-

Run#2, when the calibrant CeO_2 was used. Experimental conditions for each run are summarized in Table 2.1.

X-ray diffraction images were integrated with the software Dioptas (*Prescher and Prakapenka*, 2015). Example x-ray diffraction patterns for body centered cubic (bcc)- and hcp-$Fe_{0.91}Ni_{0.09}$ and bcc- and hcp-$Fe_{0.8}Ni_{0.1}Si_{0.1}$ are shown in Figures 2.1 and 2.2, respectively. The structural phase transition from bcc to hcp was identified by the appearance of peaks associated with the hcp phase and the disappearance of peaks associated with the bcc phase. Lattice parameters of the iron alloys and of the tungsten powder were determined using full profile Pawley refinement and were consistent with those obtained using the Pawley refinement approach in the GSAS-II software package (*Toby and Von Dreele*, 2013). The sample and tungsten unit cell volumes were calculated from the refined lattice parameters a for bcc phases and a and c for hcp phases.

The tungsten equation of state from *Dorogokupets and Oganov* (2006) was used to determine sample pressure. This equation of state has been calibrated with modern shock wave, x-ray, and ultrasonic measurements collectively. Use of this pressure calibration allows for a systematic comparison of our $Fe_{0.91}Ni_{0.09}$ and $Fe_{0.8}Ni_{0.1}Si_{0.1}$ studies with the study by *Dewaele et al.* (2006) on pure iron, which also used the *Dorogokupets and Oganov* (2006) tungsten pressure calibration.

Lattice parameter error analysis

The lattice parameter uncertainties for $Fe_{0.91}Ni_{0.09}$, $Fe_{0.8}Ni_{0.1}Si_{0.1}$, and tungsten were obtained from the refinement of each x-ray diffraction pattern. However, full-profile refinement methods are known to significantly underestimate lattice parameter uncertainties (*Angel*, 2000). We estimate the lattice parameter uncertainty with scaling factors k, where the lattice parameter uncertainty σ obtained from refinement of an individual pattern for a given phase is replaced by $k\sigma$ (*Angel*, 2000). We apply the same scaling parameter k to all data within a given phase. To estimate the uncertainty scaling parameters for each phase of a particular composition (bcc Fe-alloys, hcp Fe-alloys, and bcc-tungsten), we used two general principles. First, when fitting an equation of state to experimental pressure-volume data from a single run, the reduced goodness of fit (χ^2) should be close to 1. The uncertainty on each data point should not be smaller than is justified by the scatter of the data, assuming the

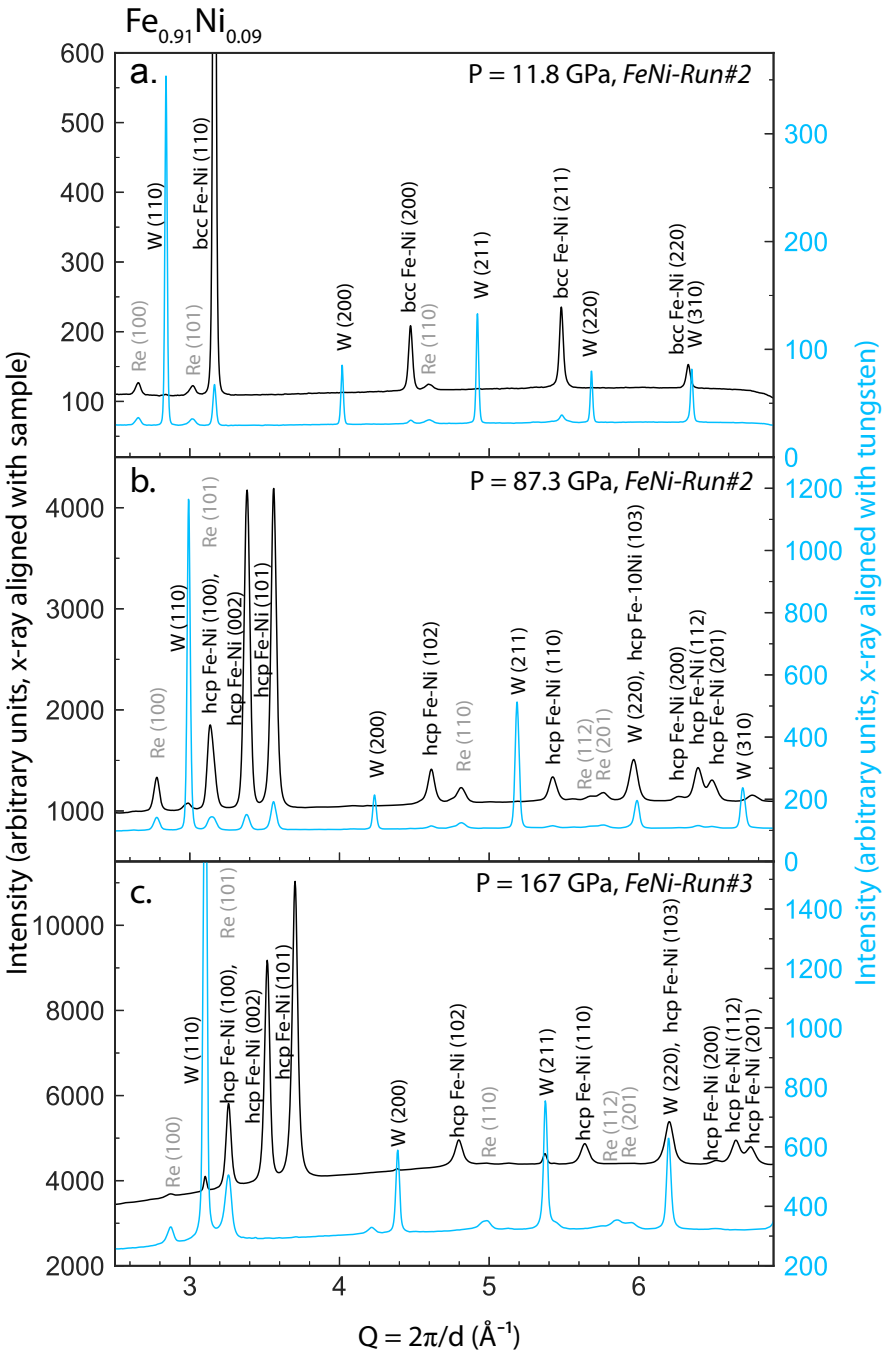

Figure 2.1: X-ray diffraction patterns at 300 K for a) bcc-$Fe_{0.91}Ni_{0.09}$ at 11.8 GPa, b) hcp-$Fe_{0.91}Ni_{0.09}$ at 87.3 GPa, and c) hcp-$Fe_{0.91}Ni_{0.09}$ at 167 GPa. Patterns are plotted against Q ($=2\pi/d$) instead of 2θ to remove the dependency on wavelength. Patterns were collected with the sample (black curves, left y-axis) and with the tungsten powder (blue curves, right y-axis) aligned with the x-ray focus. Patterns are plotted before background subtraction.

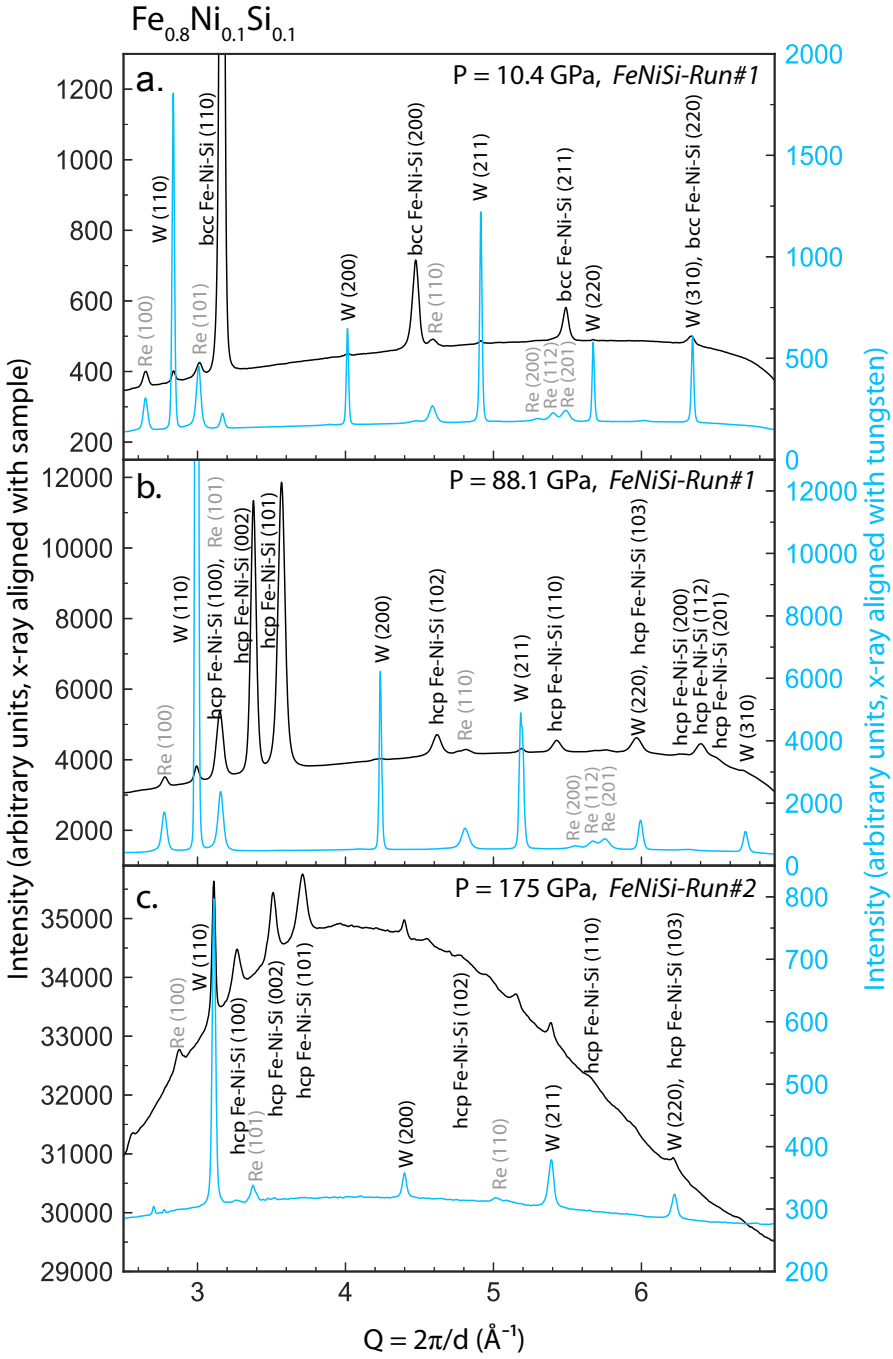

Figure 2.2: X-ray diffraction patterns at 300 K for a) bcc-$Fe_{0.8}Ni_{0.1}Si_{0.1}$ at 10.4 GPa, b) hcp-$Fe_{0.8}Ni_{0.1}Si_{0.1}$ at 88.1 GPa, and c) hcp-$Fe_{0.8}Ni_{0.1}Si_{0.1}$ at 175 GPa. Patterns are plotted against Q ($=2\pi/d$) instead of against 2θ to remove the dependency on wavelength. Patterns were collected with the sample (black curves, left y-axis) and with the tungsten powder (blue curves, right y-axis) aligned with the x-ray focus. Patterns are plotted before background subtraction.

model to fit the data (i.e., the EOS) is reasonable. Second, when an equation of state is fit to data combined from multiple runs, the χ^2 should be approximately 1, because a better estimate of uncertainty is obtained from multiple repetitions of the same experiment than is obtained from a single experiment; thus, when an equation of state is fit to data combined from multiple runs, the reduced χ^2 should be approximately 1. As a result of this uncertainty estimation, the reduced goodness of fit (χ^2) is $\sim$1 for each of our equation of state fits.

Proper propagation of uncertainty from a particular pressure calibrant requires knowledge of the corresponding error correlation matrix of the data used to create the pressure scale. As the error correlation matrix for the *Dorogokupets and Oganov* (2006) tungsten equation of state is not available, the pressure calibration is treated as given. Nevertheless, the uncertainty for the *Dorogokupets and Oganov* (2006) tungsten pressure standard agrees with aluminum, gold, copper, platinum, and tantalum pressure standards within 2 GPa at 160 GPa and 300 K (*Dorogokupets and Oganov*, 2006), which is of comparable magnitude with our reported pressure uncertainty (see Tables A.1–A.4 in Appendix A).

2.3 X-ray diffraction results

$Fe_{0.91}Ni_{0.09}$

X-ray diffraction images were collected from pressures ranging from 0 to 167 GPa over three separate experimental runs (FeNi-Run#1, FeNi-Run#2, FeNi-Run#3) at 300 K. Example x-ray diffraction patterns for $Fe_{0.91}Ni_{0.09}$ are shown in Figure 2.1. $Fe_{0.91}Ni_{0.09}$ is stable in the bcc-structure at ambient conditions, and a phase transition to the hcp-structure was constrained to pressures between 12.5 GPa and 17.2 GPa. $Fe_{0.91}Ni_{0.09}$ is thought to be stable in the hcp phase in the Earth's inner core (*Tateno et al.*, 2012). Minor texturing was observed in the x-ray diffraction images at all pressures due to cold rolling of the samples during synthesis. However, the sample x-ray diffraction peak 2θ positions did not vary radially around the x-ray diffraction image, indicating the minor texturing of the sample had a negligible effect on the determined peak positions. The bcc-$Fe_{0.91}Ni_{0.09}$ lattice parameters were determined from the d-spacings of the following four reflections: 110, 200, 211, and 220. The hcp-$Fe_{0.91}Ni_{0.09}$ lattice parameters were determined from the d-spacings of the following nine reflections: 100, 002, 101, 102, 110, 103, 200, 112, and 201.

The bcc-tungsten lattice parameters were determined from the d-spacings of the following five reflections: 110, 200, 211, 220, and 310. Lattice parameters, volumes, and pressures are given in Tables A.1 and A.2 in Appendix A.

$Fe_{0.8}Ni_{0.1}Si_{0.1}$

X-ray diffraction images were collected from pressures ranging from 0 to 175 GPa over two separate experimental runs (FeNiSi-Run#1, FeNiSi-Run#2) at 300 K. Example x-ray diffraction patterns for $Fe_{0.8}Ni_{0.1}Si_{0.1}$ are shown in Figure 2.2. $Fe_{0.8}Ni_{0.1}Si_{0.1}$ is also stable in the bcc structure at ambient conditions and undergoes a phase transition to the hcp-structure at a higher pressure than $Fe_{0.91}Ni_{0.09}$. The bcc-hcp phase transition for $Fe_{0.8}Ni_{0.1}Si_{0.1}$ was constrained to be above 18.7 GPa and below 24.5 GPa, demonstrating that 10 at% Si stabilizes the bcc phase by about 6 GPa. Similar to the $Fe_{0.91}Ni_{0.09}$ samples, minor texturing was observed in the $Fe_{0.8}Ni_{0.1}Si_{0.1}$ samples at all pressures due to cold rolling. As in the case of the $Fe_{0.91}Ni_{0.09}$ samples, the sample x-ray diffraction peak 2θ positions did not vary radially around the x-ray diffraction image. The higher background in FeNiSi-Run#2 at higher pressures is likely due to a combination of Compton scattering from thicker diamond anvils ($\sim$2.2 mm compared with $\sim$2.0 mm) and minor sample thickness variations at higher pressures. For consistency, the bcc- and hcp-$Fe_{0.8}Ni_{0.1}Si_{0.1}$ lattice parameters and the bcc-tungsten lattice parameters were constrained using the same set of reflections as for the $Fe_{0.91}Ni_{0.09}$ data in this study. Lattice parameters, volumes, and pressures are given in Tables A.3 and A.4 in Appendix A.

2.4 Equations of state

We used the open-source software package MINeral physics UTIlities (MINUTI) version 2.0.0 (*Sturhahn*, 2017) to fit both Vinet and third order Birch-Murnaghan EOSs to the 300 K bcc- and hcp-$Fe_{0.91}Ni_{0.09}$ and $Fe_{0.8}Ni_{0.1}Si_{0.1}$ data. For each phase of each composition, we combine all runs into a single data set and fit three parameters: ambient volume V_0, ambient isothermal bulk modulus K_{T0}, and the ambient pressure derivative of the bulk modulus K'_{T0}. No parameters were fixed in these equation of state fits, and no priors based on other studies were applied. The resulting equation of state parameters are given in Table 2.2, and the correlations between model parameters are given in Tables 2.3 and 2.4.

Table 2.2: Equation of state fitting parameters

Ref	Phase	Composition	V_0 (Å^3)	K_0 (GPa)	K_0'	P range (GPa)	P medium	P gauge	EOS
This study	bcc	$Fe_{0.91}Ni_{0.09}$	23.635(6)	146.7(30)	6.42(60)	0-15.2	He	W	Vinet
			23.635(6)	146.8(31)	6.39(64)				BM3
This study	bcc	$Fe_{0.8}Ni_{0.1}Si_{0.1}$	23.385(9)	155.6(74)	5.7(12)	0-21.6	He	W	Vinet
			23.384(9)	155.9(75)	5.6(13)				BM3
This study	hcp	$Fe_{0.91}Ni_{0.09}$	22.505(42)	157.5(39)	5.61(10)	14.6-167	He	W	Vinet
			22.436(40)	167.4(40)	5.07(10)				BM3
This study	hcp	$Fe_{0.8}Ni_{0.1}Si_{0.1}$	22.952(72)	125.2(46)	6.38(12)	21.6-175	He	W	Vinet
			22.837(71)	135.8(52)	5.84(14)				BM3
Dewaele et al. (2006)	bcc	Fe (Our fit)[a]	23.524(18)	168.1(83)	4.7(13)	0-14.6	He	W, ruby	Vinet
Dewaele et al. (2006)	hcp	Fe	22.428(98)	163.4(79)	5.38(16)	17-197	He	W, ruby	Vinet
			22.468(24)	165(fixed)	4.97(4)				BM3
		(Refit)[b]	22.425(54)	162.9(45)	5.40(9)				Vinet

[a]As *Dewaele et al.* (2006) report no bcc-iron equation of state, we fit a Vinet EOS to their reported bcc-iron data.
[b]We refit hcp-iron data (*Dewaele et al.*, 2006) with a Vinet EOS to obtain fit parameter correlations. Our refit is consistent with the original Vinet EOS fit by *Dewaele et al.* (2006).

Table 2.3: Vinet equation of state parameter correlations. Correlations for bcc- and hcp-Fe are for our fits to data from *Dewaele et al.* (2006).

	V_0	K_0	K_0'		V_0	K_0	K_0'
	bcc $Fe_{0.91}Ni_{0.09}$				hcp $Fe_{0.91}Ni_{0.09}$		
V_0	+1.00	-0.65	+0.48	V_0	+1.00	-0.98	+0.93
K_0		+1.00	-0.96	K_0		+1.00	-0.98
K_0'			+1.00	K_0'			+1.00
	bcc $Fe_{0.8}Ni_{0.1}Si_{0.1}$				hcp $Fe_{0.8}Ni_{0.1}Si_{0.1}$		
V_0	+1.00	-0.42	+0.30	V_0	+1.00	-0.99	+0.96
K_0		+1.00	-0.97	K_0		+1.00	-0.99
K_0'			+1.00	K_0'			+1.00
	bcc Fe (*Dewaele et al.*, 2006)				hcp Fe (*Dewaele et al.*, 2006)		
V_0	+1.00	-0.82	+0.66	V_0	+1.00	-0.98	+0.93
K_0		+1.00	-0.96	K_0		+1.00	-0.98
K_0'			+1.00	K_0'			+1.00

Table 2.4: Third order Birch-Murnaghan equation of state parameter correlations

	V_0	K_0	K_0'		V_0	K_0	K_0'
	bcc $Fe_{0.91}Ni_{0.09}$				hcp $Fe_{0.91}Ni_{0.09}$		
V_0	+1.00	-0.65	+0.48	V_0	+1.00	-0.98	+0.93
K_0		+1.00	-0.96	K_0		+1.00	-0.98
K_0'			+1.00	K_0'			+1.00
	bcc $Fe_{0.8}Ni_{0.1}Si_{0.1}$				hcp $Fe_{0.8}Ni_{0.1}Si_{0.1}$		
V_0	+1.00	-0.42	+0.30	V_0	+1.00	-0.99	+0.96
K_0		+1.00	-0.97	K_0		+1.00	-0.99
K_0'			+1.00	K_0'			+1.00

$Fe_{0.91}Ni_{0.09}$

We present the bcc- and hcp-$Fe_{0.91}Ni_{0.09}$ pressure-volume data and Vinet equation of state fits in Figure 2.3. We compare to the hcp-Fe x-ray diffraction study up to 205 GPa at 300 K, which was conducted with a helium pressure medium and a tungsten pressure calibrant and fit with a Vinet EOS (*Dewaele et al.*, 2006). We also compare to the hcp-Fe and hcp-$Fe_{0.8}Ni_{0.2}$ x-ray diffraction studies up to 300.6 GPa and 255.0 GPa, respectively, at 300 K, which were conducted with no pressure medium and a platinum pressure calibrant and fit with third order Birch-Murnaghan EOSs (*Mao et al.*, 1990). In the lower panel of Figure 2.3, the hcp-$Fe_{0.91}Ni_{0.09}$ equation of state from

this study was subtracted from all hcp data and fits to elucidate the difference between each equation of state. When plotting uncertainty on data in the lower panel, we employ the effective variance method, whereby the uncertainty in pressure is projected into an effective contribution to volume using error propagation. This allows us to effectively one-dimensionalize the plot to more easily distinguish between equations of state. Note a pressure medium dramatically improves the statistical quality of the data. Although uncertainties for the pressure-volume data were not published in *Dewaele et al.* (2006), and are thus not shown in Figure 2.3, one can see that the volumes of iron and $Fe_{0.91}Ni_{0.09}$ diverge by $\sim$0.1 Å^3 at $\sim$150 GPa. Therefore, only with high-precision x-ray diffraction data can such differences, or lack thereof, be resolved (Figures 2.3–2.5).

$Fe_{0.8}Ni_{0.1}Si_{0.1}$

The bcc- and hcp-$Fe_{0.8}Ni_{0.1}Si_{0.1}$ pressure-volume data and Vinet EOS fits are displayed in Figure 2.4. We compare to the hcp-$Fe_{0.83}Ni_{0.09}Si_{0.08}$ and hcp-$Fe_{0.93}Si_{0.07}$ x-ray diffraction studies up to 374 GPa and 252 GPa, respectively, which were conducted with a NaCl pressure medium and fit with third order Birch-Murnaghan equations of state (*Asanuma et al.*, 2011). The NaCl pressure medium also served as a pressure calibrant; however, uncertainties on pressure are not published. We also compare to the hcp-$Fe_{0.85}Si_{0.15}$ x-ray diffraction study up to 54.3 GPa, which was conducted in an ethanol-methanol (1:4) pressure medium with a gold pressure calibrant and fit with a third-order Birch-Murnaghan equation of state (*Lin*, 2003). The *Lin* (2003) $Fe_{0.85}Si_{0.15}$ study collected x-ray diffraction data both on compression and decompression, and the bcc-hcp transition occurs at lower pressures upon decompression. The hcp-$Fe_{0.91}Ni_{0.09}$ Vinet equation of state (this study) and the pure iron Vinet equation of state (*Dewaele et al.*, 2006) are also plotted for reference. In the lower panel of Figure 2.4, the hcp-$Fe_{0.8}Ni_{0.1}Si_{0.1}$ equation of state from our study was subtracted from all hcp data and EOS fits to elucidate the difference between each equation of state. As described above, when plotting the uncertainty on data in the lower panel, we employ the effective variance method to one-dimensionalize the uncertainties. As uncertainties on pressure are not reported in *Asanuma et al.* (2011), the uncertainty for the *Asanuma et al.* (2011) data cannot be properly calculated in the lower panel of Figure 2.4. Note that a helium pressure medium improves the statistical quality

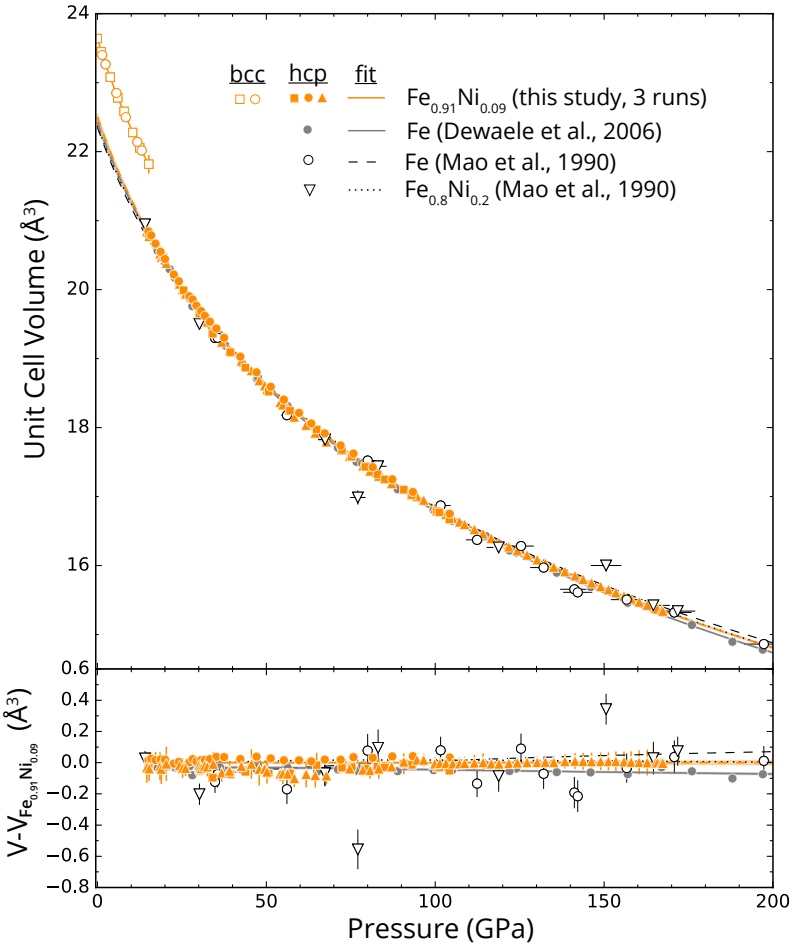

Figure 2.3: Volume-pressure relation for data and equation of state fits for bcc- and hcp-$Fe_{0.91}Ni_{0.09}$, where the symbols refer to different experimental runs. We compare to hcp-Fe (*Dewaele et al.*, 2006), hcp-Fe (*Mao et al.*, 1990), and hcp-$Fe_{0.8}Ni_{0.2}$ (*Mao et al.*, 1990). In the bottom panel, the hcp-$Fe_{0.91}Ni_{0.09}$ EOS (this study) is subtracted from all hcp data and fits.

of hcp-iron alloy pressure-volume data.

Comparison of Fe-Ni-Si alloys

In Figure 2.5, we compare the fitted equations of state for the three iron alloy studies conducted in a helium pressure transmitting medium: bcc- and hcp-$Fe_{0.91}Ni_{0.09}$ (this study), bcc- and hcp-$Fe_{0.8}Ni_{0.1}Si_{0.1}$ (this study), and hcp-Fe (*Dewaele et al.*, 2006). As *Dewaele et al.* (2006) do not report an equation of state for bcc-Fe, we fit their bcc-Fe pressure-volume data with a Vinet equation of state using MINUTI. The resulting EOS parameters and their correlations are given in Tables 2.2 and 2.3, respectively. The addition of 9 at% Ni to bcc-

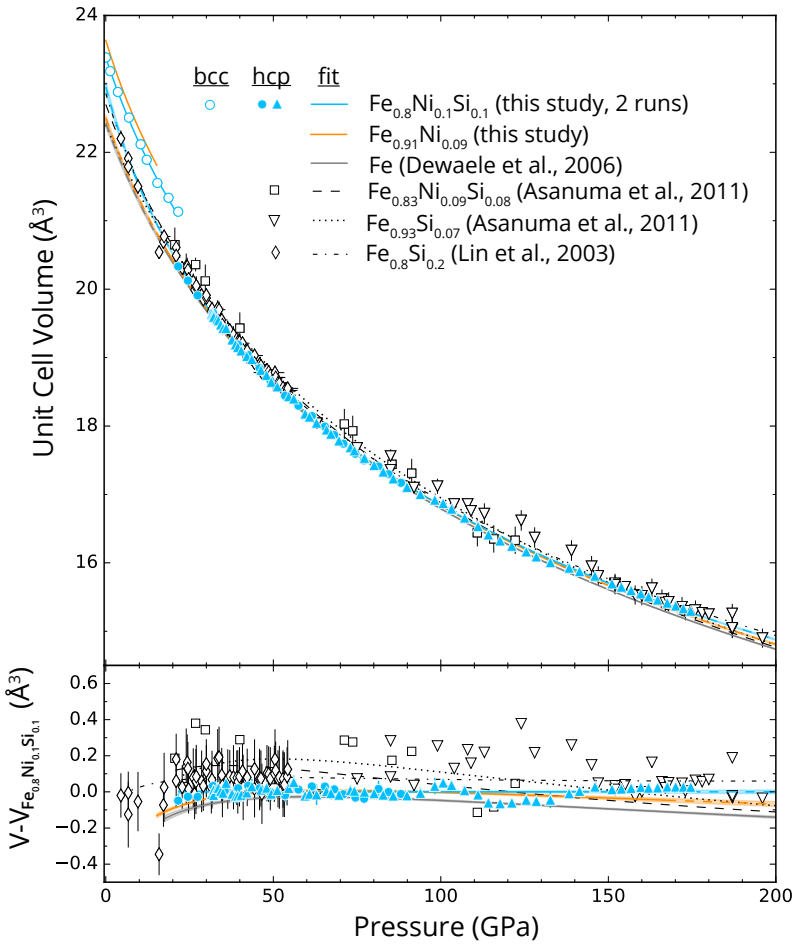

Figure 2.4: Volume-pressure relation for data and equation of state fits for bcc- and hcp-$Fe_{0.8}Ni_{0.1}Si_{0.1}$, where the symbols refer to different experimental runs. We compare to hcp-$Fe_{0.83}Ni_{0.09}Si_{0.08}$ (*Asanuma et al.*, 2011), hcp-$Fe_{0.93}Si_{0.07}$ (*Asanuma et al.*, 2011), and hcp-$Fe_{0.85}Si_{0.15}$ (*Lin*, 2003). For reference, the equations of state for $Fe_{0.91}Ni_{0.09}$ (this study) and Fe (*Dewaele et al.*, 2006) are also plotted. In the bottom panel, the hcp-$Fe_{0.8}Ni_{0.1}Si_{0.1}$ EOS (this study) is subtracted from all hcp data and fits.

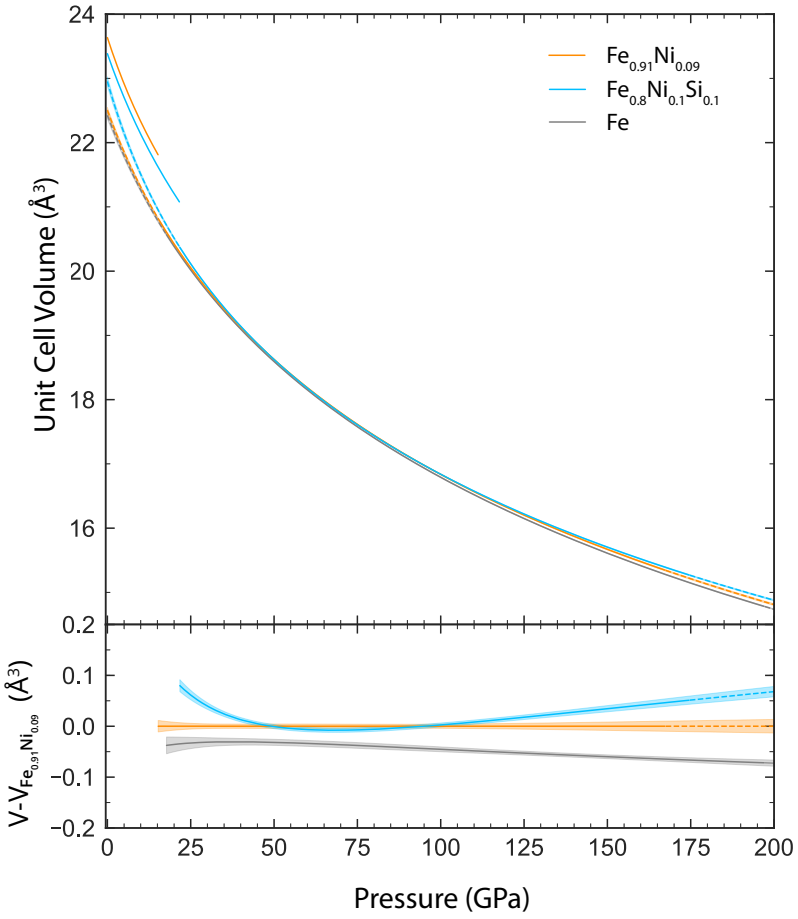

Figure 2.5: Volume-pressure relation for bcc- and hcp-$Fe_{0.91}Ni_{0.09}$ (this study), bcc- and hcp-$Fe_{0.8}Ni_{0.1}Si_{0.1}$ (this study), and hcp-Fe (*Dewaele et al.*, 2006). All three studies were performed with a helium pressure transmitting medium and used the tungsten pressure calibration by *Dorogokupets and Oganov* (2006). In the bottom panel, the hcp-$Fe_{0.91}Ni_{0.09}$ EOS (this study) is subtracted from all hcp fits.

iron has a measurable effect on the equation of state (Figure 2.6). The further addition of 10 at% Si to bcc-iron decreases the volume and increases the bcc stability field, in agreement with *Zhang and Guyot* (1999) and *Lin* (2003). The addition of 9 at% Ni to hcp-iron increases the volume slightly by ∼0.5% at all pressures. The further addition of 10 at% Si results in greater curvature of the pressure-volume relation, thus exhibiting a measurable increase in the pressure derivative of bulk modulus K'_{T0}.

Confidence ellipses provide a valuable assessment tool for comparing model parameters, their uncertainties, and their correlations for equation of state fits. In Figure 2.6, we plot the K_{T0} and K'_{T0} 68% joint confidence ellipses for

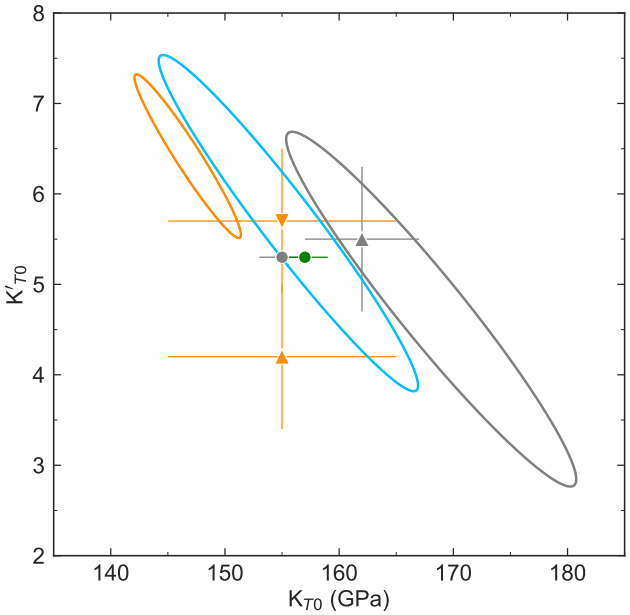

Figure 2.6: 68% confidence ellipses for bulk modulus at 0 GPa K_{T0} and for the pressure derivative of bulk modulus at 0 GPa K'_{T0} for bcc-$Fe_{0.91}Ni_{0.09}$ (orange ellipse), bcc-$Fe_{0.8}Ni_{0.1}Si_{0.1}$ (blue ellipse), and our Vinet fit to bcc-Fe data of *Dewaele et al.* (2006) (gray ellipse). Equations of state without reported correlation matrices are plotted as points with error bars as reported: bcc-Fe (gray triangle), bcc-$Fe_{0.95}Ni_{0.05}$ (orange upright triangle), and bcc-$Fe_{0.90}Ni_{0.10}$ (orange inverted triangle) (*Takahashi et al.*, 1968); bcc-Fe (gray circle) and bcc-$Fe_{0.91}Si_{0.09}$ (green circle) (*Zhang and Guyot*, 1999).

our bcc-$Fe_{0.91}Ni_{0.09}$ and bcc-$Fe_{0.8}Ni_{0.1}Si_{0.1}$ studies. We compare these results to our fit of the bcc-Fe data from *Dewaele et al.* (2006), to the bcc-Fe, bcc-$Fe_{0.95}Ni_{0.05}$, and bcc-$Fe_{0.90}Ni_{0.10}$ equations of state by *Takahashi et al.* (1968), and to the bcc-Fe and bcc-$Fe_{0.91}Si_{0.09}$ equations of state by *Zhang and Guyot* (1999). The bcc-$Fe_{0.91}Ni_{0.09}$ confidence ellipse is noticeably smaller than the bcc-$Fe_{0.8}Ni_{0.1}Si_{0.1}$ and bcc-Fe (*Dewaele et al.*, 2006) confidence ellipses due the higher density of data in the bcc-$Fe_{0.91}Ni_{0.09}$ data set.

In Panel a of Figure 2.7, we plot the K_{T0} and K'_{T0} 68% and 95% joint confidence ellipses for our hcp-$Fe_{0.91}Ni_{0.09}$ and $Fe_{0.8}Ni_{0.1}Si_{0.1}$ studies. We compare to the reported equation of state parameters from iron alloy x-ray diffraction studies at 300 K described in earlier in this section (*Asanuma et al.*, 2011; *Dewaele et al.*, 2006; *Lin*, 2003; *Mao et al.*, 1990). Confidence ellipses for these studies were not plotted in Figure 2.7A as none of these studies reported fit-parameter correlations. Uncertainties for parameters are plotted as reported. While the

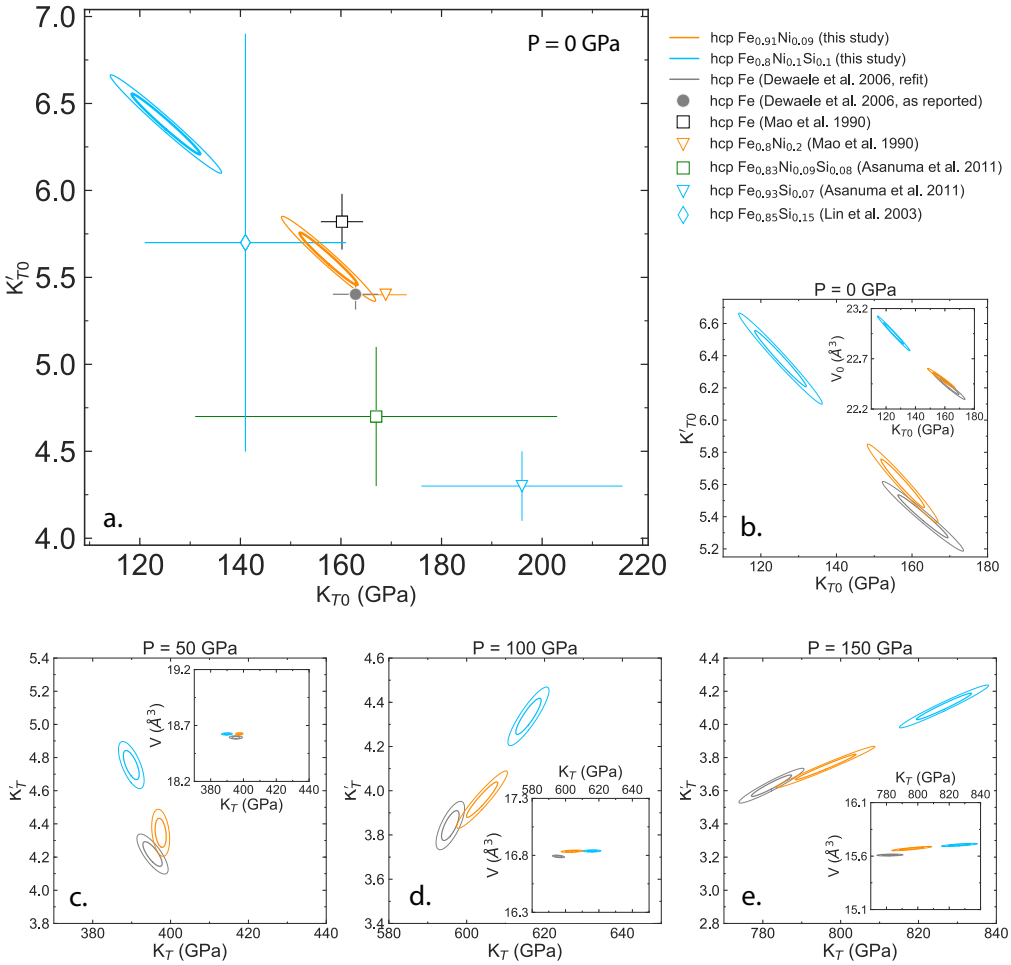

Figure 2.7: (a) Confidence ellipses for EOS parameters K_{T0} (bulk modulus at 0 GPa) and K'_{T0} (pressure derivative of bulk modulus at 0 GPa) for hcp-$Fe_{0.91}Ni_{0.09}$ and $Fe_{0.8}Ni_{0.1}Si_{0.1}$. Outer thin ellipses represent 95% confidence; inner bold ellipses represent 68% confidence. EOSs without reported correlation matrices are plotted with error bars as reported (see legend). (b-e) Confidence ellipses for K_T and K'_T for hcp-$Fe_{0.91}Ni_{0.09}$, hcp-$Fe_{0.8}Ni_{0.1}Si_{0.1}$, and our refitting of hcp-Fe data (*Dewaele et al.*, 2006) anchored at a variety of pressures. When the EOS is anchored at a pressure outside or near the endpoints of the data range, the EOS parameters are strongly correlated.

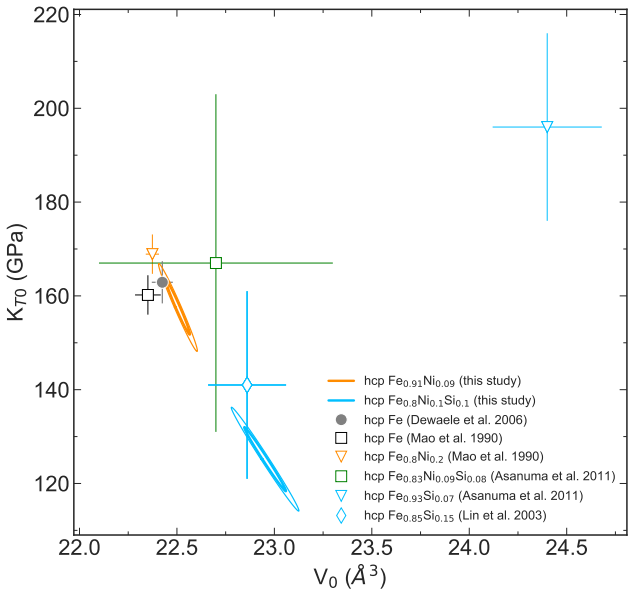

Figure 2.8: Confidence ellipses for EOS parameters V_0 (unit cell volume at 0 GPa) and K_{T0} (bulk modulus at 0 GPa) for hcp-$Fe_{0.91}Ni_{0.09}$ and hcp-$Fe_{0.8}Ni_{0.1}Si_{0.1}$. EOSs without reported correlation matrices are plotted with error bars as reported (see legend). Outer thin ellipses represent 95% confidence; inner bold ellipses represent 68% confidence.

K_{T0} and K'_{T0} for hcp-$Fe_{0.91}Ni_{0.09}$ (this study), hcp-Fe (*Dewaele et al.*, 2006), and hcp-Fe and hcp-$Fe_{0.8}Ni_{0.2}$ (*Mao et al.*, 1990) have similar values, we find adding 10 at% Ni to Fe slightly decreases K_{T0} and increases K'_{T0}, whereas the opposite conclusions would be reached from the study of (*Mao et al.*, 1990). Note that the effects of Si on the equation of state parameters K_{T0} and K'_{T0} of Fe and Fe-Ni alloys were previously poorly constrained and produced contradictory conclusions. We find adding 10 at% Si to our iron-nickel alloy decreases K_{T0} and increases K'_{T0}. By using the same pressure calibrants and a helium pressure transmitting media, the hcp-$Fe_{0.91}Ni_{0.09}$ and hcp-$Fe_{0.8}Ni_{0.1}Si_{0.1}$ studies paired with the hcp-Fe *Dewaele et al.* (2006) study provide a systematic constraint on the effect of Si on Fe and Fe-Ni alloys with high statistical quality. Similar plots demonstrating the V_0 and K_{T0} correlation and the V_0 and K'_{T0} correlation for our hcp-$Fe_{0.91}Ni_{0.09}$ and $Fe_{0.8}Ni_{0.1}Si_{0.1}$ studies are shown in Figures 2.8–2.9.

The equation of state fit parameters are typically defined at 0 GPa for convenience (e.g., V_0, K_{T0}, and K'_{T0}). However, the equation of state parameters could just as easily be defined at any other pressure (e.g., $V_{P=50}$, $K_{T,P=50}$,

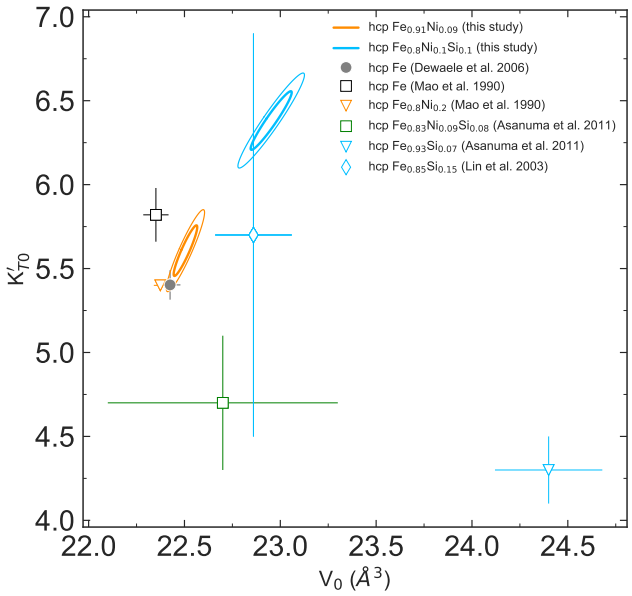

Figure 2.9: Confidence ellipses for EOS parameters V_0 (unit cell volume at 0 GPa) and K'_{T0} (bulk modulus pressure derivative at 0 GPa) for hcp-$Fe_{0.91}Ni_{0.09}$ and hcp-$Fe_{0.8}Ni_{0.1}Si_{0.1}$. EOSs without reported correlation matrices are plotted with error bars as reported (see legend). Outer thin ellipses represent 95% confidence; inner bold ellipses represent 68% confidence.

and $K'_{T,P=50}$). As hcp-structure iron alloys are unstable and unquenchable at ambient pressure and temperature, we highlight the importance of comparing various equations of state at pressures where the hcp-phases are stable. For instance, at 0 GPa it is not a surprise that the correlation of parameters is quite large for the hcp phases, especially when compared to the correlation of the parameters of the bcc-phases (Table 2.3).

To clearly identify the effects of Ni and Si on the equation of state of hcp-iron, we also plot confidence ellipses at 50, 100, and 150 GPa, all of which are within the hcp stability field and within the experimentally measured regions. We plot confidence ellipses from the three studies that were conducted with a helium pressure medium and used the *Dorogokupets and Oganov* (2006) tungsten pressure calibration: hcp-$Fe_{0.91}Ni_{0.09}$ (this study), hcp-$Fe_{0.8}Ni_{0.1}Si_{0.1}$ (this study), and hcp-Fe (*Dewaele et al.*, 2006). As *Dewaele et al.* (2006) do not publish EOS parameter correlations, we refit their hcp-Fe data with a Vinet EOS in MINUTI to plot confidence ellipses in Figure 2.7b–e. The resulting EOS parameters and correlations from our fit to the hcp-Fe pressure-volume data from *Dewaele et al.* (2006) are given in Tables 2.2 and 2.3, respectively.

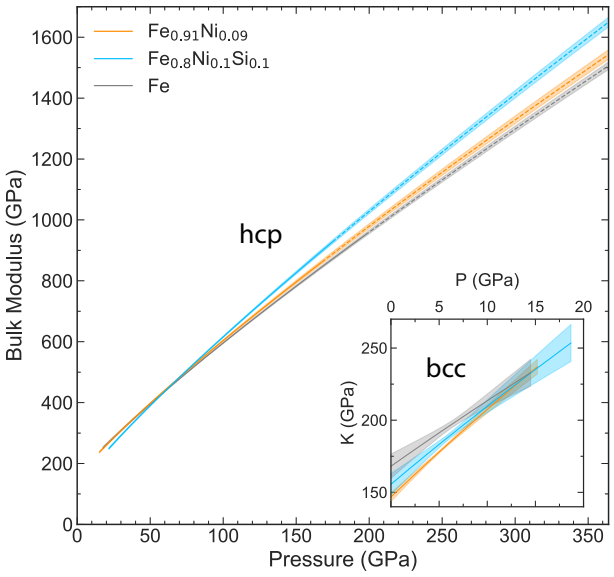

Figure 2.10: Isothermal bulk modulus at 300 K as a function of pressure for Vinet EOSs of hcp-$Fe_{0.91}Ni_{0.09}$, hcp-$Fe_{0.8}Ni_{0.1}Si_{0.1}$, and our refitting of hcp-Fe data reported in *Dewaele et al.* (2006). The uncertainties (shaded) reflect error propagation that includes parameter correlations. Inset: Isothermal bulk modulus at 300 K as a function of pressure for Vinet EOSs of bcc-$Fe_{0.91}Ni_{0.09}$, bcc-$Fe_{0.8}Ni_{0.1}Si_{0.1}$, and our fit of bcc-Fe data reported in *Dewaele et al.* (2006).

In Figure 2.7c, note the decrease in correlation between K_T and K'_T at 50 GPa, compared to that at 0 GPa (Figure 2.7b). At higher pressures, the confidence ellipses demonstrate positive correlation, and the correlation again increases with increasing pressure. At 50 GPa, the low correlation between K_T and K'_T allows the effect of alloying iron with Ni and Si to be more readily observed. Regardless of which pressure is chosen as an anchor for the equation of state parameters, 9 at% nickel slightly increases the bulk modulus pressure derivative of hcp-iron, and 10 at% silicon noticeably increases the bulk modulus pressure derivative of hcp-$Fe_{0.91}Ni_{0.09}$. This effect is most evident in Figure 2.10 where the isothermal bulk moduli of bcc- and hcp-$Fe_{0.91}Ni_{0.09}$ (this study), $Fe_{0.8}Ni_{0.1}Si_{0.1}$ (this study), and Fe (*Dewaele et al.*, 2006) are plotted as a function of pressure. The plotted uncertainties reflect error propagation that includes parameter correlations.

The density of bcc- and hcp-$Fe_{0.91}Ni_{0.09}$ (this study), $Fe_{0.8}Ni_{0.1}Si_{0.1}$ (this study), and Fe (*Dewaele et al.*, 2006) are also plotted as a function of pressure with appropriate error propagation of the fit parameters (Figure 2.11). The densities of $Fe_{0.91}Ni_{0.09}$ and $Fe_{0.8}Ni_{0.1}Si_{0.1}$ are computed assuming natural iron isotopic

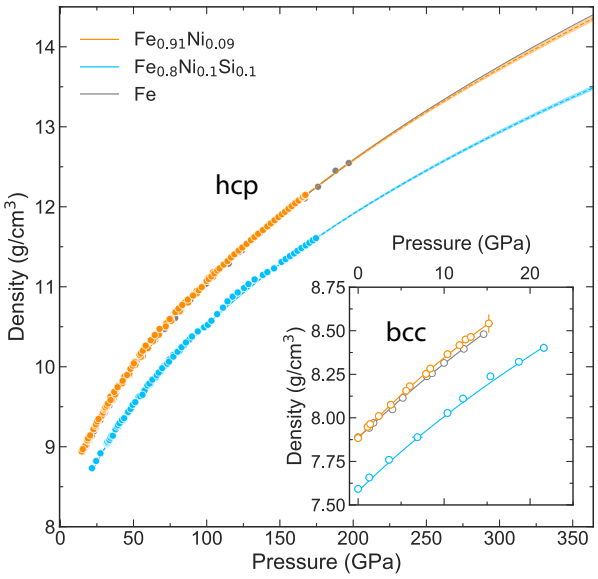

Figure 2.11: Density at 300 K as a function of pressure for bcc- and hcp-$Fe_{0.91}Ni_{0.09}$, bcc- and hcp-$Fe_{0.8}Ni_{0.1}Si_{0.1}$, and our refitting of hcp-Fe data reported in *Dewaele et al.* (2006), all assuming natural levels of ^{57}Fe enrichment. Open circles refer to bcc-structured data; filled circles refer to hcp-structured data. The uncertainties (shaded) reflect error propagation that includes parameter correlations.

abundance. We find hcp-Fe and hcp-$Fe_{0.91}Ni_{0.09}$ are virtually indistinguishable in the pressure range investigated, but small measurable differences in their EOSs produce an hcp-$Fe_{0.91}Ni_{0.09}$ that is 0.3% lighter than pure iron at 330 GPa and 300 K. As expected, silicon substantially decreases the density of iron or of an iron-nickel alloy. The addition of 10 at% Si decreases the density of hcp-$Fe_{0.91}Ni_{0.09}$ by $\sim$5% over all pressures investigated.

Bulk sound speed is of interest as it is related to the seismically observable compressional and shear sound velocities v_P and v_S. To determine bulk sound speed for hcp alloys, we first convert the experimentally constrained isothermal bulk modulus to an adiabatic bulk modulus with the thermal EOS parameters $\Theta_0 = 417$ K, $\gamma_0 = 2.0$, and $q = 1.0$. (See Section 2.5 for these details.) For bcc alloys, we assume the adiabatic and isothermal bulk moduli are approximately equal. We then calculate bulk sound speed at 300 K from the adiabatic bulk modulus combined with our experimentally determined density. We compare the bulk sound speeds of bcc- and hcp-$Fe_{0.91}Ni_{0.09}$ (this study), bcc- and hcp-$Fe_{0.8}Ni_{0.1}Si_{0.1}$ (this study), and hcp-Fe (*Dewaele et al.*, 2006) as a function of density at 300 K using the natural isotopic abundance of iron in Figure 2.12.

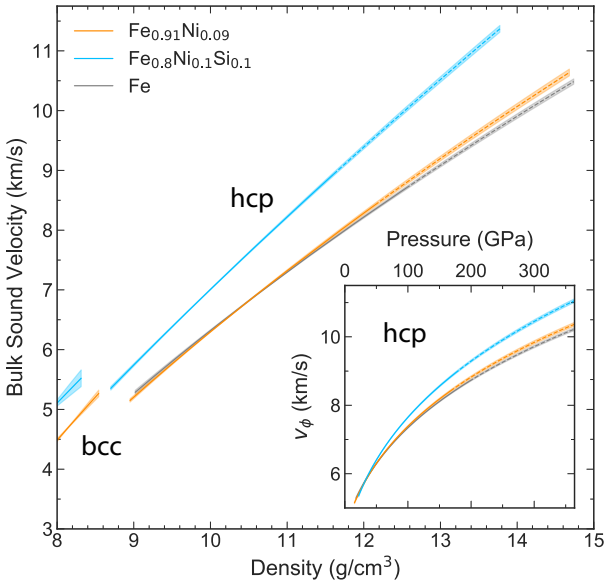

Figure 2.12: A Birch plot of bulk sound speed v_ϕ as a function of density at 300 K. Isothermal Vinet EOSs for bcc- and hcp-$Fe_{0.91}Ni_{0.09}$, hcp-$Fe_{0.8}Ni_{0.1}Si_{0.1}$, and our refitting of hcp-Fe (*Dewaele et al.*, 2006) are paired with thermal EOS parameters $\Theta_0 = 417$ K, $\gamma_0 = 2.0$, and $q = 1.0$ at 300 K. The uncertainties (shaded) reflect error propagation that includes parameter correlations for V_0, K_{T0}, and K'_{T0}. The hcp phases are plotted up to 364 GPa. Inset: Bulk sound speed at 300 K as a function of pressure for Vinet EOSs of hcp-$Fe_{0.91}Ni_{0.09}$, hcp-$Fe_{0.8}Ni_{0.1}Si_{0.1}$, and our refitting of hcp-Fe data reported in *Dewaele et al.* (2006).

Compared to pure iron, the effect of alloying 9 at% nickel is negligible, whereas the addition of 10 at% silicon increases the bulk sound speed. Furthermore, the difference between the bulk sound speed of the silicon alloy compared to that of hcp-Fe increases with increasing pressure. In particular, the bulk sound speed of hcp-$Fe_{0.8}Ni_{0.1}Si_{0.1}$ increases from being 1.7% higher than hcp-Fe at 30 GPa to being 5.5% higher than hcp-Fe at 150 GPa.

2.5 Extrapolation to inner core conditions

Geophysical observations paired with seismic models provide constraints for the density, adiabatic bulk modulus, and bulk sound speed of the inner core (e.g., *Dziewonski and Anderson*, 1981; *Kennett et al.*, 1995). Knowledge of these properties at inner core conditions is an essential aspect of constraining the composition of the inner core. The phases hcp-Fe and hcp-$Fe_{0.91}Ni_{0.09}$ are thought to be stable at inner core conditions (*Sakai et al.*, 2011; *Tateno et al.*, 2010, 2012). $Fe_{0.8}Ni_{0.1}Si_{0.1}$ at inner core conditions is thought to adopt

an hcp-structure or a mixture of hcp and B2 phases (*Fischer and Campbell*, 2015; *Fischer et al.*, 2013; *Sakai et al.*, 2011; *Tateno et al.*, 2015), where the B2 phase of Fe-Si and Fe-Ni-Si becomes more favorable as Si content or temperature is increased. We combine our 300 K equations of state with existing thermal parameters to obtain high-temperature equations of state from which we can estimate the density, adiabatic bulk modulus, and bulk sound speed of hcp-$Fe_{0.91}Ni_{0.09}$ and $Fe_{0.8}Ni_{0.1}Si_{0.1}$ at inner core conditions. We then place constraints on the composition of Earth's inner core by combining these results with available data on light-element alloys of iron and geophysical observations.

Thermal equation of state

We extrapolate to inner core conditions with a thermal equation of state,

$$P(V,T) = P_{300K}(V) + \Delta P_{Th}(V,T), \tag{2.1}$$

where $P_{300K}(V)$ is the 300 K Vinet equation of state, and the thermal pressure $\Delta P_{Th}(V,T)$ is approximated using the following terms: a Debye model for vibrational energy, which is a quasi-harmonic model of the vibrations referred to as the Mie-Grüneisen-Debye equation of state, as well as electronic (P_{el}) and anharmonic (P_{anh}) terms (*Sturhahn*, 2017),

$$\Delta P_{Th}(V,T) = P_{Th}(V,T) - P_{Th}(V,300K) \tag{2.2}$$

and

$$P_{Th}(V,T) = \frac{\gamma(V)}{V}\left[9k_BT\left(\frac{T}{\Theta(V)}\right)^3\int_0^{\Theta(V)/T}\frac{x^3dx}{e^x-1} + \frac{9}{8}k_B\Theta(V)\right] + P_{el} + P_{anh}. \tag{2.3}$$

We express the Grüneisen parameter $\gamma(V)$ with a volume dependent scaling law,

$$\gamma(V) = \gamma_0\left(\frac{V}{V_0}\right)^q, \tag{2.4}$$

where γ_0 is the Grüneisen parameter at 1 bar and q is a scaling parameter. We express the Debye temperature as

$$\Theta(V) = \Theta_0\exp\left[\frac{\gamma_0-\gamma(V)}{q}\right]. \tag{2.5}$$

A nuclear resonant inelastic x-ray scattering (NRIXS) study to 171 GPa determined the phonon density of states of hcp-Fe as a function of volume, from

Table 2.5: Thermal equation of state parameters used to extrapolate to inner core conditions.

Phase	V_0 (Å^3)	K_0 (GPa)	K_0'	Θ_0 (K)	γ_0	q
hcp-$Fe_{0.91}Ni_{0.09}$[a,b]	22.505(42)	157.5(39)	5.61(10)	417[c]	2.0(1)[d]	1.0(2)[d]
hcp-$Fe_{0.8}Ni_{0.1}Si_{0.1}$[a,b]	22.952(72)	125.2(46)	6.38(12)	417[c]	2.0(1)[d]	1.0(2)[d]
hcp-Fe[a,c]	22.428(98)	163.4(79)	5.38(16)	417	2.0(1)[d]	1.0(2)[d]
B1-FeO[a,e]	20.352	149.4(10)	3.60(4)	417	1.41(5)	0.5
Fe_7C_3[a,f]	182.87(38)	307(6)	3.2(1)	920(140)	2.57(5)	2.2(5)
FeS_2[g]	158.59(7)	139.7(15)	5.69(19)	624(14)	1.39	2.04(28)

[a]The electronic and anharmonic contributions to thermal pressure are approximated by adding the theoretically determined P_{el} and P_{anh} of hcp-Fe (*Dewaele et al.*, 2006) to the pressure.
[b]This study: XRD at 300 K up to 167 GPa (hcp-$Fe_{0.91}Ni_{0.09}$) and 175 GPa (hcp-$Fe_{0.8}Ni_{0.1}Si_{0.1}$)
[c]*Dewaele et al.* (2006): XRD at 300 K up to 205 GPa and ab initio calculations
[d]*Murphy et al.* (2011a): XRD and NRIXS at 300 K up to 171 GPa
[e]*Fischer et al.* (2011): XRD with laser heating up to 156 GPa and 3100 K
[f]*Chen et al.* (2012): XRD at ambient temperature up to 167 GPa
[g]*Thompson et al.* (2016): XRD with laser heating up to 80 GPa and 2400 K. The electronic and anharmonic contribution to thermal pressure (A_2) as reported in *Thompson et al.* (2016) is included in this treatment.

which the ambient pressure Grüneisen parameter γ_0=2.0±0.10 and the scaling parameter q=1±0.2 were determined (*Murphy et al.*, 2011a). We apply these values of γ_0 and q to the equations of state for hcp-$Fe_{0.91}Ni_{0.09}$, $Fe_{0.8}Ni_{0.1}Si_{0.1}$, and Fe. For hcp-$Fe_{0.91}Ni_{0.09}$ and $Fe_{0.8}Ni_{0.1}Si_{0.1}$, we assume the pure iron Debye temperature Θ_0=417 K (*Dewaele et al.*, 2006). The thermal EOS parameters used for hcp-$Fe_{0.91}Ni_{0.09}$, $Fe_{0.8}Ni_{0.1}Si_{0.1}$, and Fe are shown in Table 2.5.

At temperatures relevant to the inner core, electronic (P_{el}) and anharmonic (P_{anh}) contributions to the thermal pressure become non-negligible. To account for this contribution, we estimate P_{el} and P_{anh} using ab initio calculations. For hcp-Fe, we use the theoretically determined hcp-Fe P_{el} and P_{anh} from *Dewaele et al.* (2006). As calculations constraining the electronic and anharmonic contributions to thermal pressure for Fe-Ni alloys are limited, we estimate P_{el} and P_{anh} of hcp-$Fe_{0.91}Ni_{0.09}$ and $Fe_{0.8}Ni_{0.1}Si_{0.1}$ as those of hcp-Fe from *Dewaele et al.* (2006).

Density ρ at inner core conditions was calculated as a function of pressure and

temperature from the hcp-Fe, $Fe_{0.91}Ni_{0.09}$, and $Fe_{0.8}Ni_{0.1}Si_{0.1}$ thermal equations of state. Natural isotopic enrichment was assumed for density calculations. Isothermal bulk modulus K_T was calculated from the thermal equation of state,

$$K_T = -V\left(\frac{\partial P}{\partial V}\right)_T. \tag{2.6}$$

The adiabatic bulk modulus at inner core conditions, which can be compared with seismic models, was calculated with

$$K_S = K_T\left(1 + \gamma\alpha T\right), \tag{2.7}$$

where the thermal expansion α is calculated from the thermal equation of state with

$$\alpha = \frac{1}{V}\left(\frac{\partial V}{\partial T}\right)_P, \tag{2.8}$$

and the Grüneisen parameter γ is calculated with Equation 2.4. The bulk sound speed at inner core conditions, which is related to v_S and v_P, is then calculated by

$$v_\Phi = \left(\frac{K_S}{\rho}\right)^{1/2} = \left(v_P^2 - \frac{4}{3}v_S^2\right)^{1/2}, \tag{2.9}$$

where the density ρ is calculated with natural isotopic abundance.

Iron alloys at inner core conditions

We use a few recent studies to estimate a plausible range of inner core temperatures. Although large discrepancies exist in reported inner core boundary (ICB) temperatures, one can use them as bounds in this analysis. For instance, *Anzellini et al.* (2013) report an inner core boundary temperature of 6230 ± 500 K for a pure iron core. *Zhang et al.* (2016) measured the melting temperature of compressed iron and hcp-$Fe_{0.9}Ni_{0.1}$ samples using synchrotron Mössbauer spectroscopy and a fast temperature readout spectrometer (*Zhang et al.*, 2016). From these measurements, they estimate an upper bound for the inner core boundary (ICB) temperature of 5500 ± 200 K. The studies by *Zhang et al.* (2016) were conducted on $Fe_{0.91}Ni_{0.09}$ samples from the same synthesis as those used in this study. It is also well known that the addition of light elements to hcp-iron can lower the melting temperature. For instance, silicon may depress the melting point of hcp-iron by 0–400 K, and sulfur may depress the melting point of hcp-iron by 900–1200 K (as reviewed in *Fischer*, 2016). As the change in temperature with radius in the inner core is thought

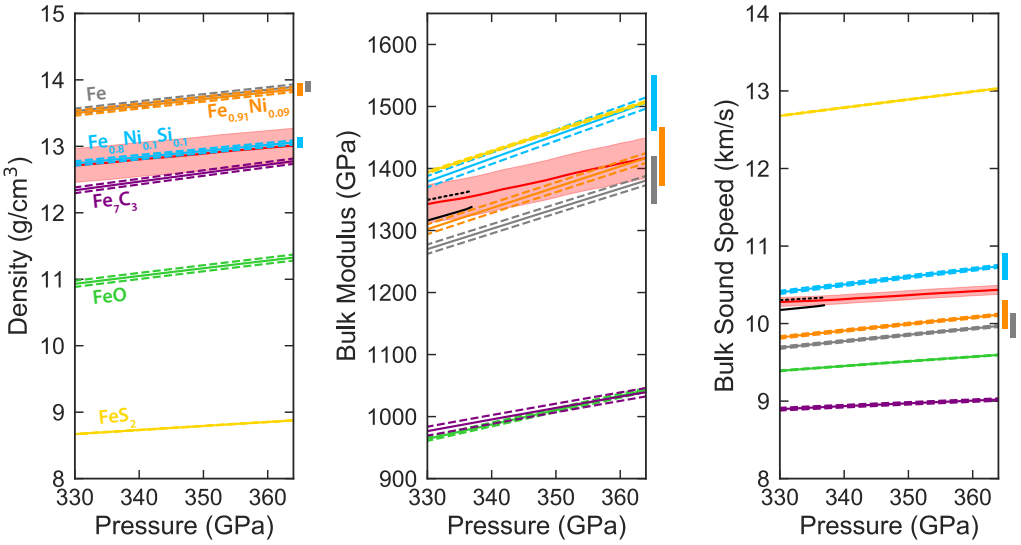

Figure 2.13: Thermal EOSs for hcp-$Fe_{0.91}Ni_{0.09}$, $Fe_{0.8}Ni_{0.1}Si_{0.1}$ (this study), and Fe (*Dewaele et al.*, 2006) are extrapolated to inner core conditions to calculate density ρ, adiabatic bulk modulus K_S, and bulk sound speed v_ϕ as a function of pressure at 5500 K (see text for details). Estimated electronic and anharmonic contributions to thermal pressure are included. Bars (right) represent uncertainty due to EOS parameters for hcp-Fe, $Fe_{0.91}Ni_{0.09}$, and $Fe_{0.8}Ni_{0.1}Si_{0.1}$. Upper and lower dashed lines represent -500 K and +500 K, respectively. We compare to the seismic model AK135-F (red line) (*Kennett et al.*, 1995) with estimated uncertainties for ρ (2%), K_S (2.3%), and v_ϕ (0.6%) (*Deuss*, 2008; *Masters and Gubbins*, 2003). We include K_S and v_ϕ of the eastern (Bin 3, black dashed line) and western (Bin 6, black solid line) hemispheres of the inner core, as determined by combining v_P (*Attanayake et al.*, 2014) with ρ and v_S from AK135-F. The ρ, K_S, and v_ϕ from thermal EOSs FeO (*Fischer et al.*, 2011), Fe_7C_3 (*Chen et al.*, 2012), and FeS_2 (*Thompson et al.*, 2016) are included.

to be small in comparison to the inner core temperature uncertainty (*Brown and Shankland*, 1981; *Pozzo et al.*, 2014), we assume a uniform temperature in our analysis. For these reasons, we assess the compositional constraints using ICB temperatures of 5000 K, 5500 K, and 6000 K. The density, adiabatic bulk modulus, and bulk sound speed of hcp-Fe, $Fe_{0.91}Ni_{0.09}$, and $Fe_{0.8}Ni_{0.1}Si_{0.1}$, including their uncertainties, are thus calculated along the inner core pressure gradient from 330 to 364 GPa (Figure 2.13).

To calculate the uncertainty on density, adiabatic bulk modulus, and bulk sound speed from the hcp-Fe, $Fe_{0.91}Ni_{0.09}$, and $Fe_{0.8}Ni_{0.1}Si_{0.1}$ thermal equations of state, we propagate uncertainty from our isothermal EOS fit parameters V_0,

K_{T0}, K'_{T0} and fix $\gamma_0 = 2.0$ with $q = 1.0$ (*Murphy et al.*, 2011a) using MINUTI. To estimate the uncertainty from γ_0 and q, we repeat this calculation using $\Theta_0 = 417$ K and the range of γ_0 and q reported in *Murphy et al.* (2011a): $\gamma_0 = 1.9$ with $q = 0.8$ and $\gamma_0 = 2.1$ with $q = 1.2$ (Figure 2.14). The uncertainty contributions from V_0, K_{T0}, and K'_{T0} and from γ_0 and q are listed in Table 2.6. The uncertainty contributions due to the isothermal equation of state parameters V_0, K_{T0}, and K'_{T0} for hcp-Fe, hcp-$Fe_{0.91}Ni_{0.09}$ and hcp-$Fe_{0.8}Ni_{0.1}Si_{0.1}$ are found to be of similar magnitude to the uncertainty due to γ_0 and q, which highlights the importance of accurately constraining the parameters V_0, K_{T0}, and K'_{T0} to obtain reliable thermal equations of state. One of the greatest sources of uncertainty is due to the electronic and anharmonic contributions to the thermal pressure, which are not well constrained (e.g., *Alfè et al.*, 2001; *Fei et al.*, 2016; *Martorell et al.*, 2013a,b, 2016; *Moustafa et al.*, 2017). To account for this, we enlarge our error bars on density, adiabatic bulk modulus, and bulk sound speed. The total uncertainty on density, adiabatic bulk modulus, and bulk sound speed for these three alloys at inner conditions is denoted by the vertical bars to the right of each panel in Figure 2.13.

To compare with the inner core, we plot density, adiabatic bulk modulus, and bulk sound speed from AK135-F as a function of pressure (*Kennett et al.*, 1995) in red in Figure 2.13. The uncertainty of the inner core density is estimated at 2% by *Masters and Gubbins* (2003), and the uncertainty of the bulk sound speed of the inner core is estimated to be 0.6% by *Deuss* (2008). The uncertainty of the inner core adiabatic bulk modulus from AK135-F can then be estimated from error propagation to be 2.3%. The AK135-F model does not explicitly include pressure, so pressure is estimated from depth using the PREM model (*Dziewonski and Anderson*, 1981).

We first assess the constraints provided for Fe, $Fe_{0.91}Ni_{0.09}$, and $Fe_{0.8}Ni_{0.1}Si_{0.1}$. The density of hcp-$Fe_{0.8}Ni_{0.1}Si_{0.1}$ matches AK135-F throughout the inner core, suggesting $Fe_{0.8}Ni_{0.1}Si_{0.1}$ may be a reasonable composition for the Earth's inner core. While the adiabatic bulk modulus and bulk sound speed of hcp-$Fe_{0.8}Ni_{0.1}Si_{0.1}$ at the inner core boundary are close to the uncertainty range of AK135-F, the pressure gradients of K_S and v_ϕ of $Fe_{0.8}Ni_{0.1}Si_{0.1}$ are significantly higher than those of AK135-F, a topic we will return to later in this chapter.

To examine the effect of other light elements, we include three thermal equation of state studies in Figure 2.13: FeO (*Fischer et al.*, 2011), Fe_7C_3 (*Chen*

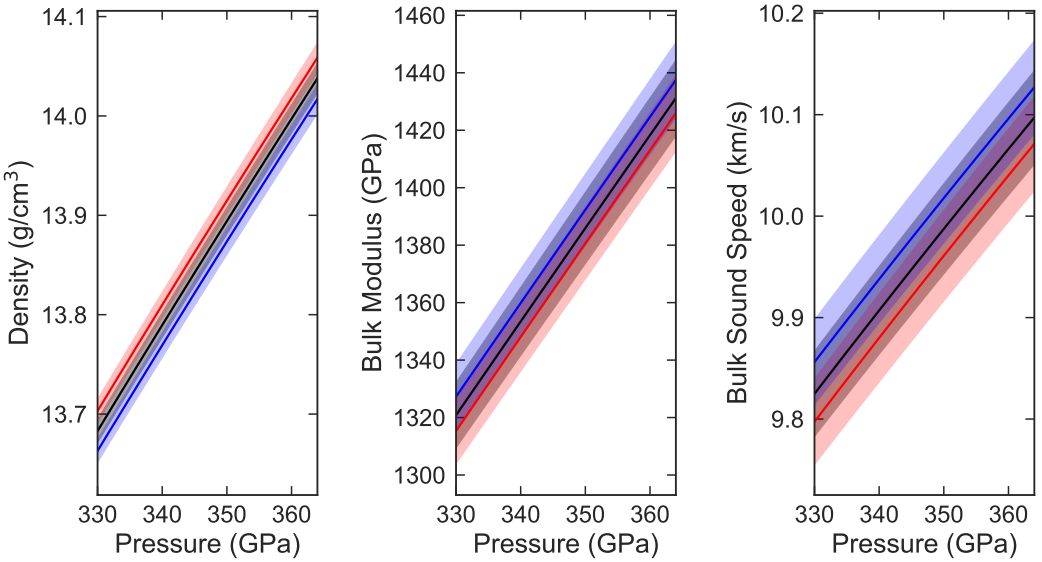

Figure 2.14: We illustrate the uncertainty contribution from the quasi-harmonic terms of hcp-Fe's thermal equation of state to density, bulk modulus, and bulk sound velocity at 330–366 GPa and 5500 K. We propagate the uncertainty from our 300 K EOS fit parameters V_0, K_{T0}, and K'_{T0} and fix $\gamma_0 = 2.0$ and $q = 1.0$ (*Murphy et al.*, 2011a) (black). To estimate the uncertainty from γ_0 and q, we repeat this calculation using the range of γ_0 and q reported in *Murphy et al.* (2011a): $\gamma_0 = 1.9$ with $q = 0.8$ (blue) and $\gamma_0 = 2.1$ with $q = 1.2$ (red). The range of values spanned by these three uncertainty calculations at 330–366 GPa and 5500 K represent uncertainty on density, bulk modulus, and bulk sound speed for hcp-Fe. The same uncertainty calculation was repeated for hcp-$Fe_{0.91}Ni_{0.09}$ and hcp-$Fe_{0.8}Ni_{0.1}Si_{0.1}$. These values are broken down in Table 2.6. While this plot excludes uncertainty from electronic and anharmonic contributions to thermal pressure (P_{el} and P_{anh}), uncertainty from P_{el} and P_{anh} was included in Figure 2.13.

et al., 2012), and FeS_2 (*Thompson et al.*, 2016). High temperature diamond anvil cell experiments by *Fischer et al.* (2011) investigated B1-structured FeO with x-ray diffraction and laser heating using a NaCl pressure medium and an iron pressure standard. Single crystal diamond anvil cell experiments at 300 K by *Chen et al.* (2012) investigated non-magnetic hexagonal Fe_7C_3 with x-ray diffraction and synchrotron Mössbauer spectroscopy using a neon pressure medium and pressure marker. *Chen et al.* (2012) approximated the effects of temperature on non-magnetic Fe_7C_3 using multi-anvil experiments on paramagnetic Fe_7C_3 by *Nakajima et al.* (2011). High temperature diamond anvil cell experiments by *Thompson et al.* (2016) investigated cubic FeS_2 (pyrite) with x-ray diffraction and laser heating using a KBr pressure medium and pressure

Table 2.6: Density, adiabatic bulk modulus, and bulk sound velocity uncertainties at high temperature at the ICB (330 GPa).

	Fe			$Fe_{0.91}Ni_{0.09}$			$Fe_{0.8}Ni_{0.1}Si_{0.1}$		
	ρ (g/cm^3)	K_s (GPa)	v_ϕ (km/s)	ρ (g/cm^3)	K_s (GPa)	v_ϕ (km/s)	ρ (g/cm^3)	K_s (GPa)	v_ϕ (km/s)
Uncertainty from V_0, K_{T0}, K'^a_{T0}	0.012	11	0.042	0.021	15	0.056	0.016	15	0.055
Uncertainty from γ_0, q^b	0.020	6.0	0.029	0.019	5.8	0.028	0.018	4.9	0.025
Total uncertainty without P_{el} and P^c_{anh}	0.032	17	0.071	0.040	21	0.085	0.033	20	0.080

[a]The V_0, K_{T0}, K'_{T0} contribution to uncertainties of ρ, K_s, and v_ϕ for Fe were obtained by fitting an EOS to the *Dewaele et al.* (2006) data set with MINUTI and extrapolating to 330 GPa and 5500 K with fixed γ_0 and q. Similarly, the V_0, K_{T0}, K'_{T0} contribution to uncertainties of ρ, K_s, and v_ϕ for $Fe_{0.91}Ni_{0.09}$ and $Fe_{0.8}Ni_{0.1}Si_{0.1}$ were obtained by fitting data from this study with MINUTI and extrapolating to 330 GPa and 5500 K with fixed γ_0 and q.

[b]The uncertainty from γ_0 and q was estimated repeating the fits in (a) using the range of γ_0 and q reported in *Murphy et al.* (2011a): $\gamma_0 = 1.9$ with $q = 0.8$ and $\gamma_0 = 2.1$ with $q = 1.2$.

[c]The total uncertainties on density, adiabatic bulk modulus, and bulk sound speed at high temperature are the range of values spanned by the uncertainty calculations in (a) and (b). The uncertainty due to electronic and anharmonic contributions to thermal pressure is not accounted for here but is included in Figure 2.13.

calibrant. *Thompson et al.* (2016) constrained the cubic FeS_2 (pyrite) equation of state at 300 K with a neon pressure medium and a gold pressure calibrant. The thermal equation of state parameters used for FeO, Fe_7C_3, and FeS_2 are shown in Table 2.5. While the methodology of our work allows for a systematic comparison of hcp-Fe, hcp-$Fe_{0.91}Ni_{0.09}$, and hcp-$Fe_{0.8}Ni_{0.1}Si_{0.1}$, the studies of FeO, Fe_7C_3, and FeS_2 were performed with varied methodology, so comparison to these alloys is more speculative.

The electronic and anharmonic contributions to thermal pressure for FeS_2 were constrained by *Thompson et al.* (2016) and are thus used for FeS_2. However, because these terms have not been constrained for FeO and Fe_7C_3, P_{el} and P_{anh} are approximated as the hcp-Fe P_{el} and P_{anh} terms reported by *Dewaele et al.* (2006). While hydrogen is suggested to be one of the light elements in Earth's core (e.g., *Stevenson*, 1977), Fe-Ni-H alloys were excluded here due to a sparsity of thermal EOSs with relevance to Earth's inner core conditions. The uncertainties on density, adiabatic bulk modulus, and bulk sound speed at high temperature for FeO, FeS_2, and Fe_7C_3 were not estimated, as proper uncertainty propagation would require knowledge of the covariance matrix relating the fitted parameters V_0, K_{T0}, K'_{T0}, γ_0, and q.

Concerning the stability of these phases in the inner core, *Ozawa et al.* (2011) find B2-FeO to be favored over B1-FeO above 240 GPa at 4000 K, thereby suggesting the B2 phase is stable in the inner core, and ab initio studies by *Huang et al.* (2018) propose *I4/mmm*-Fe_2O is energetically favorable above 270 GPa. However, experimental equations of state are not presently available for B2-FeO or *I4/mmm*-Fe_2O. Shock experiments by *Ahrens and Jeanloz* (1987) suggest cubic pyrite is stable up to 320 GPa. While recent theory suggests *C2/m*-FeS_2 may be stable at inner core conditions (*Bazhanova et al.*, 2017), experimental equations of state are also not presently available for this phase. In a recent review, *Li and Fei* (2014) suggest Fe_7C_3 is favored over Fe_3C as the liquidus phase of the Fe-C system at pressures above 7 GPa and therefore favored as a phase in the inner core.

The trends shown in Figure 2.13 suggest neither oxygen nor carbon is likely to satisfy the geophysical constraints as the sole light element in the inner core. While it is not readily apparent from this figure whether sulfur alone could satisfy the density, adiabatic bulk modulus, and bulk sound speed of the inner core, it is clear that none of the examined alloys match the seismic gradi-

ents of AK135-F. Next, we will explore and attempt to quantify geophysically permissible mixtures of these iron-rich light-element alloys.

Seismic and experimental constraints on core composition Fe-Ni-Si system

We examine hypothetical compositions in the Fe-Ni-Si compositional space to determine whether silicon could be the dominant light element in the inner core. To do so, we apply a linear mixing model. *Badro et al.* (2007) propose linear mixing should hold for hcp-iron alloyed with low concentrations of light elements, and this approach has been applied to various solid iron alloys (e.g., *Antonangeli et al.*, 2010, 2018; *Badro et al.*, 2007; *Fiquet et al.*, 2009; *Ohtani*, 2013). Linear mixing is therefore a reasonable approximation for a mixing of hcp-Fe, hcp-$Fe_{0.91}Ni_{0.09}$, and hcp-$Fe_{0.8}Ni_{0.1}Si_{0.1}$. Density can be calculated as

$$\rho_{avg} = \frac{\sum_i x_i m_i}{\sum_i \frac{x_i m_i}{\rho_i}}, \tag{2.10}$$

where x_i are atomic percents and m_i are the molecular weights. Voigt averaging is used to calculate the average adiabatic bulk modulus, and bulk sound speed is calculated from the adiabatic bulk modulus and density (Equation 2.9).

For each hypothetical composition, we compare the resulting density, adiabatic bulk modulus, and bulk sound speed to AK135-F at the inner core boundary (330 GPa, Figure 2.13). If the density, adiabatic bulk modulus, and bulk sound speed of the given hypothetical composition fall strictly within 2% of AK135-F's density, 2.3% of adiabatic bulk modulus, and 0.6% of bulk sound speed at 330 GPa (*Deuss*, 2008; *Masters and Gubbins*, 2003), we consider the given hypothetical composition to be a possible core composition. Otherwise, the hypothetical composition is excluded. While all calculations are performed with atomic percent compositions, possible core compositions are selected and plotted as weight percent for literature comparison convenience.

We explore the compositional space within 0–10 wt% nickel and 0–12 wt% silicon. The resulting compositional space in agreement with AK135-F at the inner core boundary at 5000 K, 5500 K, and 6000 K is plotted in Figure 2.15. If nickel content is fixed at 5 wt%, we find a silicon content of 4.3–5.3 wt% satisfies the density, bulk modulus, and bulk sound speed of the ICB at 5500 K. With nickel content fixed at 5 wt%, a temperature of 5000 K lowers the al-

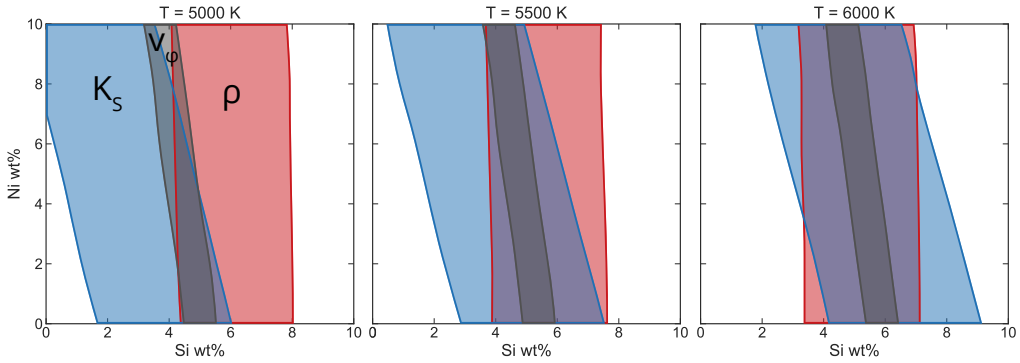

Figure 2.15: A range of inner core compositions in the Fe-Ni-Si system using experimental constraints on hcp-Fe, $Fe_{0.91}Ni_{0.09}$, and $Fe_{0.8}Ni_{0.1}Si_{0.1}$ with a linear mixing model. The regions represent agreement with the seismic model AK135-F within 2% of the density (red), 0.6% of the bulk sound speed (gray), and 2.3% of the adiabatic bulk modulus (blue). Seismically consistent compositions lie within the intersection of the three regions. Estimated electronic and anharmonic contributions to thermal pressure are included. Pressure is fixed at 330 GPa. See text for more details.

lowable silicon content to 4.2–4.8 wt%, and a temperature of 6000 K raises the allowable silicon content to 4.7–5.8 wt%. While cosmochemical analyses suggest a Ni core content of 5 wt% (*Allègre et al.*, 1995; *McDonough*, 2003), iron-nickel meteorites inferred to be remnants of differentiated protoplanets have variable nickel content. We find any concentration of nickel in the investigated range of 0–10 wt% can satisfy the density, bulk modulus, and bulk sound speed at the ICB at 5500 K and 6000 K. For a cooler ICB temperature of 5000 K, only up to 7.5 wt% nickel satisfies the density, bulk modulus, and bulk sound speed of the ICB. The nickel content has a small effect on the allowable silicon content in the inner core. Lowering the nickel content to 0 wt% would raise the allowable silicon content to 4.9–5.9 wt%, and raising the nickel content to 10 wt% would lower the allowable silicon content to 3.7–4.6 wt%. Therefore, we find an inverse relationship between the nickel and silicon content of the inner core.

Fe-Ni-Si-O-C-S system

As it is unlikely that the inner core contains only one light element, we extrapolate our analysis to the Fe-Ni-Si-O-C-S compositional space. While our Fe-Ni-Si compositional analysis is based on systematic experimental studies, this Fe-Ni-Si-O-C-S compositional analysis is necessarily based on studies with var-

ied methodology and is therefore more speculative. While linear mixing may be a reasonable approximation for a mixing of hcp-Fe-Ni-Si with sufficiently small quantities of Ni and Si, immiscible phases and phases with different crystal structures are unlikely to follow a linear mixing model. A mixing of the phases hcp-Fe, B1-FeO, cubic FeS_2, and Fe_7C_3, which all have different crystal structures, may be better described by a bulk aggregate model. The accuracy of and deviation from these mixing models will be enlightened by future experimental studies on samples of intermediate compositions.

We therefore apply two basic models to explore the Fe-Ni-Si-O-C-S system: a linear mixing model and a bulk aggregate model. The calculation of density will be the same for both assumptions (see Equation 2.10). In the linear mixing case, Voigt averaging is used to calculate the average adiabatic bulk modulus as before. In the bulk aggregate case, Voigt-Reuss-Hill averaging is used to calculate the average adiabatic bulk modulus. As before, bulk sound speed is calculated from the adiabatic bulk modulus and density for both models (Equation 2.9).

For each hypothetical composition in the Fe-Ni-Si-O-C-S system, we compare the resulting density, adiabatic bulk modulus, and bulk sound speed to AK135-F at the inner core boundary (330 GPa). We explore the compositional space within 0–10 wt% nickel, 0–12 wt% silicon, 0–8 wt% oxygen, 0–4 wt% carbon, and 0–12 wt% sulfur (*Li and Fei*, 2014; *Sata et al.*, 2010). For subsequent results, we fix the nickel concentration of the bulk core composition at 5 wt% (*Allègre et al.*, 1995; *McDonough*, 2003).

Select slices of the resulting compositional space in agreement with AK135-F at the inner core boundary are plotted in Figure 2.16 and tabulated in Table 2.7. We find that as the carbon content of a hypothetical inner core composition increases, the allowable oxygen content decreases and silicon content increases. As the sulfur content of the inner core composition increases, the allowable oxygen and silicon contents decrease.

Using either a bulk aggregate or linear mixing assumption and a nickel content of 5 wt%, a silicon content of 4.3–5.3 wt% alone satisfies the density, bulk modulus, and bulk sound speed at the inner core boundary, consistent with our analysis in just the Fe-Ni-Si compositional space (Figure 2.16a). A maximum value of 1.0 wt% carbon is allowed with a bulk aggregate or linear mixing assumption, requiring the presence of up to 6.5 wt% silicon (Figure 2.16c). A

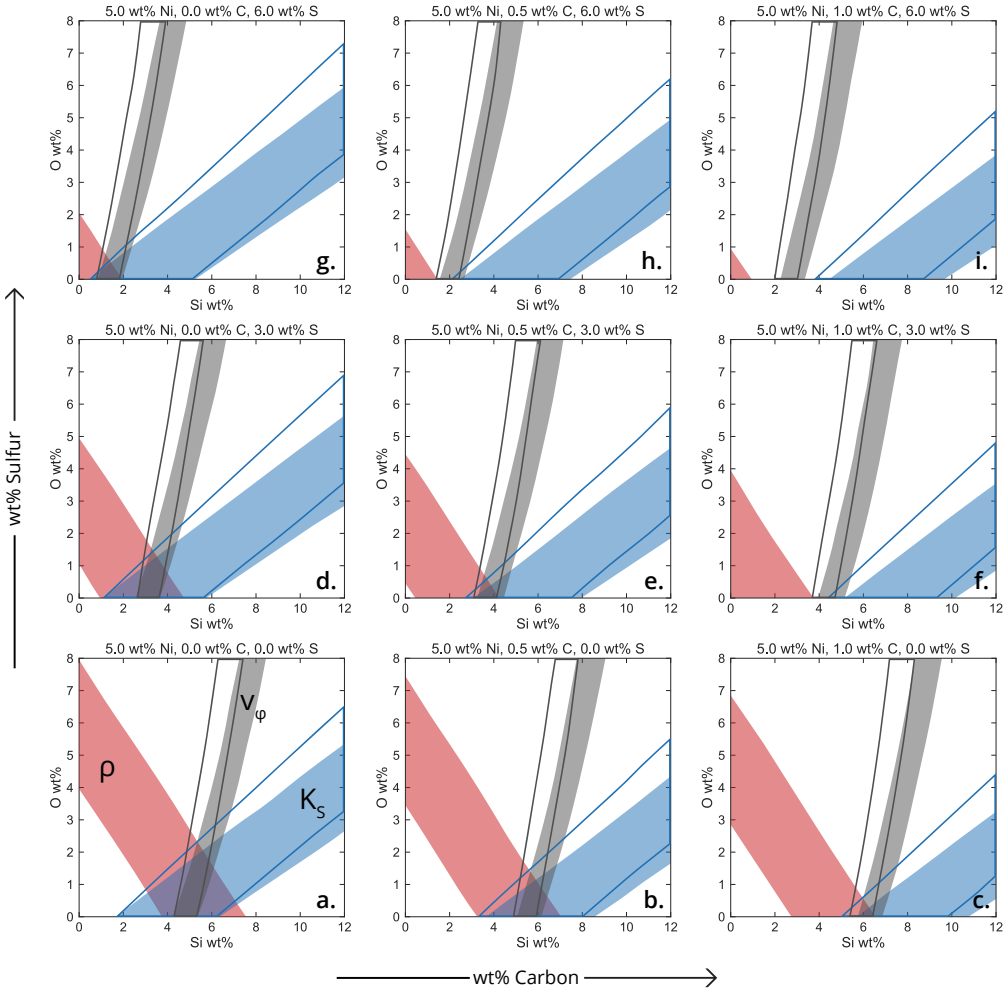

Figure 2.16: A range of inner core compositions in the Fe-Ni-Si-O-C-S system using experimental constraints on hcp-Fe, hcp-$Fe_{0.91}Ni_{0.09}$, hcp-$Fe_{0.8}Ni_{0.1}Si_{0.1}$, Fe-O, Fe_7C_3, and FeS_2 with a linear mixing model (outlined regions) and a bulk aggregate model (shaded regions). The shaded and outlined regions represent the compositions in agreement with AK135-F within 2% of density ρ (red), within 0.6% of bulk sound speed K_S (gray), and within 2.3% of adiabatic bulk modulus v_ϕ (blue). Density is the same for both models. Seismically consistent compositions lie within the intersection of the ρ, K_S, and v_ϕ regions in agreement with AK135-F. Estimated electronic and anharmonic contributions to thermal pressure are included. Nickel content is fixed at 5 wt%, and 5500 K and 330 GPa are assumed. See text for more details.

Table 2.7: Iron alloy compositional models in agreement with the density, adiabatic bulk modulus, and bulk sound velocity of AK135-F at the ICB. Ni concentration is fixed at 5 wt%.

Corresponding Panel in Figure 2.16	S (wt%, fixed)	C (wt%, fixed)	Bulk aggregate Si (wt%)	Bulk aggregate O (wt%)	Linear mixing Si (wt%)	Linear mixing O (wt%)
a	0	0	4.3-6.1	0.0-2.0	4.3-5.8	0.0-2.3
b	0	0.5	5.1-6.4	0.0-1.1	4.9-6.1	0.0-1.4
c	0	1	5.8-6.5	0.0-0.2	5.4-6.4	0.0-0.6
d	3	0	2.6-3.9	0.0-1.2	2.6-3.8	0.0-1.4
e	3	0.5	3.3-4.2	0.0-0.3	3.1-4.1	0.0-0.5
f	3	1	—	—	—	—
g	6	0	0.9-1.9	0.0-0.4	0.8-1.8	0.0-0.5
h	6	0.5	—	—	—	—
i	6	1	—	—	—	—

maximum value of 2.0 wt% oxygen is allowed with a bulk aggregate assumption (or 2.3 wt% with a linear mixing assumption). This oxygen content requires 5.6 wt% silicon (5.3 wt% with linear mixing) to also be present (Figure 2.16a). We therefore find that neither oxygen nor carbon can be the only light element in the inner core containing 5 wt% nickel. On the other hand, a maximum sulfur content of 7.5 wt% requires only 0.2 to 0.5 wt% silicon and no oxygen or carbon (with either a bulk aggregate or linear mixing assumption). Lower values of sulfur content (5 wt%) require a higher silicon content of 1.4 to 2.5 wt% silicon with a bulk aggregate assumption, or 1.5 to 2.6 wt% silicon with a linear mixing assumption (Figure 2.16g).

We also explore the effect of varying nickel and temperature in the Fe-Ni-Si-O-C-S system. As the nickel content of the inner core increases, we find the allowable silicon content decreases and the allowable oxygen, carbon, and sulfur content increases (Figure 2.17 and Tables 2.8 and 2.9). Temperature has a strong effect on the allowable core compositions. A cooler inner core boundary temperature of 5000 K increases the seismic favorability of oxygen, carbon, and sulfur in the core, while a hotter temperature of 6000 K strongly decreases the seismic favorability of oxygen, carbon, and sulfur (Figures 2.18 and 2.19 and Tables 2.10 and 2.10). Therefore silicon is more seismically favorable as the dominant light element for hotter inner core boundary temperatures. This is consistent with data on the melting point depression due to the addition of light elements. Silicon is estimated to decrease the temperature at the in-

Table 2.8: Iron alloy compositional models in agreement with the ρ, K_S, and v_ϕ of AK135-F with Ni concentration fixed at 0 wt%. Temperature is fixed at 5500 K. Compare to Tables 2.7 and 2.9.

Corresponding			Bulk aggregate		Linear mixing	
Panel in	S	C	Si	O	Si	O
Figure 2.17	(wt%, fixed)	(wt%, fixed)	(wt%)	(wt%)	(wt%)	(wt%)
a	0	0	5.0-6.5	0.0-1.6	4.9-6.3	0.0-1.8
b	0	0.5	5.7-6.9	0.0-0.7	5.5-6.6	0.0-1.0
c	0	1	—	—	6.2-6.6	0.0-0.1
d	3	0	3.3-4.4	0.0-0.8	3.2-4.3	0.0-1.0
e	3	0.5	—	—	3.9-4.3	0.0-0.1
f	3	1	—	—	—	—
g	6	0	1.8-2.0	0.0	1.7-2.0	0.0-0.1
h	6	0.5	—	—	—	—
i	6	1	—	—	—	—

Table 2.9: Iron alloy compositional models in agreement with the ρ, K_S, and v_ϕ of AK135-F with Ni concentration fixed at 10 wt%. Temperature is fixed at 5500 K. Compare to Tables 2.7 and 2.8.

Corresponding			Bulk aggregate		Linear mixing	
Panel in	S	C	Si	O	Si	O
Figure 2.17	(wt%, fixed)	(wt%, fixed)	(wt%)	(wt%)	(wt%)	(wt%)
a	0	0	3.7-5.6	0.0-2.4	3.7-5.3	0.0-2.7
b	0	0.5	4.4-5.9	0.0-1.5	4.2-5.6	0.0-1.9
c	0	1	5.1-6.2	0.0-0.6	4.8-5.9	0.0-1.0
d	3	0	1.9-3.5	0.0-1.6	1.9-3.3	0.0-1.8
e	3	0.5	2.7-3.8	0.0-0.7	2.5-3.6	0.0-1.0
f	3	1	—	—	3.2-3.6	0.0-0.1
g	6	0	0.2-1.4	0.0-0.8	0.2-1.3	0.0-1.0
h	6	0.5	1.3-1.3	0.0	0.9-1.3	0.0-0.1
i	6	1	—	—	—	—

ner core boundary by 0–400 K, oxygen by 700–1100 K, carbon by 600–800 K, and sulfur by 900–1200 K (as reviewed in *Fischer*, 2016). Therefore, an inner core with predominately silicon as the light element would be associated with a hotter inner core boundary, and an inner core with predominately oxygen, carbon, or sulfur as the light element would be associated with a cooler inner core boundary.

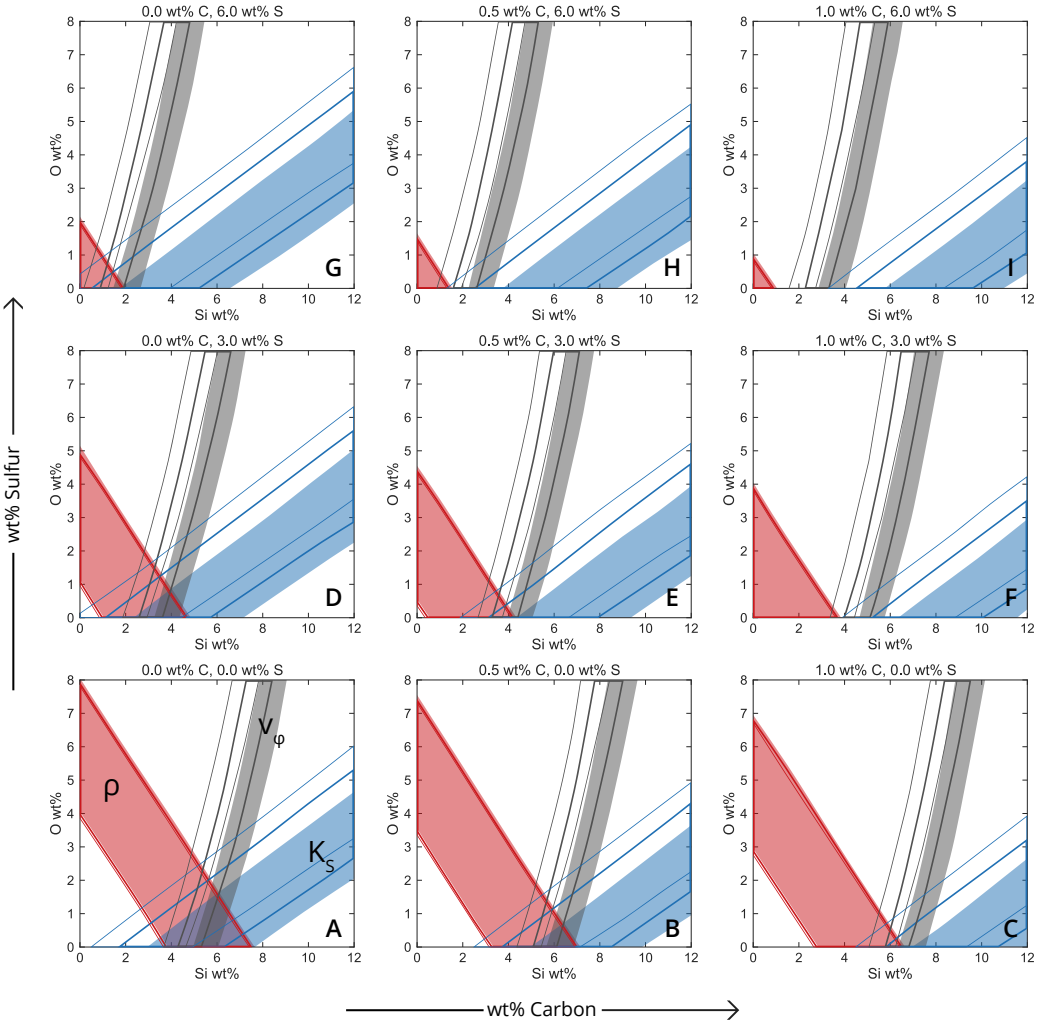

Figure 2.17: We explore the effect of Ni on the range of compositions in the Fe-Ni-Si-O-C-S system. Ni content is fixed at 0 wt% (shaded regions), 5 wt% (thick lines), and 10 wt% (thin lines) using the experimental constraints on the following alloys: hcp-Fe, hcp-$Fe_{0.91}Ni_{0.09}$, hcp-$Fe_{0.8}Ni_{0.1}Si_{0.1}$, Fe-O, Fe_7C_3, and FeS_2. Only the bulk aggregate mixing model is shown. The shaded and outlined regions represent the compositions in agreement with AK135-F within 2% of density ρ (red), within 0.6% of bulk sound speed K_S (gray), and within 2.3% of adiabatic bulk modulus v_ϕ (blue). Pressure is fixed at 330 GPa, temperature is fixed at 5500 K, and estimated electronic and anharmonic contributions to thermal pressure are included.

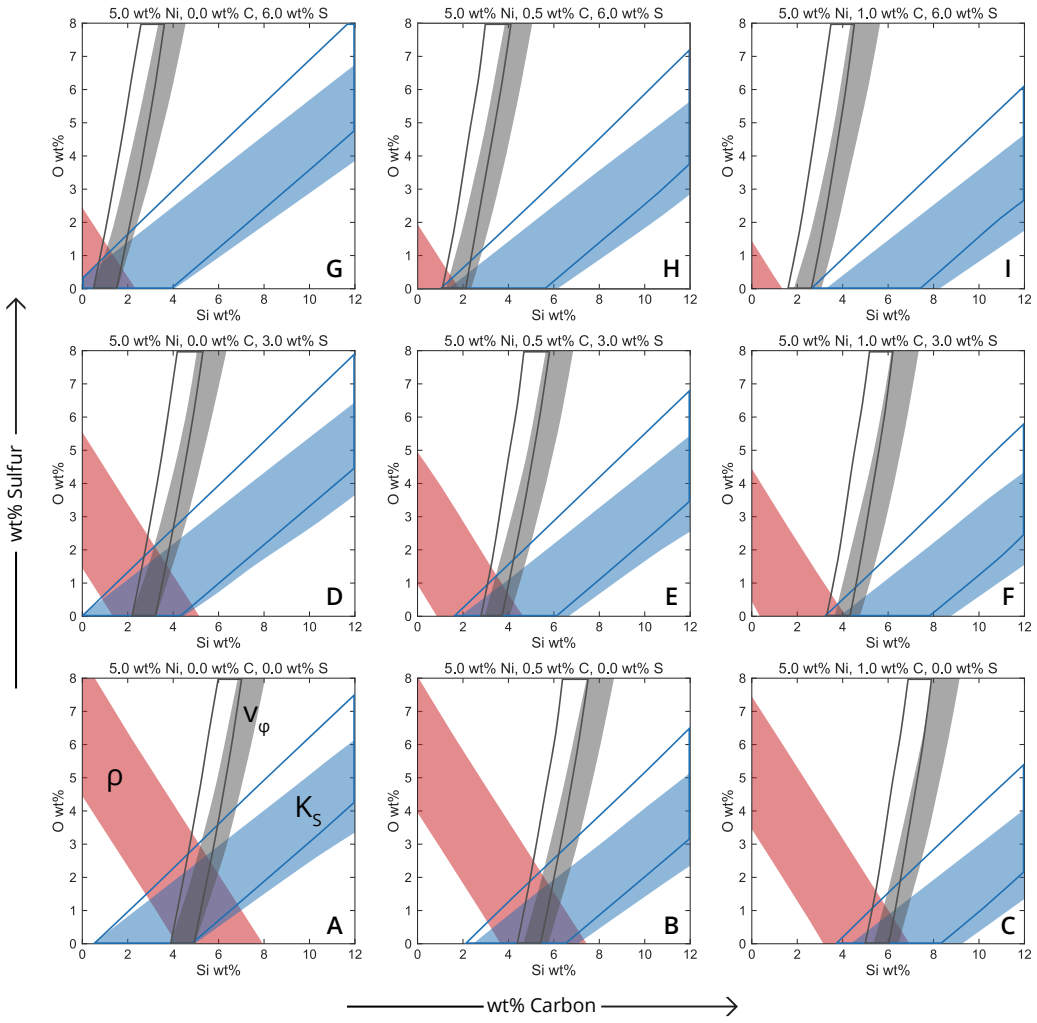

Figure 2.18: The effect of a cooler inner core boundary temperature on the compositional analysis is explored (as compared to Figures 2.16 and 2.19). A range of compositions are explored in the Fe-Ni-Si-O-C-S system with temperature fixed at 5000 K using experimental constraints on hcp-Fe, hcp-$Fe_{0.91}Ni_{0.09}$, hcp-$Fe_{0.8}Ni_{0.1}Si_{0.1}$, Fe-O, Fe_7C_3, and FeS_2. The shaded and outlined regions represent the compositions in agreement with AK135-F within 2% of density ρ (red), within 0.6% of bulk sound speed K_S (gray), and within 2.3% of adiabatic bulk modulus v_ϕ (blue). A bulk aggregate model (shaded regions) and a linear mixing model (outlined regions) are employed. Density is the same for both models. Pressure is fixed at 330 GPa, nickel content is fixed at 5 wt%, and estimated electronic and anharmonic contributions to thermal pressure are included.

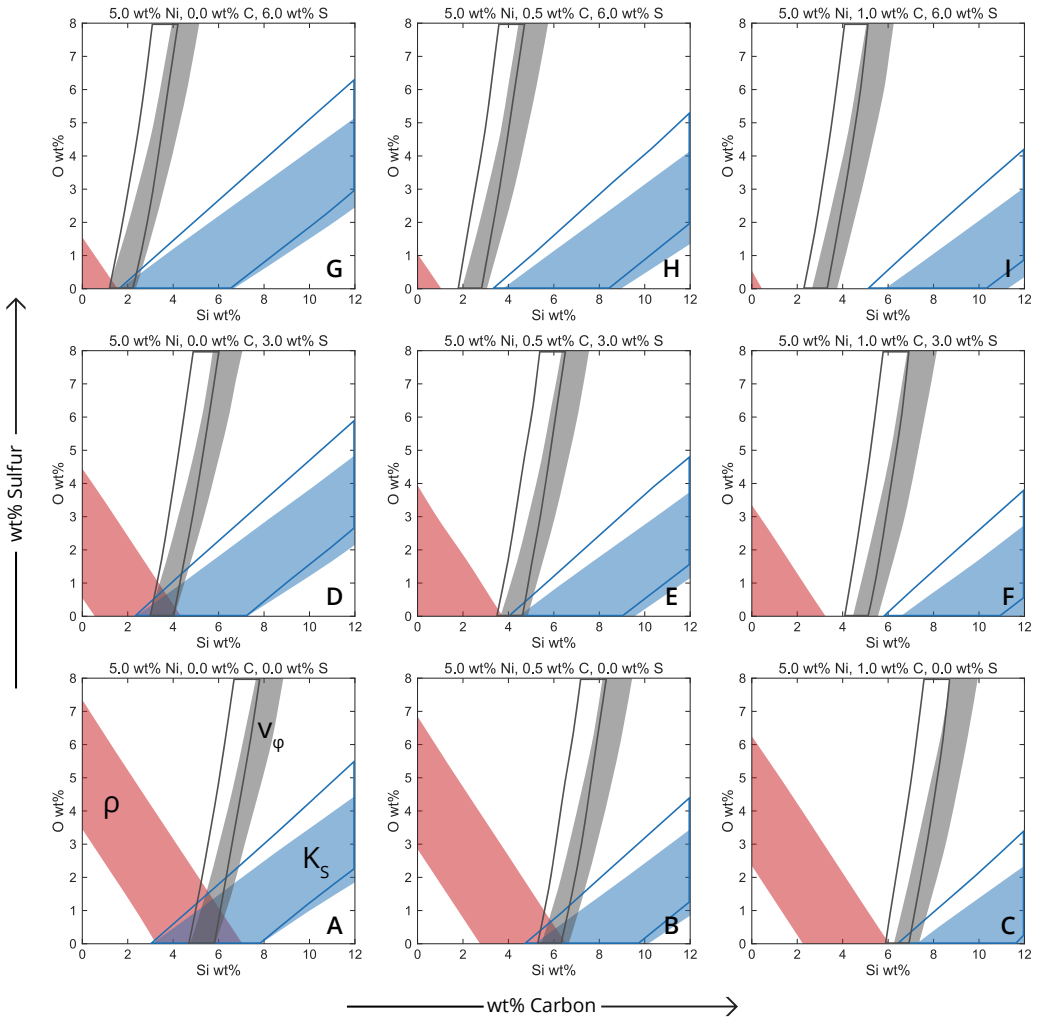

Figure 2.19: The effect of a hotter inner core boundary temperature on the compositional analysis is explored (as compared to Figures 2.16 and 2.18). A range of compositions are explored in the Fe-Ni-Si-O-C-S system with temperature fixed at 6000 K using experimental constraints on hcp-Fe, hcp-$Fe_{0.91}Ni_{0.09}$, hcp-$Fe_{0.8}Ni_{0.1}Si_{0.1}$, Fe-O, Fe_7C_3, and FeS_2. The shaded and outlined regions represent the compositions in agreement with AK135-F within 2% of density ρ (red), within 0.6% of bulk sound speed K_S (gray), and within 2.3% of adiabatic bulk modulus v_ϕ (blue). A bulk aggregate model (shaded regions) and a linear mixing model (outlined regions) are employed. Density is the same for both models. Pressure is fixed at 330 GPa, nickel content is fixed at 5 wt%, and estimated electronic and anharmonic contributions to thermal pressure are included.

Table 2.10: The effect of a cooler inner core boundary temperature on the compositional analysis is explored. We tabulate iron alloy compositional models in agreement with the ρ, K_S, and v_ϕ of AK135-F with temperature fixed at 5000 K. Ni concentration is fixed at 5 wt%. Compare to Tables 2.7 and 2.11.

Corresponding			Bulk aggregate		Linear mixing	
Panel in	S	C	Si	O	Si	O
Figure 2.18	(wt%, fixed)	(wt%, fixed)	(wt%)	(wt%)	(wt%)	(wt%)
a	0	0	4.1-5.9	0.0-2.6	4.0-5.6	0.0-3.0
b	0	0.5	4.7-6.2	0.0-1.7	4.4-5.9	0.0-2.1
c	0	1	5.4-6.6	0.0-0.9	5.0-6.2	0.0-1.3
d	3	0	2.2-3.8	0.0-1.8	2.2-3.6	0.0-2.0
e	3	0.5	3.0-4.1	0.0-0.9	2.8-4.0	0.0-1.2
f	3	1	3.9-4.1	0.0	3.3-4.1	0.0-0.3
g	6	0	0.5-1.8	0.0-1.0	0.5-1.7	0.0-1.1
h	6	0.5	1.4-1.8	0.0-0.1	1.1-1.8	0.0-0.3
i	6	1	—	—	—	—

Table 2.11: The effect of a hotter inner core boundary temperature on the compositional analysis is explored. We tabulate iron alloy compositional models in agreement with the ρ, K_S, and v_ϕ of AK135-F with temperature fixed at 6000 K. Ni concentration is fixed at 5 wt%. Compare to Tables 2.7 and 2.10.

Corresponding			Bulk aggregate		Linear mixing	
Panel in	S	C	Si	O	Si	O
Figure 2.19	(wt%, fixed)	(wt%, fixed)	(wt%)	(wt%)	(wt%)	(wt%)
a	0	0	4.8-6.2	0.0-1.3	4.7-6.1	0.0-1.5
b	0	0.5	5.5-6.5	0.0-0.4	5.3-6.4	0.0-0.6
c	0	1	—	—	—	—
d	3	0	3.0-4.1	0.0-0.6	3.0-4.0	0.0-0.7
e	3	0.5	—	—	—	—
f	3	1	—	—	—	—
g	6	0	—	—	—	—
h	6	0.5	—	—	—	—
i	6	1	—	—	—	—

Assessing the effects of P_{el} and P_{anh}

We now assess the effects of P_{el} and P_{anh} on the density, adiabatic bulk modulus, and bulk sound speed of iron alloys at inner core conditions. We repeat the above calculations and analysis with thermal pressure approximated only as a Debye model of vibrational energy, i.e., with the electronic and anharmonic contributions to the thermal pressure in Equation 2.3 neglected. We refer to this model as the Vinet-Mie-Grüneisen-Debye (Vinet-MGD) equation of state. We show the resulting density, adiabatic bulk modulus, and bulk sound speed at inner core conditions in Figure 2.20. When P_{el} and P_{anh} are neglected, the properties change noticeably with respect to AK135-F. We find the absence of the P_{el} and P_{anh} contributions to the thermal pressure of hcp-$Fe_{0.8}Ni_{0.1}Si_{0.1}$ increase K_s and v_ϕ away from the values of AK135-F, which would, for all other things being equal, decrease the favorability of Si as a light element in the inner core. We also repeat the compositional mixing analysis with the Vinet-MGD equation of state (i.e., neglecting P_{el} and P_{anh}). Several slices of the resulting allowable compositional space are shown in Figure 2.21. Neglecting P_{el} and P_{anh} increases the overall compositional space in agreement with AK135-F. The overall effect of neglecting these terms is to decrease allowable concentration of Si while increasing the allowable concentrations of O, C, and S in the inner core. Therefore, accurately constraining the P_{el} and P_{anh} contributions to the thermal pressure of iron alloys is necessary to further constrain the composition of the inner core.

Seismic gradients in the inner core

As previously mentioned, the gradients of adiabatic bulk modulus and bulk sound speed of all the examined iron alloys do not match those of AK135-F. If the average seismic gradients are true, we repeat the above mixing analysis at 364 GPa and 5500 K to assess permissible compositions. For this calculation, we include the electronic and anharmonic contributions to thermal pressure as previously detailed. Several slices of the resulting allowable compositional space are shown in Figure 2.22. The overall effect of this analysis at 364 GPa is similar to the effect of neglecting P_{el} and P_{anh}. The allowable compositional space is generally increased, Si becomes less favorable, and O and C become more favorable. A recent study investigated the longitudinal variation of compressional wave speeds in the uppermost 80 km of the inner core (*Attanayake*

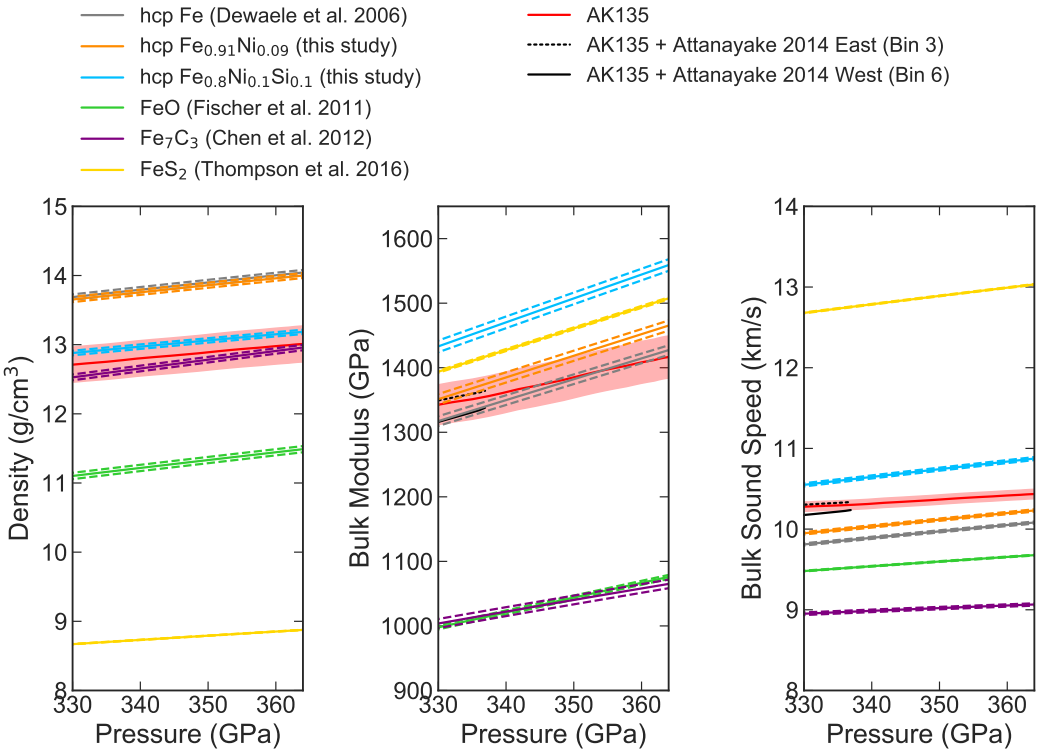

Figure 2.20: We demonstrate how neglecting the estimated electronic and anharmonic contributions to thermal pressure affects the high temperature equations of state. (Compare to Figure 2.13). Thermal equations of state for hcp-$Fe_{0.91}Ni_{0.09}$ and hcp-$Fe_{0.8}Ni_{0.1}Si_{0.1}$ (this study) are extrapolated to core conditions to calculate density ρ, adiabatic bulk modulus K_S, and bulk sound speed v_ϕ as a function of pressure at 5500 K at 330 GPa. Here, estimated electronic and anharmonic contributions to thermal pressure are *not* included. We compare to Fe (*Dewaele et al.*, 2006), FeO (*Fischer et al.*, 2011), Fe_7C_3 (*Chen et al.*, 2012), and FeS_2 (*Thompson et al.*, 2016). Dashed lines represent a temperature of $\pm$500 K. We compare to AK135-F with an estimated 2% uncertainty for ρ, 2.3% uncertainty for K_S, and 0.6% uncertainty for v_ϕ (*Deuss*, 2008; *Masters and Gubbins*, 2003). We include K_S and v_ϕ of the eastern (Bin 3, black dashed line) and western (Bin 6, black solid line) hemispheres of the inner core, as determined by combining v_P from *Attanayake et al.* (2014) with ρ and v_S from AK135-F.

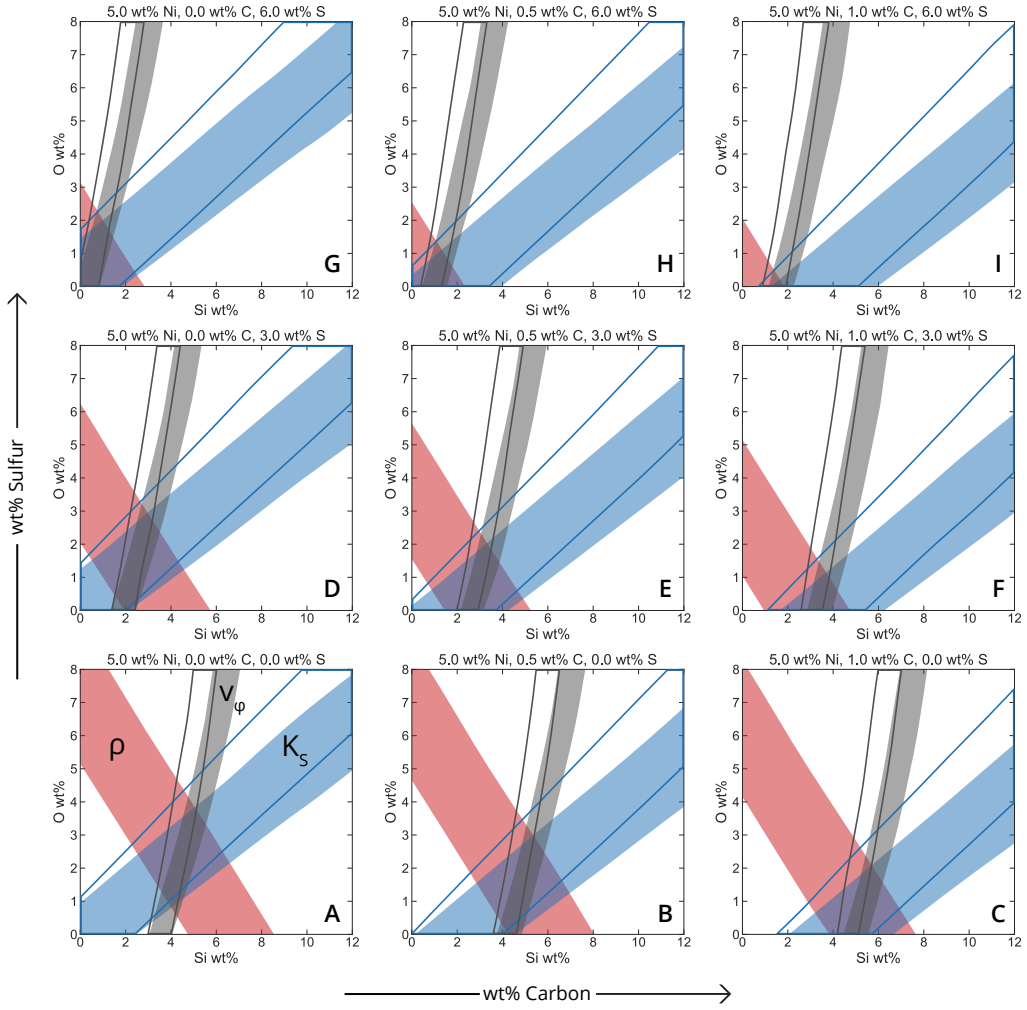

Figure 2.21: We demonstrate how neglecting the estimated electronic and anharmonic contributions to thermal pressure affects the compositional analysis. (Compare to Figure 2.16). A range of inner core compositions are explored in the Fe-Ni-Si-O-C-S system using the experimental constraints on the following alloys: hcp-Fe, hcp-$Fe_{0.91}Ni_{0.09}$, hcp-$Fe_{0.8}Ni_{0.1}Si_{0.1}$, Fe-O, Fe_7C_3, and FeS_2. The mixing calculation assumes 5500 K and 330 GPa, and the estimated electronic and anharmonic contributions to thermal pressure are *not* included here. The shaded and outlined regions represent the compositional space in agreement with the seismic model AK135-F within 2% of the density ρ (red), within 0.6% of the bulk sound speed K_S (gray), and within 2.3% of the adiabatic bulk modulus v_ϕ (blue). Two mixing models are employed: a bulk aggregate model (shaded regions) and a linear mixing model (outlined regions). Density is the same for both models. The nickel content is fixed at 5 wt%.

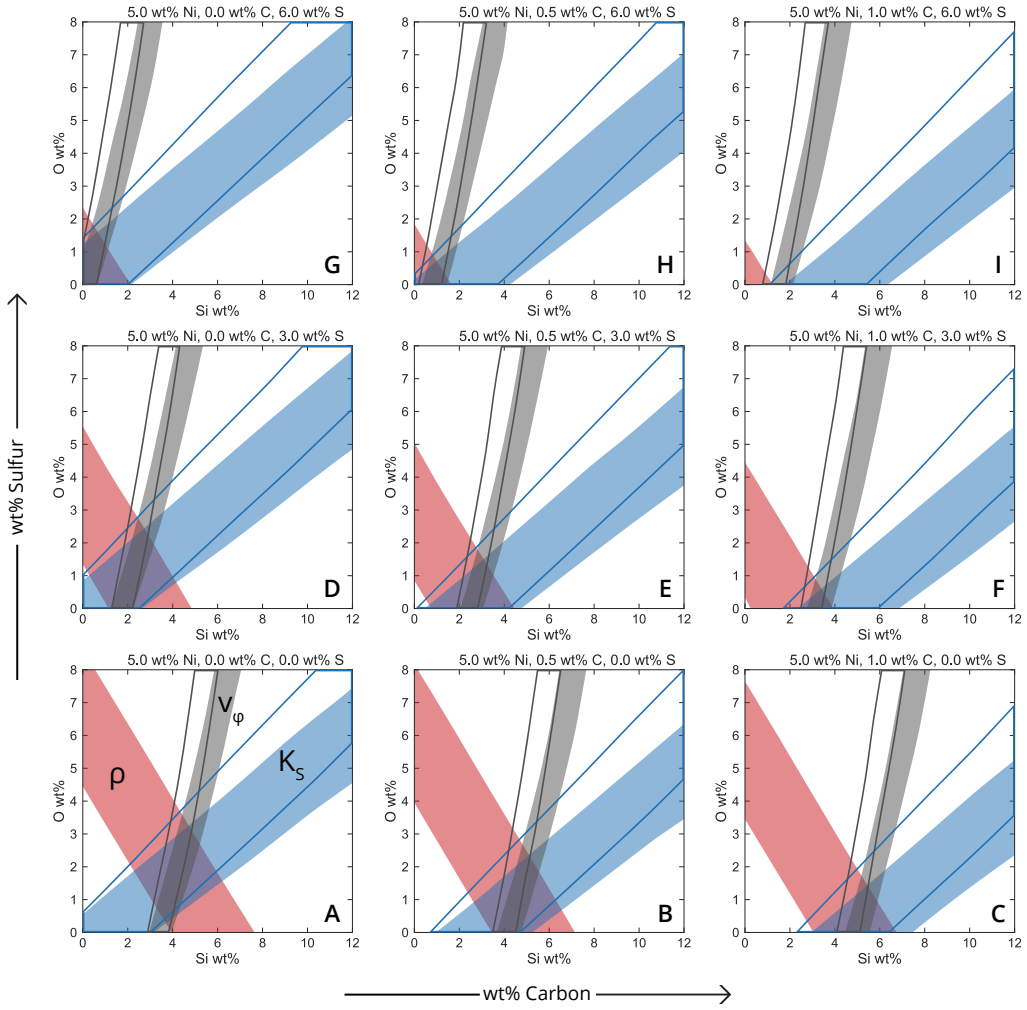

Figure 2.22: A range of compositions at the center of the Earth (364 GPa) are explored in the Fe-Ni-Si-O-C-S system using the experimental constraints on the following alloys: hcp-Fe, hcp-$Fe_{0.91}Ni_{0.09}$, hcp-$Fe_{0.8}Ni_{0.1}Si_{0.1}$, Fe-O, Fe_7C_3, and FeS_2. (Compare to Figure 2.16). The shaded and outlined regions represent the compositional space in agreement with AK135-F within 2% of the density ρ (red), within 0.6% of the bulk sound speed K_S (gray), and within 2.3% of the adiabatic bulk modulus v_ϕ (blue). Two mixing models are employed: a bulk aggregate model (shaded regions) and a linear mixing model (outlined regions). Density is the same for both models. The nickel content is fixed at 5 wt%. The mixing calculation assumes 5500 K, and estimated electronic and anharmonic contributions to thermal pressure are included.

et al., 2014). To draw comparisons with our analysis, we combine the compressional velocities from two of *Attanayake et al.* (2014)'s longitudinal bins (bin 3 in the eastern hemisphere and bin 6 in the western hemisphere) with the density and shear velocity of AK135-F to calculate the adiabatic bulk modulus and bulk sound speed. The longitudinal variation estimates are plotted as black dotted (east) and solid (west) lines in Figure 2.13. The K_S and v_ϕ gradients for all alloys appear to agree well with those reported for the upper inner core in the western hemisphere (bin 6), but not with those of the eastern hemisphere (bin 3) (*Attanayake et al.*, 2014). Thus, chemical and/or physical variations could exist laterally and radially, throughout the inner core. For example, there could be a gradient in composition or distinct phase/chemical boundaries within the inner core.

Discussion

We now compare our compositional mixing analysis at 5500 K at 330 GPa (Figure 2.16) to other proposed inner core compositions. *Antonangeli et al.* (2010) use inelastic x-ray scattering (IXS) results on the compressional wave velocity of $Fe_{0.89}Ni_{0.04}Si_{0.07}$ as a function of density (pressure) and suggest an inner core composition of 4–5 wt% Ni and 1–2 wt% Si, a composition also favored as a joint solution to geochemical, seismological, and mineral physics constraints of the outer core (*Badro et al.*, 2015; *Brodholt and Badro*, 2017). We find that 1–2 wt% of Si alone is insufficient to match the density of the inner core. Later IXS and x-ray diffraction measurements up to 140 GPa determined the compressional waves of Fe alloyed with 9 wt% Si at 300 K (*Antonangeli et al.*, 2018) and found up to 3 $\pm$ 2 wt% Si could explain inner core properties for relatively high temperatures of 6200 to 6500 K. These silicon concentrations are lower than we suggest, as we find that an ICB temperature of 6000 K has an allowable silicon content of 4.7–5.8 wt%, and the concentration of silicon required increases with temperature. However, both our findings and those of *Antonangeli et al.* (2018) depend on how the electronic and anharmonic contributions to thermal pressure are modeled. Ab initio calculations by *Martorell et al.* (2016) find the addition of silicon decreases density and increases both the compressional and shear velocities of iron at 360 GPa such that the density and velocities for a single Fe-Si composition cannot simultaneously satisfy seismic observations. They therefore suggest silicon is unlikely to be the sole light element in the inner core, although this study did not consider the effects

of nickel that we report here.

High pressure partitioning experiments demonstrate that the simultaneous solubilities of Si and O increase substantially with temperature (*Bouhifd and Jephcoat*, 2011; *Hirose et al.*, 2017; *Siebert et al.*, 2012; *Takafuji et al.*, 2004). To this end, a range of solutions containing both silicon and oxygen in our analysis would be permitted (Figure 2.16a). Ab initio partitioning studies between solid and liquid iron containing Si, S, and O by *Alfè et al.* (2002, 2007) find weak partitioning of Si and S between liquid and solid iron and conclude that Si and S are insufficient to explain the density jump at the inner core boundary. Based on their finding that O is highly incompatible in solid iron and the seismically observed density jump reported by *Masters and Gubbins* (2003) of 6.5 ± 1.4%, *Alfè et al.* (2007) estimate an inner core composition of 4.5 wt% of Si or S with trace amounts (0.06 wt%) of O and an outer core composition of 4.6 wt% of Si or S and 4.3 wt% of O. Our compositional analysis, which favors silicon and/or sulfur over oxygen and carbon in the inner core, is in agreement with this model (Figure 2.16, panels a, d, and g). An outer core containing larger amounts of silicon, such as 8-9 wt% (*Fischer et al.*, 2015; *Rubie et al.*, 2015), would not be favored by our compositional mixing analysis. A melting relation study by *Komabayashi* (2014) based on high-pressure and high-temperature experiments in the Fe-FeO system found oxygen reduces the compressional wave velocity of liquid iron away from seismologically constrained values, thereby suggesting the bulk outer core of the Earth is oxygen poor. This would suggest the inner core is also oxygen poor. This is in agreement with the oxygen poor region of our compositional models (Figure 2.16, bottom of panels a–e and g).

The amount of carbon in the Earth is difficult to estimate as carbon may have accreted primarily as volatile hydrocarbons (*Lodders*, 2003) or as carbides or graphite which have greater thermal stabilities (*Buchwald*, 1975; *Wood*, 1993; *Wood et al.*, 2013). Using a combination of cosmochemical, partitioning, density, and sound velocity studies, *Wood et al.* (2013) estimate the total upper carbon limit in the whole core at ∼1 wt%. Ab initio partitioning calculations between iron and silicate melts by *Zhang and Yin* (2012) similarly estimate the carbon content in the whole core at 0.1–0.7 wt%. An ab initio study by *Li et al.* (2016) on the velocity and density of Fe_7C_3 found the density of Fe_7C_3 to be too low to be a major component of the inner core. Our compositional analysis

is in qualitative agreement with *Wood et al.* (2013), *Zhang and Yin* (2012), and *Li et al.* (2016) as we find the maximum carbon content in the inner core to be 1.0 wt% coexisting with ∼5 wt% Si. In contrast, *Chen et al.* (2014) suggest the shear softening of Fe_7C_3 could explain the low shear velocity of the inner core. They propose a core composed of predominately Fe_7C_3, which would correspond to 8.4 wt% C in the inner core and a minimum of approximately 0.3 wt% of C in the bulk core. While our compositional analysis does not address shear velocities, the trends for density, bulk modulus, and bulk sound velocity do not favor an inner core carbon concentration of this magnitude.

2.6 Conclusions

We present a suite of powder x-ray diffraction data sets collected at 300 K on bcc- and hcp-$Fe_{0.91}Ni_{0.09}$ from 0 to 167 GPa and on bcc- and hcp-$Fe_{0.8}Ni_{0.1}Si_{0.1}$ from 0 to 175 GPa. Vinet equations of state were fit to the resulting pressure-volume data sets. By systematically comparing our findings to those of pure iron conducted under similar conditions (*Dewaele et al.*, 2006), we constrain the effect of nickel and silicon on the density, bulk modulus, and bulk sound speed of iron alloys, which is a critical step in constraining the inner core's composition. By computing the confidence ellipses for the fitted equation of state parameters at a range of pressures where hcp alloys are stable, we show that the addition of 9 at% Ni to hcp-Fe slightly increases the bulk modulus pressure derivative at all pressures. The further addition of 10 at% Si noticeably increases the pressure derivative of bulk modulus at all pressures.

The density, adiabatic bulk modulus, and bulk sound speed of hcp-$Fe_{0.91}Ni_{0.09}$ and hcp-$Fe_{0.8}Ni_{0.1}Si_{0.1}$ were extrapolated to 5500 K along the inner core pressure gradient from 330 to 364 GPa and compared to the seismic model AK135-F. We estimate the effect of the ICB temperature, as well as the electronic and anharmonic contributions to thermal pressure, in our calculations. We applied a linear mixing model to the Fe-Ni-Si system to determine to what extent silicon is seismically consistent with the density, adiabatic bulk modulus, and bulk sound speed observations of the inner core at 330 GPa. We found 4.3 to 5.3 wt% silicon alone could explain the density, adiabatic bulk modulus, and bulk sound speed of the inner core. Silicon concentrations above ∼6 wt% are not favored.

We extrapolated our compositional analysis to the Fe-Ni-Si-O-C-S system by

applying both a bulk aggregate model and a linear mixing model at 330 GPa. A mixture of silicon and oxygen (with or without sulfur) could also explain the density, adiabatic bulk modulus, and bulk sound speed of the inner core. Our analysis points to a low oxygen content of the inner core (less than $\sim$2 wt%) as well as a low carbon content (less than 1 wt%). We find that an inner core with predominately silicon as the light element would be associated with a hotter ICB, and an inner core with predominately oxygen, carbon, or sulfur as the light element would be associated with a cooler ICB.

The inclusion of electronic and anharmonic contributions to thermal pressure has a noticeable effect on decreasing the allowable compositions. Therefore, constraining the electronic and anharmonic contributions to thermal pressure for a range of iron alloys at inner core conditions is necessary to further constrain core composition. Constraints on the shear properties and phase equilibria of iron alloys at inner core conditions, as well as constraints on the core temperature, are similarly important to further constrain core composition.

Chapter 3

AXIAL RATIOS AND ANISOTROPY OF HCP-STRUCTURED MATERIALS[1]

3.1 Introduction

Seismic studies provide evidence for an anisotropic inner core (e.g., *Lythgoe et al.* (2014), and for a recent review, see *Deuss* (2014)). Various origins of this seismic anisotropy have been suggested, including preferred alignment of elastically anisotropic crystallites of iron alloys (e.g., *Deuss*, 2014; *Hirose et al.*, 2013; *Mainprice*, 2015). However, the elastic anisotropy of hcp-Fe alloys are not very well constrained and currently debated. Elastic anisotropy of a material is directly determined by its single-crystal elastic modulus tensor, which can be experimentally or theoretically constrained by various approaches. One common measure of elastic anisotropy for hcp-structured materials is the ratio of compressional elastic moduli $\phi = C_{33}/C_{11}$, where the elastic moduli C_{11} and C_{33} are expressed in the condensed Voigt notation (e.g., *Mainprice*, 2015; *Maupin and Park*, 2015). However, hcp-iron is unstable at ambient pressure and temperature, and the high-pressure synthesis of an hcp-iron single crystal large enough to reliably determine elastic constants remains a challenge. Previous studies have attempted to experimentally constrain the relative magnitudes of C_{11} and C_{33} by inducing texture in polycrystalline hcp-iron in diamond anvil cells and analyzing data collected at a range of angles compared to the direction of compression, using x-ray diffraction (*Mao et al.*, 1998; *Merkel et al.*, 2005; *Singh et al.*, 1998) or inelastic x-ray scattering (*Antonangeli et al.*, 2004a; *Mao et al.*, 2008). However, inducing texture in hcp-iron under such large compressions has been suggested to cause the material to behave plastically, so the results from such studies have been called into question (*Antonangeli et al.*, 2006; *Daymond et al.*, 1999; *Li et al.*, 2004; *Weidner et al.*, 2004; *Wenk et al.*, 2000).

Multiple studies have suggested that the anisotropy of hcp-structured materi-

[1]This chapter contains material previously published as part of Morrison, R. A., J. M. Jackson, W. Sturhahn, D. Zhang, and E. Greenberg (2018), Equations of state and anisotropy of Fe-Ni-Si alloys, *Journal of Geophysical Research: Solid Earth*, 122, doi:10.1029/2017JB015343.

als may be related to the ratio of the c- to a-unit cell parameters (*Asker et al.*, 2009; *Fischer and Campbell*, 2015; *Gannarelli et al.*, 2005; *Ono et al.*, 2010; *Sha and Cohen*, 2006), which implies the elastic anisotropy may be constrained by experimentally feasible c/a axial ratio measurements. For instance, *Wenk et al.* (1988) noted that at ambient pressure and temperature, the hcp-structured materials Zn and Cd which had c/a axial ratios greater than the ideal hcp value of 1.633 also had strong elastic anisotropy with $C_{33}/C_{11} \approx 0.4$. They also noted that the materials Ti and Zr which had c/a axial ratios less than 1.633 also had weak seismic anisotropy with $C_{33}/C_{11} \approx 1.15$. For reference, a $C_{33}/C_{11} = 1$ would correspond to a minimum compressional wave anisotropy. *Steinle-Neumann et al.* (2001) employ a conceptual argument, whereby the expansion of the c-axis with constant density may induce a softening along the c-axis, resulting in a decrease in C_{33}/C_{11}.

Theoretical calculations have noted a connection between c/a and anisotropy. *Vočadlo et al.* (2009) observe that in ab initio molecular dynamics calculations of elastic constants, it is critical to ensure the simulated crystal structure is in equilibrium before a strain matrix is applied. They conclude that choice of the c/a axial ratio is therefore of particular importance to obtain realistic elastic constants in theoretical calculations. *Grechnev et al.* (2003) suggest theoretical calculations with high c/a yield calculations of high elastic anisotropy where $C_{33}/C_{11} < 1$. This argument is in agreement with that of *Wenk et al.* (1988), who also suggest a high c/a is correlated with $C_{33}/C_{11} < 1$.

There is little consensus on the values and trends of axial ratios of iron alloys at ambient temperature (e.g., *Asker et al.*, 2009; *Fischer and Campbell*, 2015; *Gannarelli et al.*, 2005; *Ono et al.*, 2010; *Sha and Cohen*, 2006), making the act of benchmarking the correlation between axial ratios and anisotropy difficult. Using x-ray diffraction data presented in Chapter 2 and Appendix A, we precisely determine the c/a axial ratio of hcp-$Fe_{0.91}Ni_{0.09}$ and hcp-$Fe_{0.8}Ni_{0.1}Si_{0.1}$ at 300 K as a function of pressure, compare to that of hcp-Fe, and examine the connection between the c/a axial ratio, its pressure derivative, and elastic anisotropy in hcp-structured materials.

3.2 Axial ratios of iron alloys

The unit-cell axial ratios (c/a) for hcp-$Fe_{0.91}Ni_{0.09}$ and hcp-$Fe_{0.8}Ni_{0.1}Si_{0.1}$ determined in this study from x-ray diffraction are shown in Figure 3.1 (see also

Tables A.1–A.4 in Appendix A). We find the hcp-$Fe_{0.91}Ni_{0.09}$ axial ratio ranges from 1.609 (20 GPa) to 1.604 (170 GPa) and the hcp-$Fe_{0.8}Ni_{0.1}Si_{0.1}$ ranges from 1.614 (30 GPa) to 1.608 (170 GPa). We compare to the axial ratios of pure hcp-Fe from *Dewaele et al.* (2006) and *Boehler et al.* (2008), which range from 1.604 (20 GPa) to 1.597 (170 GPa). The axial ratios of hcp-$Fe_{0.91}Ni_{0.09}$ and hcp-$Fe_{0.8}Ni_{0.1}Si_{0.1}$ decrease with pressure with a slope similar to that of hcp-Fe (*Boehler et al.*, 2008; *Dewaele et al.*, 2006), and all three materials have an axial ratio below the ideal hcp axial ratio of 1.633. The c/a axial ratios of the three materials are measurably distinct. The hcp-$Fe_{0.91}Ni_{0.09}$ axial ratio is offset from the pure iron axial ratio by +0.005 to +0.007, and the hcp-$Fe_{0.8}Ni_{0.1}Si_{0.1}$ axial ratio is further offset by roughly +0.005. Alloying iron with nickel therefore has a measurable effect on the c/a axial ratio of the alloy, as does alloying iron-nickel with silicon. This is in agreement with theoretical calculations from *Asker et al.* (2009) and *Ekholm et al.* (2011) and existing experimental results from *Lin et al.* (2002), *Tateno et al.* (2012), *Sakai et al.* (2014), and *Tateno et al.* (2015).

Fischer and Campbell (2015) formulate a functional fit of the axial ratio data of hcp alloys in the Fe-Ni-Si system in volume, temperature, and compositional space based on a range of axial ratio measurements that include diamond anvil and multi anvil cell experiments in various pressure media: He, Ne, KCl, NaCl, SiO_2, and MgO. We compare the *Fischer and Campbell* (2015) multi-compositional c/a fit to our data as a function of volume in Figure 3.2. The axial ratios of these three compositions decrease with increasing pressure (or decreasing volume), the addition of nickel to iron increases the axial ratio, and the further addition of silicon also increases the axial ratio. However, we find a more shallow decrease in axial ratio with compression than *Fischer and Campbell* (2015), which may be due to different pressure media. Many pressure media (e.g., NaCl) are less hydrostatic at 300 K. Helium, however, is much more hydrostatic at 300 K. Therefore, axial ratio measurements conducted in a helium pressure medium may more accurately constrain the axial ratio slope with pressure (or volume) at 300 K. The axial ratios of hcp-Fe (*Boehler et al.*, 2008; *Dewaele et al.*, 2006) and of hcp-$Fe_{0.91}Ni_{0.09}$ (this study) demonstrate a non-linear curvature with pressure. We therefore fit the axial ratios of hcp-Fe, hcp-$Fe_{0.91}Ni_{0.09}$, and hcp-$Fe_{0.8}Ni_{0.1}Si_{0.1}$ with the empirical exponential decay

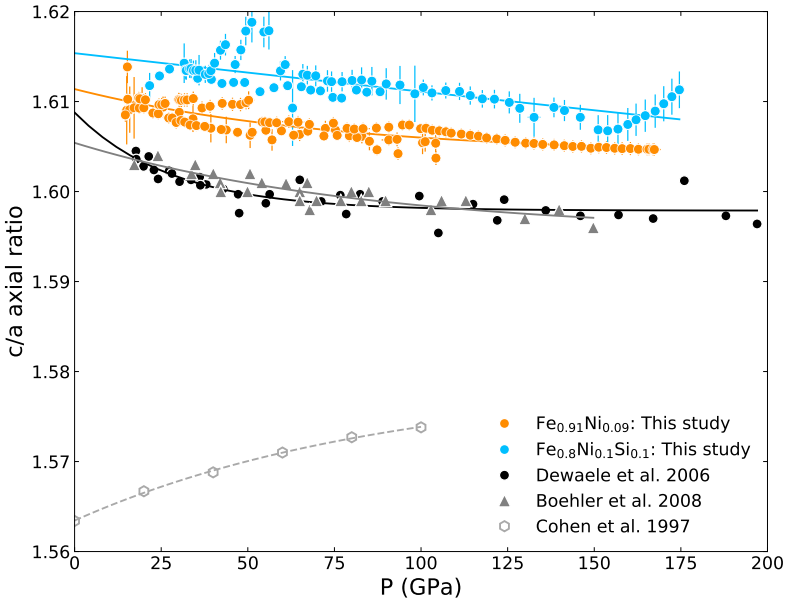

Figure 3.1: The c/a axial ratios of hcp-$Fe_{0.91}Ni_{0.09}$ (orange, this study) and $Fe_{0.8}Ni_{0.1}Si_{0.1}$ (blue, this study) determined with x-ray diffraction at 300 K fit with exponential functions (Equation 3.1). X-ray diffraction studies and exponential fits for pure hcp-Fe at 300 K by *Dewaele et al.* (2006) (black) and (*Boehler et al.*, 2008) (gray triangles) are included. The ab initio hcp-Fe study at 0 K by *Cohen et al.* (1997) (gray open hexagons) is plotted to demonstrate the c/a change in slope and curvature as temperature rises from 0 K to 300 K.

function

$$\frac{c}{a}(P) = A + B \exp\left(\frac{-P}{C}\right). \tag{3.1}$$

Our fits are plotted with the hcp-iron alloy x-ray diffraction data in Figure 3.1.

In Figure 3.3, we compare the axial ratios of hcp-Fe reported from several studies at a range of temperatures. Diamond anvil cell x-ray diffraction experiments at 300 K were conducted by *Dewaele et al.* (2006) in a helium pressure medium and by *Boehler et al.* (2008) in various pressure media including Ar, Xe, KCl, and Al_2O_3 and annealed. Laser heated diamond anvil cell x-ray diffraction experiments were conducted by *Ma et al.* (2004) up to 161 GPa and 3000 K in NaCl, MgO, and Al_2O_3 pressure media; by *Tateno et al.* (2010) up to 377 GPa and 5700 K with no pressure medium; by *Sakai et al.* (2011) up to 273 GPa and 4490 K in a NaCl pressure medium; by *Fischer et al.* (2011) up to 156 GPa and 3100 K in a NaCl pressure medium; by *Anzellini et al.* (2013) up to 200 GPa and 4900 K in a KCl pressure medium; and by *Fei et al.* (2016) up to 205 GPa and 1800 K in Ne and MgO pressure media.

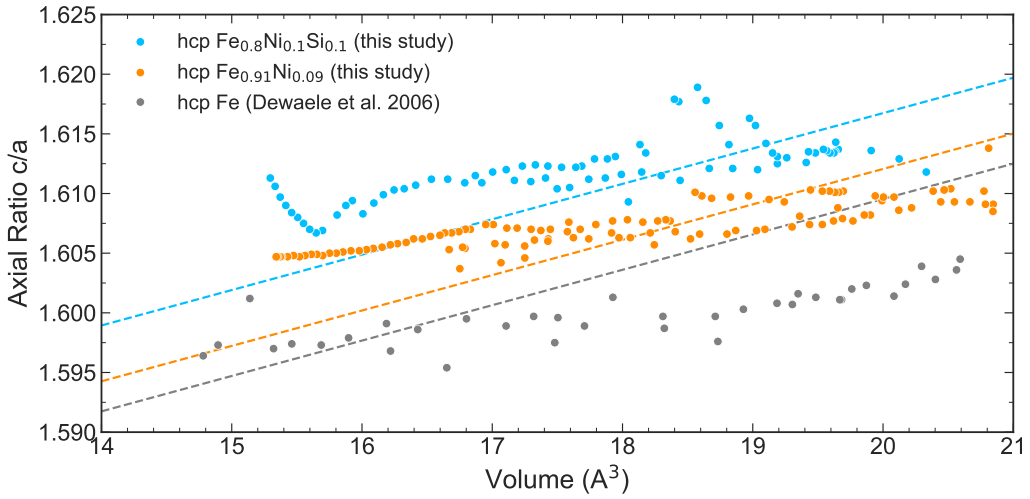

Figure 3.2: Axial ratios c/a of hcp-$Fe_{0.91}Ni_{0.09}$ (orange, this study), hcp-$Fe_{0.8}Ni_{0.1}Si_{0.1}$ (blue, this study), and hcp-Fe (grey) (*Dewaele et al.*, 2006). The compositionally dependent axial ratio trends reported in *Fischer and Campbell* (2015) are plotted for comparison. These trends are based on a fit to a collection of existing 300 K and high temperature experimental data in the Fe-Ni-Si compositional system.

Multi-anvil x-ray diffraction experiments by *Uchida et al.* (2001) up to 20 GPa and 1500 K and by *Yamazaki et al.* (2012) up to 80 GPa and 1900 K were conducted in MgO pressure media. We include ab initio hcp-Fe studies at 0 K from *Cohen et al.* (1997), *Steinle-Neumann et al.* (1999), and *Gannarelli et al.* (2005). Plotted ab initio hcp-Fe studies accounting for temperature effects include *Steinle-Neumann et al.* (2001), *Vočadlo et al.* (2009), *Mattesini et al.* (2010), *Niu et al.* (2015), and *Pourovskii et al.* (2014). *Steinle-Neumann et al.* (2001) was excluded from Figure 3.3 for clarity.

Several general conclusions can be drawn about the c/a axial ratios of pure iron. At 300 K, there is a weak decrease in the axial ratio of iron with pressure (e.g., *Boehler et al.*, 2008; *Dewaele et al.*, 2006; *Fei et al.*, 2016; *Steinle-Neumann et al.*, 2001). However, ab initio calculations at 0 K instead show a weak increase in the axial ratio of iron with pressure (*Cohen et al.*, 1997; *Gannarelli et al.*, 2005; *Steinle-Neumann et al.*, 1999, 2001). Between 0 K and 300 K, there appears to be a transition from a positive slope of c/a with pressure to a negative slope of c/a with pressure. As temperature increases, the slope of c/a with pressure appears to become increasingly negative (e.g., *Fischer and Campbell*, 2015). These studies suggest both temperature and

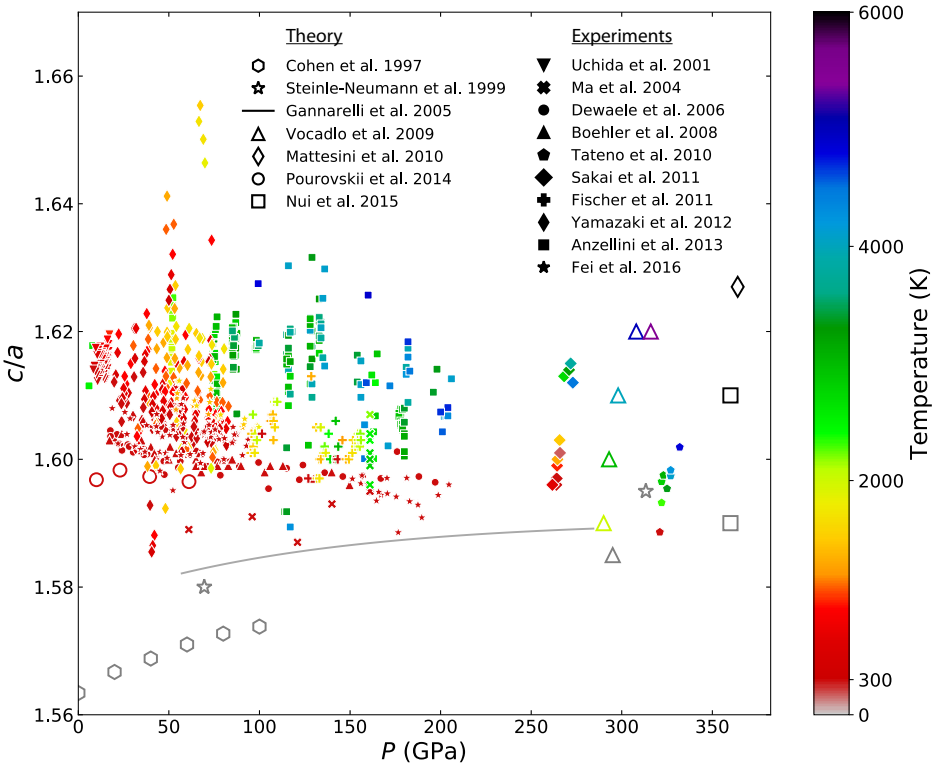

Figure 3.3: Axial ratios for hcp-Fe include diamond anvil studies (*Anzellini et al.*, 2013; *Boehler et al.*, 2008; *Dewaele et al.*, 2006; *Fei et al.*, 2016; *Fischer et al.*, 2011; *Ma et al.*, 2004; *Sakai et al.*, 2011; *Tateno et al.*, 2010), multi-anvil studies (*Uchida et al.*, 2001; *Yamazaki et al.*, 2012), and ab initio studies (*Cohen et al.*, 1997; *Gannarelli et al.*, 2005; *Mattesini et al.*, 2010; *Niu et al.*, 2015; *Pourovskii et al.*, 2014; *Steinle-Neumann et al.*, 1999; *Vočadlo et al.*, 2009).

pressure influence the c/a axial ratio.

At constant temperature, we propose that the pressure-dependent functional form of c/a in Equation 3.1 is generally applicable to hcp-Fe as an empirical fit. We fit the equation to the theoretically determined c/a axial ratio of hcp-Fe at 0 K from *Cohen et al.* (1997) (Figure 3.1). Only the *Cohen et al.* (1997) ab initio data set contains a large enough number of data points at a constant temperature to obtain a reasonable fit. At 0 K, the sign of the scaling parameter B is negative. This is consistent with the observation that the slope of c/a with pressure transitions from positive at 0 K to negative at 300 K.

3.3 The c/a axial ratio as it relates to elastic anisotropy

A variety of mechanisms have been proposed to explain seismically observed anisotropy of the inner core, and distinguishing between these mechanisms requires knowledge of the elastic anisotropy of hcp-iron alloys. However, experimentally measuring the elastic constants of hcp-iron is complicated by the difficulty of synthesizing hcp-iron single crystals. The c/a axial ratio of hcp-iron is thought to be an indirect measure of elastic anisotropy. Here, we explore the mathematical relation between the c/a axial ratio and elastic anisotropy.

The elastic behavior of an anisotropic medium is described by an extended version of Hooke's law,

$$\sigma_{ij} = \sum_{kl} E_{ijkl}\epsilon_{kl}, \quad i,j,k,l = 1...3, \tag{3.2}$$

where the second rank tensors σ and ϵ describing stress and strain are linearly related by the fourth rank elastic tensor E. It is common to use the condensed Voigt notation for these quantities, i.e., $C_{11} = E_{1111}$, $C_{12} = E_{1122}$, $C_{13} = E_{1133}$, $\sigma_1 = \sigma_{11}$, $\sigma_2 = \sigma_{22}$, etc.

$$\sigma_i = \sum_j C_{ij}\epsilon_j \text{ and } \epsilon_i = \sum_j S_{ij}\sigma_j \quad i,j = 1...6, \tag{3.3}$$

where we have defined the elastic stiffness matrix C_{ij} and its inverse S_{ij}, the elastic compliance matrix.

An isotropic stress tensor describes hydrostatic compression, and the elastic response of the material to a pressure increase δP is then

$$\epsilon_i = -\delta P \sum_{j=1}^{3} S_{ij}, \tag{3.4}$$

where the minus sign accounts for the conventional view that positive pressure causes compression. The volume change is then

$$\frac{\delta V}{V} = \sum_{i=1}^{3} \epsilon_i = -\delta P \sum_{i,j=1}^{3} S_{ij}. \tag{3.5}$$

This relation immediately provides us with an expression for the bulk modulus K as determined by a compression experiment, e.g., using x-ray diffraction,

$$K = -V\frac{\delta P}{\delta V} = \left[\sum_{i,j=1}^{3} S_{ij}\right]^{-1}, \tag{3.6}$$

where the sample's pressure (P) and unit-cell volume (V) are determined. This expression is identical to the Reuss bound of the bulk modulus, which assumes uniform stress. This is a more relevant assumption for a diamond anvil cell than the Voigt bound, which assumes uniform strain, because a pressure transmitting medium such as helium can be used in the diamond anvil cell sample-chamber to evenly distribute stress around the sample.

In the case of cubic symmetry, where the Reuss and Voigt bounds are equivalent, we obtain the following expression for the bulk modulus,

$$K_{R=V} = \frac{1}{3}[C_{11} + 2C_{12}]. \tag{3.7}$$

In the case of hexagonal symmetry (e.g., the hexagonal close-packed crystal structure), the Reuss bound of the bulk modulus takes on the following form (*Grimvall*, 1999; *Ledbetter*, 1977):

$$K_R = \frac{(C_{11} + C_{12})C_{33} - 2C_{13}^2}{C_{11} + C_{12} + 2C_{33} - 4C_{13}}. \tag{3.8}$$

In the isotropic limit for a hexagonal system, we have $C_{11} = C_{33}$, $C_{12} = C_{13}$, and $C_{11} - C_{12} = C_{44}$. The bulk modulus for a hexagonal elastically isotropic material then reduces to

$$K = \frac{1}{3}[C_{11} + 2C_{12}], \tag{3.9}$$

which is identical to the bulk modulus for cubic symmetry. We will return to this later in the case of helium.

The hcp lattice parameters respond to compression as

$$\frac{\delta a}{a} = \epsilon_1 = -(S_{11} + S_{12} + S_{13})\delta P \tag{3.10}$$

and

$$\frac{\delta c}{c} = \epsilon_3 = -(S_{33} + 2S_{13})\delta P. \tag{3.11}$$

These equations can be integrated to obtain

$$a(P) = a_0 \exp\left[-\int_0^P (S_{11}(P') + S_{12}(P') + S_{13}(P'))\, dP'\right] \tag{3.12}$$

and

$$c(P) = c_0 \exp\left[-\int_0^P (S_{33}(P') + 2S_{13}(P'))\, dP'\right]. \tag{3.13}$$

The c/a ratio is accordingly

$$\begin{aligned}\frac{c}{a}(P) &= \frac{c_0}{a_0}\exp\left[-\int_0^P (S_{33}-S_{11}+S_{13}-S_{12})dP'\right] \\ &= \frac{c_0}{a_0}\exp\left[-\int_0^P \frac{C_{11}-C_{33}+C_{12}-C_{13}}{(C_{11}+C_{12})C_{33}-2C_{13}^2}dP'\right]. \end{aligned} \tag{3.14}$$

The derivative of Equation 3.14 then gives

$$\frac{C_{11}-C_{33}+C_{12}-C_{13}}{(C_{11}+C_{12})C_{33}-2C_{13}^2} = -\frac{d\ln(c/a)}{dP}. \tag{3.15}$$

The left hand side of Equation 3.15 is experimentally accessible from single crystal ultrasonic and inelastic x-ray scattering studies, and the right hand side is accessible from carefully conducted x-ray diffraction experiments which can deliver reliable lattice parameters as a function of pressure. Both sides of this equation are accessible by ab initio calculations.

The bulk modulus K in Equation 3.8 can be extracted from Equation 3.14 to yield

$$\frac{c}{a} = \frac{c_0}{a_0}\exp\left[-\int_0^P \frac{C_{11}-C_{33}+C_{12}-C_{13}}{C_{11}+2C_{33}+C_{12}-4C_{13}}\frac{dP'}{K}\right]. \tag{3.16}$$

The derivative of Equation 3.16 then yields the following relation, where we see that the Reuss bound of the bulk modulus is simply a scaling factor,

$$\frac{C_{11}-C_{33}+C_{12}-C_{13}}{C_{11}+2C_{33}+C_{12}-4C_{13}} = -K_R(P)\frac{d\ln(c/a)}{dP}. \tag{3.17}$$

Again, the left hand side is accessible from single crystal elasticity studies. The right hand side is accessible from x-ray diffraction experiments, as high quality x-ray diffraction data as a function of pressure can provide pressure derivatives of the bulk modulus and the c/a axial ratio. This formulation may be preferable if the bulk modulus is well constrained by carefully conducted x-ray diffraction experiments. Both sides of this equation are also accessible by ab initio calculations.

As C_{44} and C_{55} are absent under these circumstances, the pressure derivative of the c/a axial ratio is only sensitive to anisotropy measures involving volumetric terms (C_{11}, C_{33}, C_{12}, and C_{13}), not shear terms (C_{44}, C_{55}). For hcp materials characterized by negligible anisotropy in the volumetric terms (that is, $C_{11} = C_{33}$ values, and $C_{12} = C_{13}$), we arrive at the following expression:

$$-K(P)\frac{d\ln(c/a)}{dP} = 0. \tag{3.18}$$

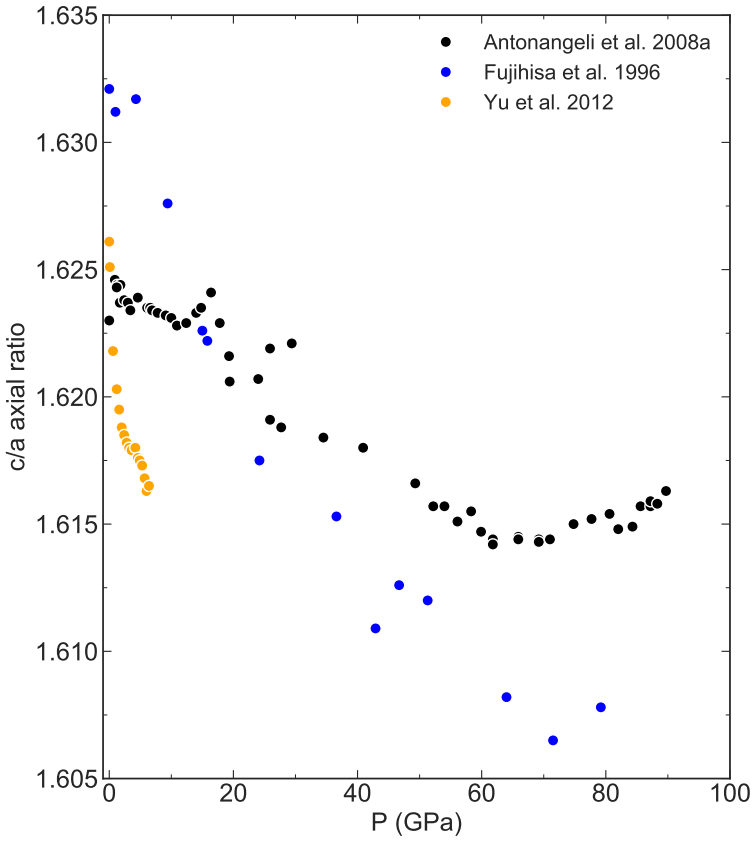

Figure 3.4: Axial ratios for hcp-cobalt are plotted as determined from diamond anvil cell measurements with no pressure medium (*Fujihisa and Takemura*, 1996), from diamond anvil cell measurements with a neon pressure medium *Antonangeli et al.* (2008a), and from cubic-anvil measurements with a NaCl pressure medium *Yu et al.* (2012).

3.4 Cobalt c/a axial ratio and anisotropy

While synthesizing single crystals of hcp-iron remains challenging, single crystals of hcp-structured cobalt are readily available at ambient conditions. Cobalt, and other hcp-structured materials, have therefore been proposed to serve as proxies for understanding the elastic behavior of hcp-iron. Here, we review the axial ratio and the anisotropy of hcp-cobalt.

X-ray diffraction measurements constraining the c/a axial ratio of hcp-cobalt are plotted as a function of pressure in Figure 3.4. *Fujihisa and Takemura* (1996) study polycrystalline cobalt in a diamond anvil cell with no pressure media up to 79 GPa, while *Antonangeli et al.* (2008a) study polycrystalline cobalt in a diamond anvil cell with a neon pressure medium up to 90 GPa. *Yu et al.* (2012) study polycrystalline cobalt in a cubic anvil apparatus with

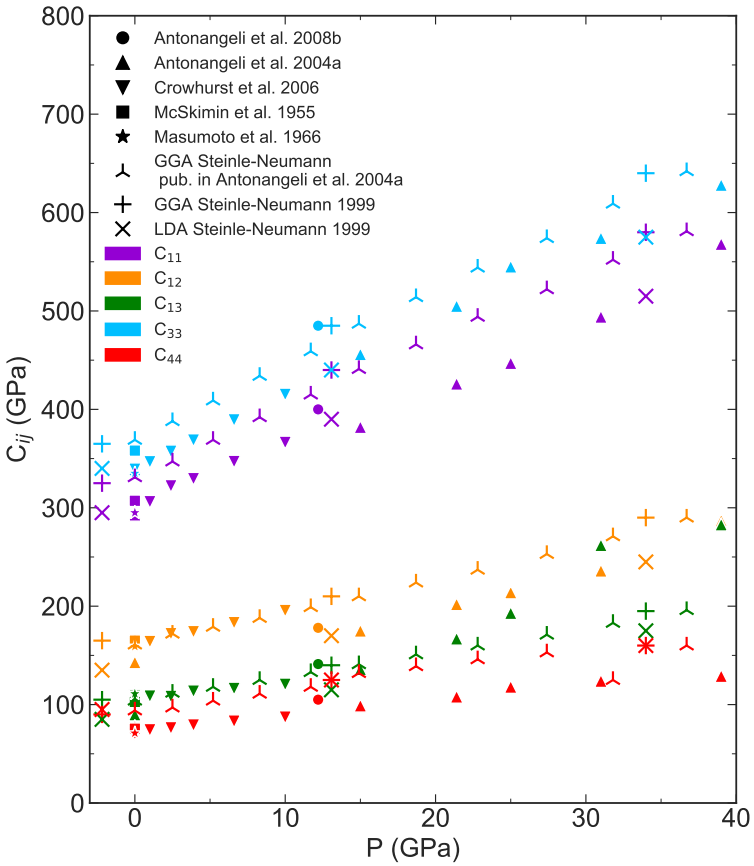

Figure 3.5: Experimentally determined elastic constants C_{ij} for hcp-cobalt include single crystal ultrasonic studies at ambient pressure (*Masumoto et al.*, 1966; *McSkimin*, 1955), single crystal impulsive stimulated light scattering in a diamond anvil cell with a helium pressure medium (*Crowhurst et al.*, 2006), and single crystal inelastic x-ray scattering in a diamond anvil cell with a helium and neon pressure medium (*Antonangeli et al.*, 2004b, 2008b). *Ab initio* calculations of C_{ij} using density functional theory include *Steinle-Neumann et al.* (1999) and *Antonangeli et al.* (2004b). Ambient pressure *Steinle-Neumann et al.* (1999) C_{ij} are slightly offset to the left of 0 GPa for clarity.

a NaCl pressure medium up to 6.5 GPa. As the two studies with a pressure medium (*Antonangeli et al.*, 2008a; *Yu et al.*, 2012) are in agreement at ambient conditions, we reference a c/a axial ratio of 1.625 for cobalt at 0 GPa and 300 K in Figure 3.10.

Experimentally and theoretically determined elastic constants C_{ij} for hcp-cobalt are plotted as a function of pressure in Figure 3.5. The elastic moduli of single crystal cobalt were measured with ultrasonic studies at ambient pres-

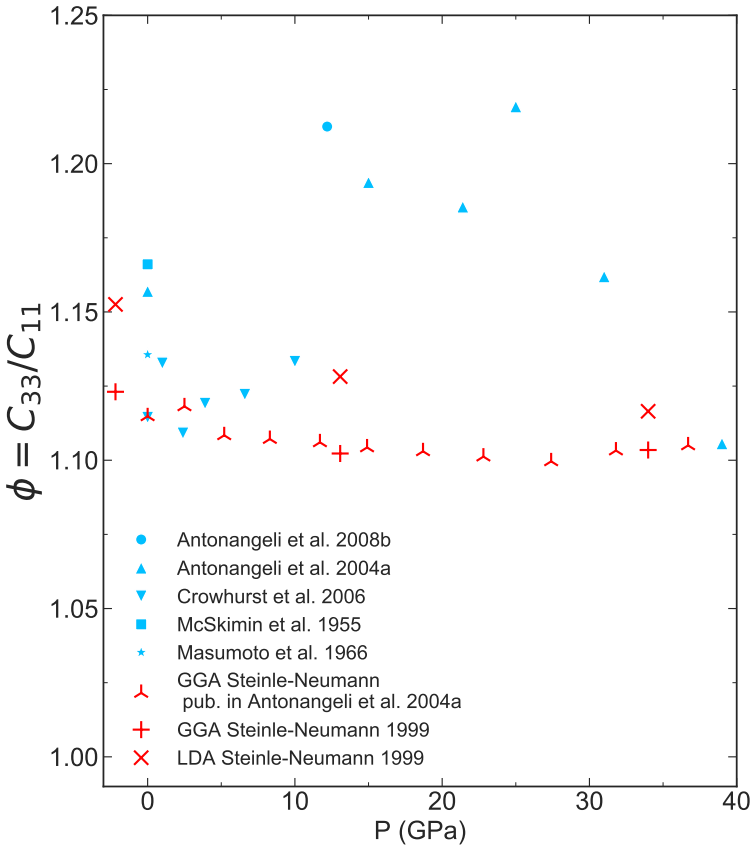

Figure 3.6: The anisotropy measure $\phi = C_{33}/C_{11}$ for hcp-cobalt is calculated from the C_{ij} values reported in experimental studies (*Antonangeli et al.*, 2004b, 2008b; *Crowhurst et al.*, 2006; *Masumoto et al.*, 1966; *McSkimin*, 1955) and theoretical studies (*Antonangeli et al.*, 2004b; *Steinle-Neumann et al.*, 1999).

sure (*Masumoto et al.*, 1966; *McSkimin*, 1955). The elastic moduli of cobalt as a function of pressure were constrained by single crystal impulsive stimulated light scattering in helium (*Crowhurst et al.*, 2006) and by single crystal inelastic x-ray scattering in helium and neon (*Antonangeli et al.*, 2004b, 2008b). We compare the experimental measurements of C_{ij} to theoretical ab initio calculations which employ density functional theory (*Antonangeli et al.*, 2004a; *Steinle-Neumann et al.*, 1999). The *Antonangeli et al.* (2008b) and *Steinle-Neumann et al.* (1999) studies do not report elastic moduli as a function of pressure, so we convert volume to pressure with the cobalt equation of state reported in *Antonangeli et al.* (2008a), where $K_0 = 203 \pm 2$ GPa and $K_0' = 3.6 \pm 0.1$. *Antonangeli et al.* (2008b) does not measure C_{13}, so we use the C_{13} fit published in *Antonangeli et al.* (2004b). They report $C_{13}(P = 0) = 90 \pm 10$ GPa and $\partial C_{13}/\partial P = 4.2 \pm 0.6$. Similarly, *Crowhurst et al.*

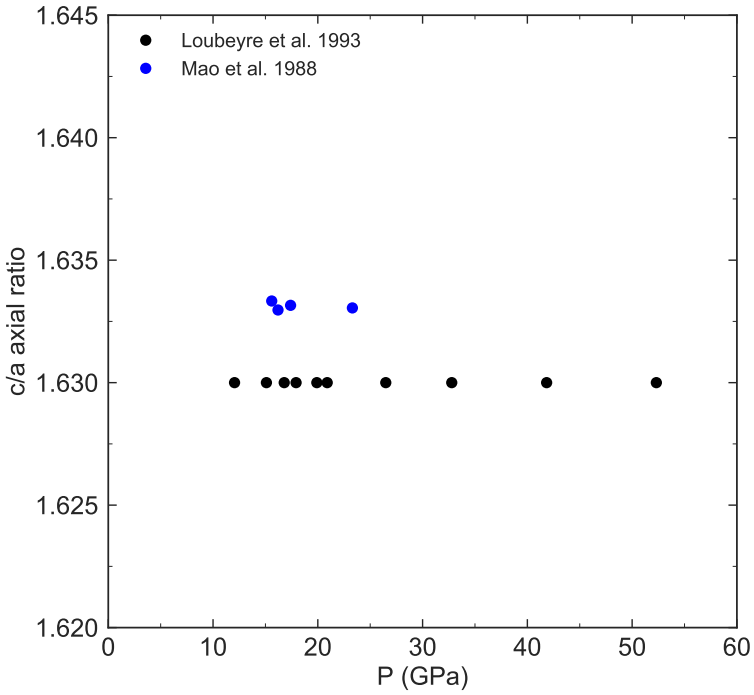

Figure 3.7: Axial ratios for hcp-helium are plotted as determined from single crystal diamond anvil cell measurements using x-ray diffraction (*Loubeyre et al.*, 1993; *Mao et al.*, 1988).

(2006) do not measure C_{33}, so they report a C_{33} estimated from the C_{33} fit from *Antonangeli et al.* (2004b): $C_{13}(P=0) = 339 \pm 4$ GPa, $\partial C_{13}/\partial P = 7.6 \pm 0.2$. The anisotropy measure $\phi = C_{33}/C_{11}$ is plotted in Figure 3.6. There is overall agreement in ϕ at 0 GPa and at 300 K. We obtain an average value of $\phi_0 = 1.14$ from the experimental measurements at 0 GPa. However, the spread in ϕ at higher pressures is broad, from approximately 1.10 to 1.22 in the range of 15-40 GPa.

3.5 Helium c/a axial ratio and anisotropy

Helium has substantially lower bulk and shear moduli than either hcp-iron or hcp-cobalt (*Zha et al.*, 2004). We examine the relationship between the c/a axial ratio, its pressure derivative, and the elastic anisotropy of hcp-helium to determine whether there are observable trends.

Two single crystal hcp-helium x-ray diffraction studies in diamond anvil cells constrained the a and c lattice parameters as a function of pressure up to 58 GPa (*Loubeyre et al.*, 1993) and up 23.3 GPa (*Mao et al.*, 1988). The resulting c/a axial ratios are plotted in Figure 3.7. While cobalt features a

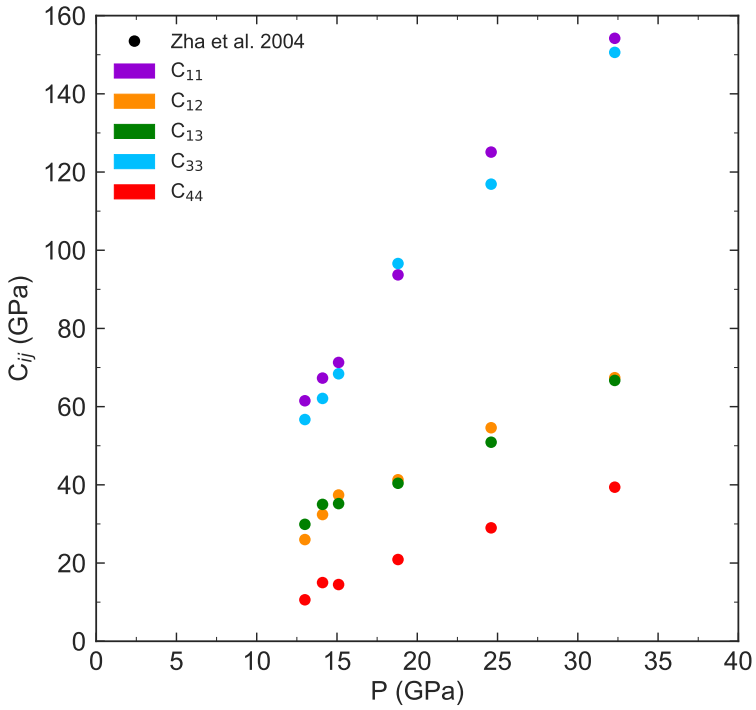

Figure 3.8: Experimentally determined elastic constants C_{ij} for hcp-helium were measured in a diamond anvil cell using Brillouin scattering (*Zha et al.*, 2004).

steadily declining axial ratio with pressure, helium's axial ratio appears to be independent of pressure, as is the case described using Equation 3.18. We plot an average c/a of 1.632 at 0 GPa and 300 K for helium in Figure 3.10. From Equation 3.15, the c/a trend with pressure suggests that helium is nearly elastically isotropic in terms of C_{11}, C_{33}, C_{12}, and C_{13}.

Zha et al. (2004) measured the C_{ij} values for hcp-helium in a diamond anvil cell up to 32 GPa using Brillouin scattering (Figure 3.8). The resulting anisotropy measure $\phi = C_{33}/C_{11}$ is plotted in Figure 3.9. We assume a constant ϕ as a function of pressure and average ϕ at all pressures to obtain a value of 0.96 at 300 K for hcp-helium, which is included in Figure 3.10.

3.6 Relationship between the axial ratio and anisotropy of iron alloys

To examine the connection between the c/a axial ratio and the anisotropy measure $\phi = C_{33}/C_{11}$, we plot ab initio studies of hcp-Fe which report both measures in Figure 3.10. We compare to the c/a axial ratio and anisotropy

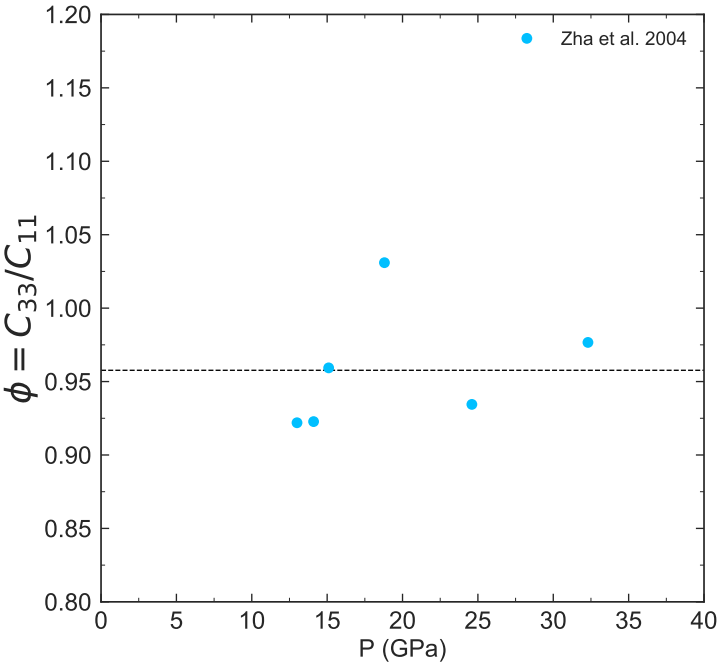

Figure 3.9: The anisotropy measure $\phi = C_{33}/C_{11}$ for hcp-helium is calculated from the C_{ij} values reported in *Zha et al.* (2004). An average value of $C_{33}/C_{11} = 0.96$ is plotted as a dashed line.

measure ϕ for other hcp-structured materials at 300 K and 0 GPa including Zn (*Ledbetter*, 1977), Cd, Zr, Ti (*Wenk et al.*, 1988), Co (*Antonangeli et al.*, 2004b, 2008a,b; *Crowhurst et al.*, 2006; *Fujihisa and Takemura*, 1996; *Masumoto et al.*, 1966; *McSkimin*, 1955; *Yu et al.*, 2012) (see Figures 3.4–3.6), and He (*Loubeyre et al.*, 1993; *Mao et al.*, 1988; *Zha et al.*, 2004)(see Figures 3.7–3.9). While a correlation between the c/a axial ratio and the anisotropy measure $\phi = C_{33}/C_{11}$ has been suggested in several studies, several ab initio studies do not follow this trend. For instance, ab initio results are contradictory and often report different ϕ values for very similar c/a values, e.g., *Vočadlo et al.* (2009) and *Niu et al.* (2015). Note that while Co and He have similar c/a axial ratios of ∼1.63, they have noticeably different ϕ anisotropy values, with helium having $C_{33}/C_{11} \approx 0.95$ and cobalt having $C_{33}/C_{11} \approx 1.15$. We therefore conclude that while Figure 3.10 suggests a correlation between the c/a axial ratio and the anisotropy measure $\phi = C_{33}/C_{11}$, the relation between c/a and ϕ is likely non-unique, and c/a may be unable to reliably predict ϕ anisotropy.

We now examine the relationship between ϕ and the pressure derivative of c/a in Figure 3.11 for hcp-Fe. The mathematical relationship between the

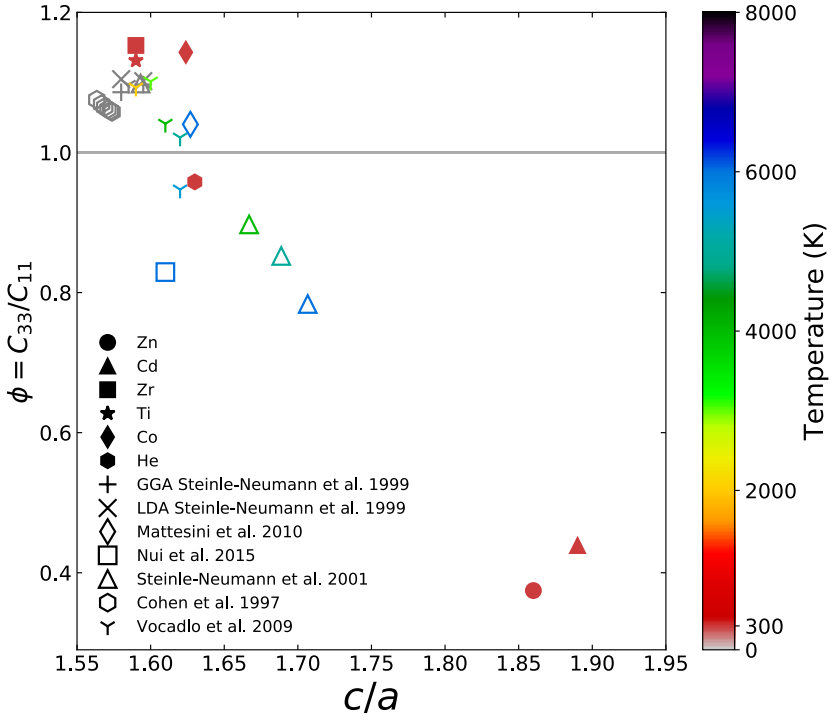

Figure 3.10: The c/a axial ratio and anisotropy measure ϕ for hcp-iron determined via ab initio calculations (*Cohen et al.*, 1997; *Mattesini et al.*, 2010; *Niu et al.*, 2015; *Steinle-Neumann et al.*, 1999, 2001; *Vočadlo et al.*, 2009). We compare to hcp-structured materials Zn (*Ledbetter*, 1977), Cd, Zr, Ti (*Wenk et al.*, 1988), Co, and He. (The c/a and ϕ values for Co and He are determined in sections 3.4 and 3.5, respectively.) For a compressionally isotropic material, $\phi = 1$ (gray line). For an ideal hcp-structure, $c/a = 1.633$.

elastic tensor components, C_{ij}, of hcp materials and the c/a axial ratio was demonstrated in equation 3.15.

The pressure derivative of c/a values at 0 K from *Cohen et al.* (1997) was calculated from the c/a vs. pressure fit shown in Figure 3.1. As *Steinle-Neumann et al.* (2001) do not have enough reported c/a values for a given temperature to fit an exponential function, the pressure derivative of c/a was calculated from a linear fit of c/a vs. pressure for 0 K, 4000 K, 5000 K, and 6000 K. The trends demonstrated in Figure 3.11 lend support for a positive correlation between $d(c/a)/dP$ and ϕ. If one uses the correlation in Figure 3.11 suggested by the cited ab initio studies, then the pressure derivatives of c/a for hcp-Fe (*Dewaele et al.*, 2006), $Fe_{0.91}Ni_{0.09}$ (this study), and $Fe_{0.8}Ni_{0.1}Si_{0.1}$ (this study) at 300 K and up to 170 GPa as shown in Figure 3.1 would correspond to anisotropies of $\phi = 0.91$–1.02 as illustrated in Figure 3.11. Nevertheless,

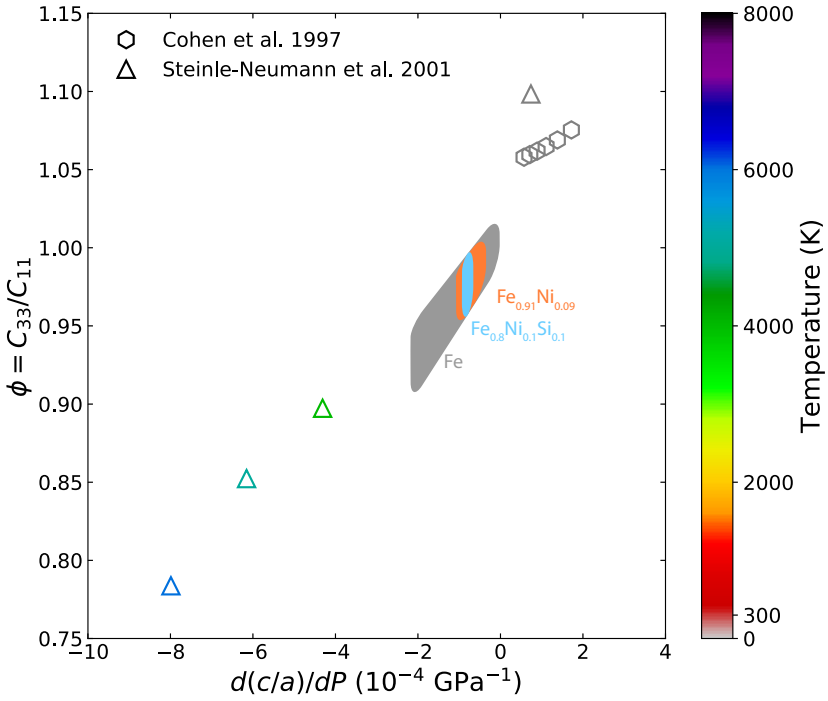

Figure 3.11: A positive correlation between the anisotropy measure ϕ and the pressure derivative of the axial ratio $d(c/a)/dP$ is suggested by the ab initio studies *Cohen et al.* (1997) at 0 K and *Steinle-Neumann et al.* (2001) at 0 K, 4000 K, 5000 K, and 6000 K. The shaded regions are a guide to the eye to indicate the $d(c/a)/dP$ of hcp-Fe, hcp-$Fe_{0.91}Ni_{0.09}$, and hcp-$Fe_{0.8}Ni_{0.1}Si_{0.1}$ at 300 K and their corresponding ϕ if they follow the same $d(c/a)/dP$ vs. ϕ trend as the *Cohen et al.* (1997) or *Steinle-Neumann et al.* (2001) data. The hcp-Fe region is greater in size due to its larger c/a vs. P curvature (see Figure 3.1), which results in a greater range of $d(c/a)/dP$ values. Regardless of the exact value of the slope of the correlation, a relationship between $d(c/a)/dP$ and ϕ will exist according to Equation 3.16.

regardless of the exact value of the slope of the correlation, a relationship between $d(c/a)/dP$ and ϕ will exist according to Equation 3.16.

3.7 Conclusions

We find that hcp-$Fe_{0.91}Ni_{0.09}$ and hcp-$Fe_{0.8}Ni_{0.1}Si_{0.1}$ have greater c/a axial ratios compared to hcp-Fe at all measured pressures. We investigate the relationship between the c/a axial ratio and the compressional anisotropy measure $\phi = C_{33}/C_{11}$. Rather than relying on the c/a axial ratio to infer elastic anisotropy, which is shown to provide non-unique results, we propose a relationship between the pressure derivative of the c/a axial ratio and the anisotropy measure $\phi = C_{33}/C_{11}$. From our analysis, the pressure derivatives

of c/a for hcp-Fe, $Fe_{0.91}Ni_{0.09}$, $Fe_{0.8}Ni_{0.1}Si_{0.1}$ at 300 K and up to 170 GPa would correspond to anisotropies of $\phi = 0.91$–1.02. Future high precision x-ray diffraction measurements of the pressure derivative of c/a at a range of pressures and temperatures will provide important constraints on the compressional anisotropy measure.

Chapter 4

THERMOELASTIC QUANTITIES AND SOUND VELOCITIES OF IRON-NICKEL-SILICON ALLOYS

4.1 Introduction

Seismological observations place constraints on the shear and compressional sound velocities and density of the inner core (e.g., *Dziewonski and Anderson*, 1981; *Kennett et al.*, 1995) and the discontinuity in compressional sound velocity and density at the inner core boundary (e.g., *Deuss*, 2008; *Masters and Gubbins*, 2003). These observations in conjunction with cosmochemical and mineral physics studies place constraints on the composition and thermal profile of the inner core. The density of the inner core is ∼3–5% lighter than hcp-iron at inner core conditions (reviewed in *Li and Fei*, 2014), which supports the presence of light elements (e.g., Si, O, S, C, H) in the inner core (reviewed in *Li and Fei*, 2014; *Litasov and Shatskiy*, 2016; *Vočadlo*, 2015). A plausible inner core composition must also match the compressional and shear velocities of the inner core, which are reported to be respectively ∼4–10% slower (e.g., *Sakamaki et al.*, 2016) and >30% slower than hcp-iron (e.g., *Martorell et al.*, 2013a).

A detailed understanding of the effect of composition on the sound velocities and densities of iron alloys at core pressures and temperatures is necessary to constrain the inner core composition and the melting temperature at the inner core boundary, as well as to better constrain outer core composition and to understand the nature of anisotropy and heterogeneity in the inner and outer core. Furthermore, an understanding of the thermoelastic properties of these alloys at core conditions can constrain geodynamical simulations of the evolution and ongoing processes of the core.

The sound velocities of hcp-iron have been extensively studied through shock-wave experiments (*Brown and Mcqueen*, 1986; *Jeanloz*, 1979; *Nguyen and Holmes*, 2004), 300 K static compression experiments (*Antonangeli et al.*, 2004a, 2018; *Decremps et al.*, 2014; *Giefers et al.*, 2002; *Gleason et al.*, 2013; *Lin et al.*, 2005; *Liu et al.*, 2014, 2016; *Lübbers et al.*, 2000; *Mao et al.*, 2001, 2008, 2012; *Murphy et al.*, 2013; *Ohtani et al.*, 2013), high temperature static

compression experiments (*Lin et al.*, 2005; *Mori et al.*, 2017; *Sakamaki et al.*, 2016), and ab initio studies (*Laio et al.*, 2000; *Mao et al.*, 2001; *Martorell et al.*, 2013a; *Niu et al.*, 2015; *Steinle-Neumann et al.*, 2001; *Vočadlo et al.*, 2009). Similarly, numerous experimental and ab initio studies have investigated hcp-iron's isothermal equation of state (e.g. *Boehler et al.*, 2008; *Dewaele et al.*, 2006; *Dubrovinsky et al.*, 2000; *Mao et al.*, 1990; *Ono et al.*, 2010; *Steinle-Neumann et al.*, 1999) and thermal equation of state (*Dubrovinsky et al.*, 1998; *Fei et al.*, 2016; *Garai et al.*, 2011; *Sakai et al.*, 2014; *Sha and Cohen*, 2010; *Stixrude et al.*, 1997; *Uchida et al.*, 2001; *Wasserman et al.*, 1996; *Yamazaki et al.*, 2012).

An important element in constraining the thermal equation of state of hcp-iron is the thermal Grüneisen parameter, which relates thermal pressure to thermal energy per unit volume and can be used to reduce shock data for comparison with isothermal compression studies. As the thermal Grüneisen parameter is composed of vibrational and electronic contributions, constraints on hcp-iron's vibrational Grüneisen parameter have helped further constrain its thermal equation of state (*Dewaele et al.*, 2006; *Dubrovinsky et al.*, 2000; *Murphy et al.*, 2011a; *Uchida et al.*, 2001; *Yamazaki et al.*, 2012). Furthermore, hcp-iron's thermal pressure can be estimated by pairing the vibrational component of thermal pressure, directly accessed through phonon density of states (DOS) measurements (*Murphy et al.*, 2011b), with ab initio constraints on the electronic and anharmonic components of thermal pressure (*Alfè et al.*, 2001; *Dewaele et al.*, 2006; *Martorell et al.*, 2013a,b; *Sha and Cohen*, 2010; *Wasserman et al.*, 1996).

Despite the presence of nickel in the Earth's core (*Allègre et al.*, 1995; *McDonough and Sun*, 1995; *McDonough*, 2003), the sound velocities and thermoelasticity of hcp-structured iron-nickel alloys have received comparatively little attention. *Lin et al.* (2003) studied the shear and compressional sound velocities of bcc- and hcp-$Fe_{0.92}Ni_{0.08}$ with nuclear resonant inelastic x-ray scattering (NRIXS). A variety of experimental studies investigated the equations of state of hcp-iron-nickel at 300 K as well as at high temperatures (*Asanuma et al.*, 2011; *Mao et al.*, 1990; *McQueen and Marsh*, 1966; *Morrison et al.*, 2018; *Sakai et al.*, 2014; *Takahashi et al.*, 1968) (e.g., see work presented in Chapter 2); however, constraints on the thermal pressure of hcp-iron-nickel are limited (*Côté et al.*, 2012; *Ekholm et al.*, 2011; *Martorell et al.*, 2013a). Exper-

imental constraints on the thermal pressure of iron-nickel alloys from phonon density of states measurements, including constraints on the Grüneisen parameter, are still lacking.

A variety of studies have investigated the sound velocities of iron-silicon alloys at 300 K (*Antonangeli et al.*, 2018; *Badro et al.*, 2007; *Lin et al.*, 2003; *Liu et al.*, 2014; *Mao et al.*, 2012; *Ono*, 2013; *Sakairi et al.*, 2018). Fewer studies have investigated the sound velocities of iron-nickel-silicon alloys at 300 K (*Antonangeli et al.*, 2010; *Lin et al.*, 2003; *Liu et al.*, 2016). Recently, *Sakairi et al.* (2018) investigated the compressional sound velocity of hcp-$Fe_{0.89}Si_{0.11}$ up to 1800 K and 84 GPa with inelastic x-ray scattering (IXS). However, existing studies constraining the shear velocity of iron-nickel-silicon alloys are sparse (*Lin et al.*, 2003; *Liu et al.*, 2016), and systematic studies independently constraining the effects of nickel and silicon on sound velocity are rare (e.g. *Antonangeli et al.*, 2018; *Lin et al.*, 2003; *Liu et al.*, 2014; *Mao et al.*, 2012). Many constraints on iron-silicon sound velocities at inner core conditions come from ab initio studies (*Martorell et al.*, 2016; *Ono*, 2013; *Tsuchiya and Fujibuchi*, 2009; *Vočadlo*, 2007). Isothermal equations of state of these alloys include *Asanuma et al.* (2011); *Hirao et al.* (2004); *Lin* (2003); *Ono et al.* (2007); *Sata et al.* (2010); *Tateno et al.* (2015) and work presented in Chapter 2 (*Morrison et al.*, 2018), and experimental thermal equations of state include *Fischer et al.* (2012, 2014); *Zhang and Guyot* (1999), and *Tateno et al.* (2015). However, to date, the thermal pressure of iron-nickel-silicon alloys, including constraints on the Grüneisen parameter, have not been investigated with experimental phonon DOS measurements.

We present NRIXS measurements on bcc- and hcp-$Fe_{0.91}Ni_{0.09}$ and $Fe_{0.8}Ni_{0.1}Si_{0.1}$ up to 104 GPa and 86 GPa, respectively. To ensure a systematic comparison with hcp-Fe by avoiding differences in analyses methods, we re-analyze hcp-Fe NRIXS data from (*Murphy et al.*, 2011a,b, 2013). We present derived phonon DOSs for each composition. We determine the Debye sound velocity from the low energy region of the phonon DOS using a new analysis method which better constrains the Debye sound velocity uncertainty. We present two separate constraints on the vibrational component of thermal pressure for the hcp phases. First, we determine the Grüneisen parameter by applying a volume scaling relation to the phonon DOSs. Second, we estimate vibrational thermal pressure from the vibrational free energy derived from the phonon DOS.

Additional parameters are derived from the phonon DOS including the Lamb-Mössbauer factor, and the thermal expansion is determined using constraints on the bulk modulus from the same alloys.

4.2 Experimental methods

Samples were synthesized by arc-melting individual pieces of Ni, Si, and 95%-enriched ^{57}Fe in an argon atmosphere to produce $Fe_{0.91}Ni_{0.09}$ and $Fe_{0.8}Ni_{0.1}Si_{0.1}$. Samples were then cold rolled to ∼10 μm. SEM measurements confirmed the molar sample compositions to be $Fe_{0.91(1)}Ni_{0.09(1)}$ and $Fe_{0.80(1)}Ni_{0.10(1)}Si_{0.10(1)}$, and sample homogeneity was observed at a scale of 1 μm. Samples from this synthesis batch were previously used to constrain the melting temperature of $Fe_{0.91}Ni_{0.09}$ (*Zhang et al.*, 2016) and to constrain the equations of state of $Fe_{0.91}Ni_{0.09}$ and $Fe_{0.8}Ni_{0.1}Si_{0.1}$ in Chapter 2 (*Morrison et al.*, 2018).

High pressure conditions were achieved using modified panoramic diamond anvil cells (DACs) with 90° openings and cubic boron nitride backing seats on the downstream side. These modifications maximize the accessible angle range for in situ x-ray diffraction (XRD). One $Fe_{0.91}Ni_{0.09}$ and one $Fe_{0.8}Ni_{0.1}Si_{0.1}$ experimental run (hereafter referred to as FeNi-Run#1 and FeNiSi-Run#1) were each conducted with beryllium gaskets and loaded with a neon pressure medium to ensure nearly hydrostatic conditions. These experimental runs focused on lower pressures where both $Fe_{0.91}Ni_{0.09}$ and $Fe_{0.8}Ni_{0.1}Si_{0.1}$ were in the bcc phase. An $Fe_{0.91}Ni_{0.09}$ and an $Fe_{0.8}Ni_{0.1}Si_{0.1}$ experimental run (FeNi-Run#2 and FeNiSi-Run#2) were each prepared with a beryllium gasket and a boron-epoxy insert to stabilize the chamber at higher pressures, and then loaded with a neon pressure medium. An $Fe_{0.8}Ni_{0.1}Si_{0.1}$ experimental run (FeNiSi-Run#3) was prepared with a beryllium gasket and a boron-epoxy insert, but with no additional pressure medium. Experimental conditions for each run are summarized in Table 4.1. Additional bcc-$Fe_{0.91}Ni_{0.09}$ and $Fe_{0.8}Ni_{0.1}Si_{0.1}$ foil samples were placed on Kapton tape for ambient pressure measurements. Powdered 95%-enriched ^{57}Fe was also placed on Kapton tape for an ambient pressure measurement of bcc-Fe.

We collected nuclear resonant inelastic x-ray scattering (NRIXS) measurements on each sample at 300 K at Sector 3-ID-B at the Advanced Photon Source. The storage ring was run with 24-bunch top-up mode, with each bunch separated by 153 ns. Incoherent inelastic x-ray scattering was measured

Table 4.1: Experimental conditions for NRIXS and NFS studies

Run	Phase	P (GPa)	Energy range (meV)	Points per scan	Scan length (s/pt)	Stokes peak (counts)	Number of scans
Fe							
Ambient	bcc	0	-80 to +90	681	5	327	2
$Fe_{0.91}Ni_{0.09}$							
Ambient	bcc	0	-80 to +90	681	11	407	4
FeNi-Run#1	bcc	1.7(1)	-80 to +100	721	55	332	11
		4.5(1)	-80 to +100	721	35	247	7
FeNi-Run#2	bcc	3.8(1)	-80 to +100	721	13	226	3
		8.1(1)	-80 to +100	721	23	211	4
	hcp	18.0(1)	-70 to +100	681	20	226	4
		22.8(2)	-70 to +100	681	18	229	4
		41(1)	-70 to +100	681	30	265	6
		48(1)	-70 to +100	681	25	170	5
		63(1)	-70 to +100	681	38	197	8
		75(1)	-70 to +100	681	38	181	8
		83(1)	-70 to +100	681	30	155	7
		104(3)	-70 to +100	681	35	203	9
$Fe_{0.8}Ni_{0.1}Si_{0.1}$							
Ambient	bcc	0	-80 to +100	681	6	570	2
FeNiSi-Run#1	bcc	7.1(1)	-80 to +110	761	36	289	8
FeNiSi-Run#2	bcc	6.5(1)	-80 to +100	721	39	299	12
FeNiSi-Run#3	hcp	27.9(3)	-80 to +100	721	39	257	12
		37.1(6)	-80 to +100	721	48	371	12
		41(1)	-80 to +100	721	56	327	20
		55(1)	-80 to +100	721	63	273	21
		69(1)	-80 to +100	721	61	273	23
		86(3)	-80 to +100	721	60	156	23

with three avalanche photodiode detectors (APDs) positioned radially around the sample, and forward elastic scattering was measured with a single APD downstream from the sample to constrain the resolution function. The x-ray energy was tuned around the nuclear resonance of ^{57}Fe (14.4125 keV) with a state-of-the-art high-resolution monochrometer (*Toellner*, 2000). The energy ranges scanned over for each compression point are summarized in Table 4.1. For $Fe_{0.91}Ni_{0.09}$ measurements, greater counting rates at lower pressures allowed us to scan over larger energy ranges for our bcc compression points. For $Fe_{0.8}Ni_{0.1}Si_{0.1}$ measurements, we observed higher energy phonon modes which necessitated using a larger energy scan range. The typical energy resolution

(full width at half maximum at zero energy transfer) was 1.1 meV. For four $Fe_{0.91}Ni_{0.09}$ compression points between 83 and 104 GPa, large tails around the resolution peak severely impacted the quality of the data, and these compression points were discarded. The NRIXS spectra for each compression point are plotted in Figures 4.1 and 4.2.

In situ x-ray diffraction (XRD) was collected before and after each set of NRIXS scans and averaged to determine the unit cell volume of the sample at each pressure point (e.g., *Gao et al.*, 2009; *Murphy et al.*, 2013). The x-ray wavelength energy was 14.4125 keV (0.086 nm), corresponding to a nuclear resonance of ^{57}Fe. XRD images were calibrated with a CeO_2 crystal and integrated with the Dioptas software package (*Prescher and Prakapenka*, 2015). We fit the resulting x-ray diffraction patterns with full-profile Pawley refinement to determine the bcc phase lattice parameter a using reflections (100) and the hcp phase lattice parameters a and c using reflections (100), (101), and (002). We observed some texturing for our six largest compression points of hcp-$Fe_{0.91}Ni_{0.09}$ ($P > 41$ GPa) and for hcp-$Fe_{0.8}Ni_{0.1}Si_{0.1}$ as indicated by a loss of intensity in the (002) diffraction reflection. Our remaining diffraction reflections for these compression points were sufficient to determine a and c, as the (100) reflection is sensitive to the a lattice parameter and the (101) reflections is sensitive to both the a and c lattice parameters. The exact amount of uncertainty introduced by determining the sample volume with fewer diffraction peaks is difficult to quantify, so we follow *Murphy et al.* (2013) and double our determined volume uncertainty for these compression points. The resulting lattice parameters and unit cell volumes are reported in Table 4.2.

Density was determined from our in situ volume measurements and accounts for the 95% ^{57}Fe isotopic enrichment of our samples (Table 4.2). Throughout the NRIXS data analysis, we relied on our measured in situ volumes and densities. For convenience, we convert our sample volumes to pressure using external 300 K equations of state (EOSs). For our bcc-Fe data, we use the Vinet EOS for bcc-Fe reported in Chapter 2 (*Morrison et al.*, 2018) based on compression data from *Dewaele et al.* (2006). For bcc- and hcp-$Fe_{0.91}Ni_{0.09}$ and $Fe_{0.8}Ni_{0.1}Si_{0.1}$, we use the Vinet EOSs also reported in Chapter 2. These EOSs were conducted with samples synthesized from the same $Fe_{0.91}Ni_{0.09}$ and $Fe_{0.8}Ni_{0.1}Si_{0.1}$ batches used in the NRIXS experiments. All of the EOSs referenced in this study were determined using the same pressure transmitting

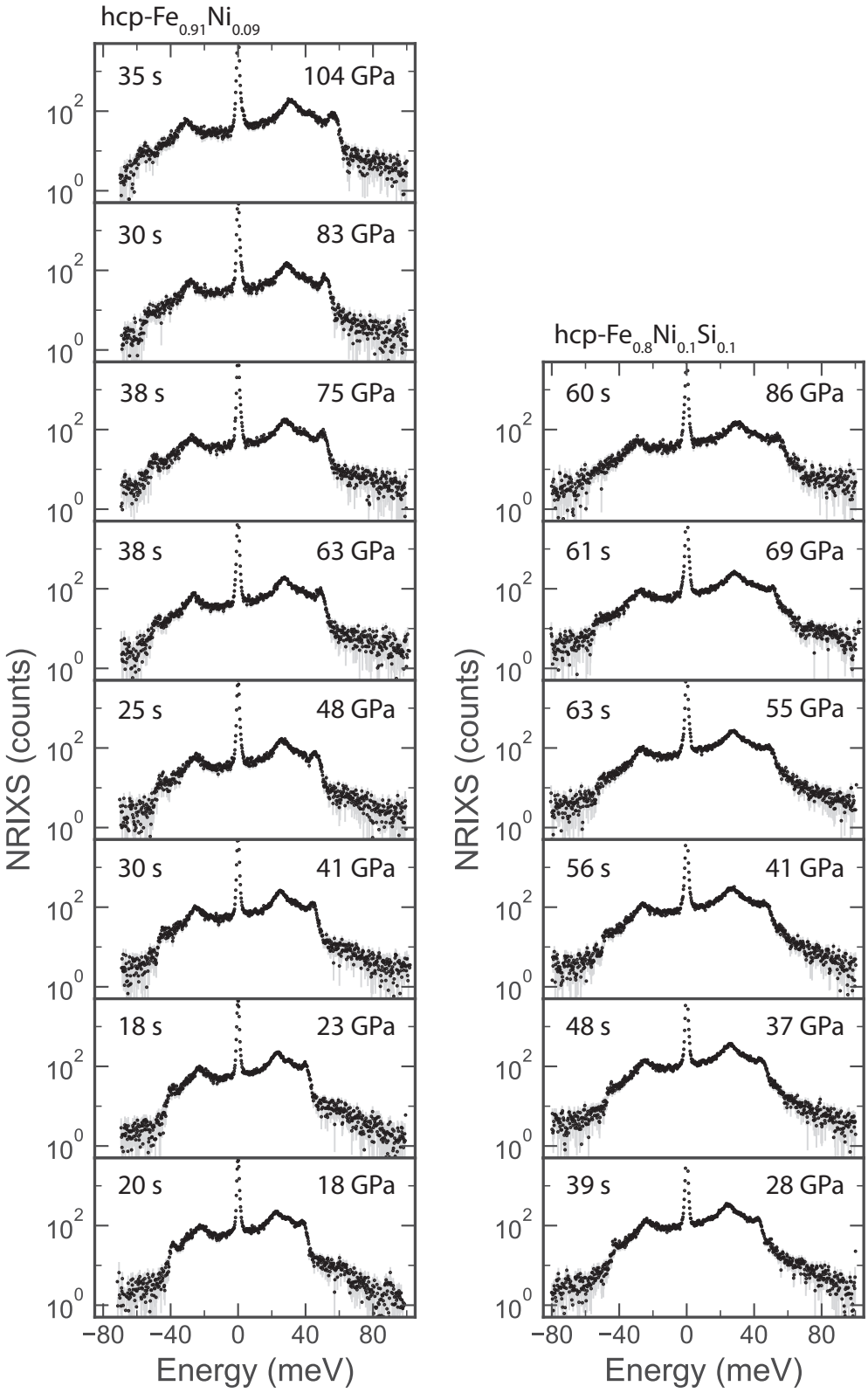

Figure 4.1: Raw (unnormalized) NRIXS spectra for hcp-$Fe_{0.91}Ni_{0.09}$ and $Fe_{0.8}Ni_{0.1}Si_{0.1}$ at 300 K collected around the resonance energy of ^{57}Fe at 14.5125 keV with a step size of 0.25 meV.

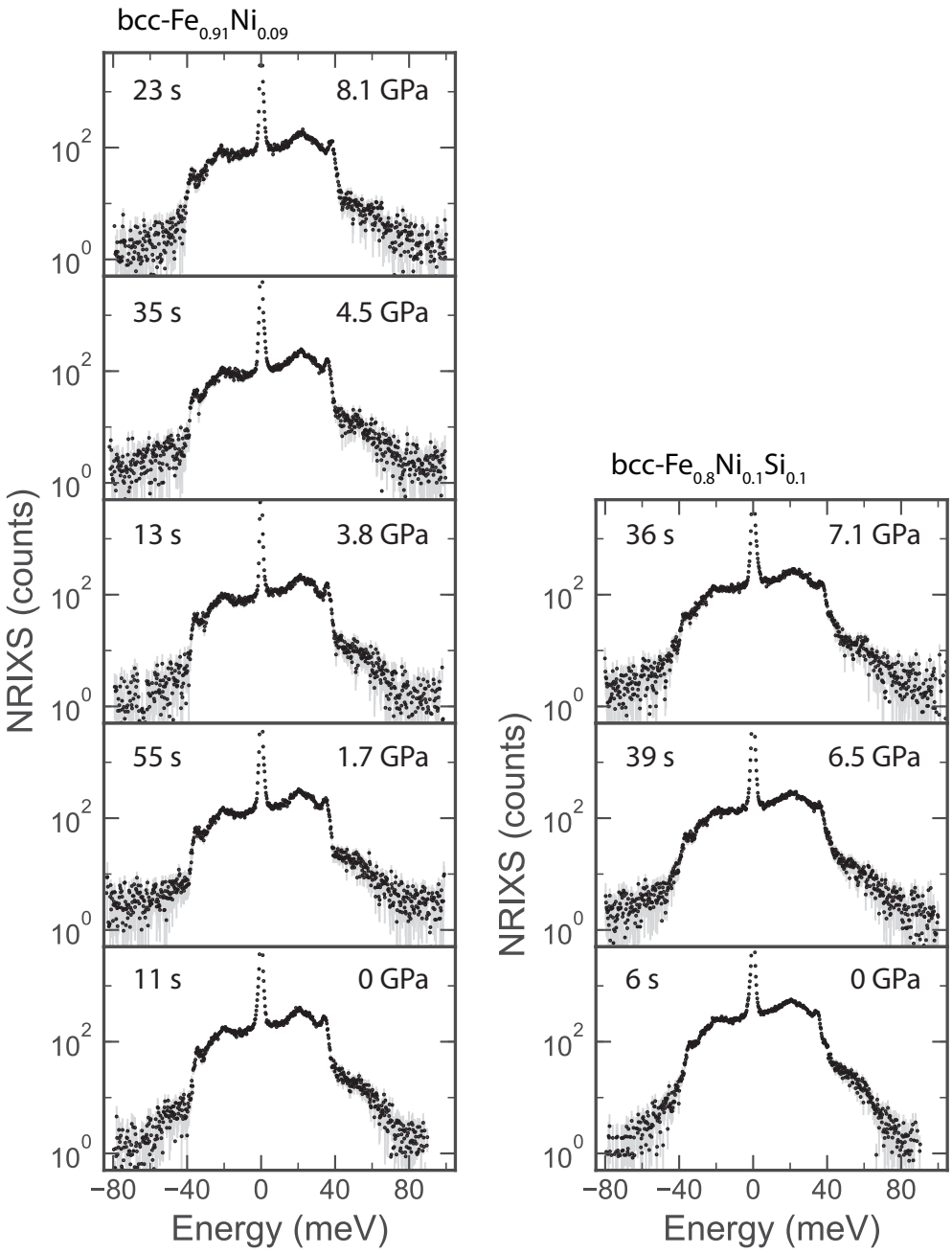

Figure 4.2: Raw (unnormalized) NRIXS spectra for bcc-$Fe_{0.91}Ni_{0.09}$ and $Fe_{0.8}Ni_{0.1}Si_{0.1}$ at 300 K collected around the resonance energy of ^{57}Fe at 14.5125 keV with a step size of 0.25 meV. We note that the NRIXS spectra of bcc-Fe is not displayed here and is plotted in Figure 4.3.

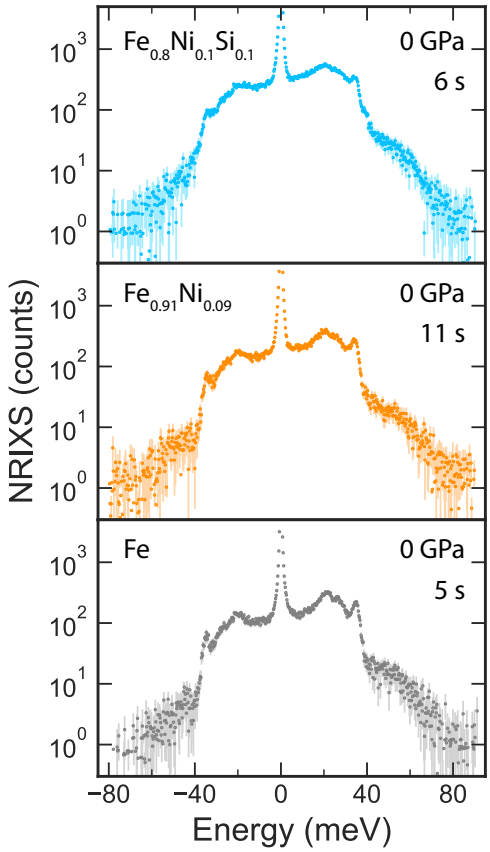

Figure 4.3: Comparison of raw (unnormalized) NRIXS spectra for bcc-$Fe_{0.91}Ni_{0.09}$, $Fe_{0.8}Ni_{0.1}Si_{0.1}$, and Fe at 0 GPa and 300 K collected around the resonance energy of ^{57}Fe at 14.5125 keV with a step size of 0.25 meV.

medium (helium) and the same pressure calibrant (tungsten with the *Dorogokupets and Oganov* (2006) pressure scale). The experimental conditions and resulting parameters from each EOS study are listed in Table 2.2 (Chapter 2). For each compression point, we also calculated the isothermal bulk modulus K_T and the pressure derivative of the isothermal bulk modulus K'_T using these same EOSs. The resulting pressure, K_T, and K'_T are listed in Table 4.2.

The NRIXS data were analyzed with the PHOENIX software package (www.NRIXS.com) to obtain the partial phonon density of states (DOS) $D(E, V_i)$ and various thermodynamic quantities including the Lamb-Mössbauer factor, kinetic energy, thermal expansion, and vibrational free energy. As detailed in *Sturhahn* (2000, 2004) and *Sturhahn and Jackson* (2007), the background and the measured elastic peak were subtracted from the measured NRIXS spectrum to obtain the pure phonon excitation spectrum, $I'(E)$. The excitation probability density

Table 4.2: Results from x-ray diffraction and 300 K equations of state

Phase	a (Å)	c (Å)	Volume (Å^3)	Density[a] (g/cm^3)	Pressure[b] (GPa)	K_T (GPa)	K'_T
bcc-Fe							
	2.863(1)		23.46(3)	8.062(9)	0	168(8)	4.7(1.3)
bcc-$Fe_{0.91}Ni_{0.09}$							
	2.874(1)		23.73(2)	7.99(1)	0	147(3)	6.4(6)
	2.859(1)		23.38(3)	8.11(1)	1.7(1)	158(2)	6.3(6)
	2.847(1)		23.08(3)	8.22(1)	3.8(1)	171(1)	6.1(6)
	2.843(1)		22.98(3)	8.25(1)	4.5(1)	175(1)	6.1(5)
	2.825(1)		22.54(2)	8.41(1)	8.1(1)	196(2)	5.9(5)
hcp-$Fe_{0.91}Ni_{0.09}$							
	2.454(1)	3.948(2)	20.59(2)	9.21(1)	18.0(1)	251(2)	4.88(7)
	2.438(1)	3.925(4)	20.21(3)	9.38(1)	22.8(2)	274(2)	4.77(7)
	2.399(2)	3.831(10)	19.09(6)	9.93(3)	41(1)	357(1)	4.46(6)
	2.389(1)	3.788(7)	18.72(4)	10.13(2)	48(1)	388(1)	4.37(6)
	2.359(1)	3.748(6)	18.07(4)	10.50(2)	63(1)	453(1)	4.22(6)
	2.341(1)	3.708(4)	17.60(2)	10.77(1)	75(1)	504(2)	4.12(5)
	2.330(1)	3.687(5)	17.33(3)	10.94(2)	83(1)	538(2)	4.06(5)
	2.299(1)	3.654(9)	16.72(4)	11.34(3)	104(3)	620(3)	3.94(5)
bcc-$Fe_{0.8}Ni_{0.1}Si_{0.1}$							
	2.859(1)		23.38(3)	7.70(1)	0	156(8)	5.7(1.2)
	2.821(1)		22.46(2)	8.02(1)	7.1(1)	194(2)	5.3(1.1)
	2.824(1)		22.53(3)	8.00(1)	6.5(1)	191(2)	5.3(1.1)
hcp-$Fe_{0.8}Ni_{0.1}Si_{0.1}$							
	2.432(1)	3.886(6)	19.9(3)	9.05(2)	27.9(3)	281(2)	5.12(6)
	2.408(1)	3.846(8)	19.31(5)	9.33(2)	37.1(6)	327(2)	4.94(6)
	2.379(2)	3.896(10)	19.09(6)	9.44(3)	41(1)	347(2)	4.88(6)
	2.366(1)	3.796(9)	18.40(5)	9.79(3)	55(1)	413(1)	4.70(6)
	2.346(1)	3.740(7)	17.83(4)	10.10(2)	69(1)	478(1)	4.56(6)
	2.331(2)	3.669(10)	17.26(6)	10.44(4)	86(3)	553(2)	4.43(5)

[a]Density calculations account for sample enrichment

[b]Pressure, isothermal bulk modulus (K_T), and pressure derivative of bulk modulus (K'_T) were calculated from volumes paired with Vinet EOSs listed in Table 2.2.

$S(E, V_i)$) was then obtained by applying a normalization procedure to $I'(E)$ based on the property that the first moment of $S(E, V_i)$) is equal to the recoil energy of the resonant isotope E_R. For ^{57}Fe, $E_R = 1.956$ meV. PHOENIX applies the Fourier-log method to decompose $S(E, V_i)$ into n-phonon contributions,

$$S_n(E, V_i) = \int E^n S(E, V_i) dE, \tag{4.1}$$

for $n = 0, 1, 2, 3$. The Lamb-Mössbauer factor and the kinetic energy can be directly determined from the 0th- and 2nd-order moments ($S_0(E, V_i)$ and $S_2(E, V_i)$), respectively (see sections 4.6 and 4.8).

To obtain the phonon DOS from $S_1(E, V_i)$, the quasi-harmonic approximation was applied, which assumes the interatomic potential is harmonic and accounts for thermal expansion. This approximation is thought to be reasonable for NRIXS measurements at 300 K (*Alfè et al.*, 2001). The resulting projected partial phonon DOS $D(E, V_i)$ was normalized by $\int D(E, V_i)dE = 3$. The phonon DOS is 'projected' due to the dependency on the direction of incident x-rays and 'partial' as NRIXS is only sensitive to the resonant isotope ^{57}Fe. For the bcc phase, $D(E, V_i)$ is isotropic (*Sturhahn and Kohn*, 1999). For our samples in the hcp phase, we note our sample is polycrystalline, so dependency on the angle of incident x-rays should be minimal. Additionally, anisotropy of the phonon DOS for hcp Fe was found to be minimal in the low energy region used for sound velocity determinations (*Giefers et al.*, 2002). Because our alloys are predominantly 95%-enriched ^{57}Fe, the partial phonon DOS is a very close approximation to the total phonon DOS, and for iron, it is the total phonon DOS. The resulting projected partial phonon DOSs for bcc and hcp phases are plotted in Figures 4.4 and 4.5, respectively.

To compare our results to those of hcp-iron in a consistent manner, we re-analyzed data from the hcp-iron NRIXS study of *Murphy et al.* (2011a,b, 2013) using the same methods as for $Fe_{0.91}Ni_{0.09}$ and $Fe_{0.8}Ni_{0.1}Si_{0.1}$. The resulting phonon DOSs for hcp-iron are plotted in Figure 4.5. We excluded the 36 GPa hcp-Fe NRIXS scan from our re-analysis, as we found the statistical quality of this scan to be inferior to the other scans in this study. The 36 GPa scan was collected over a much shorter integration time (18s, compared to an average of 53s), and the number of counts in the Stokes region of this NRIXS scan was much smaller (70 counts, compared to an average of ∼183 counts).

We compare the phonon DOS of the bcc and hcp phases of Fe, $Fe_{0.91}Ni_{0.09}$, and $Fe_{0.8}Ni_{0.1}Si_{0.1}$ in Figure 4.6. The phonon DOSs for the bcc phases are plotted as measured at 0 GPa. The total phonon DOS for hcp-Fe at 90 GPa, and the partial phonon DOS for hcp-$Fe_{0.91}Ni_{0.09}$ at 48 GPa and for hcp-$Fe_{0.8}Ni_{0.1}Si_{0.1}$ at 41 GPa are scaled to 0 GPa using the phonon DOS scaling method outlined in Section 4.4. Note the difference in relative phonon mode intensity between bcc and hcp-structured iron alloys. Also, note the differences between the

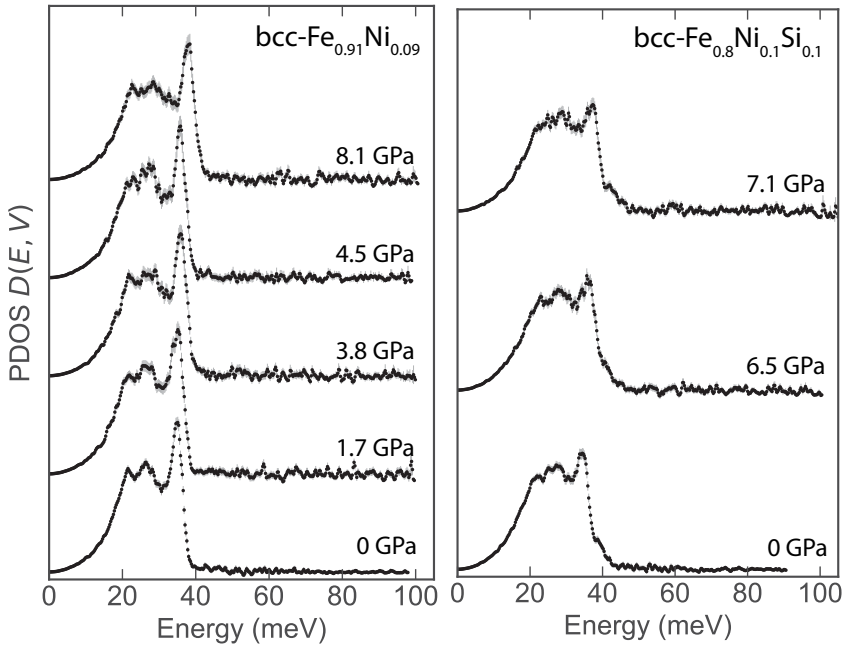

Figure 4.4: Partial phonon density of states (DOS) of bcc-$Fe_{0.91}Ni_{0.09}$ and $Fe_{0.8}Ni_{0.1}Si_{0.1}$ as determined by subtracting the elastic peak from measured NRIXS spectra and applying the quasi-harmonic model. Phonon DOSs are offset for visibility. Pressures were determined from volumes measured in situ.

phonon DOSs of different compositions. For instance, the phonon DOSs of bcc- and hcp-$Fe_{0.8}Ni_{0.1}Si_{0.1}$ extend to higher energies than the phonon DOSs of Fe and $Fe_{0.91}Ni_{0.09}$.

4.3 Sound velocities

Debye sound velocity

The Debye sound velocity (v_D) can be determined from the Debye-like low-energy region of the phonon DOS via

$$v(E) = \left[\frac{\widetilde{m}}{2\pi^2 \hbar^3 \rho} \frac{1}{D(E)} E^2 \right]^{1/3}, \tag{4.2}$$

where $\widetilde{m}$ is the mass of the resonant isotope, and $v(E) = v_D$ in the limit where E approaches zero (e.g., *Sturhahn*, 2004). As an example, we illustrate select phonon DOSs of hcp-Fe, $Fe_{0.91}Ni_{0.09}$, and $Fe_{0.8}Ni_{0.1}Si_{0.1}$ scaled according to equation 4.2 in Figure 4.7. Two different phonon dispersion models are applied to the scaled phonon DOSs. A 'Debye-like' model varies quadratically with energy and therefore plots as a constant value in Figure 4.7. The parabolic 'Debye-like' regions of Fe and $Fe_{0.91}Ni_{0.09}$ extend to a large enough energy

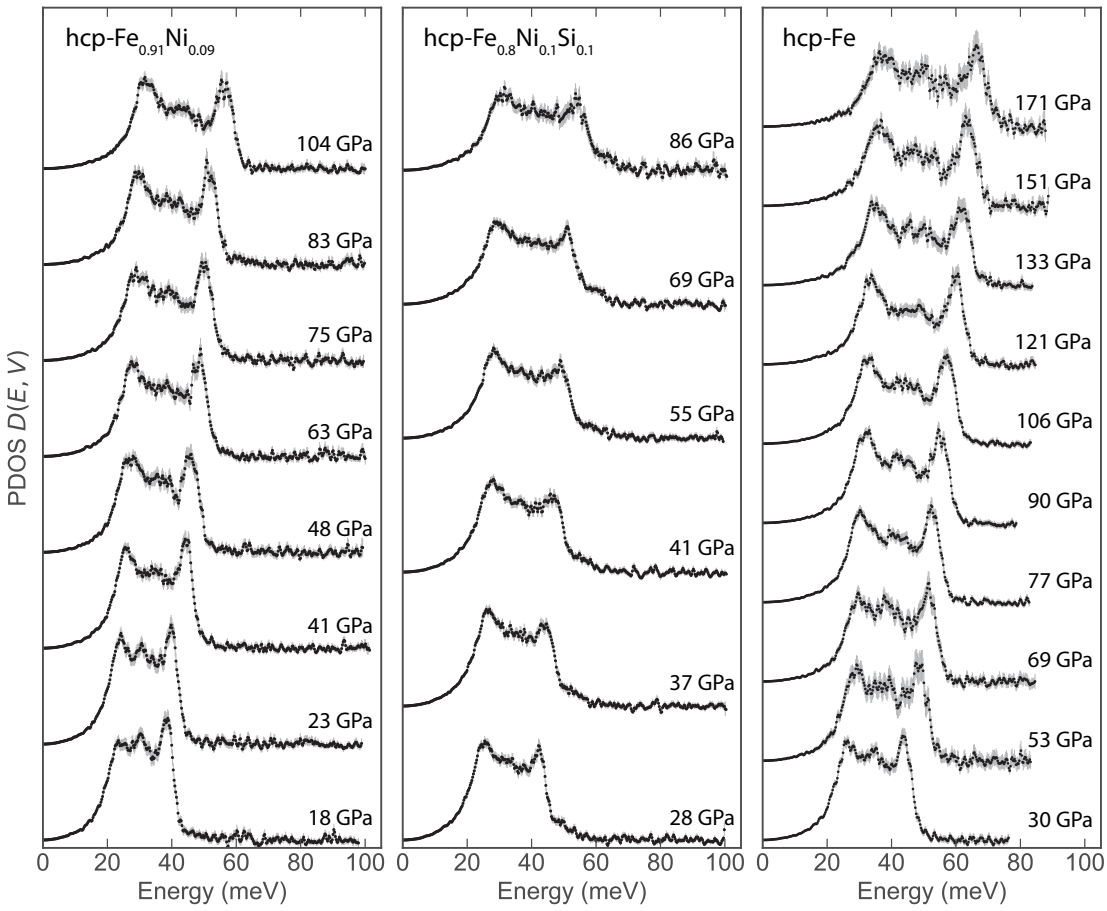

Figure 4.5: Partial phonon density of states (DOS) of hcp-$Fe_{0.91}Ni_{0.09}$ and $Fe_{0.8}Ni_{0.1}Si_{0.1}$ and total phonon DOS of hcp-Fe re-analyzed from *Murphy et al.* (2013). Phonon DOSs were determined by subtracting the elastic peak from measured NRIXS spectra and applying the quasi-harmonic model. Phonon DOSs are offset for visibility. Pressures were determined from unit-cell volumes measured in situ.

to obtain a suitable constraint on the Debye velocity. However, the parabolic region of $Fe_{0.8}Ni_{0.1}Si_{0.1}$ at 41 GPa is noticeably smaller than that of $Fe_{0.91}Ni_{0.09}$ at the same pressure. A greater amount of data can be included if instead an empirical power law model of the phonon dispersion curve is applied,

$$v(E) = v_D \left[1 - (x/A_1)^4\right]. \tag{4.3}$$

In both cases, the limit of $v(E)$ as E approaches zero provides v_D. For consistency, we apply the phonon dispersion curve in equation 4.3 to the phonon DOSs of both hcp-$Fe_{0.91}Ni_{0.09}$ and $Fe_{0.8}Ni_{0.1}Si_{0.1}$, as well as to our re-analysis of hcp-Fe data from *Murphy et al.* (2013).

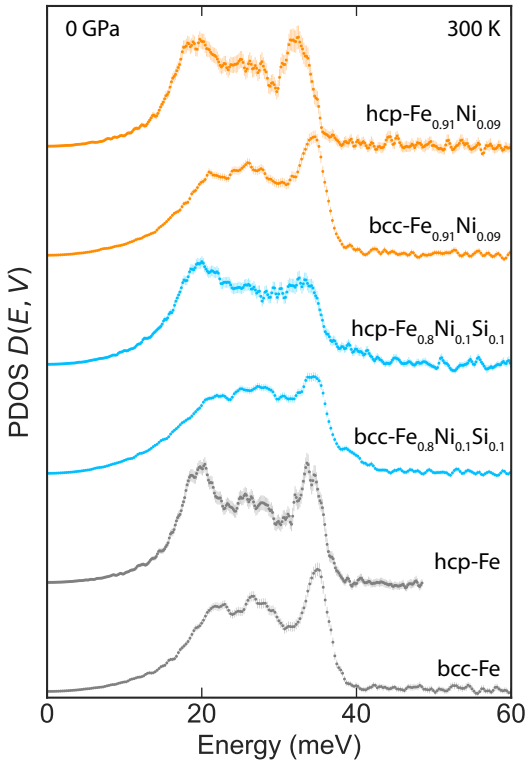

Figure 4.6: Phonon DOS of bcc-$Fe_{0.91}Ni_{0.09}$, $Fe_{0.8}Ni_{0.1}Si_{0.1}$, and Fe at 0 GPa are compared to phonon DOS of hcp-$Fe_{0.91}Ni_{0.09}$ (48 GPa), $Fe_{0.8}Ni_{0.1}Si_{0.1}$ (41 GPa), and Fe (90 GPa, re-analyzed from *Murphy et al.* (2013)) scaled to 0 GPa using our $\gamma_{0,vib}$ and q for each composition and the scaling procedure detailed in section 4.4.

An outstanding question in how to accurately determine the Debye velocity is how to optimally select the energy range of $v(E)$ over which to fit the phonon dispersion curve. An ideal method should be repeatable, consistent, and meaningful. Previous selection criteria have involved selecting an energy range that corresponds to a low reduced goodness of fit (χ^2) and a stable v_D (e.g., *Murphy et al.*, 2013). The metric χ^2 is meaningful in that it detects deviations in the model from the data (i.e., it is sensitive to under-fitting of the data). However, χ^2 is not sensitive to over-fitting of the data, as only a few data points may yield a very good (low) χ^2.

A better choice would be a metric that prefers both a good fit of the model to the data and an energy range with more data points (i.e., a criteria that disfavors both under-fitting and over-fitting of the data). Essentially, an energy range choice should yield the maximum information from the data.

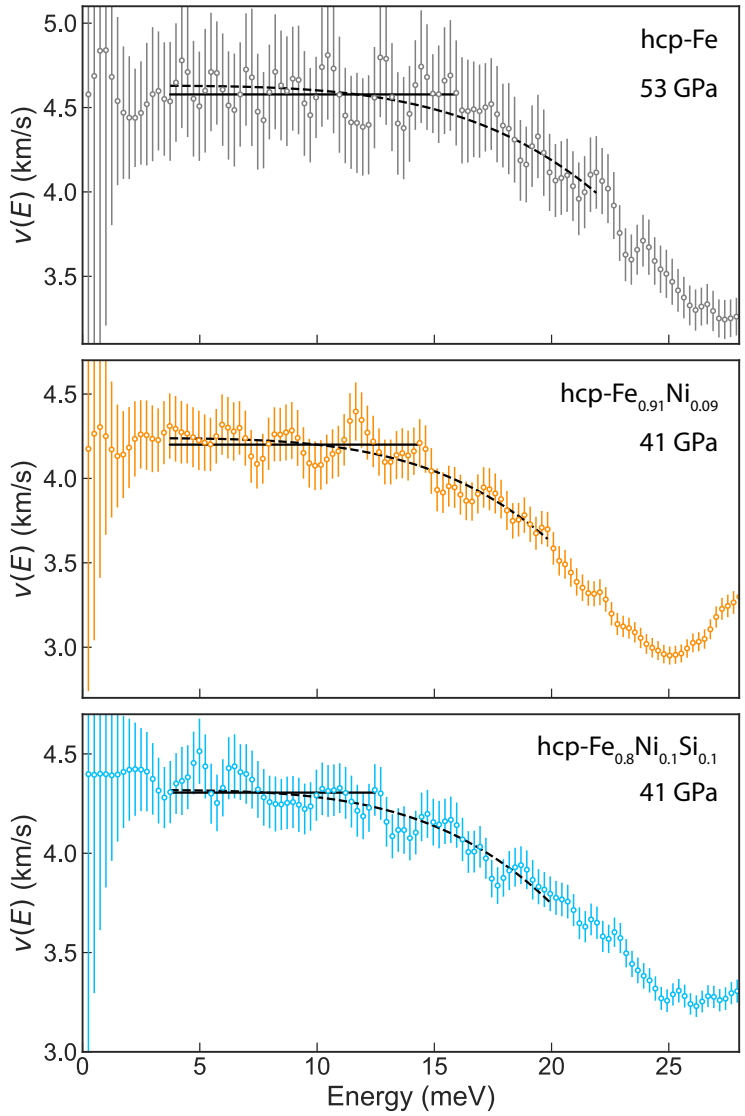

Figure 4.7: Phonon DOSs of hcp-Fe, $Fe_{0.91}Ni_{0.09}$, and $Fe_{0.8}Ni_{0.1}Si_{0.1}$ scaled according to equation 4.2 to allow for visual representation of the low energy constant Debye-velocity region used to constrain the Debye sound velocity. Examples of two models used to constrain the Debye sound velocity are plotted: the constant Debye-fit model (parabolic black solid line) and the power law model (equation 4.3, black dashed line). The hcp-Fe data is from our re-analysis of *Murphy et al.* (2013), and all other data is from this study. $Fe_{0.91}Ni_{0.09}$ and $Fe_{0.8}Ni_{0.1}Si_{0.1}$ data were conveniently collected at the same pressure of 41 GPa. The flat region at low energy appropriate for fitting a constant Debye-velocity model is much larger for hcp-$Fe_{0.91}Ni_{0.09}$ than for hcp-$Fe_{0.8}Ni_{0.1}Si_{0.1}$. We note that the fit models plotted here are purely demonstrative and do not directly reflect our reported Debye velocities. See text for a detailed description of our Debye velocity determination method.

There are a variety of methods of estimating information, some more computationally intensive than others. Two common information estimates that are easily computationally accessible are the Akaike Information Criteria (AIC) and the Bayesian Information Criteria (BIC). Both of these criteria assume a large number of data points. When selecting between energy fit ranges, the number of data points will vary, so it is important to not assume the number of data points is large. A common correction to the AIC (known as the AICc) corrects for the case where the number of data points is small (*Hurvich and Tsai*, 1989). The AICc has the form

$$AICc = \chi^2 + 2M + \frac{2M(M+1)}{N-M-1}, \tag{4.4}$$

where χ^2 is the goodness of fit of the model to the data, M is the number of model parameters, and N is the number of data points. In our case, $M = 1$ for a 'Debye-like' model where the model parameter is v_D, and $M = 2$ for a power law model (equation 4.3) where the model parameters are v_D and A_1, and N is the number of data points in the selected energy range. The third term of equation 4.4 is critical, as it provides a sensitivity to over-fitting of the data, which a traditional goodness of fit lacks.

As an example, we plot the effective probability $\exp(-AICc/2)$ of each fit as a function of the start and end of the fit range (E_{min} and E_{max}, respectively) for $Fe_{0.91}Ni_{0.09}$ at 41 GPa in the top panel of Figure 4.8. Low values of $\exp(-AICc/2)$, e.g., where the number of data points is too small or where E_{max} is too large, provide a poor constraint on the Debye velocity v_D, whereas high values of $\exp(-AICc/2)$ provide a better constraint on v_D. This plot demonstrates there are many choices of E_{min} and E_{max} that are equally favorable, e.g., choices that yield equally large values of $\exp(-AICc/2)$. We also plot the v_D as a function of E_{min} and E_{max} in the middle panel of Figure 4.8. Depending on the quality of the NRIXS spectra and the phonon dispersions for the sample, the value of v_D obtained from a given data set may vary widely for different fit ranges, even for fit ranges with similar AICc values. As a result, two different fit ranges may yield equal values of $\exp(-AICc/2)$ but noticeably different Debye velocities.

We propose binning the v_D for many fit ranges, weighted by $\exp(-AICc/2)$, to create a probability distribution function of v_D. By accounting for many possible fit ranges in the calculation of v_D, this method provides a more reasonable constraint on the uncertainty of v_D than would be obtained by using

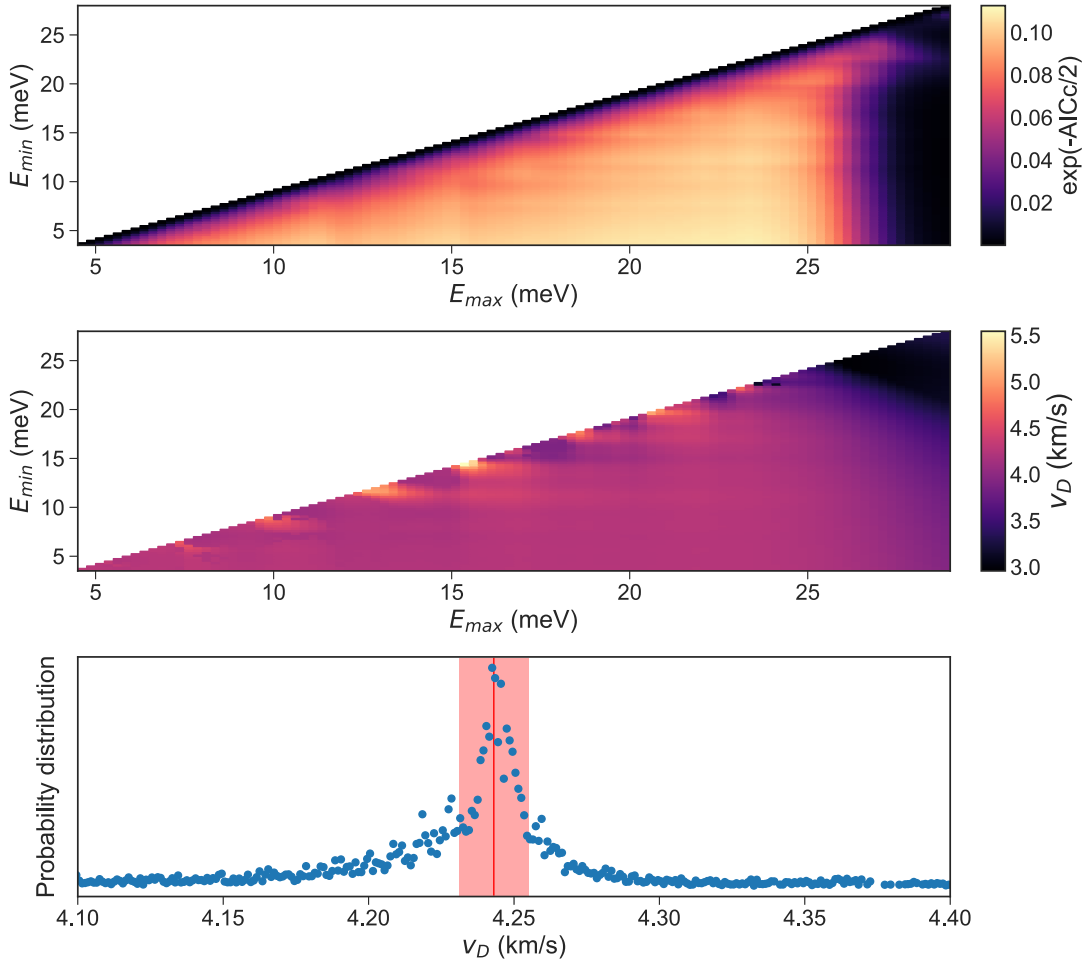

Figure 4.8: To illustrate our Debye velocity determination, the power law function (equation 4.3) is applied to the low energy region of the phonon DOS of hcp-$Fe_{0.91}Ni_{0.09}$ at 41 GPa. In the top panel, we plot the fit quality of the model as a function of starting energy range E_{min} and ending energy range E_{max}. Fit quality is assessed as $\exp(-AICc/2)$, where the corrected Akaike Information Criteria (AICc) is defined in equation 4.4. Larger values of $\exp(-AICc/2)$ represent higher quality fits. In the middle panel, we plot the resulting Debye velocity as a function of E_{min} and E_{max}. Notice the streaks in the top and middle panel. These variations in Debye velocity highlight the advantage of our Debye velocity analysis method over a fixed energy range, which may influence the resulting Debye velocity. In the bottom panel, we plot the probability distribution of the Debye velocity as calculated from the top two panels. The red line and shaded region represent the mean v_D and standard deviation, respectively. See section 4.3 for a detailed description of the analysis methods used.

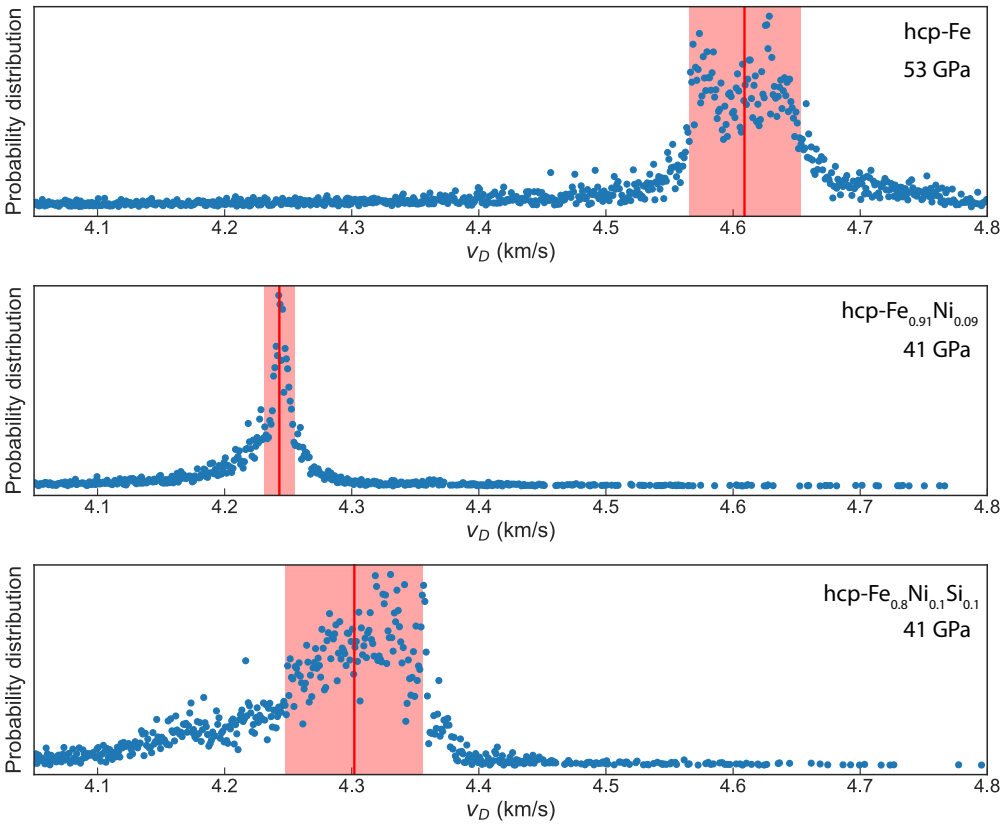

Figure 4.9: Debye velocity (v_D) probability distribution functions of hcp-Fe, $Fe_{0.91}Ni_{0.09}$, and $Fe_{0.8}Ni_{0.1}Si_{0.1}$ at 300 K. The hcp-Fe data is from our re-analysis of *Murphy et al.* (2013), and all other data is from this study. The red line and shaded region represent the mean v_D and standard deviation, respectively. The uncertainty of v_D can vary noticeably depending on the NRIXS spectra and the phonon dispersions.

a single energy range. For example, in Figure 4.8 we include all fit ranges that fall within E_{min}=3.5–27.0 meV and E_{max}=4.5–28.0 meV. The v_D of these fits are weighted by their corresponding $exp(-AICc/2)$ and binned to produce a probability distribution function of v_D (bottom panel of Figure 4.8). We note this method is more computationally intensive than previous analysis methods, as it requires fitting a model (e.g., equation 4.4) to the low energy region of the phonon DOS many times, once for each fit range explored, and then binning the results into a probability distribution function. However, the added benefits are repeatable, consistent Debye velocities with meaningful uncertainties.

We compare the obtained probability distribution functions for hcp-Fe, $Fe_{0.91}Ni_{0.09}$,

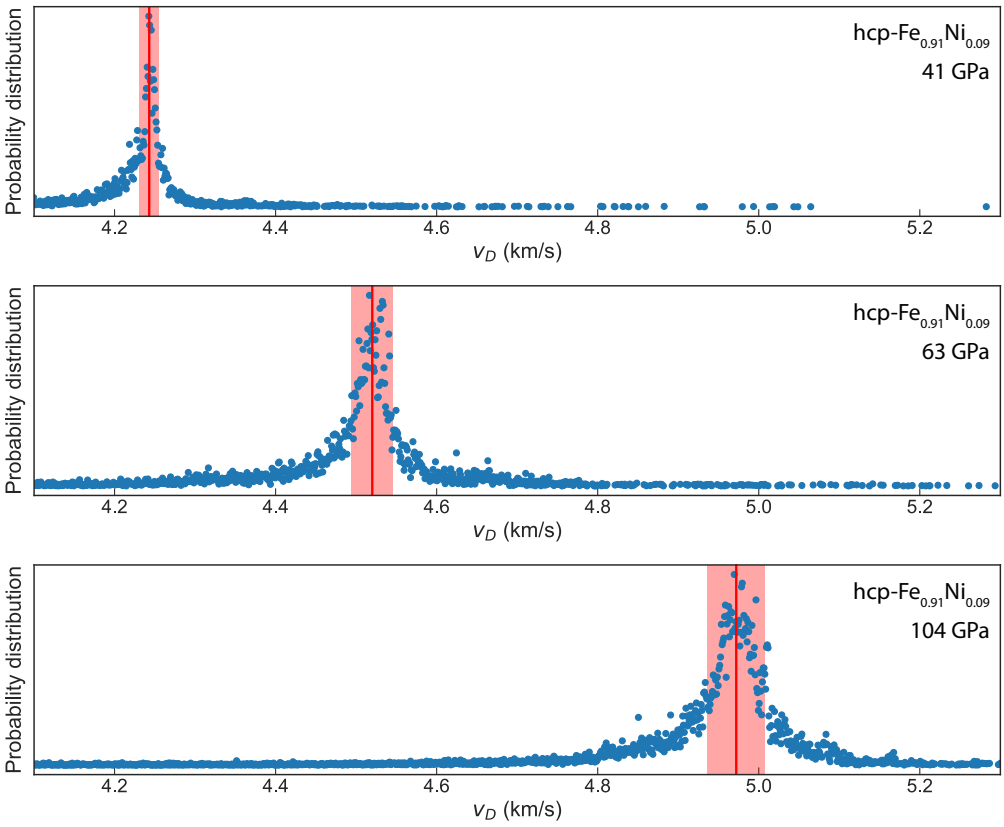

Figure 4.10: Debye velocity (v_D) probability distribution functions of hcp-$Fe_{0.91}Ni_{0.09}$ at 41, 63, and 104 GPa and 300 K. The red line and shaded region represent the mean v_D and standard deviation, respectively. The increase in v_D with pressure is clearly resolvable given the size of v_D uncertainty.

and $Fe_{0.8}Ni_{0.1}Si_{0.1}$ in Figure 4.9. $Fe_{0.91}Ni_{0.09}$ and $Fe_{0.8}Ni_{0.1}Si_{0.1}$ are most directly comparable, as they are conveniently measured at the same pressure of 41 GPa. These probability distribution functions illustrate that the uncertainty on v_D can vary noticeable depending on the quality of the NRIXS spectra and the phonon dispersions for the sample. In Figures 4.10 and 4.11, we plot the v_D probability distribution functions at three different pressures for hcp-$Fe_{0.91}Ni_{0.09}$ and $Fe_{0.8}Ni_{0.1}Si_{0.1}$, respectively. The increase in v_D with pressure is clearly resolvable given the size of the v_D uncertainty. The Debye velocities for bcc- and hcp-Fe, $Fe_{0.91}Ni_{0.09}$, and $Fe_{0.8}Ni_{0.1}Si_{0.1}$ computed via this method are listed in Table 4.3 and plotted as a function of density and pressure in Figure 4.12.

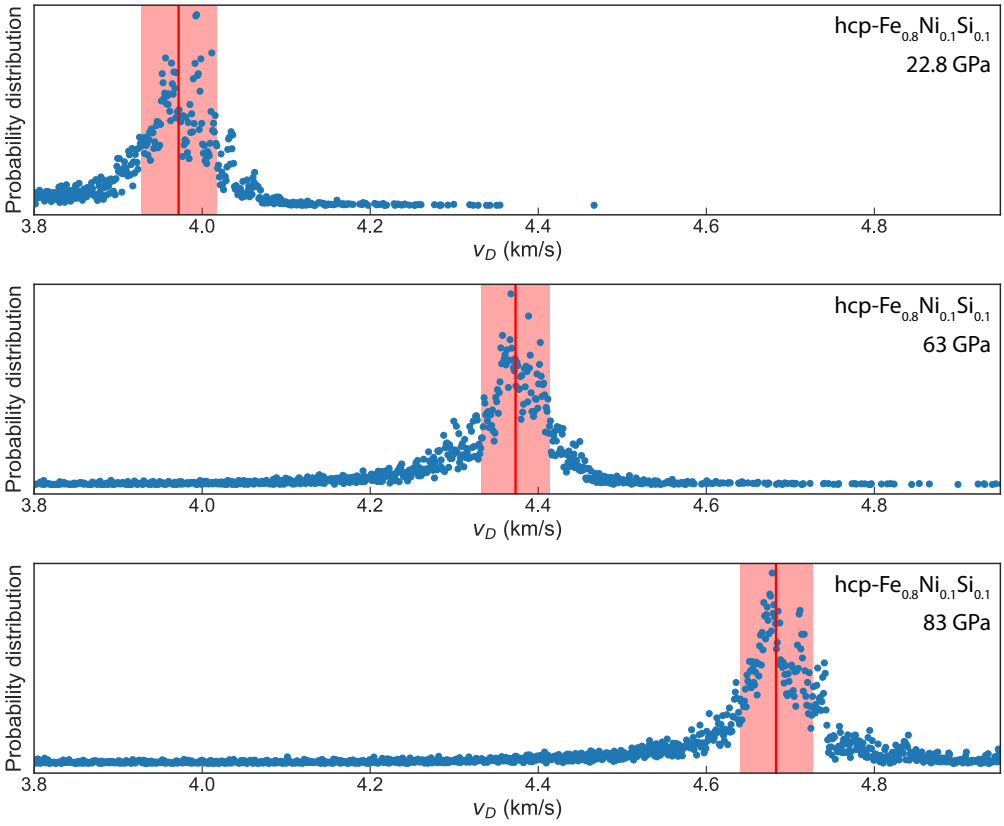

Figure 4.11: Debye velocity (v_D) probability distribution functions of hcp-$Fe_{0.8}Ni_{0.1}Si_{0.1}$ at 22.8, 63, and 83 GPa and 300 K. The red line and shaded region represent the mean v_D and standard deviation, respectively. The increase in v_D with pressure is clearly resolvable given the size of v_D uncertainty.

Table 4.3: Results from NRIXS sound velocity analysis

V (Å^3)	ρ^a (g/cm^3)	P (GPa)	${v_D}^a$ (km/s)	K_S (GPa)	${v_\phi}^a$ (km/s)	${v_P}^a$ (km/s)	${v_S}^a$ (km/s)	G (GPa)
bcc-Fe								
23.46(3)	8.06(1)	0	3.47(3)	168(8)	4.57(11)	5.81(9)	3.11(3)	78(1)
hcp-Fe[b]								
19.66(7)	9.61(3)	30(2)	4.42(6)	312(3)	5.70(3)	7.31(5)	3.96(6)	151(4)
18.47(3)	10.25(1)	53(2)	4.61(4)	411(2)	6.33(1)	7.92(3)	4.12(4)	174(3)
17.80(3)	10.63(1)	69(3)	4.83(5)	476(1)	6.69(1)	8.35(4)	4.32(5)	198(5)
17.50(7)	10.80(2)	77(3)	4.94(2)	506(1)	6.85(1)	8.53(2)	4.41(2)	210(2)
17.10(7)	11.06(2)	90(3)	5.13(3)	558(1)	7.10(1)	8.86(2)	4.59(3)	233(3)
16.61(7)	11.38(5)	106(3)	5.21(3)	621(2)	7.39(2)	9.13(3)	4.65(3)	246(3)
16.24(7)	11.64(2)	121(3)	5.36(4)	677(2)	7.63(2)	9.42(3)	4.78(4)	266(4)
15.97(7)	11.84(2)	133(4)	5.40(8)	721(3)	7.80(2)	9.58(5)	4.82(7)	275(8)
15.61(7)	12.13(3)	151(5)	5.56(3)	786(4)	8.05(2)	9.88(3)	4.96(3)	298(4)
15.21(7)	12.43(3)	171(5)	5.68(7)	859(5)	8.31(2)	10.17(4)	5.07(6)	320(8)
bcc-$Fe_{0.91}Ni_{0.09}$								
23.73(2)	7.99(1)	0	3.27(2)	147(3)	4.29(5)	5.46(4)	2.93(2)	69(1)
23.38(3)	8.11(1)	1.7(1)	3.28(2)	158(2)	4.41(3)	5.56(3)	2.93(2)	70(1)
23.08(3)	8.22(1)	3.8(1)	3.31(2)	171(1)	4.56(2)	5.69(2)	2.96(2)	72(1)
22.98(3)	8.25(1)	4.5(1)	3.39(2)	175(1)	4.60(1)	5.78(2)	3.03(2)	76(1)
22.54(2)	8.41(1)	8.1(1)	3.46(1)	196(2)	4.83(2)	6.01(2)	3.09(1)	80(1)
hcp-$Fe_{0.91}Ni_{0.09}$								
20.59(2)	9.21(1)	18.0(1)	3.84(5)	254(3)	5.26(3)	6.58(4)	3.43(5)	109(3)
20.21(3)	9.38(1)	22.8(2)	3.94(3)	278(2)	5.44(2)	6.79(3)	3.52(3)	116(2)
19.09(6)	9.93(3)	41(1)	4.24(1)	360(1)	6.02(1)	7.44(1)	3.79(1)	142(1)
18.72(4)	10.13(2)	48(1)	4.36(4)	391(1)	6.22(1)	7.67(2)	3.89(3)	153(3)
18.07(4)	10.50(2)	63(1)	4.52(3)	456(1)	6.59(1)	8.07(2)	4.03(2)	170(2)
17.60(2)	10.77(1)	75(1)	4.60(2)	507(2)	6.86(1)	8.33(1)	4.10(2)	181(2)
17.33(3)	10.94(2)	83(1)	4.67(4)	541(2)	7.03(1)	8.51(3)	4.16(3)	189(3)
16.72(4)	11.34(3)	104(3)	4.97(4)	623(3)	7.41(2)	9.01(3)	4.43(3)	223(3)
bcc-$Fe_{0.8}Ni_{0.1}Si_{0.1}$								
23.38(3)	7.70(1)	0	3.21(1)	156(8)	4.49(11)	5.58(9)	2.86(1)	63(1)
22.53(3)	8.00(1)	6.5(1)	3.26(3)	191(2)	4.92(3)	5.95(3)	2.90(3)	67(1)
22.46(2)	8.02(1)	7.1(1)	3.23(3)	194(2)	4.89(3)	5.91(3)	2.87(3)	66(1)
hcp-$Fe_{0.8}Ni_{0.1}Si_{0.1}$								
19.90(3)	9.05(2)	27.9(3)	3.97(5)	284(3)	5.61(3)	6.94(3)	3.54(4)	114(3)
19.31(5)	9.33(2)	37.1(6)	4.16(4)	330(2)	5.95(2)	7.32(3)	3.70(3)	127(2)
19.09(6)	9.44(3)	41(1)	4.30(5)	350(2)	6.09(2)	7.53(4)	3.84(5)	139(3)
18.40(5)	9.79(3)	55(1)	4.37(4)	416(1)	6.52(1)	7.92(3)	3.90(4)	148(3)
17.83(4)	10.10(2)	69(1)	4.55(6)	480(1)	6.90(1)	8.33(3)	4.05(5)	165(4)
17.26(6)	10.44(4)	86(3)	4.68(4)	555(2)	7.30(2)	8.74(3)	4.17(4)	181(3)

[a]The tabulated values for density, and Debye sound velocity, bulk sound speed, compressional velocity, and shear velocity all account for ^{57}Fe enrichment
[b]Re-analyzed from *Murphy et al.* (2013)

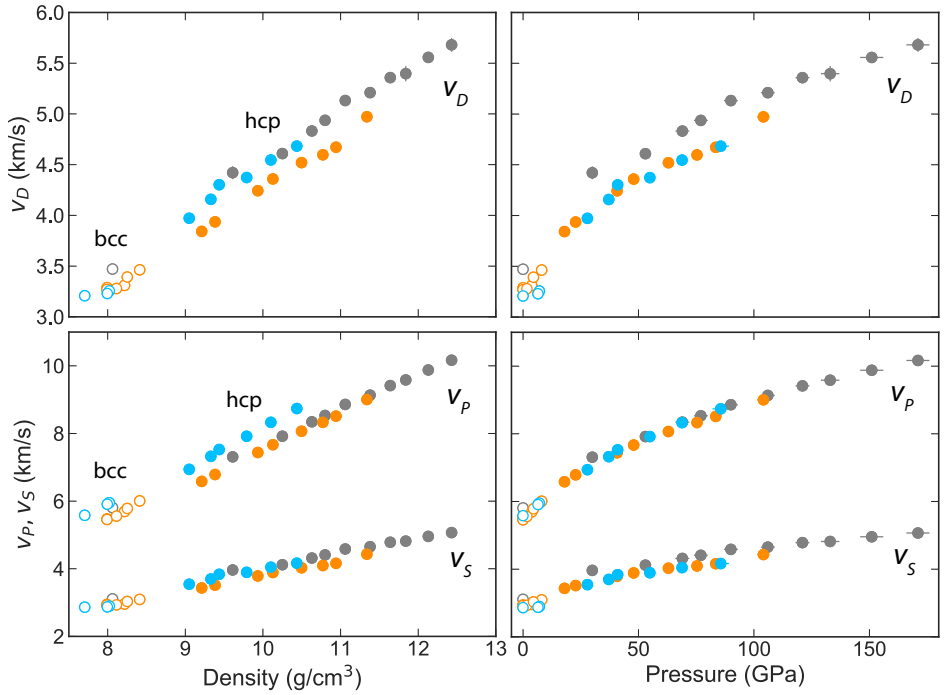

Figure 4.12: Debye velocity (v_D), compressional velocity (v_P), and shear velocity (v_S) for Fe (gray), $Fe_{0.91}Ni_{0.09}$ (orange), and $Fe_{0.8}Ni_{0.1}Si_{0.1}$ (blue) as a function of density and pressure. The bcc-phase (open circles) is distinguished from the hcp-phase (filled circles). The hcp-Fe data is from our re-analysis of *Murphy et al.* (2013), and all other data is from this study. Sound velocity and density values account for the ^{57}Fe enrichment of the samples.

Compressional and shear sound velocities

We combine our Debye velocities with existing equations of state to constrain the seismically observable compressional and shear sound velocities v_P and v_S via

$$\frac{3}{v_D^3} = \frac{1}{v_P^3} + \frac{2}{v_S^3} \tag{4.5}$$

and

$$\frac{K_S}{\rho} = v_P^2 - \frac{4}{3}v_S^2, \tag{4.6}$$

where K_S is the isentropic bulk modulus and ρ is the density of our ^{57}Fe enriched samples. K_S is related to the isothermal bulk modulus K_T via the following relation,

$$K_S = K_T(1 + \gamma\alpha T), \tag{4.7}$$

where γ is the Grüneisen parameter and α is the thermal expansion. For a given composition and volume, K_T is determined from existing 300 K equations

of state. For bcc-Fe data, we apply the Vinet EOS for bcc-Fe reported in Chapter 2 *Morrison et al.* (2018) based on compression data from *Dewaele et al.* (2006). For hcp-Fe, we apply the hcp-Fe EOS from *Dewaele et al.* (2006). For bcc- and hcp-$Fe_{0.91}Ni_{0.09}$ and $Fe_{0.8}Ni_{0.1}Si_{0.1}$, we apply the Vinet EOSs also reported in Chapter 2. Experimental details for each equation of state are summarized in Table 2.2. The EOS studies for $Fe_{0.91}Ni_{0.09}$ and $Fe_{0.8}Ni_{0.1}Si_{0.1}$ were conducted using samples from the same synthesis batches as the samples in this study. For samples in the bcc phase, we assume $K_S \approx K_T$. For samples in the hcp phase, we calculate K_S using our reported γ_{vib} and α_{vib} determined from the phonon DOS of each composition (see sections 4.4 and 4.7). The shear modulus G is then calculated via

$$G = v_S^2 \rho. \tag{4.8}$$

The determined K_S, v_P, v_S, and G are reported in Table 4.3, and v_P, v_S are plotted as a function of density and pressure in Figure 4.12. The density and sound velocities in Table 4.3 and Figure 4.12 account for the ^{57}Fe enrichment of the samples. From equation 4.5, one can see that the Debye velocity is more sensitive to shear velocity than to compressional velocity. Therefore, NRIXS measurements are better suited to constraining shear velocities, whereas the resulting compressional sound velocities are more strongly affected by the applied equation of state (*Sturhahn and Jackson*, 2007).

We find that for a given pressure, alloying iron with nickel has a minimal effect on compressional velocity, and further alloying $Fe_{0.91}Ni_{0.09}$ with silicon similarly has a minimal effect on compressional velocity. However, alloying hcp-iron with 9 at% nickel decreases the shear velocity by ∼6% for a given pressure. Further alloying with 10 at% silicon has a negligible effect on the shear velocity (Figure 4.12). These findings suggest than nickel decreases the shear velocity of iron but not the compressional velocity of iron, while silicon has little to no effect on the compressional and shear velocities of iron-nickel alloys for a given pressure. Because $Fe_{0.8}Ni_{0.1}Si_{0.1}$ is less dense than iron or $Fe_{0.91}Ni_{0.09}$, when plotted as a function of density, $Fe_{0.8}Ni_{0.1}Si_{0.1}$ has a greater v_P than that of hcp-Fe or $Fe_{0.91}Ni_{0.09}$ and a comparable v_S to that of hcp-Fe (Figure 4.12). Our findings are in agreement with ab initio studies by *Martorell et al.* (2013a) which predict a ∼5% shear velocity decrease at 360 GPa and 0 K when ∼10 at% nickel is added to iron. However, *Martorell et al.* (2013a)

Table 4.4: Natural and enriched molecular masses M of samples

Composition	M_{enr} [a] (g/mol)	M_{nat} [b] (g/mol)
Fe	56.942	55.845
$Fe_{0.91}Ni_{0.09}$	57.100	56.101
$Fe_{0.8}Ni_{0.1}Si_{0.1}$	54.231	53.354

[a] Fe 95% enriched in ^{57}Fe
[b] Fe with natural isotopic enrichment

suggest the effect of nickel on the shear velocity of iron is highly temperature dependent, and they predict the effect of nickel on v_S becomes minimal at 5500 K.

Comparison with previous studies

To compare with seismic observations or studies using samples of natural isotopic enrichment, our reported density and sound velocities can be corrected to values corresponding to natural isotopic enrichment with the following relation,

$$\rho_{nat} = \rho_{enr} \left(M_{nat}/M_{enr} \right) \tag{4.9}$$

and the following approximation,

$$v_{nat} = v_{enr} \sqrt{M_{enr}/M_{nat}}, \tag{4.10}$$

where M is the molecular mass of the alloy. The subscripts *nat* and *enr* denote samples with natural isotopic enrichment and samples enriched in ^{57}Fe, respectively. Values of M_{enr} and M_{nat} are listed in Table 4.4.

We plot the 300 K Debye, compressional, and shear sound velocities of our bcc-Fe data and our re-analyzed hcp-Fe data from *Murphy et al.* (2013) in Figure 4.13. We plot these as a function of pressure to compare with other NRIXS, IXS, and ultrasonic inferometry bcc- and hcp-Fe studies, some of which do not report volumes determined in situ. We compare to NRIXS studies by *Mao et al.* (2001), *Lin et al.* (2005), *Gleason et al.* (2013), and *Liu et al.* (2016); IXS studies by *Mao et al.* (2012), *Ohtani et al.* (2013), *Liu et al.* (2014), and *Antonangeli et al.* (2018); a combined NRIXS and IXS study by *Mao et al.* (2008); and a picosecond ultrasonic study by *Decremps et al.* (2014).

Unlike NRIXS studies, IXS and ultrasonic sound velocity studies do not require ^{57}Fe sample enrichment. Therefore, the plotted v_D, v_P and v_S values for bcc-

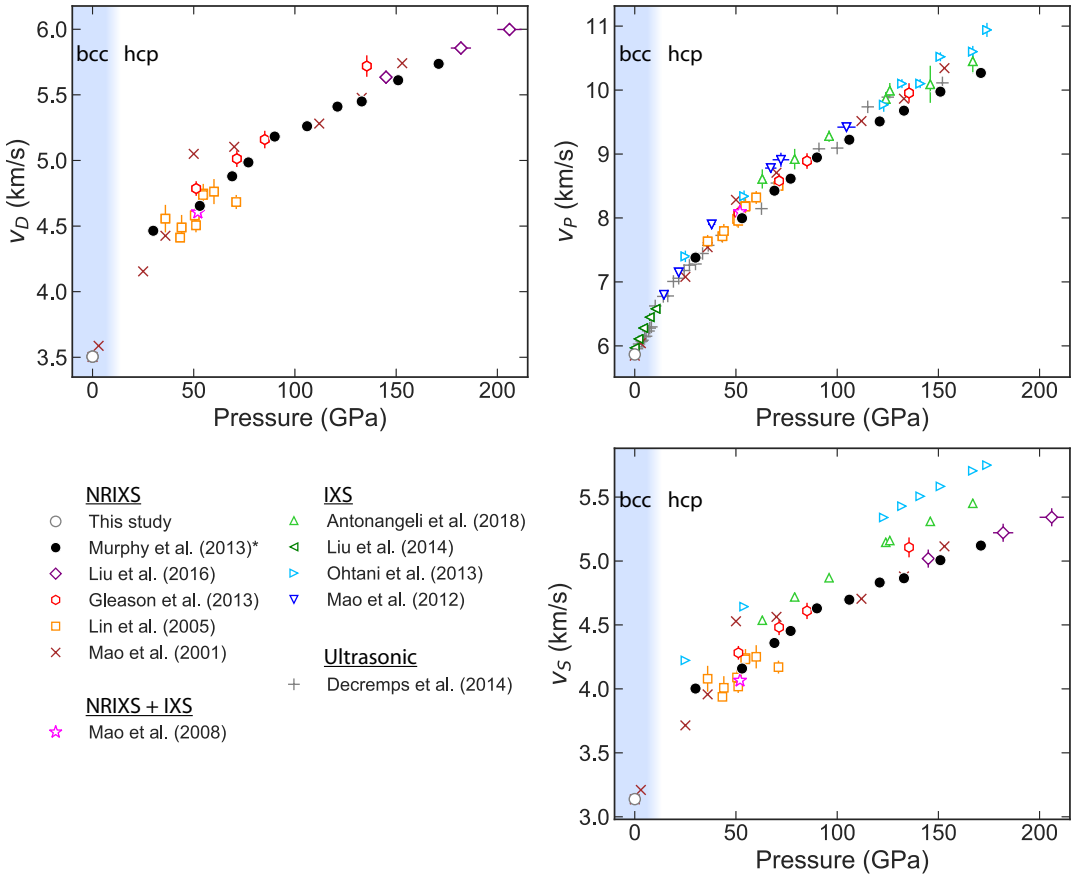

Figure 4.13: A comparison of Debye (v_D), compressional (v_P), and shear (v_S) sound velocities for bcc- and hcp-Fe from NRIXS, IXS, and ultrasonic experimental studies at 300 K. Data from *Murphy et al.* (2013) has been re-analyzed. For NRIXS studies conducted with ^{57}Fe enriched samples, we plot sound velocities that have been corrected to those of natural enrichment via equation 4.10, except for velocities from (*Liu et al.*, 2016), where their reported natural enrichment correction was applied.

Fe from this study and our re-analysis of hcp-Fe from *Murphy et al.* (2013) have been corrected to natural enrichment via equation 4.10. We have also corrected the reported v_D, v_P, and v_S from *Lin et al.* (2005), *Liu et al.* (2016), *Mao et al.* (2001), and *Gleason et al.* (2013) to natural isotopic enrichment using equation 4.10. As *Mao et al.* (2008) report v_P from samples with natural isotopic enrichment and v_D from samples enriched in ^{57}Fe, we correct their reported v_D to natural isotopic enrichment and re-calculate v_S for natural isotopic enrichment.

The v_D for hcp-Fe re-analyzed from *Murphy et al.* (2013) agrees well with *Mao*

et al. (2008) and *Liu et al.* (2016), and it agrees with *Mao et al.* (2001) and *Lin et al.* (2005) within the scatter of those studies. Our v_D hcp-Fe trends 2–4% below that of *Gleason et al.* (2013). *Liu et al.* (2016) suggests v_D of *Gleason et al.* (2013) may be larger due to a fit range starting at 1.7 meV, which is partially within the measured resolution function width (*Gleason et al.*, 2013). The compressional sound velocities from IXS studies still trend above those from NRIXS studies, even after correcting for enrichment effects. This may be due to differences between NRIXS and IXS in energy and polarization of phonons used to constrain sound velocities. However, we note NRIXS measurements have little sensitivity to v_P. We point the reader to *Sturhahn and Jackson* (2007) for a description of the relative sensitivities of NRIXS to v_ϕ, v_P, and v_S. Similar to the comparison of v_D for hcp-Fe, our reported v_P for hcp-Fe agrees well with *Mao et al.* (2001), *Lin et al.* (2005), *Mao et al.* (2008) and *Liu et al.* (2016) and trends slightly below that of *Gleason et al.* (2013). This is expected based on the v_D results, as v_D is strongly sensitive to v_S (*Sturhahn and Jackson*, 2007). The IXS studies by *Antonangeli et al.* (2018) and *Ohtani et al.* (2013) report curves for v_S at 300 K based on their measured v_P combined with existing equations of state (*Dewaele et al.*, 2006; *Sakai et al.*, 2014). The v_S of *Antonangeli et al.* (2018) and *Ohtani et al.* (2013) trend respectively ∼5% and ∼11% above our reported v_S for hcp-Fe, due to IXS experiments' insensitivity to v_S and their use of a different EOS.

Debye, compressional, and shear sound velocities of bcc- and hcp-$Fe_{0.91}Ni_{0.09}$ at 300 K are plotted in Figure 4.14 and compared to results from *Lin et al.* (2003) for $Fe_{0.92}Ni_{0.08}$. Velocities from both studies have been corrected to natural enrichment via equation 4.10. The Debye velocities from both studies are in close agreement, as are the compressional and shear velocities. Improved statistics due smaller energy step sizes (0.25 meV compared to 2.2 meV) along with our improved Debye velocity analysis method have allowed us to improve the constraint on hcp-$Fe_{0.91}Ni_{0.09}$ shear velocities.

In Figure 4.15, we compare our Debye, compressional, and shear sound velocities of bcc- and hcp-$Fe_{0.8}Ni_{0.1}Si_{0.1}$ at 300 K with existing sound velocity studies on Fe-Si and Fe-Ni-Si alloys. Previous studies include an NRIXS study on bcc- and hcp-$Fe_{0.85}Si_{0.15}$ (*Lin et al.*, 2003); a combined NRIXS and IXS study on hcp-$Fe_{0.868}Ni_{0.086}Si_{0.046}$ (*Liu et al.*, 2016); and IXS studies on hcp-$Fe_{0.89}Ni_{0.04}Si_{0.07}$ (*Antonangeli et al.*, 2010), hcp-$Fe_{0.91}Si_{0.09}$ (*Antonangeli et al.*,

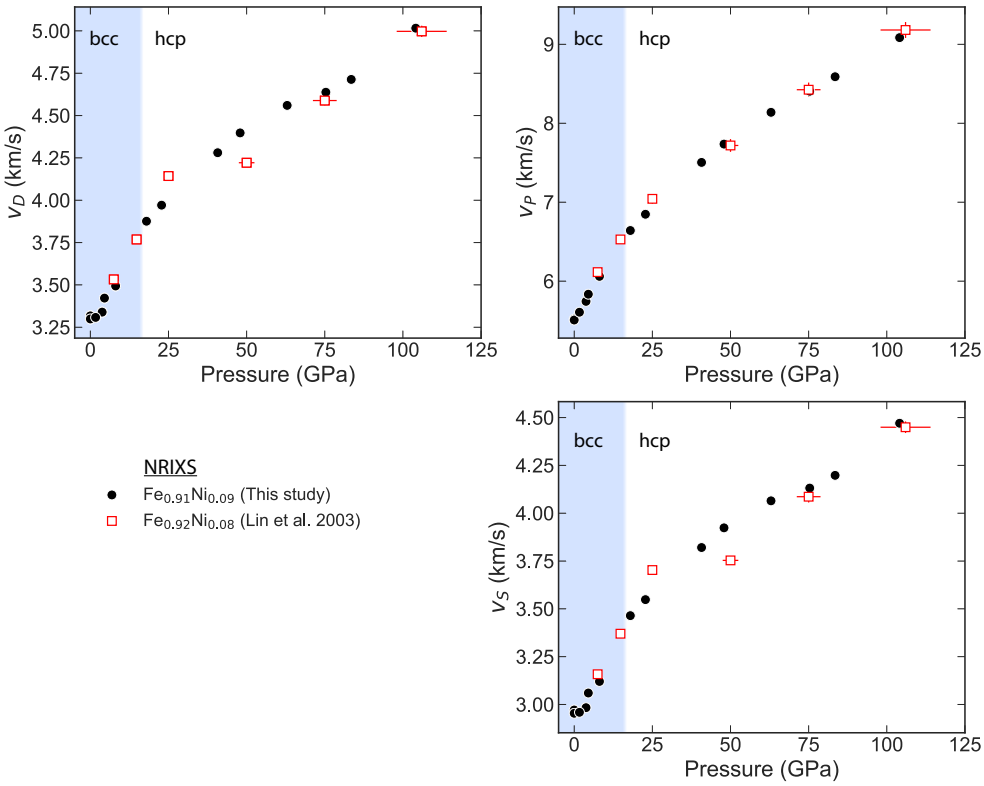

Figure 4.14: A comparison of Debye (v_D), compressional (v_P), and shear (v_S) sound velocities for bcc- and hcp-Fe-Ni alloys from NRIXS experimental studies at 300 K. Both studies were conducted with ^{57}Fe enriched samples, and we plot sound velocities that have been corrected to those of natural enrichment via equation 4.10.

2018), hcp-$Fe_{0.89}Si_{0.11}$ (*Sakairi et al.*, 2018), bcc- and hcp-$Fe_{0.85}Si_{0.15}$ (*Liu et al.*, 2014), and hcp-$Fe_{0.85}Si_{0.15}$ (*Mao et al.*, 2012). Sound velocities from this study and those from *Lin et al.* (2003) and *Liu et al.* (2014) have been corrected to natural enrichment via equation 4.10. The v_S from IXS studies by *Antonangeli et al.* (2010, 2018) are from their reported v_S curves, which are based on their measured v_P paired with equations of state.

Our reported v_D and v_S of hcp-$Fe_{0.8}Ni_{0.1}Si_{0.1}$ are similar to those of hcp-$Fe_{0.85}Si_{0.15}$ (*Lin et al.*, 2003). Based on our findings that nickel decreases the shear velocity of iron and that silicon has a minimal effect on the shear velocity of $Fe_{0.91}Ni_{0.09}$ for a given pressure (Figure 4.12), we would expect hcp-$Fe_{0.85}Si_{0.15}$ to instead have a higher shear velocity than hcp-$Fe_{0.8}Ni_{0.1}Si_{0.1}$. Our determined v_D and v_S of hcp-$Fe_{0.8}Ni_{0.1}Si_{0.1}$ deviate from those of hcp-$Fe_{0.868}Ni_{0.086}Si_{0.046}$ (*Liu et al.*, 2016), especially at higher pressures where hcp-

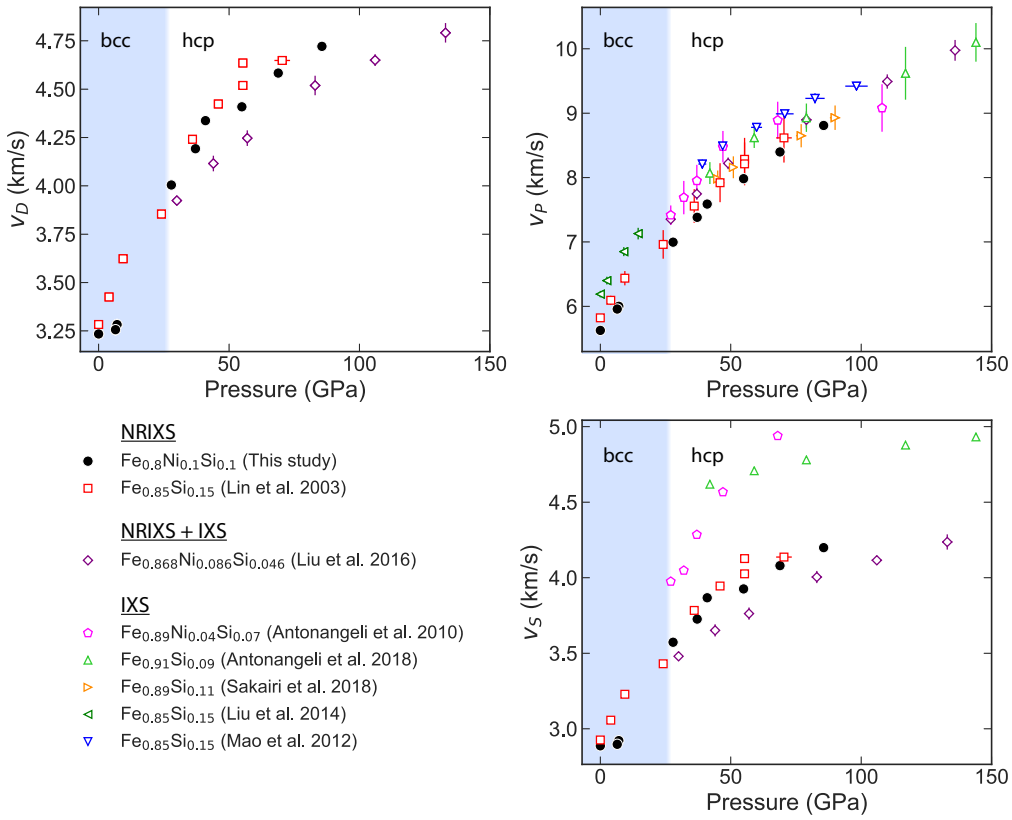

Figure 4.15: A comparison of Debye (v_D), compressional (v_P), and shear (v_S) sound velocities for Fe-Si and Fe-Ni-Si alloys from NRIXS and IXS studies at 300 K. For NRIXS studies conducted with ^{57}Fe enriched samples, we plot sound velocities that have been corrected to those of natural enrichment via equation 4.10, except for velocities from (*Liu et al.*, 2016), where their reported natural enrichment correction was applied.

$Fe_{0.868}Ni_{0.086}Si_{0.046}$ is noticeably lower than hcp-$Fe_{0.8}Ni_{0.1}Si_{0.1}$. Based on our finding that silicon has a minimal effect on the shear velocity of $Fe_{0.91}Ni_{0.09}$ for a given pressure, we would expect these studies to more closely agree. Both *Lin et al.* (2003) and *Liu et al.* (2016) apply a parabolic 'Debye-like' phonon dispersion model to the low energy region of their phonon DOSs. *Lin et al.* (2003) use a fixed energy range of 3.5–14 meV for the entire pressure range. *Liu et al.* (2016) used E_{min}=3.5 meV and varied E_{max} according to the goodness of fit χ^2 (E_{max}=13 meV for 30 GPa and E_{max}=16.5 meV for 133 GPa). Because alloying iron with silicon appears to decrease the parabolic 'Debye-like' region of the phonon DOS (see Figure 4.7), a 'Debye-like' fit to Fe-Si and Fe-Ni-Si alloys, if extended to too large of an energy range, would produce artificially lower Debye velocities, resulting in systematically lower shear velocities. This

could explain why the Debye and shear velocities of hcp-$Fe_{0.85}Si_{0.15}$ (*Lin et al.*, 2003) and hcp-$Fe_{0.868}Ni_{0.086}Si_{0.046}$ (*Liu et al.*, 2016) are lower than would be expected given our sound velocities findings. We note that v_P and v_S from this study are constrained by combining NRIXS determined v_D with equations of state from Chapter 2 *Morrison et al.* (2018), which were conducted with samples from the same $Fe_{0.8}Ni_{0.1}Si_{0.1}$ synthesis batch as in this study. The v_P and v_S from (*Lin et al.*, 2003) are constrained by combining v_D with existing equations of state on the same composition (*Lin*, 2003). *Liu et al.* (2016) instead combines NRIXS constrained v_D with IXS constrained v_P to determine v_S, and pressure is determined with an equation of state for the same sample from the same study. This difference in method may also introduce differences in reported v_P and v_S values. The v_S from IXS studies by *Antonangeli et al.* (2010, 2018) deviate noticeably from NRIXS determined v_S, due to the insensitivity of IXS measurement to v_S.

Light elements

We compare our reported v_D, v_P, v_S for bcc- and hcp-Fe, $Fe_{0.91}Ni_{0.09}$ and $Fe_{0.8}Ni_{0.1}Si_{0.1}$ at 300 K to the sound velocities of other candidate core compositions in Figure 4.16. We include NRIXS studies on Fe_3S (*Lin et al.*, 2004), Fe_3C (*Gao et al.*, 2008), Fe_7C_3 (*Chen et al.*, 2014), FeO, $(Mg_{0.06}Fe_{0.94})O$, $(Mg_{0.16}Fe_{0.84})O$ (*Wicks et al.*, 2017), FeH_x (*Mao et al.*, 2004), and FeH_x (*Thompson et al.*, 2018). We also include IXS studies on Fe_3C (*Fiquet et al.*, 2009) and FeH_x (*Shibazaki et al.*, 2012).

When plotted as a function of pressure, the v_P of $Fe_{0.91}Ni_{0.09}$ and $Fe_{0.8}Ni_{0.1}Si_{0.1}$ at 300 K show negligible differences with our re-analysis of hcp-Fe (*Murphy et al.*, 2013). The v_P of Fe_3S (*Lin et al.*, 2004) trends ∼4% below hcp-Fe, while the v_P of iron-hydrides (*Mao et al.*, 2004; *Shibazaki et al.*, 2012; *Thompson et al.*, 2018) and Fe_3C (*Fiquet et al.*, 2009; *Gao et al.*, 2008) trend above hcp-Fe. The compressional velocities of Fe_7C_3 from an NRIXS study (*Chen et al.*, 2014) shows a noticeably different dv_P/dP slope than Fe_3C. As a result, the v_P of Fe_3C falls above that of Fe above ∼25 GPa, while the v_P of Fe_7C_3 falls below iron above ∼70 GPa. The v_P of (Mg,Fe)O (*Wicks et al.*, 2017) deviates from that of hcp-Fe above ∼50 GPa, as the dv_P/dP slope of (Mg,Fe)O is noticeably different from that of hcp-Fe. At 100 GP, the v_P of FeO is ∼11% below that of hcp-Fe.

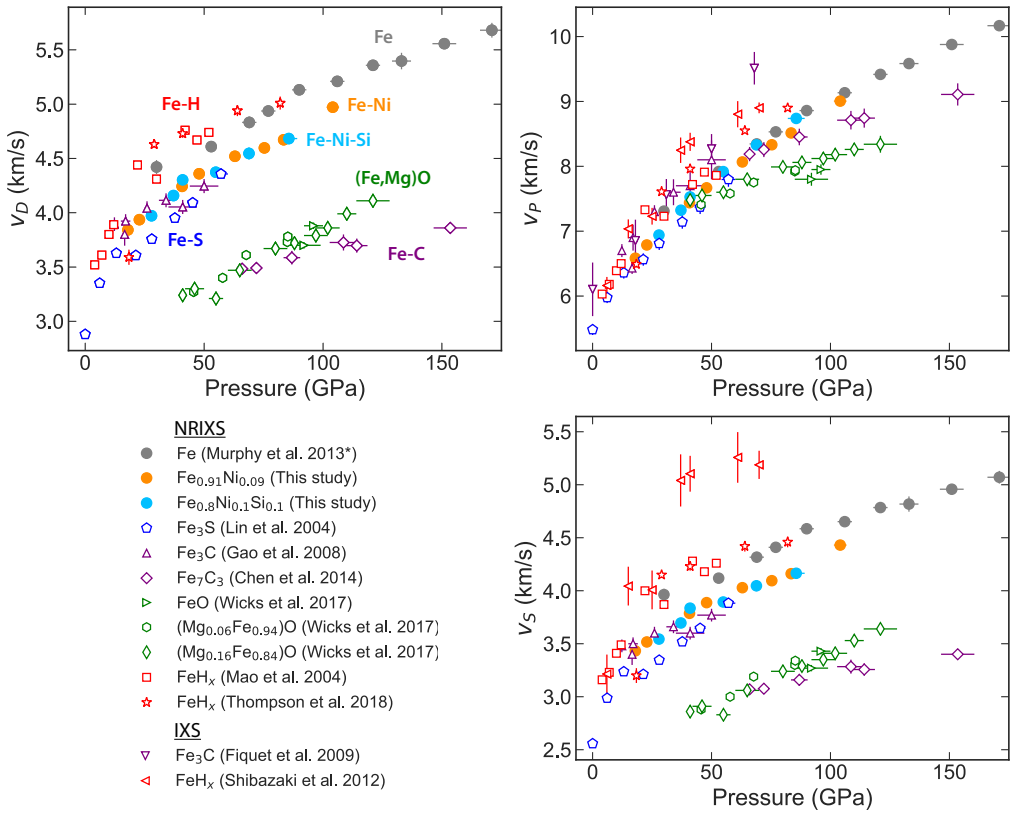

Figure 4.16: Debye (v_D), compressional (v_P), and shear (v_S) sound velocities at 300 K of hcp-$Fe_{0.91}Ni_{0.09}$ and $Fe_{0.8}Ni_{0.1}Si_{0.1}$ and our re-analysis of hcp-Fe data from *Murphy et al.* (2013). We compare to other iron-light-element compositions. The sound velocities are plotted as reported without a correction to natural enrichment.

As v_D is predominately influenced by v_S rather than by v_P, the plots of v_D and v_S at 300 K in Figure 4.16 show the same trends. Therefore we focus our following discussion on v_S. The constraints on v_S as a function of pressure suggest that silicon has a negligible effect on the v_S of hcp-Fe and that iron-hydrides (*Mao et al.*, 2004; *Shibazaki et al.*, 2012; *Thompson et al.*, 2018) have a higher v_S than hcp-Fe. The elements nickel, silicon, oxygen, and carbon all appear to decrease v_S when alloyed with hcp-Fe, so these elements may therefore help explain the low v_S of the inner core. The v_S of $Fe_{0.91}Ni_{0.09}$ trends ~6.5% below that of hcp-Fe at 100 GPa. Fe_3S (*Lin et al.*, 2004) falls ~10% below hcp-Fe at 60 GPa, although the dv_S/dP of Fe_3S is slightly steeper than hcp-Fe, so this difference may decrease at higher pressures. At 100 GPa, the v_S of iron-rich (Mg,Fe)O (*Wicks et al.*, 2017) is ~26% lower than that of hcp-Fe. The v_S of Fe_7C_3 (*Chen et al.*, 2014) is noticeably slower than that of

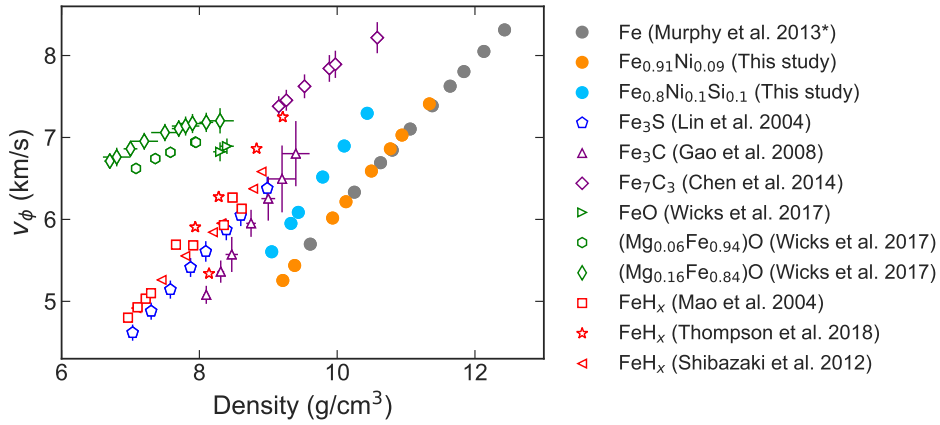

Figure 4.17: Birch plot showing the bulk sound speed v_ϕ at 300 K plotted as a function of density for hcp-$Fe_{0.91}Ni_{0.09}$ and $Fe_{0.8}Ni_{0.1}Si_{0.1}$ and our re-analysis of hcp-Fe data from *Murphy et al.* (2013). We compare to other iron-light element compositions. The sound velocities are plotted as reported without a correction to natural enrichment.

Fe_3C (*Gao et al.*, 2008). From 30–50 GPa, the v_S of Fe_3C is ~7–10% slower than that of hcp-Fe, while the v_S of Fe_7C_3 is ~31% slower than that of hcp-Fe. The dv_S/dP slope of Fe_7C_3 is slightly lower than that of hcp-Fe, so the difference between Fe_7C_3 and hcp-Fe may increase with pressure.

We plot bulk sound speed v_ϕ for hcp-Fe, $Fe_{0.91}Ni_{0.09}$ and $Fe_{0.8}Ni_{0.1}Si_{0.1}$ at 300 K in Figure 4.17. We note that the trends of hcp-Fe, $Fe_{0.91}Ni_{0.09}$ and $Fe_{0.8}Ni_{0.1}Si_{0.1}$ are all remarkably linear, suggesting the validity of Birch's law for these compositions, at least in the pressure range investigated. We compare to v_ϕ from other NRIXS iron-light element studies, including Fe_3S (*Lin et al.*, 2004), Fe_3C (*Gao et al.*, 2008), Fe_7C_3 (*Chen et al.*, 2014), FeO, $(Mg_{0.06}Fe_{0.94})O$, $(Mg_{0.16}Fe_{0.84})O$ (*Wicks et al.*, 2017), FeH_x (*Mao et al.*, 2004), and FeH_x (*Thompson et al.*, 2018). We note that only (Mg,Fe)O noticeably deviates from Birch's law, which can be explained by a spin pairing transition that occurs around a density of 8.3 g/cm^3 at 300 K for iron-rich (Mg,Fe)O (*Wicks et al.*, 2010).

Discussion

We observe in Figures 4.13, 4.15, and 4.16 that many shear sound velocities reported in IXS studies deviate substantially both from other IXS v_S studies of similar compositions (e.g., *Antonangeli et al.*, 2018; *Ohtani et al.*, 2013) and from NRIXS constraints on v_S (e.g., *Antonangeli et al.*, 2010, 2018; *Ohtani et al.*, 2013; *Shibazaki et al.*, 2012). These IXS studies constrain v_S by com-

bining their constrained v_P with existing equations of state. While NRIXS experiments similarly constrain v_S by combining their constrained v_D with existing equations of state, the v_D is strongly influenced by v_S and therefore can provide a stronger constraint on v_S.

The extrapolation of v_P and v_S of candidate iron alloys to inner core conditions requires a fairly accurate constraint on the pressure and temperature derivatives of these quantities. Due to necessary long integration times and technique requirements for IXS and NRIXS studies, the number of data points and compression range in v_P and v_S data sets is typically much less than in, for instance, equation of state studies. This hinders the ability to extrapolate v_P and v_S to pressures relevant to the inner core. Furthermore, the thermal effects dv_P/dT and dv_S/dT are poorly constrained, even for hcp-Fe. For example, the largest reported magnitude of dv_S/dT for hcp-Fe is -3.7×10^{-4} km s^{-1} K^{-1} and comes from a comparison of static elasticity and shock-compression studies (*Mao et al.*, 1998). A more recent constraint based on hcp-Fe ab initio constraints from *Martorell et al.* (2013a) gives $dv_S/dT = -3.2 \times 10^{-4}$ km s^{-1} K^{-1}.

Chen et al. (2014) suggest an inner core composed entirely of Fe_7C_3 would explain the ρ, v_P, and v_S of the inner core without invoking large sound velocity temperature effects. However, cosmochemical and iron-silicate melt partitioning studies have suggested the carbon content of the whole core is <0.7–1 wt% (*Wood et al.*, 2013; *Zhang and Yin*, 2012). An ab initio study suggested the density of Fe_7C_3 was too low to be a substantial component of the inner core (*Li et al.*, 2016), and, in our analysis of equations of state and seismic observations (Chapter 2 *Morrison et al.*, 2018), we find a carbon content of less than 1 wt%. FeO and iron-rich (Mg,Fe)O also have a low v_S compared to that of hcp-Fe, suggesting a large oxygen content could explain the low v_S of the inner core. However, solid-liquid iron partitioning studies have suggested oxygen is largely incompatible in the inner core (*Alfè et al.*, 2002, 2007). Additionally, we previously found the bulk sound speed of FeO limited the oxygen content of the inner core to 2 wt% (Chapter 2 *Morrison et al.*, 2018). We conclude that constraining the effect of large compression and very high temperatures (∼4000–5000 K) on the sound velocities, combined with tighter seismic constraints, will be essential to take the next steps in constraining inner core composition.

4.4 Grüneisen parameter

Vibrational Grüneisen parameter

The vibrational component of the Grüneisen parameter γ_{vib} for a given phonon mode can be defined as the volume dependence of energy of that phonon mode,

$$\gamma_{vib} = -\frac{\partial \ln \omega}{\partial \ln V} = -\frac{\partial \ln E}{\partial \ln V}, \tag{4.11}$$

where ω is the frequency corresponding to the given phonon mode, and E is the corresponding energy. As we have measured the phonon DOS for each composition as a function of volume, we can constrain the vibrational Grüneisen parameter using a phonon DOS scaling relation after *Murphy et al.* (2011a). We plot our phonon DOSs for each hcp phase in Figure 4.18. Upon visual inspection, the phonon DOSs for a given composition appear to be related by a single scaling parameter. For a given hcp-phase, we scale a single phonon DOS $D(E, V_i)$ to all other phonon DOSs $D(E, V)$ using the relation

$$D(E, V) = \xi(V, V_i) D\left[\xi(V, V_i) E, V_i\right], \tag{4.12}$$

where V_i is the volume of the reference phonon DOS, V is the volume to which the reference phonon DOS is scaled, $\xi(V, V_i)$ is an energy independent scaling parameter, and $\xi(V, V_i) = 1$ when $V = V_i$. For hcp-$Fe_{0.91}Ni_{0.09}$, we compare the measured phonon DOSs to the scaled phonon DOS measured at $V_i = 18.72 \pm 0.04$ Å^3 ($P = 48 \pm 1$ GPa) in the left panel of Figure 4.18. Similarly, for hcp-$Fe_{0.8}Ni_{0.1}Si_{0.1}$, we compare the measured phonon DOSs to the scaled phonon DOS measured at $V_i = 19.09 \pm 0.06$ Å^3 ($P = 41 \pm 1$ GPa) in the middle panel of Figure 4.18. For our re-analysis of hcp-Fe, we follow *Murphy et al.* (2011a) and compare the measured phonon DOSs to the scaled phonon DOS measured at $V_i = 17.10 \pm 0.07$ Å^3 ($P = 90 \pm 3$ GPa) in the right panel of Figure 4.18.

For a given hcp-phase, we apply equation 4.12 to scale a reference phonon DOS $D(E, V_i)$ to all other phonon DOSs $D(E, V)$ using a linear least squares regression, thereby obtaining a scaling parameter corresponding to each pair of phonon DOSs. We repeat this process with the other phonon DOS acting as the reference to obtain a total of $7 \times 8 = 56$ scaling parameters for hcp-$Fe_{0.91}Ni_{0.09}$, $5 \times 6 = 30$ scaling parameters for hcp-$Fe_{0.8}Ni_{0.1}Si_{0.1}$, and $9 \times 10 = 90$ scaling parameters for hcp-Fe. These scaling parameters are plotted as a function of V/V_i in Figure 4.19. The near-linear trend of the scaling parameter

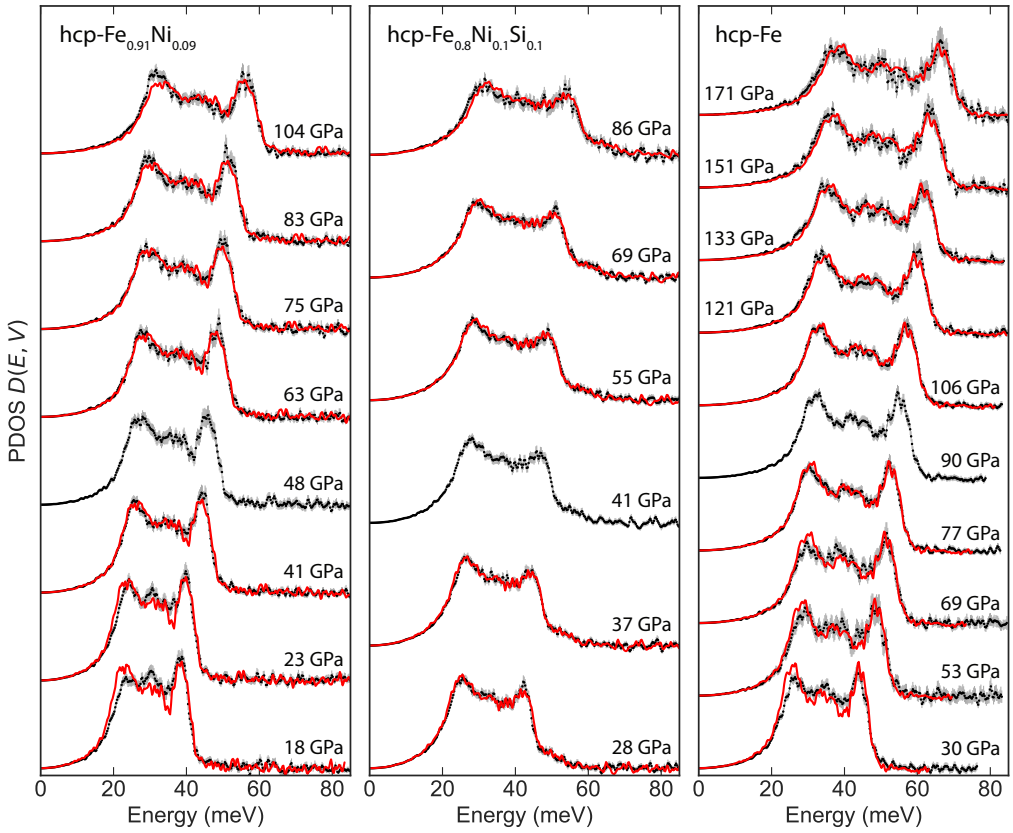

Figure 4.18: Examples of scaled phonon DOSs (red) compared to measured phonon DOS (black with gray error bars) for hcp-structured $Fe_{0.91}Ni_{0.09}$, $Fe_{0.8}Ni_{0.1}Si_{0.1}$, and our re-analysis of Fe data from *Murphy et al.* (2011a). The hcp-$Fe_{0.91}Ni_{0.09}$ at 48 GPa phonon DOS and the hcp-$Fe_{0.8}Ni_{0.1}Si_{0.1}$ at 41 GPa phonon DOS are scaled to each compression point according to equation 4.12. Similarly, our re-analyzed phonon DOS of hcp-Fe from *Murphy et al.* (2013) at 90 GPa is scaled to each compression point following the same method.

ξ with respect to V/V_i demonstrates the applicability of the scaling law in equation 4.12.

We combine a rephrasing of equation 4.11,

$$\gamma_{vib} = -\frac{\partial \ln \xi(V, V_i)}{\partial \ln V_i}, \tag{4.13}$$

with the commonly applied empirical relation,

$$\gamma_{vib} = \gamma_{vib,i} \left(\frac{V}{V_i}\right)^q, \tag{4.14}$$

where q is a fitting parameter, and the subscript i refers to a reference phonon

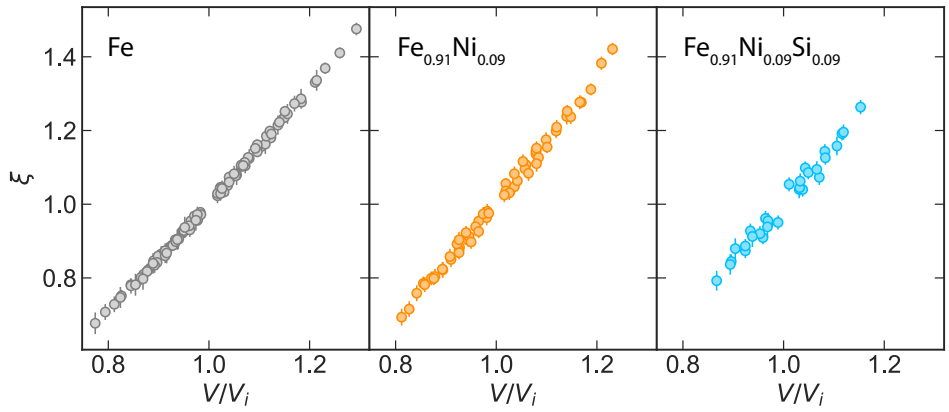

Figure 4.19: Phonon DOS scaling parameters for hcp-$Fe_{0.91}Ni_{0.09}$, $Fe_{0.8}Ni_{0.1}Si_{0.1}$, and Fe as determined from equation 4.12 and the procedure detailed in section 4.4. Data for hcp-Fe is re-analyzed from *Murphy et al.* (2011a).

DOS. Combining equations 4.13 and 4.14 and integrating yields

$$\xi(V, V_i) = \exp\left\{\frac{\gamma_{vib,i}}{q}\left[\left(\frac{V}{V_i}\right)^q - 1\right]\right\}, \tag{4.15}$$

where $q \neq 0$. Substituting an analogous relation to equation 4.14,

$$\gamma_{vib,i} = \gamma_{vib,0}\left(\frac{V_i}{V_0}\right)^q, \tag{4.16}$$

into equation 4.15 yields

$$\xi(V, V_i) = \exp\left\{\frac{\gamma_{vib,0}}{q}\left(\frac{V_i}{V_0}\right)^q\left[\left(\frac{V}{V_i}\right)^q - 1\right]\right\}, \tag{4.17}$$

where ξ is the scaling parameter as a function of volume V and reference volume V_i. V_0 is the volume at 0 GPa, as determined with an external equation of state. The vibrational Grüneisen parameter at 0 GPa, $\gamma_{vib,0}$, and q are fitting parameters. We applied equation 4.17 to the scaling parameters in Figure 4.19 using a linear least squares regression to determine $\gamma_{vib,0}$ and q. Then equation 4.16 was applied to determine the vibrational Grüneisen parameter as a function of volume V_i.

We applied a grid search to the regression of equation 4.17, and we found the scaling parameter values shown in Figure 4.19 do not constrain q. Therefore, we fix q at the commonly assumed value of 1, and obtain values of $\gamma_{vib,0} = 2.04\pm0.01$ for hcp-Fe, $\gamma_{vib,0} = 2.07\pm0.02$ for hcp-$Fe_{0.91}Ni_{0.09}$, and $\gamma_{vib,0} = 2.03\pm$

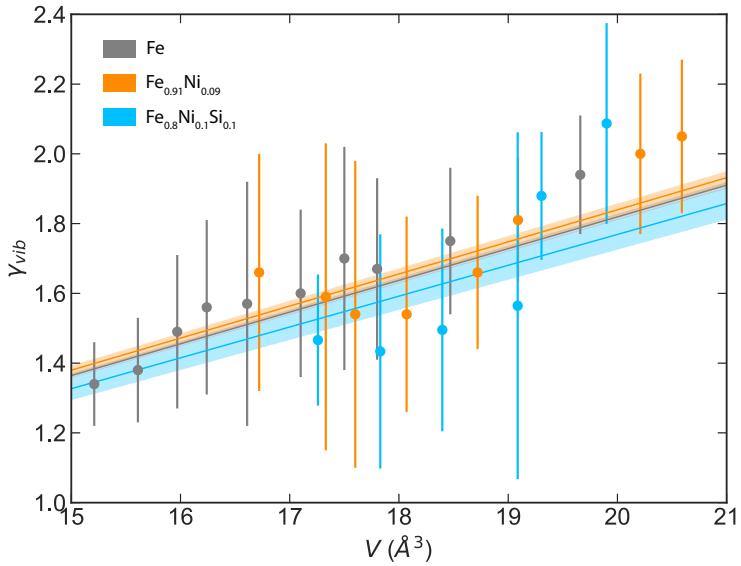

Figure 4.20: The vibrational Grüneisen parameter γ_{vib} for hcp-$Fe_{0.91}Ni_{0.09}$, $Fe_{0.8}Ni_{0.1}Si_{0.1}$, and Fe calculated using two methods. The hcp-Fe data is based on our re-analysis of data from *Murphy et al.* (2011a). The first method applies equation 4.17 (curves with shaded regions representing uncertainty). The second method applies equation 4.20 (filled circles) and is a rough approximation with larger uncertainties. It serves as a validity check on the assumptions of method 1, as it does not rely on the empirical relation of equation 4.14.

0.05 for hcp-$Fe_{0.8}Ni_{0.1}Si_{0.1}$. The resulting vibrational Grüneisen parameters are plotted as lines with shaded uncertainties in Figure 4.20.

To test the robustness and validity of the above method, we approximate the vibrational Grüneisen parameter without the application of the empirical equations 4.14 and 4.16. The scaling parameter ξ can be expressed as a relation between phonon branch energies at different volumes V and V_i, where V_i is the reference volume,

$$\xi = E_i/E. \tag{4.18}$$

Equation 4.11 can then be coarsely approximated as

$$\gamma_{vib,i} \approx -\frac{V_i}{E_i}\left(\frac{E - E_i}{V - V_i}\right). \tag{4.19}$$

Substituting equation 4.18 into equation 4.19, we find

$$\gamma_{vib,i} \approx -\frac{V_i}{E_i}\left(\frac{(E_i/\xi) - E_i}{V - V_i}\right) \approx \frac{(1 - 1/\xi)V_i}{V - V_i}. \tag{4.20}$$

We select a single hcp phonon DOS collected at volume V_i to serve as a reference, and we pair it with each other phonon DOS of the same composition

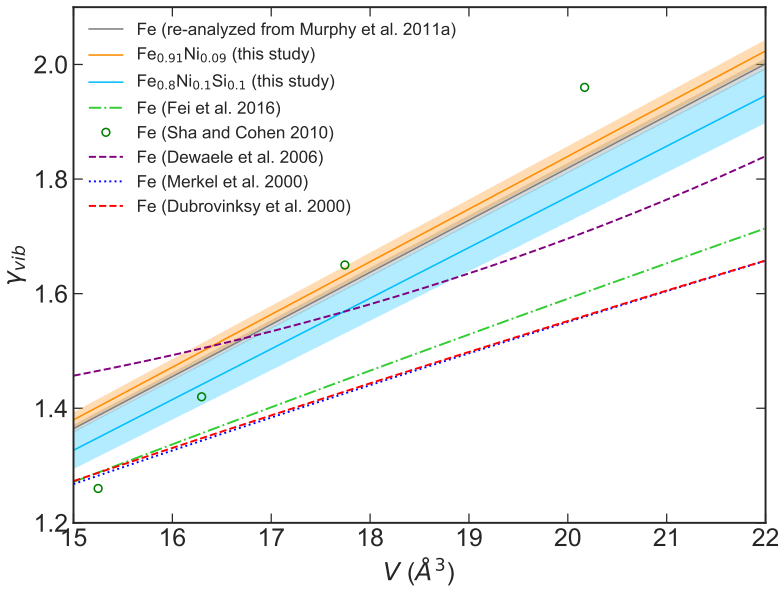

Figure 4.21: Vibrational Grüneisen parameter γ_{vib} for hcp-$Fe_{0.91}Ni_{0.09}$, $Fe_{0.8}Ni_{0.1}Si_{0.1}$, and Fe calculated with equation 4.17 compared γ_{vib} for hcp-Fe determined from results of NRIXS measurements by *Murphy et al.* (2011a) re-analyzed by *Fei et al.* (2016), ab initio calculations at 500 K (*Sha and Cohen*, 2010), shock-wave and 300 K static compression XRD data (*Dewaele et al.*, 2006), static compression Raman spectroscopy at 300 K (*Merkel et al.*, 2000), and static compression XRD data (*Dubrovinsky et al.*, 2000).

(at volume V) to estimate the corresponding $\gamma_{vib,i}$. We then average all estimated $\gamma_{vib,i}$ for a given reference phonon DOS. We repeat this process with each phonon DOS serving as a reference. While this method is an approximation for $\gamma_{vib,i}$, we note that it does not rely on the application of the empirical relation in equation 4.14, on a linear least squares fit, or on fixing the fitting parameter q. Therefore, it can serve a check of the validity of equation 4.17. We plot $\gamma_{vib,i}$ as determined from both methods as a function of volume for each composition in Figure 4.20. The two methods of determining $\gamma_{vib,i}$ agree well within error bars within the measured volume region. However, the $\gamma_{vib,i}$ curve calculated with equation 4.17 has a powerful advantage, as it can be extrapolated to 0 GPa or to higher pressures. Additionally, the $\gamma_{vib,i}$ curve is more reliable, because the other method depends on a very rough approximation for the derivative in equation 4.11. We note that the error bars of the $\gamma_{vib,i}$ curve (calculated with equation 4.17) are much smaller than those of the estimated $\gamma_{vib,i}$ (calculated with equation 4.20) due to the imposition of equation 4.14 and the lack of the rough approximation in equation 4.19.

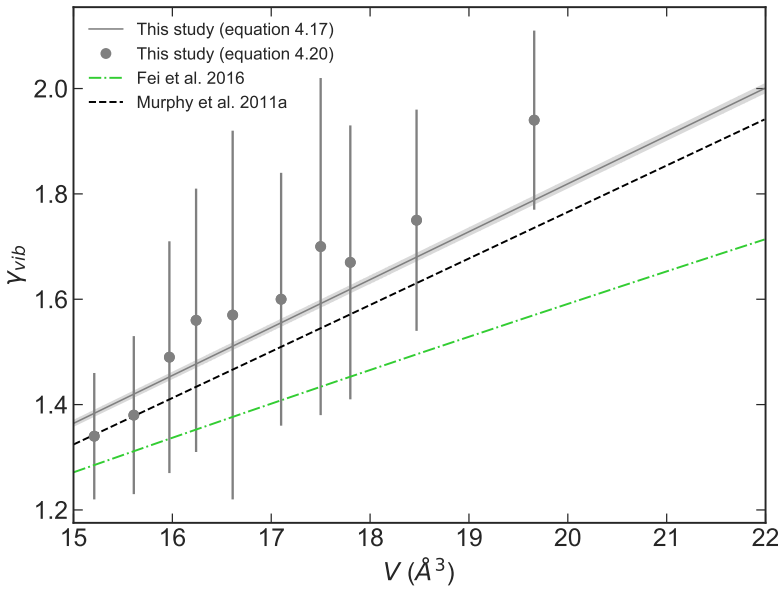

Figure 4.22: Various reported γ_{vib} determined from the hcp-Fe NRIXS data reported in *Murphy et al.* (2011a). Our analysis using equation 4.17 and $q = 1$ and our approximation using equation 4.20 are internally consistent and in agreement with published results from *Murphy et al.* (2011a) with $q = 1$. Our analysis is not in agreement with results from *Fei et al.* (2016).

The γ_{vib} for hcp-$Fe_{0.91}Ni_{0.09}$ and $Fe_{0.8}Ni_{0.1}Si_{0.1}$ and our re-analysis of hcp-Fe data from *Murphy et al.* (2011a) are within close agreement (Figure 4.21) and nearly indistinguishable within our reported error bars. We compare to previously reported values of γ_{vib} for hcp-Fe. Ab initio calculations by *Sha and Cohen* (2010) computed at 500 K are similar to our results, although the slope of γ_{vib} with respect to volume is noticeably different. The γ_{vib} reported by *Dewaele et al.* (2006) is determined with shock-wave and 300 K static compression XRD data and is in close agreement with our results. *Merkel et al.* (2000) constrain γ_{vib} with Raman spectroscopy at 300 K, and *Dubrovinsky et al.* (2000) constrain γ_{vib} with static compression XRD data. *Fei et al.* (2016) calculate γ_{vib} from the results of *Murphy et al.* (2011a), much as we do in this study.

In Figure 4.22, we compare γ_{vib} reported in *Murphy et al.* (2011a), *Fei et al.* (2016), and our study, which all use the same NRIXS hcp-Fe data set from *Murphy et al.* (2011a). We plot both our γ_{vib} results for hcp-Fe calculated using equation 4.17 and equation 4.20. Note that each study (with the exception of our approximation using equation 4.20) applies the same empirical constraint

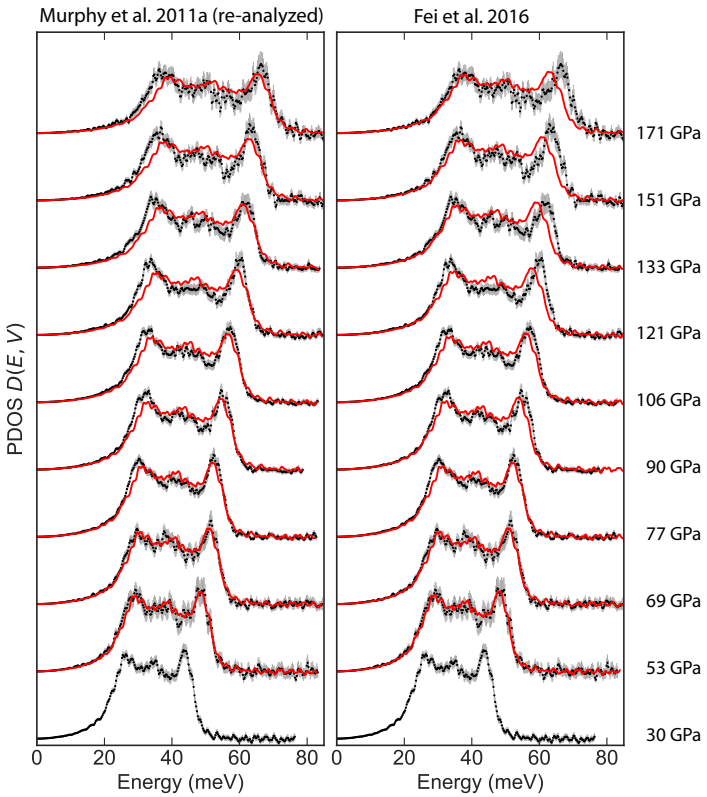

Figure 4.23: Scaled phonon DOSs (red) compared to measured phonon DOS (black with gray error bars) for hcp-structured Fe. The hcp-Fe phonon DOS at 30 GPa is scaled to each compression point according to equation 4.12. On the left is our analysis of *Murphy et al.* (2011a), and on the right is the phonon DOS scaling calculated from γ_{vib} from *Fei et al.* (2016).

of equation 4.14. Our analyses are internally consistent and in close agreement with published results from *Murphy et al.* (2011a) with $q = 1$. Small differences between our analysis using equation 4.17 and reported values from *Murphy et al.* (2011a) are likely due to our exclusion of the NRIXS data set at 36 GPa. However, our results differ from the γ_{vib} of *Fei et al.* (2016).

We investigate the difference between our γ_{vib} analysis and that of *Fei et al.* (2016), and we estimate the effect of this difference on the extrapolation of an EOS to inner core conditions. We apply equation 4.15 to the γ_{vib} of *Fei et al.* (2016), and we compare the resulting scaled phonon DOS to ours in Figures 4.23–4.25. Figure 4.23 illustrates the scaling of the 30 GPa phonon DOS, and Figures 4.24 and 4.25 illustrate the scaling of the 90 and 171 GPa phonon DOS, respectively. The phonon DOS scaling with volume deviates slightly from equation 4.12. Higher energy phonon modes shift to higher ener-

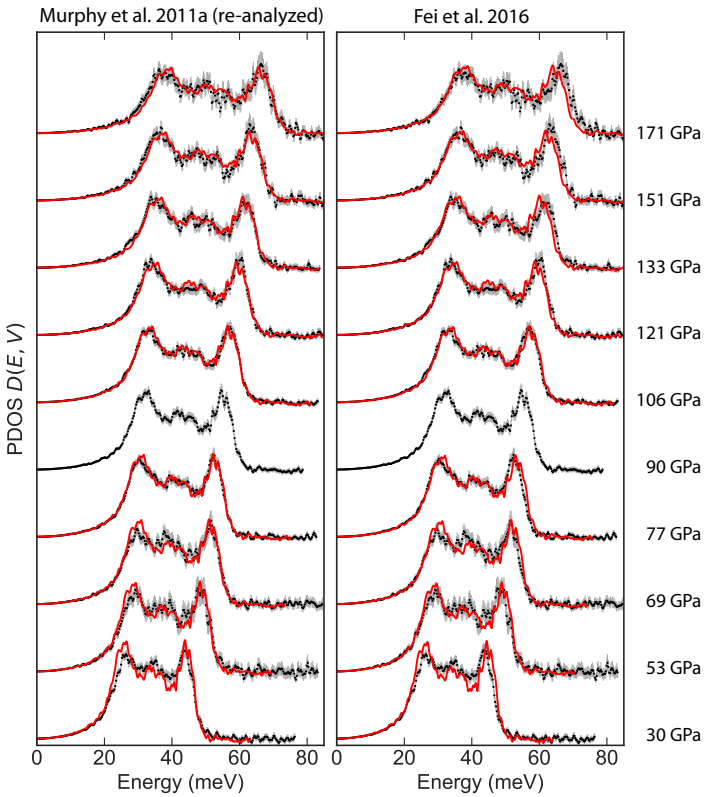

Figure 4.24: Scaled phonon DOSs (red) compared to measured phonon DOS (black with gray error bars) for hcp-structured Fe. The hcp-Fe phonon DOS at 90 GPa is scaled to each compression point according to equation 4.12. On the left is our analysis of *Murphy et al.* (2011a), and on the right is the phonon DOS scaling calculated from γ_{vib} from *Fei et al.* (2016).

gies slightly more with increasing pressure than do lower energy modes. This is particularly evident in Figures 4.23 and 4.25. Whereas the scaling fit in this study weights the phonon modes roughly evenly, the scaling fit in *Fei et al.* (2016) preferentially fits the lower energy region of the phonon DOS. We therefore suggest the γ_{vib} from *Fei et al.* (2016) is analogous to the Debye Grüneisen parameter, defined as

$$\gamma_D = \frac{1}{3} - \frac{V}{v_D}\left(\frac{v_D}{V}\right)_T . \tag{4.21}$$

This is supported by the close agreement between the γ_{vib} from *Fei et al.* (2016) and the γ_D from *Murphy et al.* (2011a).

We estimate the impact of γ_{vib} from *Murphy et al.* (2011a), *Fei et al.* (2016), and this study on isothermal EOS extrapolation to inner core conditions. We extrapolate the 300 K hcp-iron EOS from *Dewaele et al.* (2006) to 5500 K using

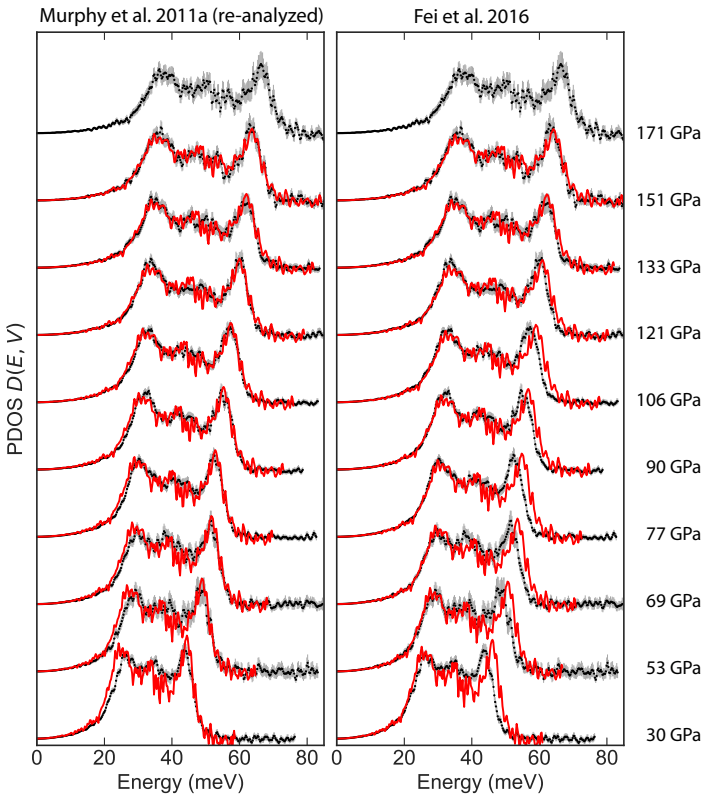

Figure 4.25: Scaled phonon DOSs (red) compared to measured phonon DOS (black with gray error bars) for hcp-structured Fe. The hcp-Fe phonon DOS at 171 GPa is scaled to each compression point according to equation 4.12. On the left is our analysis of *Murphy et al.* (2011a), and on the right is the phonon DOS scaling calculated from γ_{vib} from *Fei et al.* (2016).

the methods described in Section 2.5. We apply $\Theta_0 = 417\ K$ and each of the γ_{vib} from *Murphy et al.* (2011a), *Fei et al.* (2016), and this study. The resulting density, bulk modulus, and bulk sound speed are compared in Figure 4.26. The bars to the right represent the estimated uncertainty as reported in Table 2.6, where uncertainties from electronic or anharmonic contributions to thermal pressure are neglected. The seismic model AK135-F is plotted for reference (*Kennett et al.*, 1995) with uncertainties for ρ (2%), K_S (2.3%), and v_ϕ (0.6%) (*Deuss*, 2008; *Masters and Gubbins*, 2003).

In comparison to existing equation of state uncertainty and seismic uncertainty, the γ_{vib} from *Murphy et al.* (2011a), *Fei et al.* (2016), and this study introduce negligible differences into the thermal equation of state at 5500 K and inner core pressures. This is before taking into account the uncertainties from electronic or anharmonic contributions to thermal pressure. In Section 2.5,

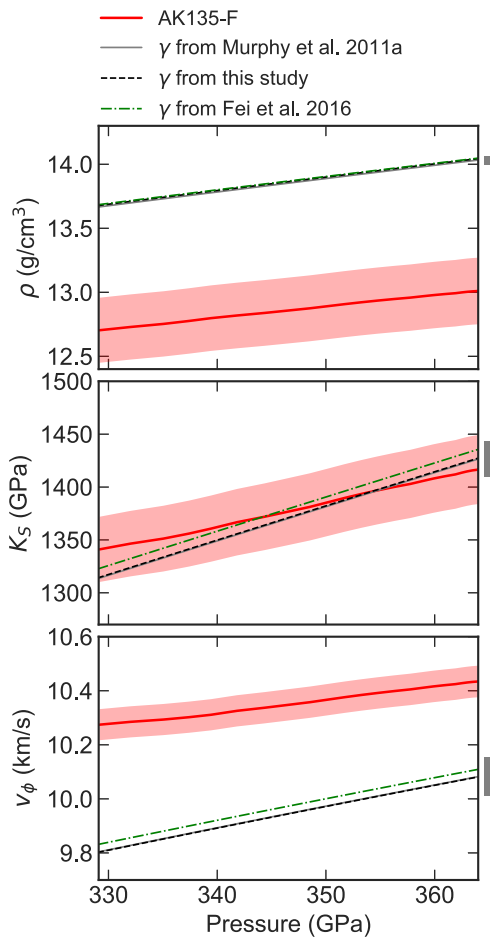

Figure 4.26: Thermal EOSs for hcp-Fe (*Dewaele et al.*, 2006) are extrapolated to inner core conditions to calculate density ρ, adiabatic bulk modulus K_S, and bulk sound speed v_ϕ as a function of pressure at 5500 K (see text for details). Estimated electronic and anharmonic contributions to thermal pressure are not included. Bars (right) represent uncertainty due to EOS parameters for hcp-Fe. We compare to the seismic model AK135-F (red line) (*Kennett et al.*, 1995) with estimated uncertainties for ρ (2%), K_S (2.3%), and v_ϕ (0.6%) (*Deuss*, 2008; *Masters and Gubbins*, 2003).

we estimate the electronic and anharmonic contributions to thermal pressure with theoretical calculations from *Dewaele et al.* (2006), and we find a combined $P_{el} + P_{ahn}$ of 14.5 GPa at 5500 K. At 5500 K and 3.7 g/cm^3 density, the formulation from *Fei et al.* (2016) estimates $P_{el} + P_{ahn} = 14.8$ GPa, in close agreement with *Dewaele et al.* (2006). Therefore, adding electronic and anharmonic contributions to thermal pressure to Figure 4.26 would not noticeably change the difference between the three compared thermal equations of state

for hcp-iron. We conclude that the differences between γ_{vib} from *Murphy et al.* (2011a), *Fei et al.* (2016), and this study have a negligible impact on ρ, K_S, and v_ϕ at inner core conditions.

Previoiusly in Section 2.5 *Morrison et al.* (2018), we applied the γ_{vib} from *Murphy et al.* (2011a) and $\Theta_0 = 417$ K (*Dewaele et al.*, 2006) to our isothermal equations of state of hcp-$Fe_{0.91}Ni_{0.09}$ and $Fe_{0.8}Ni_{0.1}Si_{0.1}$ to determine thermal equations of state. We then reported the corresponding ρ, K_S, and v_ϕ. In this section, we find the differences between the γ_{vib} of hcp-Fe, $Fe_{0.91}Ni_{0.09}$, and $Fe_{0.8}Ni_{0.1}Si_{0.1}$ to be negligible, and our re-analysis of γ_{vib} of hcp-Fe is in close agreement with that of *Murphy et al.* (2011a). Therefore, we conclude that our application of the γ_{vib} of hcp-Fe from *Murphy et al.* (2011a) to hcp-$Fe_{0.91}Ni_{0.09}$ and $Fe_{0.8}Ni_{0.1}Si_{0.1}$ in Section 2.5 is a reasonable approximation.

4.5 Vibrational free energy and thermal pressure

A key element to constrain core composition is the comparison of the densities of various iron alloys under core conditions to seismic constraints. Experimentally constraining density-pressure-temperature relations at inner core conditions remains experimentally challenging. Therefore, the thermal pressure of iron alloys (P_{th}) is critical in extrapolating equations of state conducted at lower temperatures to inner core temperatures. Previously, the P_{th} of hcp-iron has been investigated with shock-compression experiments using the thermodynamic Gruüneisen parameter and Mie-Grüneisen theory (*Brown and Mcqueen*, 1986; *Jeanloz*, 1979). Theoretical calculations have also estimated the P_{th} of hcp-iron (*Alfè et al.*, 2001; *Bouchet et al.*, 2013; *Sha and Cohen*, 2010; *Stixrude et al.*, 1997; *Vočadlo et al.*, 2000; *Wasserman et al.*, 1996). *Murphy et al.* (2011a,b) constrained the vibrational component P_{vib} of hcp-iron with NRIXS measurements via the vibrational free energy F_{vib} and the vibrational Grüneisen parameter. By comparison, the thermal pressure of iron-nickel and iron-silicon alloys has received little attention. *Zhang et al.* (2014) investigate the thermal pressure of iron-nickel-silicon alloys with shock compression, and *Côté et al.* (2010, 2012) apply theoretical calculations to study the thermal pressure of iron-silicon and iron-nickel alloys, respectively. Here, we apply the methods of *Murphy et al.* (2011a,b) to $Fe_{0.91}Ni_{0.09}$ and $Fe_{0.8}Ni_{0.1}Si_{0.1}$. For consistency, we also re-analyze NRIXS data from *Murphy et al.* (2011a,b) to ensure a systematic comparison of the alloys.

Table 4.5: Vibrational free energy and components of the thermal pressure for hcp phases

	at 300 K			at 5500 K			
V (Å^3)	P (GPa)	F_{vib} (meV/atom)	P^h_{vib} (GPa)	P^h_{vib} (GPa)	P^h_{anh} (GPa)	P_{el} (GPa)	P_{th} (GPa)
hcp-Fe[a]							
19.66(7)	30(2)	21.6(4)	1.83(9)	33.5(16)	3.4	13.9	50.8
18.47(3)	53(2)	29.4(10)	2.17(5)	39.7(9)	3.3	13.7	56.7
17.80(3)	69(3)	34.3(8)	2.36(3)	43.3(5)	3.2	13.5	60.0
17.50(7)	77(3)	35.8(5)	2.45(3)	44.8(5)	3.1	13.4	61.3
17.10(7)	90(3)	39.3(5)	2.56(3)	47.0(5)	3.1	13.3	63.4
16.61(7)	106(3)	42.8(5)	2.70(4)	49.5(7)	3.0	13.2	65.7
16.24(7)	121(3)	46.6(7)	2.81(5)	51.5(9)	2.9	13.1	67.5
15.97(7)	133(4)	49.1(8)	2.89(6)	52.9(10)	2.9	13.0	68.8
15.61(7)	151(5)	52.0(10)	2.99(7)	54.8(12)	2.8	12.9	70.5
15.21(7)	171(5)	56.1(12)	3.10(8)	56.9(15)	2.8	12.8	72.5
hcp-$Fe_{0.91}Ni_{0.09}$							
20.59(2)	18.0(1)	12.0(6)	1.89(22)	34.7(40)	3.6	14.1	52.4
20.21(3)	22.8(2)	13.3(7)	1.97(18)	36.1(33)	3.5	14.0	53.6
19.09(6)	41(1)	21.7(7)	2.20(8)	40.4(14)	3.3	13.7	57.4
18.72(4)	48(1)	24.4(8)	2.28(6)	41.8(11)	3.3	13.7	58.8
18.07(4)	63(1)	28.7(8)	2.41(10)	44.3(18)	3.2	13.5	61.0
17.60(2)	75(1)	31.2(8)	2.51(14)	46.0(26)	3.1	13.4	62.5
17.33(3)	83(1)	34.1(8)	2.57(17)	47.0(31)	3.1	13.3	63.4
16.72(4)	104(3)	39.9(8)	2.69(23)	49.4(43)	3.0	13.1	65.5
hcp-$Fe_{0.8}Ni_{0.1}Si_{0.1}$							
19.90(3)	27.9(3)	18.3(5)	2.30(49)	42.2(91)	3.3	13.6	59.1
19.31(5)	37.1(6)	21.9(5)	2.34(30)	42.9(54)	3.2	13.4	59.5
19.09(6)	41(1)	25.2(5)	2.35(23)	43.1(42)	3.2	13.4	59.7
18.40(5)	55(1)	29.6(8)	2.40(15)	44.0(27)	3.1	13.2	60.3
17.83(4)	69(1)	32.7(10)	2.44(29)	44.7(54)	3.0	13.1	60.8
17.26(6)	86(3)	38.4(10)	2.47(48)	45.3(89)	2.9	12.9	61.1

[a]Re-analyzed from *Murphy et al.* (2011b)

The harmonic vibrational free energy F_{vib} is accessible from the phonon DOS with

$$F_{vib} = \frac{1}{\beta} \int \ln \left(2 \sinh \frac{\beta E}{2} \right) D(E, V) dE, \tag{4.22}$$

where $\beta = (k_B T)^{-1}$. F_{vib} is related to the harmonic vibrational component of the thermal pressure P_{vib}. When combined with the electronic and anharmonic

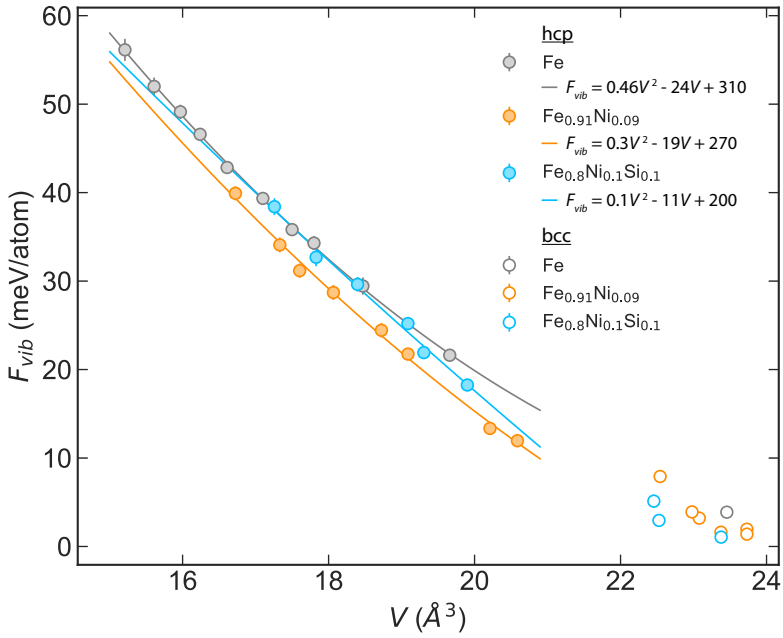

Figure 4.27: Harmonic vibrational free energy F_{vib} for $Fe_{0.91}Ni_{0.09}$, $Fe_{0.8}Ni_{0.1}Si_{0.1}$, and Fe at 300 K as determined from the phonon DOS. The hcp-Fe data is a re-analysis of data from *Murphy et al.* (2011b). Error bars where not shown are smaller than the symbols. Empirical equations for the hcp-phases are displayed.

components P_{el} and P_{anh}, this yields the total thermal pressure P_{th},

$$P_{th} = P_{vib} + P_{el} + P_{anh} = -\left(\frac{\partial F_{vib}}{\partial V}\right)_T - \left(\frac{\partial F_{el}}{\partial V}\right)_T - \left(\frac{\partial F_{anh}}{\partial V}\right)_T . \quad (4.23)$$

The harmonic vibrational free energy F_{vib} of $Fe_{0.91}Ni_{0.09}$, $Fe_{0.8}Ni_{0.1}Si_{0.1}$, and Fe at 300 K is plotted in Figure 4.27, and we fit empirical second-order polynomials to the F_{vib} of the hcp phases to calculate the derivative $(\partial F_{vib}/\partial V)_T$. The polynomials are listed in Figure 4.27, where volume V is in Å^3 and F_{vib} is in meV/atom. We find the curvature of F_{vib} for hcp-$Fe_{0.8}Ni_{0.1}Si_{0.1}$ is poorly constrained due to the smaller compression range explored for the Fe-Ni-Si alloy. We find for hcp-Fe that $P_{vib} = -0.29V + 7.5$, for hcp-$Fe_{0.91}Ni_{0.09}$ that $P_{vib} = -0.21V + 6.2$, and for that hcp-$Fe_{0.8}Ni_{0.1}Si_{0.1}$ $P_{vib} = -0.07V + 3.6$, where V is in Å^3 and P_{vib} has been converted to units of GPa. The resulting P_{vib} are plotted in Figure 4.27, and the F_{vib} and corresponding P_{vib} for each hcp volume can be found in Table 4.5.

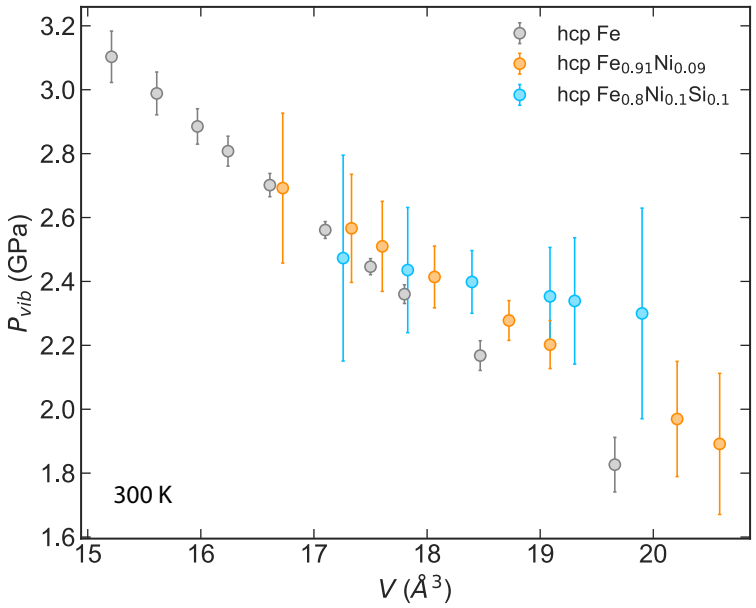

Figure 4.28: Harmonic vibrational thermal pressure P_{vib} for $Fe_{0.91}Ni_{0.09}$, $Fe_{0.8}Ni_{0.1}Si_{0.1}$, and Fe at 300 K as determined from the derivative of F_{vib}. The hcp-Fe data is a re-analysis of data from *Murphy et al.* (2011b).

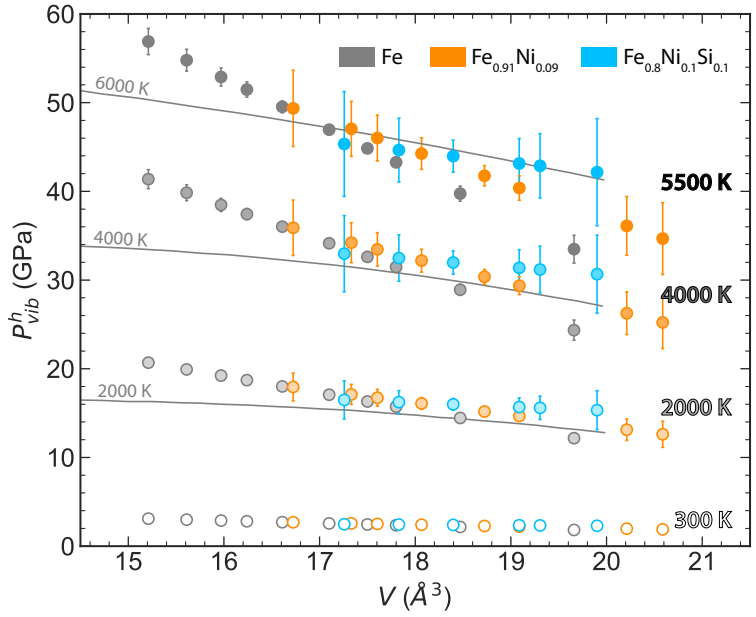

Figure 4.29: Harmonic vibrational thermal pressure P^h_{vib} as a function of volume and temperature for hcp-$Fe_{0.91}Ni_{0.09}$, $Fe_{0.8}Ni_{0.1}Si_{0.1}$, and Fe at 2000, 4000, and 5500 K (circles). The hcp-Fe data is a re-analysis of data from *Murphy et al.* (2011b). We compare to ab initio calculations of the harmonic thermal pressure for hcp-Fe by *Alfè et al.* (2001) at 2000, 4000, and 6000 K (solid lines).

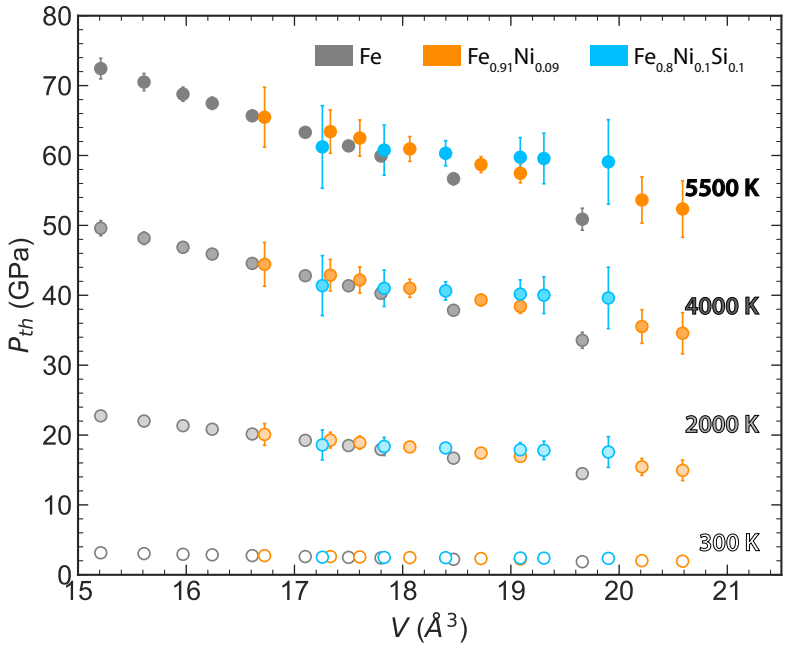

Figure 4.30: Thermal pressure P_{th} as a function of volume and temperature for hcp-$Fe_{0.91}Ni_{0.09}$, $Fe_{0.8}Ni_{0.1}Si_{0.1}$, and Fe. The hcp-Fe data is a re-analysis of data from *Murphy et al.* (2011b). We include harmonic, anharmonic, and electronic contributions to P_{th}. See text for more details.

As can be seen in equation 4.22, F_{vib} is directly proportional to temperature. Therefore, our 300 K data can be used to inform the temperature dependence of the harmonic P_{vib} with the following relation:

$$P_{vib}(V,T) = \left(\frac{T}{300\text{ K}}\right) P_{vib}(V, 300\text{ K}). \tag{4.24}$$

We plot the temperature dependent harmonic P^h_{vib} in Figure 4.29, and compare to the harmonic P^h_{vib} calculated by *Alfè et al.* (2001). We note that the slope of P^h_{vib} with volume of hcp-Fe is steeper than that previously published by *Murphy et al.* (2011b), due in part to our exclusion of the NRIXS data at 36 GPa, which had much lower counts than the other compression points in the same data set. Our re-analysis of P^h_{vib} for hcp-Fe is in close agreement with *Alfè et al.* (2001), although our slope of P^h_{vib} with volume is steeper. The P^h_{vib} for hcp-$Fe_{0.91}Ni_{0.09}$ is nearly indistinguishable from that of hcp-Fe. The slope of P_{vib} for hcp-$Fe_{0.8}Ni_{0.1}Si_{0.1}$ is much more shallow than that of hcp-Fe or $Fe_{0.91}Ni_{0.09}$, although we note the slope of of hcp-$Fe_{0.8}Ni_{0.1}Si_{0.1}$ is not as well constrained due to the smaller compression range explored.

Our above calculation of P_{vib}^{h} neglects both the anharmonic contribution P_{vib}^{anh} and the electronic contribution P_{el} to the thermal pressure P_{th}, which are important for high temperatures. The P_{vib}^{anh} and P_{el} of iron alloys are not yet well constrained by experimental data. *Murphy et al.* (2011b) and *Sakai et al.* (2014) used the P_{vib}^{anh} and P_{el} of hcp-Fe with fits from *Dewaele et al.* (2006). These fits are based on hcp-Fe ab initio calculations by *Alfè et al.* (2001) and use the P_{vib}^{h} and P_{el} formulation from *Dorogokupets and Oganov* (2006). As similar ab initio calculations are not available for hcp-$Fe_{0.91}Ni_{0.09}$ and $Fe_{0.8}Ni_{0.1}Si_{0.1}$, we applied the hcp-Fe P_{vib}^{h} and P_{el} from *Dewaele et al.* (2006) to each of our hcp compositions to estimate P_{th}. The estimated contributions of P_{vib}^{h}, P_{vib}^{anh}, and P_{el} for hcp-$Fe_{0.91}Ni_{0.09}$, $Fe_{0.8}Ni_{0.1}Si_{0.1}$, and Fe at 5500 K are tabulated in Table 4.5, and the corresponding total thermal pressures P_{th} for 300, 2000, 4000, and 5500 K are plotted in Figure 4.30.

4.6 Lamb-Mössbauer factor

The Lamb-Mössbauer factor (f_{LM}) is the probability for recoilless absorption. It contains information about the binding of the resonant nuclei (^{57}Fe in this study) in the lattice, and it therefore depends on composition, local environment structure, pressure, and temperature. In NRIXS experiments, it is the ratio of the elastic to total incoherent scattering. It takes a form similar to that of the Debye-Waller factor. While the Debye-Waller factor describes coherent, fast scattering events, f_{LM} describes slow scattering events such as those which take place over the lifetime of nuclear resonance (141 ns for ^{57}Fe) (*Sturhahn*, 2004).

There are two different methods of accessing f_{LM} from NRIXS measurements. First, f_{LM} can be determined from a moments analysis of the excitation probability density $S(E, V_i)$ (see Section 4.2), where f_{LM} is related to the 0th-order moment $S_0(E, V_i)$ (*Sturhahn and Chumakov*, 1999). Second, f_{LM} can be calculated from the determined phonon DOS, which assumes a quasi-harmonic lattice model (see Section 4.2). The quantity f_{LM} is related to the thermal motion of the resonant nuclei about their equilibrium positions, which can be quantified by the mean square atomic displacement $\langle u^2 \rangle$. From the phonon DOS, $\langle u^2 \rangle$ can be calculated as

$$\langle u^2 \rangle = \frac{E_R}{3k_0^2} \int \frac{1}{E} \coth \frac{\beta E}{2} D(E, V) dE, \tag{4.25}$$

where k_0 is the wavenumber of the resonant x-rays (k=7.306 Å^{-1} for ^{57}Fe).

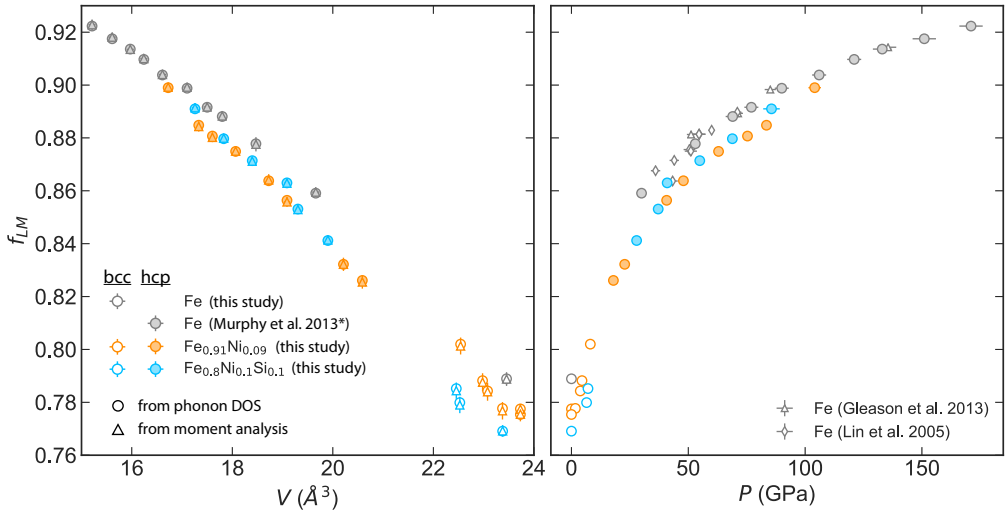

Figure 4.31: Left panel: f_{LM} for bcc- and hcp-$Fe_{0.91}Ni_{0.09}$, $Fe_{0.8}Ni_{0.1}Si_{0.1}$, and Fe calculated with a moments analysis of $S(E, V_i)$ (triangles) and determined from the phonon DOS (circles). (See text for more details.) The data for hcp-Fe is a re-analysis of data from *Murphy et al.* (2013). Error bars for f_{LM} from phonon DOS analysis are smaller than the displayed symbols. Right panel: f_{LM} phonon DOS analysis for bcc- and hcp-$Fe_{0.91}Ni_{0.09}$, $Fe_{0.8}Ni_{0.1}Si_{0.1}$, and Fe are compared to f_{LM} from existing hcp-Fe studies (*Gleason et al.*, 2013; *Lin et al.*, 2005).

The Lamb-Mössbauer factor is then

$$f_{LM} = e^{-k^2\langle u^2\rangle}. \tag{4.26}$$

While both methods of determining f_{LM} rely on $S(E, V_i)$, only the phonon DOS analysis relies on the quasi-harmonic assumption.

We compare our determined f_{LM} from the moments analysis and the phonon DOS analysis for $Fe_{0.91}Ni_{0.09}$, $Fe_{0.8}Ni_{0.1}Si_{0.1}$, and Fe in Figure 4.31. We note that both methods of determining f_{LM} are in close agreement. For the hcp phases, adding 9 at% Ni to iron decreases f_{LM} by ~1%. The f_{LM} of hcp-$Fe_{0.91}Ni_{0.09}$ and $Fe_{0.8}Ni_{0.1}Si_{0.1}$ are in close agreement, suggesting small amounts of silicon have a negligible effect on iron-nickel's f_{LM}. For the bcc-phases, the addition of nickel and silicon both decrease the f_{LM} of iron.

4.7 Entropy and thermal expansion

The volumetric thermal expansion coefficient α helps constrain the density of iron alloys at inner core conditions. Additionally, α factors into our calculation of the isentropic bulk modulus (equation 4.7), which is needed to constrain

Table 4.6: Vibrational thermodynamic quantities derived from the phonon DOS

Phase	V (Å^3)	P (GPa)	f_{LM}	S_{vib} (k_B/atom)	α_{vib} (10^{-5}K^{-1})	E_K (meV/atom)	C_{vib} (k_B/atom)
bcc-Fe							
	23.46(3)	0	0.789(1)	3.14(1)		14.2(1)	2.72(1)
hcp-Fe							
	19.66(7)	30(2)	0.859(1)	2.59(1)	1.76(4)	14.8(1)	2.60(2)
	18.47(3)	53(2)	0.878(2)	2.36(3)	1.33(3)	15.1(2)	2.53(3)
	17.80(3)	69(3)	0.888(2)	2.24(2)	1.15(2)	15.3(2)	2.49(2)
	17.50(7)	77(3)	0.892(1)	2.19(1)	1.08(2)	15.4(1)	2.47(2)
	17.10(7)	90(3)	0.899(1)	2.10(1)	0.98(2)	15.6(1)	2.44(2)
	16.61(7)	106(3)	0.904(1)	2.01(1)	0.88(2)	15.8(1)	2.40(2)
	16.24(7)	121(3)	0.910(1)	1.92(1)	0.81(2)	16.1(2)	2.36(2)
	15.97(7)	133(4)	0.914(1)	1.86(2)	0.76(1)	16.2(2)	2.33(2)
	15.61(7)	151(5)	0.918(2)	1.80(2)	0.70(1)	16.4(2)	2.30(2)
	15.21(7)	171(5)	0.922(2)	1.70(2)	0.64(1)	16.7(3)	2.25(3)
bcc-$Fe_{0.91}Ni_{0.09}$							
	23.73(2)	0	0.775(1)	3.21(1)		14.1(1)	2.74(1)
	23.38(3)	1.7(1)	0.778(2)	3.21(2)		14.1(1)	2.74(1)
	23.08(3)	3.8(1)	0.784(2)	3.17(2)		14.2(1)	2.73(2)
	22.98(3)	4.5(1)	0.788(2)	3.15(2)		14.2(1)	2.72(2)
	22.54(2)	8.1(1)	0.802(2)	3.02(2)		14.3(1)	2.70(2)
hcp-$Fe_{0.91}Ni_{0.09}$							
	20.59(2)	18.0(1)	0.826(1)	2.89(2)	2.24(5)	14.4(1)	2.68(2)
	20.21(3)	22.8(2)	0.832(1)	2.84(2)	2.05(4)	14.5(1)	2.66(2)
	19.09(6)	41(1)	0.856(1)	2.60(2)	1.57(3)	14.8(1)	2.60(2)
	18.72(4)	48(1)	0.864(1)	2.52(2)	1.45(3)	14.9(2)	2.58(2)
	18.07(4)	63(1)	0.875(1)	2.40(2)	1.24(2)	15.1(2)	2.54(2)
	17.60(2)	75(1)	0.881(1)	2.32(2)	1.11(2)	15.2(2)	2.52(2)
	17.33(3)	83(1)	0.885(1)	2.25(2)	1.04(2)	15.4(2)	2.49(2)
	16.72(4)	104(3)	0.899(1)	2.09(2)	0.91(2)	15.7(2)	2.43(2)
bcc-$Fe_{0.8}Ni_{0.1}Si_{0.1}$							
	23.38(3)	0	0.769(1)	3.23(1)		14.1(1)	2.74(1)
	22.53(3)	6.5(1)	0.780(2)	3.15(1)		14.1(1)	2.73(1)
	22.46(2)	7.1(1)	0.785(2)	3.09(1)		14.2(1)	2.72(1)
hcp-$Fe_{0.8}Ni_{0.1}Si_{0.1}$							
	19.90(3)	27.9(3)	0.841(1)	2.70(1)	2.01(4)	14.7(1)	2.62(1)
	19.31(5)	37.1(6)	0.853(1)	2.59(1)	1.72(3)	14.8(1)	2.59(1)
	19.09(6)	41(1)	0.863(1)	2.49(1)	1.63(3)	14.9(1)	2.57(1)
	18.40(5)	55(1)	0.871(1)	2.38(1)	1.37(2)	15.2(2)	2.52(2)
	17.83(4)	69(1)	0.880(1)	2.29(1)	1.18(2)	15.3(2)	2.50(2)
	17.26(6)	86(3)	0.891(1)	2.14(2)	1.02(2)	15.6(2)	2.44(2)

[a]Re-analyzed from *Murphy et al.* (2011b)

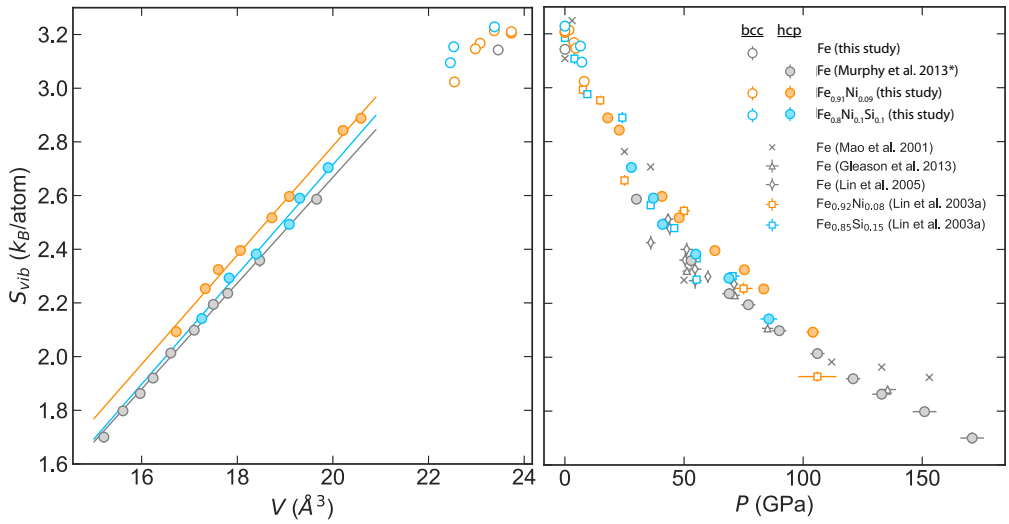

Figure 4.32: Vibrational harmonic component of entropy per ^{57}Fe resonant atom S_{vib} for bcc- and hcp-$Fe_{0.91}Ni_{0.09}$, $Fe_{0.8}Ni_{0.1}Si_{0.1}$, and Fe. The data for hcp-Fe is a re-analysis of data from *Murphy et al.* (2013). In the left panel, linear fits for the hcp phases are displayed. For hcp-Fe, we obtain a fit of $S_{vib} = 0.197V - 1.28$. For hcp-$Fe_{0.91}Ni_{0.09}$, $S_{vib} = 0.203V - 1.28$. For hcp-$Fe_{0.8}Ni_{0.1}Si_{0.1}$, $S_{vib} = 0.204V - 1.37$. In the right panel, we compare to S_{vib} from existing NRIXS studies: bcc- and hcp-Fe (*Gleason et al.*, 2013; *Lin et al.*, 2005; *Mao et al.*, 2001), $Fe_{0.92}Ni_{0.08}$, and $Fe_{0.85}Ni_{0.15}$ (*Lin et al.*, 2003).

compressional and shear sound velocities from the Debye sound velocity (section 4.3).

The vibrational component of thermal expansion α_{vib} is related to the vibrational entropy per ^{57}Fe resonant atom (S_{vib}). S_{vib} is accessible via the phonon DOS, which assumes a quasi-harmonic approximation, with

$$S_{vib} = \frac{k_B\beta}{2}\int E\coth\frac{\beta E}{2}D(E,V)dE - k_B\int \ln\left(2\sinh\frac{\beta E}{2}\right)D(E,V)dE. \tag{4.27}$$

The S_{vib} for bcc- and hcp-$Fe_{0.91}Ni_{0.09}$, $Fe_{0.8}Ni_{0.1}Si_{0.1}$, and Fe are plotted in Figure 4.32.

The derivative of S_{vib} with respect to volume is related to α_{vib} with

$$\alpha_{vib} = \frac{1}{K_T}\left(\frac{\partial S_{vib}}{\partial V}\right)_T, \tag{4.28}$$

where K_T is the isothermal bulk modulus, accessible with equations of state (EOSs). For hcp-$Fe_{0.91}Ni_{0.09}$ and $Fe_{0.8}Ni_{0.1}Si_{0.1}$, we use the corresponding Vinet

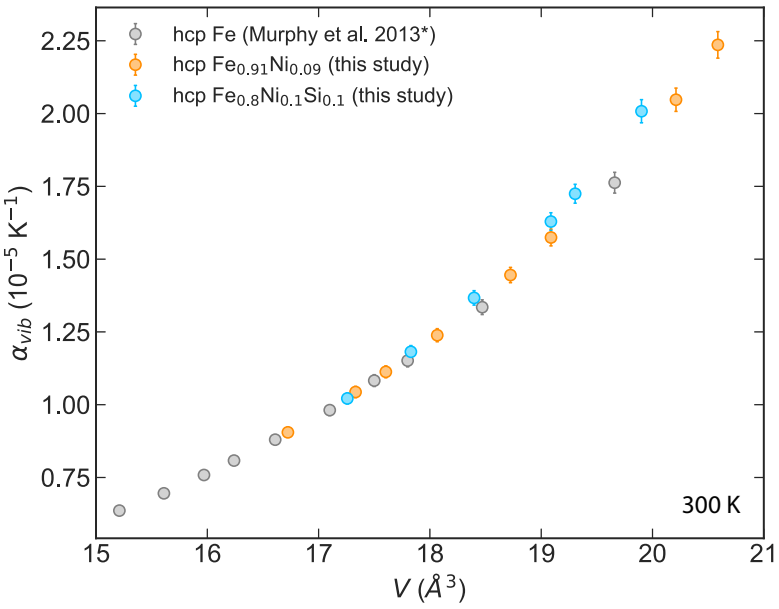

Figure 4.33: Vibrational harmonic component of thermal expansion for hcp-$Fe_{0.91}Ni_{0.09}$, $Fe_{0.8}Ni_{0.1}Si_{0.1}$, and Fe at 300 K. The data for hcp-Fe is a re-analysis of data from *Murphy et al.* (2013). If not shown, error bars are smaller than the displayed symbol.

EOSs from Chapter 2. For hcp-Fe, we use the Vinet EOS from *Dewaele et al.* (2006). The EOS experimental conditions and parameters are listed in Table 2.2. To calculate $(\partial S_{vib}/\partial V)_T$, we apply linear fits to the hcp data. These fits and their corresponding equations are displayed in Figure 4.32. Our resulting α_{vib} for the hcp phases at 300 K are plotted in Figure 4.33 and tabulated in Table 4.6. The α_{vib} of hcp-Fe and $Fe_{0.91}Ni_{0.09}$ are in close agreement, while $Fe_{0.8}Ni_{0.1}Si_{0.1}$ has a slightly higher thermal expansion at large volumes. At smaller volumes, α_{vib} of $Fe_{0.8}Ni_{0.1}Si_{0.1}$ seems to approach that of hcp-Fe and $Fe_{0.91}Ni_{0.09}$.

4.8 Other thermodynamic quantities

The vibrational kinetic energy per ^{57}Fe resonant atom E_K at 300 K can be determined from NRIXS data in two ways. The first method uses the moment analysis of the excitation probability density $S(E, V_i)$ (see section 4.2), where E_K is related to the 2nd-order moment $S_2(E, V_i)$ (*Sturhahn and Chumakov*, 1999). The second method is from the phonon DOS determined with the quasi-harmonic approximation. The vibrational internal energy per ^{57}Fe atom

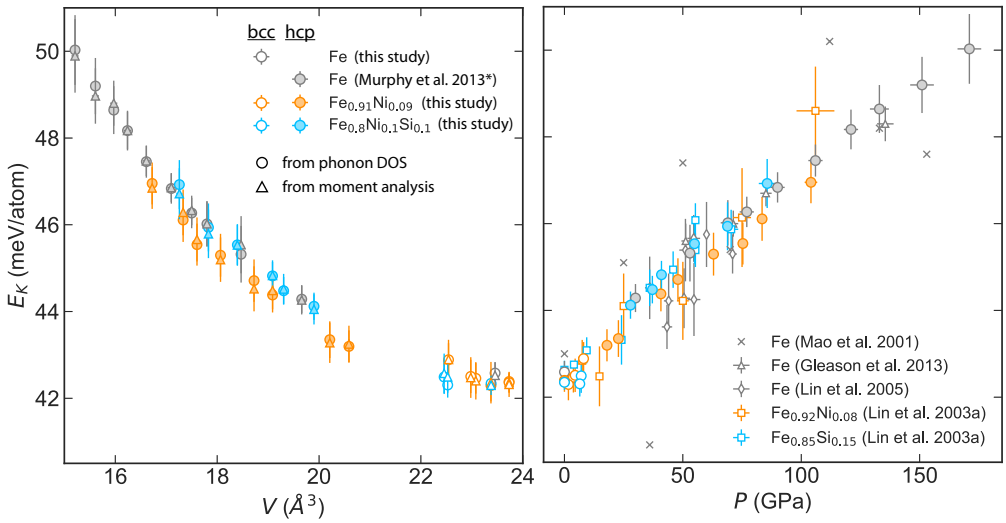

Figure 4.34: Left panel: Vibrational kinetic energy per ^{57}Fe atom E_K at 300 K for bcc- and hcp-$Fe_{0.91}Ni_{0.09}$, $Fe_{0.8}Ni_{0.1}Si_{0.1}$, and Fe calculated with a moments analysis of $S(E, V_i)$ (triangles) and from the phonon DOS (circles). (See text for more details.) The data for hcp-Fe is a re-analysis of data from *Murphy et al.* (2013). Right panel: E_K phonon DOS analysis for bcc- and hcp-$Fe_{0.91}Ni_{0.09}$, $Fe_{0.8}Ni_{0.1}Si_{0.1}$, and Fe are compared to f_{LM} from other NRIXS studies: bcc- and hcp-Fe (*Gleason et al.*, 2013; *Lin et al.*, 2005; *Mao et al.*, 2001), $Fe_{0.92}Ni_{0.08}$, and $Fe_{0.85}Ni_{0.15}$ (*Lin et al.*, 2003).

U_{vib},

$$U_{vib}(V) = \frac{1}{2}\int E \coth\frac{\beta E}{2} D(E,V)dE, \tag{4.29}$$

is composed of equal parts kinetic and potential energy, so $E_K = (1/2)U_{vib}$. Both methods use the excitation probability density $S(E, V_i)$, but only the phonon DOS method relies on the quasi-harmonic approximation. We calculate E_K for $Fe_{0.91}Ni_{0.09}$, $Fe_{0.8}Ni_{0.1}Si_{0.1}$, and Fe with the moment analysis and from the phonon DOS and compare in Figure 4.34. The E_K from both methods agree closely within error bars. The E_K as determined with the phonon DOS is listed in Table 4.6. The difference between compositions for the bcc phases is negligible. For the hcp phases, the E_K of $Fe_{0.91}Ni_{0.09}$ trends slightly below those of $Fe_{0.8}Ni_{0.1}Si_{0.1}$ and Fe; however, all three hcp phases agree within uncertainty.

Lastly, the phonon DOS also yields the vibrational component of the specific heat capacity via

$$C_{vib}(V) = k_B \int \left(\frac{\beta E}{2\sinh(\beta E/2)}\right)^2 D(E,V)dE. \tag{4.30}$$

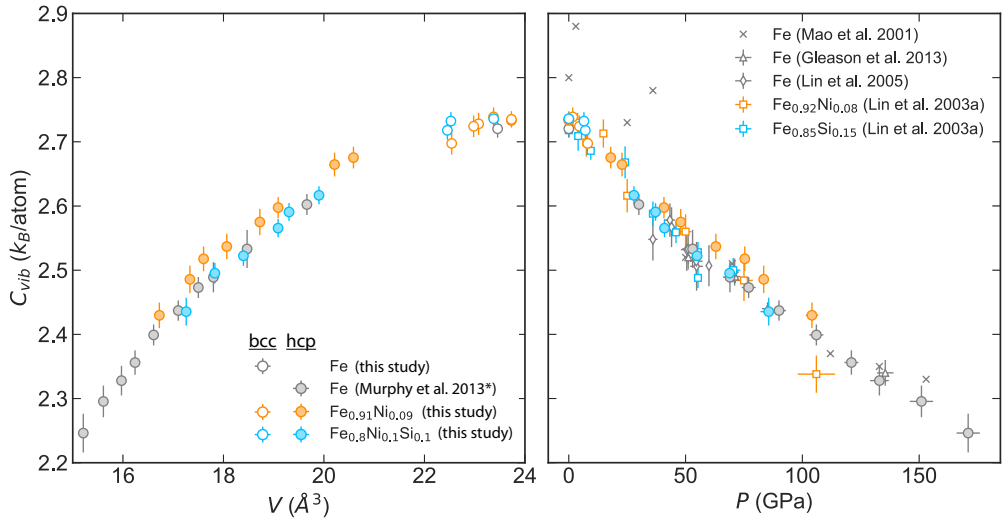

Figure 4.35: Left panel: Vibrational harmonic component of the specific heat capacity C_{vib} for bcc- and hcp-$Fe_{0.91}Ni_{0.09}$, $Fe_{0.8}Ni_{0.1}Si_{0.1}$, and Fe at 300 K. The data for hcp-Fe is a re-analysis of data from *Murphy et al.* (2013). Right panel: We compare our C_{vib} to existing studies: bcc- and hcp-Fe (*Gleason et al.*, 2013; *Lin et al.*, 2005; *Mao et al.*, 2001), $Fe_{0.92}Ni_{0.08}$, and $Fe_{0.85}Ni_{0.15}$ (*Lin et al.*, 2003).

We plot the C_{vib} as a function of volume for bcc- and hcp-$Fe_{0.91}Ni_{0.09}$, $Fe_{0.8}Ni_{0.1}Si_{0.1}$, and Fe at 300 K in Figure 4.35 and listed in Table 4.6. The three hcp phases have similar trends with volume, with the C_{vib} of hcp-$Fe_{0.91}Ni_{0.09}$ falling slightly above those of $Fe_{0.8}Ni_{0.1}Si_{0.1}$ and Fe.

4.9 Conclusions

We present high pressure NRIXS data on bcc- and hcp-$Fe_{0.91}Ni_{0.09}$ and $Fe_{0.8}Ni_{0.1}Si_{0.1}$ at 300 K with in situ XRD. From these data, we determine the partial phonon density of states for each composition. To ensure a systematic comparison to pure iron, we re-analyze the hcp-iron NRIXS data presented in *Murphy et al.* (2011a), *Murphy et al.* (2011b), and *Murphy et al.* (2013) using the same methods used to analyze our $Fe_{0.91}Ni_{0.09}$ and $Fe_{0.8}Ni_{0.1}Si_{0.1}$ data sets.

We demonstrate a new method of determining the Debye sound velocity from the low energy region of the phonon DOS. This method applies the corrected Akaike Information Criteria and uses a binning of many possible fit ranges to determine a probability distribution function of the Debye sound velocity. Unlike previous methods, this method does not depend on picking an energy fit range for the phonon DOS, and it provides an improved estimate on the Debye

sound velocity uncertainty. We present Debye sound velocities for bcc- and hcp-$Fe_{0.91}Ni_{0.09}$ and $Fe_{0.8}Ni_{0.1}Si_{0.1}$. Using our previously determined equations of state for the same compositions, we present the compressional and shear sound velocities of bcc- and hcp-$Fe_{0.91}Ni_{0.09}$ and $Fe_{0.8}Ni_{0.1}Si_{0.1}$, along with the corresponding shear modulus. At 300 K, we find that 9 at% nickel decreases the shear modulus of hcp-iron by ∼6%, and that silicon has a minimal effect on the shear modulus of hcp-$Fe_{0.91}Ni_{0.09}$.

From the volume scaling of the phonon DOS, we constrain the 300 K vibrational component of the Grüneisen parameter for hcp-$Fe_{0.91}Ni_{0.09}$ and $Fe_{0.8}Ni_{0.1}Si_{0.1}$. We find that the Grüneisen parameter of hcp-$Fe_{0.91}Ni_{0.09}$ and $Fe_{0.8}Ni_{0.1}Si_{0.1}$ are quite similar to that of hcp-Fe within uncertainties. Therefore, we find our application in Section 2.5 of the Grüneisen parameter of hcp-Fe to determine the thermal equations of state of hcp-$Fe_{0.91}Ni_{0.09}$ and $Fe_{0.8}Ni_{0.1}Si_{0.1}$ is a reasonable approximation. The phonon DOS also provides constraints on the volume dependence of vibrational free energy, which is directly related to the vibrational component of thermal pressure. Again, we find negligible differences within uncertainty between the vibrational thermal pressures of hcp-$Fe_{0.91}Ni_{0.09}$ and $Fe_{0.8}Ni_{0.1}Si_{0.1}$ to that of hcp-Fe. By combining the vibrational component with theoretical estimates of the anharmonic and electronic contributions, we provide an estimate for the total thermal pressure of hcp-$Fe_{0.91}Ni_{0.09}$ and $Fe_{0.8}Ni_{0.1}Si_{0.1}$.

The phonon DOS also provides access to the vibrational component of entropy per ^{57}Fe atom, the volume derivative of which is directly related to the product of isothermal bulk modulus and thermal expansion. Therefore, we can apply the isothermal bulk modulus constrained in Chapter 2 to determine the vibrational component of thermal expansion for hcp-$Fe_{0.91}Ni_{0.09}$ and $Fe_{0.8}Ni_{0.1}Si_{0.1}$. The vibrational thermal expansion of hcp-$Fe_{0.91}Ni_{0.09}$ is indistinguishable from that of hcp-iron. Silicon slightly increases the vibrational thermal expansion of $Fe_{0.91}Ni_{0.09}$ at low compressions, but at larger compressions above 65 GPa, the effect becomes negligible. From the NRIXS data and from the phonon DOS, we present constraints on the vibrational kinetic energy per ^{57}Fe atom and on the Lamb-Mössbauer factor, which is related to the mean square displacement. The vibrational kinetic energy of $Fe_{0.91}Ni_{0.09}$ and $Fe_{0.8}Ni_{0.1}Si_{0.1}$ are indistinguishable from that of iron within uncertainty. We find that adding 9 at% decreases the Lamb-Mössbauer factor of hcp-iron by ∼1%, and that

silicon has a minimal impact on the Lamb-Mössbauer factor of $Fe_{0.91}Ni_{0.09}$. Furthermore, we constrain the vibrational component of specific heat from the phonon DOS. The vibrational specific heat of hcp-$Fe_{0.91}Ni_{0.09}$ falls slightly above that of hcp-Fe, while the vibrational specific heat of $Fe_{0.8}Ni_{0.1}Si_{0.1}$ is in close agreement with that of hcp-iron. In summary, we provide improved constraints on the effects of nickel and silicon on the thermoelastic and vibrational properties of iron, which is a necessary step in constraining core composition, the thermal profile of the Earth, and the thermodynamic properties of the core.

Chapter 5

CONCLUSIONS

Throughout this thesis, we have investigated the thermoelastic and vibrational properties properties of bcc- and hcp-structured $Fe_{0.91}Ni_{0.09}$ and $Fe_{0.8}Ni_{0.1}Si_{0.1}$ at high pressures. At each step, we have strived to systematically compare our results to bcc- and hcp-iron, for a careful analysis of the effects of nickel and silicon on iron necessitates a systematic approach.

In Chapter 2, we investigated the equations of state of bcc- and hcp-$Fe_{0.91}Ni_{0.09}$ and $Fe_{0.8}Ni_{0.1}Si_{0.1}$ and explore implications for the composition of the Earth's inner core.

- We presented powder x-ray diffraction data and equations of state at 300 K on bcc- and hcp-$Fe_{0.91}Ni_{0.09}$ from 0 to 167 GPa and on bcc- and hcp-$Fe_{0.8}Ni_{0.1}Si_{0.1}$ from 0 to 175 GPa.

- We constrained the effect of nickel and silicon on the density, bulk modulus, and bulk sound speed of iron alloys at 300 K.

- The density, adiabatic bulk modulus, and bulk sound speed of hcp-$Fe_{0.91}Ni_{0.09}$ and $Fe_{0.8}Ni_{0.1}Si_{0.1}$ were extrapolated to 5500 K along the inner core pressure gradient from 330 to 364 GPa and compared to the seismic model AK135-F.

- We applied a linear mixing model to the Fe-Ni-Si system to determine to what extent silicon is seismically consistent with the density, adiabatic bulk modulus, and bulk sound speed observations of the inner core at 330 GPa. We found 4.3 to 5.3 wt% silicon alone could explain the density, adiabatic bulk modulus, and bulk sound speed of the inner core.

- We extrapolated our compositional analysis to the Fe-Ni-Si-O-C-S system by applying both a bulk aggregate model and a linear mixing model at 330 GPa. Our analysis pointed to a low oxygen and carbon content of the inner core ($<\sim$2 wt% O and $<$1 wt% C). These results depend on the mixing model, the temperature of the inner core boundary, and electronic and anharmonic contributions to thermal pressure.

In Chapter 3, we investigated the c/a axial ratio of hcp-structured materials and explored the its relationship to anisotropy in the inner core of the Earth.

- We found that hcp-$Fe_{0.91}Ni_{0.09}$ and hcp-$Fe_{0.8}Ni_{0.1}Si_{0.1}$ have greater c/a axial ratios compared to hcp-Fe at 300 K.
- We investigated the relationship between the c/a axial ratio and the compressional anisotropy measure $\phi = C_{33}/C_{11}$, and we proposed a relationship between the pressure derivative of the c/a axial ratio and the anisotropy measure $\phi = C_{33}/C_{11}$.

In Chapter 4, we presented experimentally determined phonon density of states of bcc- and hcp-$Fe_{0.91}Ni_{0.09}$ and $Fe_{0.8}Ni_{0.1}Si_{0.1}$, from which we constrained sound velocities and a wide array of thermoelastic parameters.

- We presented high pressure NRIXS data on bcc- and hcp-$Fe_{0.91}Ni_{0.09}$ and $Fe_{0.8}Ni_{0.1}Si_{0.1}$ at 300 K with in situ XRD.
- We determined the partial phonon density of states (DOS) for each composition. To ensure a systematic comparison to pure iron, we re-analyzed the hcp-iron NRIXS data presented in *Murphy et al.* (2011a), *Murphy et al.* (2011b), and *Murphy et al.* (2013) using the same methods.
- We constrained Debye sound velocities for the investigated bcc- and hcp-structured alloys. Using our previously determined equations of state for the same compositions, we presented the compressional and shear sound velocities and shear moduli. At 300 K, we found that 9 at% nickel decreases the shear modulus of hcp-iron by ~6%, and that silicon has a minimal effect on the shear modulus of hcp-$Fe_{0.91}Ni_{0.09}$.
- From the volume scaling of the phonon DOS, we constrained the 300 K vibrational component of the Grüneisen parameter for the investigated hcp-structured alloys. We found that the Grüneisen parameter of hcp-$Fe_{0.91}Ni_{0.09}$ and $Fe_{0.8}Ni_{0.1}Si_{0.1}$ are quite similar to that of hcp-Fe within uncertainties. Therefore, our previous application of the Grüneisen parameter of hcp-Fe to determine the thermal equations of state of hcp-$Fe_{0.91}Ni_{0.09}$ and $Fe_{0.8}Ni_{0.1}Si_{0.1}$ is a reasonable approximation (see Chapter 2).

- We investigated the volume dependence of vibrational free energy to constrain the vibrational component of thermal pressure. We found negligible differences within uncertainty between the vibrational thermal pressures of hcp-$Fe_{0.91}Ni_{0.09}$ and $Fe_{0.8}Ni_{0.1}Si_{0.1}$ to that of hcp-Fe. We provide an estimate for the total thermal pressure of hcp-Fe, $Fe_{0.91}Ni_{0.09}$, and $Fe_{0.8}Ni_{0.1}Si_{0.1}$.

- We constrained the vibrational entropy per ^{57}Fe atom, which we paired with our previously determined isothermal bulk modulus to determine thermal expansion. The vibrational thermal expansion of hcp-$Fe_{0.91}Ni_{0.09}$ is indistinguishable from that of hcp-iron. Silicon slightly increases the vibrational thermal expansion of $Fe_{0.91}Ni_{0.09}$ at low pressures, but the effect becomes negligible above 65 GPa.

- We presented constraints on the vibrational kinetic energy per ^{57}Fe atom and on the Lamb-Mössbauer factor.

- We constrained the vibrational component of specific heat from the phonon DOS.

Some of the largest sources of uncertainty in constraining inner core composition are the electronic and anharmonic contributions to thermal pressure, the effect of temperature on sound velocities, and the extrapolation of the equation of state from 175 to 330 GPa. A logical next step following this thesis would be to systematically extend these studies to compositions of iron containing small amounts of oxygen, carbon, and sulfur (around 1-10 wt%). Many existing equations of state and sound velocity constraints on iron-oxygen, iron-carbon, and iron-sulfur materials are for samples containing much larger light element contents than is often suggested to be in the core. Therefore, mixing analysis require a large extrapolation in compositional space to investigate realistic core compositions. As mixing analysis may not accurately predict the complexities of multicomponent systems, a similarly reasonable next step would be to investigate the equations of state, sound velocities, and thermoelastic properties of multi-component systems, such as those proposed in Chapter 2 of this thesis.

To further understand the source of anisotropy in the inner core, careful x-ray diffraction experiments at a range of pressures, temperatures, and compositions can improve the constraints on the pressure derivative of c/a. This would

provide important constraints on the anisotropy measure. Of course, should synthesis of a large enough high-quality hcp-iron crystal become feasible, a direct measurement of anisotropy would become accessible.

In this thesis, I have aimed to improve the constraints on the effects of nickel and silicon on the thermoelastic and vibrational properties of iron. It is my goal that conducting careful, systematic experiments with attention to uncertainty analysis will aid our community's progress in constraining the composition of the core, the thermal profile of the Earth, and the thermodynamic properties of the core.

BIBLIOGRAPHY

Ahrens, T. J., and R. Jeanloz (1987), Pyrite: Shock compression, isentropic release, and composition of the Earth's core, *Journal of Geophysical Research*, *92*(B10), 10,363–10,375, doi:10.1029/JB092iB10p10363.

Alfè, D., G. D. Price, and M. J. Gillan (2001), Thermodynamics of hexagonal-close-packed iron under Earth's core conditions, *Physical Review B*, *64*, 045123, doi:10.1103/PhysRevB.64.045123.

Alfè, D., M. J. Gillan, and G. D. Price (2002), Composition and temperature of the earth's core constrained by combining ab initio calculations and seismic data, *Earth and Planetary Science Letters*, *195*(1-2), 91–98, doi:10.1016/S0012-821X(01)00568-4.

Alfè, D., M. J. Gillan, and G. D. Price (2007), Temperature and composition of the Earth's core, *Contemporary Physics*, *48*(2), 63–80, doi:10.1080/00107510701529653.

Allègre, C., G. Manhes, and E. Lewin (2001), Chemical composition of the Earth and the volatility control on planetary genetics, *Earth and Planetary Science Letters*, *185*, 49–69, doi:10.1016/S0012-821X(00)00359-9.

Allègre, C. J., J. P. Poirier, E. Humler, and A. W. Hofmann (1995), The chemical composition of the Earth, *Earth and Planetary Science Letters*, *134*(3-4), 515–526, doi:10.1016/0012-821X(95)00123-T.

Angel, R. J. (2000), Equations of State, *Reviews in Mineralogy and Geochemistry*, *41*(1), 35–59, doi:10.2138/rmg.2000.41.2.

Antonangeli, D., F. Occelli, H. Requardt, J. Badro, G. Fiquet, and M. Krisch (2004a), Elastic anisotropy in textured hcp-iron to 112 GPa from sound wave propagation measurements, *Earth and Planetary Science Letters*, *225*(1-2), 243–251, doi:10.1016/j.epsl.2004.06.004.

Antonangeli, D., M. Krisch, G. Fiquet, D. L. Farber, C. M. Aracne, J. Badro, F. Occelli, and H. Requardt (2004b), Elasticity of cobalt at high pressure studied by inelastic x-ray scattering, *Physical Review Letters*, *93*, 215505, doi:10.1103/PhysRevLett.93.215505.

Antonangeli, D., S. Merkel, and D. L. Farber (2006), Elastic anisotropy in hcp metals at high pressure and the sound wave anisotropy of the Earth's inner core, *Geophysical Research Letters*, *33*(24), 1–5, doi:10.1029/2006GL028237.

Antonangeli, D., L. R. Benedetti, D. L. Farber, G. Steinle-Neumann, A. L. Auzende, J. Badro, M. Hanfland, and M. Krisch (2008a), Anomalous pressure evolution of the axial ratio c/a in hcp cobalt: Interplay between structure, magnetism, and lattice dynamics, *Applied Physics Letters*, *92*, 111911, doi:10.1063/1.2897038.

Antonangeli, D., M. Krisch, D. L. Farber, D. G. Ruddle, and G. Fiquet (2008b), Elasticity of hexagonal-closed-packed cobalt at high pressure and temperature: A quasiharmonic case, *Physical Review Letters*, *100*, 085501, doi:10.1103/PhysRevLett.100.085501.

Antonangeli, D., J. Siebert, J. Badro, D. L. Farber, G. Fiquet, G. Morard, and F. J. Ryerson (2010), Composition of the Earth's inner core from high-pressure sound velocity measurements in Fe–Ni–Si alloys, *Earth and Planetary Science Letters*, *295*(1-2), 292–296, doi:10.1016/j.epsl.2010.04.018.

Antonangeli, D., G. Morard, L. Paolasini, G. Garbarino, C. A. Murphy, E. Edmund, F. Decremps, G. Fiquet, A. Bosak, M. Mezouar, and Y. Fei (2018), Sound velocities and density measurements of solid hcp-Fe and hcp-Fe–Si (9 wt.%) alloy at high pressure: Constraints on the Si abundance in the Earth's inner core, *Earth and Planetary Science Letters*, *482*, 446–453, doi:10.1016/j.epsl.2017.11.043.

Anzellini, S., A. Dewaele, M. Mezouar, P. Loubeyre, and G. Morard (2013), Melting of iron at Earth's inner core boundary based on fast x-ray diffraction, *Science*, *340*, 464–466, doi:10.1126/science.1233514.

Asanuma, H., E. Ohtani, T. Sakai, H. Terasaki, S. Kamada, N. Hirao, and Y. Ohishi (2011), Static compression of $Fe_{0.83}Ni_{0.09}Si_{0.08}$ alloy to 374 GPa and $Fe_{0.93}Si_{0.07}$ alloy to 252 GPa: Implications for the Earth's inner core, *Earth and Planetary Science Letters*, *310*(1-2), 113–118, doi:10.1016/j.epsl.2011.06.034.

Asker, C., L. Vitos, and I. A. Abrikosov (2009), Elastic constants and anisotropy in FeNi alloys at high pressures from first-principles calculations, *Physical Review B*, *79*, 214112, doi:10.1103/PhysRevB.79.214112.

Attanayake, J., V. F. Cormier, and S. M. De Silva (2014), Uppermost inner core seismic structure – new insights from body waveform inversion, *Earth and Planetary Science Letters*, *385*, 49–58, doi:10.1016/j.epsl.2013.10.025.

Badro, J., G. Fiquet, F. Guyot, E. Gregoryanz, F. Occelli, D. Antonangeli, and M. D'Astuto (2007), Effect of light elements on the sound velocities in solid iron: Implications for the composition of Earth's core, *Earth and Planetary Science Letters*, *254*(1-2), 233–238, doi:10.1016/j.epsl.2006.11.025.

Badro, J., J. P. Brodholt, H. Piet, J. Siebert, and F. J. Ryerson (2015), Core formation and core composition from coupled geochemical and geophysical

constraints, *Proceedings of the National Academy of Sciences of the United States of America*, *112*(40), 12,310–12,314, doi:10.1073/pnas.1505672112.

Bazhanova, Z. G., V. V. Roizen, and A. R. Oganov (2017), High-pressure behavior of the Fe–S system and composition of the Earth's inner core, *Physics-Uspekhi*, *60*(10), 1025–1032, doi:10.3367/UFNe.2017.03.038079.

Belonoshko, A. B., P. O. Dorogokupets, B. Johansson, S. K. Saxena, and L. Koči (2008), Ab initio equation of state for the body-centered-cubic phase of iron at high pressure and temperature, *Physical Review B*, *78*(10), 104,107, doi:10.1103/PhysRevB.78.104107.

Boehler, R., D. Santamaría-Pérez, D. Errandonea, and M. Mezouar (2008), Melting, density, and anisotropy of iron at core conditions: New x-ray measurements to 150 GPa, *Journal of Physics: Conference Series*, *121*(2), 022018, doi:10.1088/1742-6596/121/2/022018.

Bouchet, J., S. Mazevet, G. Morard, F. Guyot, and R. Musella (2013), Ab initio equation of state of iron up to 1500 GPa, *Physical Review B*, *87*, 094102, doi:10.1103/PhysRevB.87.094102.

Bouhifd, M. A., and A. P. Jephcoat (2011), Convergence of Ni and Co metal–silicate partition coefficients in the deep magma–ocean and coupled silicon–oxygen solubility in iron melts at high pressures, *Earth and Planetary Science Letters*, *307*(3-4), 341–348, doi:10.1016/j.epsl.2011.05.006.

Brodholt, J. P., and J. Badro (2017), Composition of the low seismic velocity E' layer at the top of Earth's core, *Geophysical Research Letters*, *44*, 8303–8310, doi:10.1002/2017GL074261.

Brown, J., and T. Shankland (1981), Thermodynamic parameters in the Earth as determined from seismic profiles, *Geophysical Journal of the Royal Astronomical Society*, *66*, 579–596, doi:10.1111/j.1365-246X.1981.tb04891.x.

Brown, J. M., and G. Mcqueen (1986), Phase transitions, Grüneisen parameter, and elasticity for shocked iron between 77 GPa and 400 GPa, *Journal of Geophysical Research*, *91*(B7), 7485–7494, doi:10.1029/JB091iB07p07485.

Buchwald, V. F. (1975), *Handbook of Iron Meteorites: Volume 1*, University of California Press, Berkeley, California.

Campbell, A. J. (2016), Phase diagrams and thermodynamics of core materials, in *Deep Earth: Physics and Chemistry of the Lower mantle and Core, Geophysical Monograph 217*, edited by H. Terasaki and R. A. Fischer, chap. 15, pp. 191–199, John Wiley & Sons, Inc., Hoboken, New Jersey, doi:10.1002/9781118992487.ch15.

Chen, B., L. Gao, B. Lavina, P. Dera, E. E. Alp, J. Zhao, and J. Li (2012), Magneto-elastic coupling in compressed Fe_7C_3 supports carbon in Earth's inner core, *Geophysical Research Letters*, *39*(17), doi:10.1029/2012GL052875.

Chen, B., Z. Li, D. Zhang, J. Liu, M. Y. Hu, J. Zhao, W. Bi, and E. E. Alp (2014), Hidden carbon in Earth's inner core revealed by shear softening in dense Fe_7C_3, *Proceedings of the National Academy of Sciences of the United States of America*, *111*(50), 17,755–17,758, doi:10.1073/pnas.1411154111.

Cohen, R. E., L. Stixrude, and E. Wasserman (1997), Tight-binding computations of elastic anisotropy of Fe, Xe, and Si under compression, *Physical Review B*, *56*(14), 8575–8589, doi:10.1103/PhysRevB.56.8575.

Côté, A. S., L. Vočadlo, D. P. Dobson, D. Alfè, and J. P. Brodholt (2010), Ab initio lattice dynamics calculations on the combined effect of temperature and silicon on the stability of different iron phases in the Earth's inner core, *Physics of the Earth and Planetary Interiors*, *178*(1-2), 2–7, doi:10.1016/j.pepi.2009.07.004.

Côté, A. S., L. Vočadlo, and J. P. Brodholt (2012), Ab initio simulations of iron–nickel alloys at Earth's core conditions, *Earth and Planetary Science Letters*, *348*, 126–130, doi:10.1016/j.epsl.2012.06.025.

Crowhurst, J. C., D. Antonangeli, J. M. Brown, A. F. Goncharov, D. L. Farber, and C. M. Aracne (2006), Determination of the high pressure elasticity of cobalt from measured interfacial acoustic wave velocities, *Applied Physics Letters*, *89*, 111920, doi:10.1063/1.2220537.

Daymond, M. R., M. A. M. Bourke, R. B. V. Dreele, M. R. Daymond, M. A. M. Bourke, and R. B. V. Dreele (1999), Use of Rietveld refinement to fit a hexagonal crystal structure in the presence of elastic and plastic anisotropy, *Journal of Applied Physics*, *85*(739), doi:10.1063/1.369154.

Decremps, F., D. Antonangeli, M. Gauthier, S. Ayrinhac, M. Morand, G. LeMarchand, F. Bergame, and J. Philippe (2014), Sound velocity of iron up to 152 GPa by picosecond acoustics in diamond anvil cell, *Geophysical Research Letters*, *41*, 1459–1464, doi:10.1002/2013GL058859.

Deuss, A. (2008), Normal mode constraints on shear and compressional wave velocity of the Earth's inner core, *Earth and Planetary Science Letters*, *268*(3-4), 364–375, doi:10.1016/j.epsl.2008.01.029.

Deuss, A. (2014), Heterogeneity and anisotropy of Earth's inner core, *Annual Review of Earth and Planetary Sciences*, *42*, 103–126, doi:10.1146/annurev-earth-060313-054658.

Dewaele, A., P. Loubeyre, and M. Mezouar (2004), Equations of state of six metals above 94 GPa, *Physical Review B*, *70*, 094112, doi:10.1103/PhysRevB.70.094112.

Dewaele, A., P. Loubeyre, F. Occelli, M. Mezouar, P. Dorogokupets, and M. Torrent (2006), Quasihydrostatic equation of state of iron above 2 Mbar, *Physical Review Letters*, *97*, 215504, doi:10.1103/PhysRevLett.97.215504.

Dorogokupets, P. I., and A. R. Oganov (2006), Equations of state of Al, Au, Cu, Pt, Ta, and W and revised ruby pressure scale, *Doklady Earth Sciences*, *410*(1), 1091–1095, doi:10.1134/S1028334X06070208.

Dubrovinsky, L., N. Dubrovinskaia, O. Narygina, I. Kantor, A. Kuznetzov, V. B. Prakapenka, L. Vitos, B. Johansson, A. S. Mikhaylushkin, S. I. Simak, and I. A. Abrikosov (2007), Body-centered cubic iron-nickel alloy in Earth's core, *Science*, *316*(5833), 1880–3, doi:10.1126/science.1142105.

Dubrovinsky, L. S., S. K. Saxena, and P. Lazor (1998), High pressure and high temperature in situ X-ray diffraction study of iron and corundum to 68 GPa using an internally heated diamond anvil cell, *Physics and Chemistry of Minerals*, *25*, 434–441, doi:10.1007/s002690050133.

Dubrovinsky, L. S., S. K. Saxena, N. A. Dubrovinskaia, S. Rekhi, and T. Le Bihan (2000), Gruneisen parameter of ϵ-iron up to 300 GPa from in-situ X-ray study, *American Mineralogist*, *85*(2), 386–389, doi:10.2138/am-2000-2-318.

Dziewonski, A. M., and D. L. Anderson (1981), Preliminary reference Earth model, *Physics of the Earth and Planetary Interiors*, *25*(4), 297–356, doi:10.1016/0031-9201(81)90046-7.

Ekholm, M., A. S. Mikhaylushkin, S. I. Simak, B. Johansson, and I. A. Abrikosov (2011), Configurational thermodynamics of Fe–Ni alloys at Earth's core conditions, *Earth and Planetary Science Letters*, *308*(1-2), 90–96, doi:10.1016/j.epsl.2011.05.035.

Fei, Y., C. Murphy, Y. Shibazaki, A. Shahar, and H. Huang (2016), Thermal equation of state of hcp-iron: Constraint on the density deficit of Earth's solid inner core, *Geophysical Research Letters*, *43*, 6837–6843, doi:10.1002/2016GL069456.

Fiquet, G., J. Badro, E. Gregoryanz, Y. Fei, and F. Occelli (2009), Sound velocity in iron carbide (Fe_3C) at high pressure: Implications for the carbon content of the Earth's inner core, *Physics of the Earth and Planetary Interiors*, *172*(1-2), 125–129, doi:10.1016/j.pepi.2008.05.016.

Fischer, R. A. (2016), Melting of Fe alloys and the thermal structure of the core, in *Deep Earth: Physics and Chemistry of the Lower mantle and Core, Geophysical Monograph 217*, edited by H. Terasaki and R. A. Fischer, chap. 1, pp. 3–12, John Wiley & Sons, Inc., Hoboken, New Jersey, doi:10.1002/9781118992487.ch1.

Fischer, R. A., and A. J. Campbell (2015), The axial ratio of hcp Fe and Fe-Ni-Si alloys to the conditions of Earth's inner core, *American Mineralogist*, *100*(11-12), 2718–2724, doi:10.2138/am-2015-5191.

Fischer, R. A., A. J. Campbell, G. A. Shofner, O. T. Lord, P. Dera, and V. B. Prakapenka (2011), Equation of state and phase diagram of FeO, *Earth and Planetary Science Letters*, *304*(3-4), 496–502, doi:10.1016/j.epsl.2011.02.025.

Fischer, R. A., A. J. Campbell, R. Caracas, D. M. Reaman, P. Dera, and V. B. Prakapenka (2012), Equation of state and phase diagram of Fe–16Si alloy as a candidate component of Earth's core, *Earth and Planetary Science Letters*, *357-358*, 268–276, doi:10.1016/j.epsl.2012.09.022.

Fischer, R. A., A. J. Campbell, D. M. Reaman, N. A. Miller, D. L. Heinz, P. Dera, and V. B. Prakapenka (2013), Phase relations in the Fe–FeSi system at high pressures and temperatures, *Earth and Planetary Science Letters*, *373*, 54–64, doi:10.1016/j.epsl.2013.04.035.

Fischer, R. A., A. J. Campbell, R. Caracas, D. M. Reaman, D. L. Heinz, P. Dera, and V. B. Prakapenka (2014), Equations of State in the Fe-FeSi system at high pressures and temperatures, *Journal of Geophysical Research: Solid Earth*, pp. 2810–2827, doi:10.1002/2013JB010898.

Fischer, R. A., Y. Nakajima, A. J. Campbell, D. J. Frost, D. Harries, F. Langenhorst, N. Miyajima, K. Pollok, and D. C. Rubie (2015), High pressure metal-silicate partitioning of Ni, Co, V, Cr, Si, and O, *Geochimica et Cosmochimica Acta*, *167*, 177–194, doi:10.1016/j.gca.2015.06.026.

Fujihisa, H., and K. Takemura (1996), Equation of state of cobalt up to 79 GPa, *Physical Review B*, *54*(1), 5–7, doi:10.1103/PhysRevB.54.5.

Gannarelli, C. M. S., D. Alfè, and M. J. Gillan (2005), The axial ratio of hcp iron at the conditions of the Earth's inner core, *Physics of the Earth and Planetary Interiors*, *152*(1-2), 67–77, doi:10.1016/j.pepi.2005.06.003.

Gao, L., B. Chen, J. Wang, E. E. Alp, J. Zhao, M. Lerche, W. Sturhahn, H. P. Scott, F. Huang, Y. Ding, S. V. Sinogeikin, C. C. Lundstrom, J. D. Bass, and J. Li (2008), Pressure-induced magnetic transition and sound velocities of Fe_3C: Implications for carbon in the Earth's inner core, *Geophysical Research Letters*, *35*(17), 1–5, doi:10.1029/2008GL034817.

Gao, L., B. Chen, M. Lerche, E. E. Alp, W. Sturhahn, J. Zhao, H. Yavas, and J. Li (2009), Sound velocities of compressed Fe_3C from simultaneous synchrotron X-ray diffraction and nuclear resonant scattering measurements, *Journal of Synchrotron Radiation*, *16*(6), 714–722, doi:10.1107/S0909049509033731.

Garai, J., J. Chen, and G. Telekes (2011), *PVT* equation of state of epsilon iron and its densities at inner core conditions, *American Mineralogist*, *96*, 828–832, doi:10.2138/am.2011.3612.

Giefers, H., R. Lübbers, K. Rupprecht, G. Wortmann, D. Alfè, and A. Chumakov (2002), Phonon spectroscopy of oriented hcp iron, *High Pressure Research*, *22*, 501–506, doi:10.1080/08957950290011437.

Gleason, A. E., W. L. Mao, and J. Y. Zhao (2013), Sound velocities for hcp-iron compressed hydrostatically to 136 GPa from phonon density of states, *Geophysical Research Letters*, *40*, 2983–2987, doi:10.1002/grl.50588.

Grechnev, G. E., R. Ahuja, and O. Eriksson (2003), Magnetic susceptibility of hcp iron and the seismic anisotropy of Earth's inner core, *Physical Review B*, *68*, 064414, doi:10.1103/PhysRevB.68.064414.

Grimvall, G. (1999), *Thermophysical Properties of Materials*, Elsevier, Amsterdam, doi:10.1016/B978-0-444-82794-4.X5000-1.

Hirao, N., E. Ohtani, T. Kondo, and T. Kikegawa (2004), Equation of state of iron-silicon alloys to megabar pressure, *Physics and Chemistry of Minerals*, *31*(6), 329–336, doi:10.1007/s00269-004-0387-x.

Hirose, K., S. Labrosse, and J. Hernlund (2013), Composition and state of the core, *Annual Review of Earth and Planetary Sciences*, *41*(1), 657–691, doi:10.1146/annurev-earth-050212-124007.

Hirose, K., G. Morard, R. Sinmyo, K. Umemoto, J. Hernlund, G. Helffrich, and S. Labrosse (2017), Crystallization of silicon dioxide and compositional evolution of the Earth's core, *Nature*, *543*, 99–102, doi:10.1038/nature21367.

Holmes, N. C., J. A. Moriarty, G. R. Gathers, and W. J. Nellis (1989), The equation of state of platinum to 660 GPa (6.6 Mbar), *Journal of Applied Physics*, *66*(7), 2962–2967, doi:10.1063/1.344177.

Huang, E., W. A. Bassett, and M. S. Weathers (1988), Phase relationships in Fe-Ni alloys at high pressures and temperatures, *Journal of Geophysical Research*, *93*(B7), 7741–7746, doi:10.1029/JB093iB07p07741.

Huang, S., X. Wu, and S. Qin (2018), Stability and anisotropy of $(Fe_xNi_{1-x})_2O$ under high pressure and implications in Earth's and super-Earths' core, *Scientific Reports*, *8*(236), doi:10.1038/s41598-017-18678-z.

Hurvich, C. M., and C.-L. Tsai (1989), Regression and time series model selection in small samples, *Biometrika*, *76*(2), 297–307, doi:10.1093/biomet/76.2.297.

Jeanloz, R. (1979), Properties of iron at high pressures and the state of the core, *Journal of Geophysical Research*, *84*(B11), 6059–6069, doi:10.1029/JB084iB11p06059.

Kennett, B. L. N., E. R. Engdah, and R. Buland (1995), Constraints on seismic velocities in the Earth from traveltimes, *Geophysical Journal International*, *122*, 108–124, doi:10.1111/j.1365-246X.1995.tb03540.x.

Klotz, S., J.-C. Chervin, P. Munsch, and G. Le Marchand (2009), Hydrostatic limits of 11 pressure transmitting media, *Journal of Physics D: Applied Physics*, *42*(7), 075413, doi:10.1088/0022-3727/42/7/075413.

Komabayashi, T. (2014), Thermodynamics of melting relations in the system Fe-FeO at high pressure: Implications for oxygen in the Earth's core, *Journal of Geophysical Research: Solid Earth*, *119*, 4164–4177, doi:10.1002/2014JB010980.

Laio, A., S. Bernard, G. L. Chiarotti, and S. Scandolo (2000), Physics of iron at Earth's core conditions, *Science*, *287*, 1027–1031, doi:10.1126/science.287.5455.1027.

Ledbetter, H. M. (1977), Elastic properties of zinc : A compilation and a review, *Journal of Physical and Chemical Reference Data*, *6*, 1181–1203, doi:10.1063/1.555564.

Li, J., and Y. Fei (2014), Experimental constraints on core composition, in *Treatise on Geochemistry*, vol. 3, edited by H. D. Holland and K. K. Turekian, 2 ed., chap. 15, pp. 527–557, Elsevier Ltd., Amsterdam, Netherlands, doi:10.1016/B978-0-08-095975-7.00214-X.

Li, L., D. J. Weidner, J. Chen, M. T. Vaughan, M. D. B. Durham, L. Li, D. J. Weidner, J. Chen, M. T. Vaughan, M. Davis, and W. B. Durham (2004), X-ray strain analysis at high pressure: Effect of plastic deformation in MgO, *Journal of Applied Physics*, *95*(8357), doi:10.1063/1.1738532.

Li, Y., L. Vočadlo, J. Brodholt, and I. G. Wood (2016), Thermoelasticity of Fe_7C_3 under inner core conditions, *Journal of Geophysical Research: Solid Earth*, *121*(8), 5828–5837, doi:10.1002/2016JB013155.

Lin, J.-F. (2003), Static compression of iron-silicon alloys: Implications for silicon in the Earth's core, *Journal of Geophysical Research*, *108*(B1), 2045, doi:10.1029/2002JB001978.

Lin, J.-f., D. L. Heinz, A. J. Campbell, J. M. Devine, W. L. Mao, and G. Shen (2002), Iron-Nickel alloy in the Earth's core, *Geophysical Research Letters*, *29*(10), 1–3, doi:10.1029/2002GL015089.

Lin, J.-F., V. V. Struzhkin, W. Sturhahn, E. Huang, J. Zhao, M. Y. Hu, E. E. Alp, H.-k. Mao, N. Boctor, and R. J. Hemley (2003), Sound velocities of iron-nickel and iron-silicon alloys at high pressures, *Geophysical Research Letters*, *30*(21), 2112, doi:10.1029/2003GL018405.

Lin, J.-f., Y. Fei, W. Sturhahn, J. Zhao, H.-k. Mao, and R. J. Hemley (2004), Magnetic transition and sound velocities of Fe_3S at high pressure: Implications for Earth and planetary cores, *Earth and Planetary Science Letters*, *226*, 33–40, doi:10.1016/j.epsl.2004.07.018.

Lin, J.-F., W. Sturhahn, J. Zhao, G. Shen, H.-K. Mao, and R. J. Hemley (2005), Sound velocities of hot dense iron: Birch's law revisited, *Science*, *308*, 1892–1894, doi:10.1126/science.1111724.

Litasov, K. D., and A. F. Shatskiy (2016), Composition of the Earth's core: A review, *Russian Geology and Geophysics*, *57*, 22–46, doi:10.1016/j.rgg.2016.01.003.

Liu, J., J.-F. Lin, A. Alatas, and W. Bi (2014), Sound velocities of bcc-Fe and $Fe_{0.85}Si_{0.15}$ alloy at high pressure and temperature, *Physics of the Earth and Planetary Interiors*, *233*, 24–32, doi:10.1016/j.pepi.2014.05.008.

Liu, J., J.-F. Lin, A. Alatas, A. Alatas, M. Y. Hu, J. Zhao, and L. Dubrovinsky (2016), Seismic parameters of hcp-Fe alloyed with Ni and Si in the Earth's Core, *Journal of Geophysical Research: Solid Earth*, *121*, doi:10.1002/2015JB012625.

Lodders, K. (2003), Solar system abundances and condensation temperatures of the elements, *The Astrophysical Journal*, *591*(2), 1220–1247, doi:10.1086/375492.

Loubeyre, P., R. Letoullec, J. P. Pinceaux, H. K. Mao, J. Hu, and R. J. Hemley (1993), Equation of state and phase diagram of solid He from single-crystal X-ray diffraction over a large P-T domain, *Physical Review Letters*, *71*(14), 2272–2275, doi:10.1103/PhysRevLett.71.2272.

Lübbers, R., H. F. Grünsteudel, A. I. Chumakov, and G. Wortmann (2000), Density of phonon states in iron at high pressure, *Science*, *287*, 1250–1254, doi:10.1126/science.287.5456.1250.

Lythgoe, K. H., A. Deuss, J. F. Rudge, and J. A. Neufeld (2014), Earth's inner core: Innermost inner core or hemispherical variations?, *Earth and Planetary Science Letters*, *385*, 181–189, doi:10.1016/j.epsl.2013.10.049.

Ma, Y., M. Somayazulu, G. Shen, H.-K. Mao, J. Shu, and R. J. Hemley (2004), In situ X-ray diffraction studies of iron to Earth-core conditions, *Physics of the Earth and Planetary Interiors*, *143-144*, 455–467, doi:10.1016/j.pepi.2003.06.005.

Mainprice, D. (2015), Seismic anisotropy of the deep Earth from a mineral and rock physics perspective, in *Treatise on Geophysics*, vol. 2, edited by G. Schubert, 2 ed., chap. 2.20, pp. 437–491, Elsevier B.V., Oxford, UK, doi:10.1016/B978-044452748-6.00045-6.

Mao, H. K., R. J. Hemley, Y. Wu, A. P. Jephcoat, L. W. Finger, C. S. Zha, and W. A. Bassett (1988), High-pressure phase diagram and equation of state of solid helium from single-crystal x-ray diffraction to 23.3 GPa, *Physical Review Letters*, *60*(25), 2649–2652, doi:10.1103/PhysRevLett.60.2649.

Mao, H. K., Y. Wu, L. C. Chen, J. F. Shu, and A. P. Jephcoat (1990), Static compression of iron to 300 GPa and $Fe_{0.8}Ni_{0.2}$ alloy to 260 GPa: Implications for composition of the core, *Journal of Geophysical Research*, *95*(B13), 21,737–21,742, doi:10.1029/JB095iB13p21737.

Mao, H.-k., J. Shu, G. Shen, R. J. Hemley, B. Li, and A. K. Singh (1998), Elasticity and rheology of iron above 220 GPa and the nature of the Earth's inner core, *Nature*, *396*, 741–743, doi:10.1038/25506.

Mao, H. K., J. Xu, V. V. Struzhkin, J. Shu, R. J. Hemley, W. Sturhahn, M. Y. Hu, E. E. Alp, L. Vocadlo, D. Alfè, G. D. Price, M. J. Gillan, M. Schwoerer-Böhning, D. Häusermann, P. Eng, G. Shen, H. Giefers, R. Lübbers, and G. Wortmann (2001), Phonon density of states of iron up to 153 gigapascals, *Science*, *292*(914), 914–6, doi:10.1126/science.1057670.

Mao, W. L., W. Sturhahn, D. L. Heinz, H.-k. Mao, J. Shu, and R. J. Hemley (2004), Nuclear resonant x-ray scattering of iron hydride at high pressure, *Geophysical Research Letters*, *31*, L15,618, doi:10.1029/2004GL020541.

Mao, W. L., V. V. Struzhkin, A. Q. R. Baron, S. Tsutsui, C. E. Tommaseo, H.-R. Wenk, M. Y. Hu, P. Chow, W. Sturhahn, J. Shu, R. J. Hemley, D. L. Heinz, and H.-K. Mao (2008), Experimental determination of the elasticity of iron at high pressure, *Journal of Geophysical Research*, *113*, B09,213, doi:10.1029/2007JB005229.

Mao, Z., J.-F. Lin, J. Liu, A. Alatas, L. Gao, J. Zhao, and H.-K. Mao (2012), Sound velocities of Fe and Fe-Si alloy in the Earth's core, *Proceedings of the National Academy of Sciences of the United States of America*, *109*(26), 10,239–10,244, doi:10.1073/pnas.1207086109.

Martorell, B., J. Brodholt, I. G. Wood, and L. Vočadlo (2013a), The effect of nickel on the properties of iron at the conditions of Earth's inner core: Ab initio calculations of seismic wave velocities of Fe-Ni alloys, *Earth and Planetary Science Letters*, *365*, 143–151, doi:10.1016/j.epsl.2013.01.007.

Martorell, B., L. Vočadlo, J. Brodholt, and I. G. Wood (2013b), Strong premelting effect in the elastic properties of hcp-Fe under inner-core conditions, *Science*, *342*, 466–468, doi:10.1126/science.1243651.

Martorell, B., I. G. Wood, J. Brodholt, and L. Vočadlo (2016), The elastic properties of hcp-$Fe_{1-x}Si_x$ at Earth's inner-core conditions, *Earth and Planetary Science Letters*, *451*, 89–96, doi:10.1016/j.epsl.2016.07.018.

Masters, G., and D. Gubbins (2003), On the resolution of density within the Earth, *Physics of the Earth and Planetary Interiors*, *140*(1-3), 159–167, doi:10.1016/j.pepi.2003.07.008.

Masumoto, H., H. Saitô, and M. Kikuchi (1966), Thermal expansion and temperature dependence of Young's modulus of single crystal of hexagonal cobalt, *Science reports of the Research Institutes, Tohoku University. Ser. A, Physics, chemistry and metallurgy*, *19*, 172–183.

Mattesini, M., A. B. Belonoshko, E. Buforn, M. Ramírez, S. I. Simak, A. Udías, H.-k. Mao, and R. Ahuja (2010), Hemispherical anisotropic patterns of the Earth's inner core, *Proceedings of the National Academy of Sciences of the United States of America*, *107*(21), 9507–9512, doi:10.1073/pnas.1004856107.

Maupin, V., and J. Park (2015), Theory and Observations - Seismic Anisotropy, in *Treatise on Geophysics*, edited by G. Schubert, chap. 1.09, pp. 277–305, Elsevier B.V., Oxford, UK, doi:10.1016/B978-0-444-53802-4.00007-5.

McDonough, W., and S. S. Sun (1995), The composition of the Earth, *Chemical Geology*, *120*, 223–253, doi:10.1016/0009-2541(94)00140-4.

McDonough, W. F. (2003), Compositional model for the Earth's core, in *Treatise on Geochemistry Vol. 2*, edited by R. W. Carlson, chap. 2.15, pp. 547–568, Elsevier Ltd, Oxford, UK, doi:10.1016/B0-08-043751-6/02015-6.

McQueen, R. G., and S. P. Marsh (1966), Shock-wave compression of iron-nickel alloys, *Journal of Geophysical Research*, *71*(6), 1751–1756, doi:10.1029/JZ071i006p01751.

McSkimin, H. J. (1955), Measurement of the elastic constants of single crystal cobalt, *Journal of Applied Physics*, *26*, 406–409, doi:10.1063/1.1722007.

Merkel, S., A. F. Goncharov, H.-k. Mao, P. Gillet, and R. J. Hemley (2000), Raman spectroscopy of iron to 152 Gigapascals: Implications for Earth's inner core, *Science*, *288*, 1626–1629, doi:10.1126/science.288.5471.1626.

Merkel, S., J. Shu, P. Gillet, H.-k. Mao, and R. J. Hemley (2005), X-ray diffraction study of the single-crystal elastic moduli of ϵ-Fe up to 30 GPa, *Journal of Geophysical Research*, *110*(B05201), doi:10.1029/2004JB003197.

Montagner, J.-P., and B. L. N. Kennett (1996), How to reconcile body-wave and normal-mode reference earth models, *Geophysical Journal International*, *125*, 229–248, doi:10.1111/j.1365-246X.1996.tb06548.x.

Mori, Y., H. Ozawa, K. Hirose, R. Sinmyo, S. Tateno, G. Morard, and Y. Ohishi (2017), Melting experiments on Fe–Fe_3S system to 254 GPa, *Earth and Planetary Science Letters*, *464*, 135–141, doi:10.1016/j.epsl.2017.02.021.

Morrison, R. A., J. M. Jackson, W. Sturhahn, D. Zhang, and E. Greenberg (2018), Equations of state and anisotropy of Fe-Ni-Si alloys, *Journal of Geophysical Research: Solid Earth*, *123*, doi:10.1029/2017JB015343.

Moustafa, S. G., A. J. Schultz, E. Zurek, and D. A. Kofke (2017), Accurate and precise ab initio anharmonic free-energy calculations for metallic crystals: Application to hcp Fe at high temperature and pressure, *Physical Review B*, *96*, 014,117, doi:10.1103/PhysRevB.96.014117.

Murphy, C. A., J. M. Jackson, W. Sturhahn, and B. Chen (2011a), Grüneisen parameter of hcp-Fe to 171 GPa, *Geophysical Research Letters*, *38*(24), 1–5, doi:10.1029/2011GL049531.

Murphy, C. A., J. M. Jackson, W. Sturhahn, and B. Chen (2011b), Melting and thermal pressure of hcp-Fe from the phonon density of states, *Physics of the Earth and Planetary Interiors*, *188*, 114–120, doi:10.1016/j.pepi.2011.07.001.

Murphy, C. A., J. M. Jackson, and W. Sturhahn (2013), Experimental constraints on the thermodynamics and sound velocities of hcp-Fe to core pressures, *Journal of Geophysical Research: Solid Earth*, *118*, doi:10.1002/jgrb.50166.

Nakajima, Y., E. Takahashi, N. Sata, Y. Nishihara, K. Hirose, K. I. Funakoshi, and Y. Ohishi (2011), Thermoelastic property and high-pressure stability of Fe_7C_3: Implication for iron-carbide in the Earth's core, *American Mineralogist*, *96*(7), 1158–1165, doi:10.2138/am.2011.3703.

Nguyen, J. H., and N. C. Holmes (2004), Melting of iron at the physical conditions of the Earth's core, *Nature*, *427*, 339–342, doi:10.1038/nature02248.

Niu, Z.-W., Z.-Y. Zeng, L.-C. Cai, and X.-R. Chen (2015), Study of the thermodynamic stability of iron at inner core from first-principles theory combined with lattice dynamics, *Physics of the Earth and Planetary Interiors*, *248*, 12–19, doi:10.1016/j.pepi.2015.09.002.

Ohtani, E. (2013), Chemical and physical properties and thermal state of the core, in *Physics and Chemistry of the Deep Earth*, edited by S.-i. Karato, 1 ed., chap. 8, pp. 244–270, John Wiley & Sons, Ltd, Chichester, UK, doi:doi.org/10.1002/9781118529492.ch8.

Ohtani, E., Y. Shibazaki, T. Sakai, K. Mibe, H. Fukui, S. Kamada, T. Sakamaki, Y. Seto, S. Tsutsui, and A. Q. R. Baron (2013), Sound velocity of hexagonal close-packed iron up to core pressures, *Geophysical Research Letters*, *40*(19), 5089–5094, doi:10.1002/grl.50992.

Ono, S. (2013), Equation of state and elasticity of B2-type FeSi: Implications for silicon in the inner core, *Physics of the Earth and Planetary Interiors*, *224*, 32–37, doi:10.1016/j.pepi.2013.08.009.

Ono, S., T. Kikegawa, and Y. Ohishi (2007), Equation of state of the high-pressure polymorph of FeSi to 67 GPa, *European Journal of Mineralogy*, *19*, 183–187, doi:10.1127/0935-1221/2007/0019-1713.

Ono, S., T. Kikegawa, N. Hirao, and K. Mibe (2010), High-pressure magnetic transition in hcp-Fe, *American Mineralogist*, *95*(5-6), 880–883, doi:10.2138/am.2010.3430.

O'Rourke, J. G., and D. J. Stevenson (2016), Powering Earth's dynamo with magnesium precipitation from the core, *Nature*, *529*, 387–389, doi:10.1038/nature16495.

Ozawa, H., F. Takahashi, K. Hirose, Y. Ohishi, and N. Hirao (2011), Phase transition of FeO and stratification in Earth's outer core, *Science*, *334*(6057), 792–794, doi:10.1126/science.1208265.

Poirier, J.-P. (1994), Light elements in the Earth's outer core: A critical review, *Physics of the Earth and Planetary Interiors*, *85*(3-4), 319–337, doi:10.1016/0031-9201(94)90120-1.

Pourovskii, L. V., J. Mravlje, M. Ferrero, O. Parcollet, and I. A. Abrikosov (2014), Impact of electronic correlations on the equation of state and transport in ϵ-Fe, *Physical Review B*, *90*(15), 1–5, doi:10.1103/PhysRevB.90.155120.

Pozzo, M., C. Davies, D. Gubbins, and D. Alfè (2014), Thermal and electrical conductivity of solid iron and iron-silicon mixtures at Earth's core conditions, *Earth and Planetary Science Letters*, *393*, 159–164, doi:10.1016/j.epsl.2014.02.047.

Prescher, C., and V. B. Prakapenka (2015), DIOPTAS: A program for reduction of two-dimensional x-ray diffraction data and data exploration, *High Pressure Research*, *35*(3), 223–230, doi:10.1080/08957959.2015.1059835.

Ricolleau, A., Y. Fei, A. Corgne, J. Siebert, and J. Badro (2011), Oxygen and silicon contents of Earth's core from high pressure metal-silicate partitioning experiments, *Earth and Planetary Science Letters*, *310*(3-4), 409–421, doi:10.1016/j.epsl.2011.08.004.

Rubie, D. C., S. A. Jacobson, A. Morbidelli, D. P. O. Brien, E. D. Young, J. D. Vries, F. Nimmo, H. Palme, and D. J. Frost (2015), Accretion and differentiation of the terrestrial planets with implications for the compositions of early-formed Solar System bodies and accretion of water, *Icarus*, *248*, 89–108, doi:10.1016/j.icarus.2014.10.015.

Sakai, T., E. Ohtani, N. Hirao, and Y. Ohishi (2011), Stability field of the hcp-structure for Fe, Fe-Ni, and Fe-Ni-Si alloys up to 3 Mbar, *Geophysical Research Letters*, *38*(9), L09,302, doi:10.1029/2011GL047178.

Sakai, T., S. Takahashi, N. Nishitani, I. Mashino, E. Ohtani, and N. Hirao (2014), Equation of state of pure iron and $Fe_{0.9}Ni_{0.1}$ alloy up to 3 Mbar, *Physics of the Earth and Planetary Interiors*, *228*, 114–126, doi:10.1016/j.pepi.2013.12.010.

Sakairi, T., T. Sakamaki, E. Ohtani, H. Fukui, S. Kamada, S. Tsutsui, H. Uchiyama, and A. Q. R. Baron (2018), Sound velocity measurements of hcp Fe-Si alloy at high pressure and high temperature by inelastic X-ray scattering, *American Mineralogist*, *103*, 85–90, doi:10.2138/am-2018-6072.

Sakamaki, T., E. Ohtani, H. Fukui, S. Kamada, S. Takahashi, T. Sakairi, A. Takahata, T. Sakai, S. Tsutsui, D. Ishikawa, R. Shiraishi, Y. Seto, T. Tsuchiya, and A. Q. R. Baron (2016), Constraints on Earth's inner core composition inferred from measurements of the sound velocity of hcp-iron in extreme conditions, *Science Advances*, *2*, e1500802, doi:10.1126/sciadv.1500802.

Sata, N., K. Hirose, G. Shen, Y. Nakajima, Y. Ohishi, and N. Hirao (2010), Compression of FeSi, Fe_3C, $Fe_{0.95}O$, and FeS under the core pressures and implication for light element in the Earth's core, *Journal of Geophysical Research: Solid Earth*, *115*(B09204), 1–13, doi:10.1029/2009JB006975.

Sha, X., and R. Cohen (2006), Lattice dynamics and thermodynamics of bcc iron under pressure: First-principles linear response study, *Physical Review B*, *73*, 104303, doi:10.1103/PhysRevB.73.104303.

Sha, X., and R. E. Cohen (2010), First-principles thermal equation of state and thermoelasticity of hcp Fe at high pressures, *Physical Review B*, *81*, 094105, doi:10.1103/PhysRevB.81.094105.

Shibazaki, Y., E. Ohtani, H. Fukui, T. Sakai, S. Kamada, D. Ishikawa, S. Tsutsui, A. Q. R. Baron, N. Nishitani, N. Hirao, and K. Takemura (2012), Sound velocity measurements in dhcp-FeH up to 70 GPa with inelastic X-ray scattering: Implications for the composition of the Earth's core, *Earth and Planetary Science Letters*, *313-314*, 79–85, doi:10.1016/j.epsl.2011.11.002.

Siebert, J., J. Badro, D. Antonangeli, and F. J. Ryerson (2012), Metal–silicate partitioning of Ni and Co in a deep magma ocean, *Earth and Planetary Science Letters*, *321-322*, 189–197, doi:10.1016/j.epsl.2012.01.013.

Singh, A. K., H.-K. Mao, J. Shu, and R. J. Hemley (1998), Estimation of single-crystal elastic moduli from polycrystalline x-ray diffraction at high pressure: Application to FeO and iron, *Physical Review Letters*, *80*(10), 2157–2160, doi:10.1103/PhysRevLett.80.2157.

Sinogeikin, S. V., J. S. Smith, E. Rod, C. Lin, C. Kenney-Benson, and G. Shen (2015), Online remote control systems for static and dynamic compression and decompression using diamond anvil cells, *Review of Scientific Instruments*, *86*, 072,209, doi:10.1063/1.4926892.

Steinle-Neumann, G., L. Stixrude, and R. E. Cohen (1999), First-principles elastic constants for the hcp transition metals Fe, Co, and Re at high pressure, *Physical Review B*, *60*(2), 791–799, doi:10.1103/PhysRevB.60.791.

Steinle-Neumann, G., L. Stixrude, R. E. Cohen, and O. Gülseren (2001), Elasticity of iron at the temperature of the Earth's inner core, *Nature*, *413*, 57–60, doi:10.1038/35092536.

Stevenson, D. J. (1977), Hydrogen in the Earth's core, *Nature*, *268*, 130–131, doi:10.1038/268130a0.

Stixrude, L., E. Wasserman, and R. E. Cohen (1997), Composition and temperature of Earth's inner core, *Journal of Geophysical Research*, *102*(B11), 24,729–24,739, doi:10.1029/97JB02125.

Strong, H. M., R. E. Tuft, and R. E. Hanneman (1973), The iron fusion curve and the γ-δ-l triple point, *Metallurgical Transactions*, *4*, 2657, doi:10.1007/BF02644272.

Sturhahn, W. (2000), CONUSS and PHOENIX: Evaluation of nuclear resonant scattering data, *Hyperfine Interactions*, *125*, 149–172, doi:10.1023/A:1012681503.

Sturhahn, W. (2004), Nuclear resonant spectroscopy, *Journal of Physics: Condensed Matter*, *16*(5), S497–S530, doi:10.1088/0953-8984/16/5/009.

Sturhahn, W. (2017), MINeral physics UTIlities (MINUTI) open source software package, `www.nrixs.com`.

Sturhahn, W., and A. Chumakov (1999), Lamb-Mössbauer factor and second-order Doppler shift from inelastic nuclear resonant absorption, *Hyperfine Interactions*, *123/124*, 809–824, doi:10.1023/A:1017060931.

Sturhahn, W., and J. M. Jackson (2007), Geophysical applications of nuclear resonant spectroscopy, in *Advances in High-Pressure Mineralogy: Geological Society of America Special Paper 421*, edited by E. Ohtani, pp. 157–174, Geological Society of America, doi:10.1130/2007.2421(09).

Sturhahn, W., and V. G. Kohn (1999), Theoretical aspects of incoherent nuclear resonant scattering, *Hyperfine Interactions*, *123/124*, 367–399, doi:10.1023/A:1017071806.

Takafuji, N., K. Hirose, S. Ono, F. Xu, M. Mitome, and Y. Bando (2004), Segregation of core melts by permeable flow in the lower mantle, *Earth and Planetary Science Letters*, *224*(3-4), 249–257, doi:10.1016/j.epsl.2004.05.016.

Takahashi, T., W. A. Bassett, and H.-K. Mao (1968), Isothermal compression of the alloys of iron up to 300 kilobars at room temperature: Iron-nickel alloys, *Journal of Geophysical Research*, *73*(14), 4717–4725, doi:10.1029/JB073i014p04717.

Tateno, S., K. Hirose, Y. Ohishi, and Y. Tatsumi (2010), The structure of iron in Earth's inner core., *Science*, *330*, 359–361, doi:10.1126/science.1194662.

Tateno, S., K. Hirose, T. Komabayashi, H. Ozawa, and Y. Ohishi (2012), The structure of Fe-Ni alloy in Earth's inner core, *Geophysical Research Letters*, *39*(12), doi:10.1029/2012GL052103.

Tateno, S., Y. Kuwayama, K. Hirose, and Y. Ohishi (2015), The structure of Fe-Si alloy in Earth's inner core, *Earth and Planetary Science Letters*, *418*, 11–19, doi:10.1016/j.epsl.2015.02.008.

Thompson, E. C., B. A. Chidester, R. A. Fischer, G. I. Myers, D. L. Heinz, V. B. Prakapenka, and A. J. Campbell (2016), Equation of state of pyrite to 80 GPa and 2400 K, *American Mineralogist*, *101*(5), 1046–1051, doi:10.2138/am-2016-5527.

Thompson, E. C., A. H. Davis, W. Bi, J. Zhao, E. E. Alp, D. Zhang, E. Greenberg, V. B. Prakapenka, and A. J. Campbell (2018), High-pressure geophysical properties of fcc phase FeH_x, *Geochemistry, Geophysics, Geosystems*, *19*, 305–314, doi:10.1002/2017GC007168.

Toby, B. H., and R. B. Von Dreele (2013), GSAS-II: The genesis of a modern open-source all purpose crystallography software package, *Journal of Applied Crystallography*, *46*, 544–549, doi:10.1107/S0021889813003531.

Toellner, T. S. (2000), Monochromatization of synchrotron radiation for nuclear resonant scattering experiments, *Hyperfine Interactions*, *125*, 3–28, doi:10.1023/A:1012621317.

Tsuchiya, T., and M. Fujibuchi (2009), Effects of Si on the elastic property of Fe at Earth's inner core pressures: First principles study, *Physics of the Earth and Planetary Interiors*, *174*, 212–219, doi:10.1016/j.pepi.2009.01.007.

Uchida, T., Y. Wang, M. L. Rivers, S. R. Sutton, and K. Gpa (2001), Stability field and thermal equation of state of ϵ-iron determined by synchrotron X-ray diffraction in a multianvil apparatus, *Journal of Geophysical Research*, *106*(B10), 21,799–21,810, doi:10.1029/2001JB000258.

Vočadlo, L. (2007), Ab initio calculations of the elasticity of iron and iron alloys at inner core conditions: Evidence for a partially molten inner core?, *Earth and Planetary Science Letters*, *254*(1-2), 227–232, doi:10.1016/j.epsl.2006.09.046.

Vočadlo, L. (2015), Earth's Core: Iron and Iron Alloys, in *Treatise on Geophysics*, edited by G. Schubert, chap. 2.06, pp. 117–147, Elsevier B.V., Oxford, UK, doi:10.1016/B978-0-444-53802-4.00032-4.

Vočadlo, L., J. Brodholt, D. Alfè, M. J. Gillan, and G. D. Price (2000), Ab initio free energy calculations on the polymorphs of iron at core conditions, *Physics of the Earth and Planetary Interiors*, *117*, 123–137, doi:10.1016/S0031-9201(99)00092-8.

Vočadlo, L., D. P. Dobson, and I. G. Wood (2009), Ab initio calculations of the elasticity of hcp-Fe as a function of temperature at inner-core pressure, *Earth and Planetary Science Letters*, *288*(3-4), 534–538, doi:10.1016/j.epsl.2009.10.015.

Wasserman, E., L. Stixrude, and R. E. Cohen (1996), Thermal properties of iron at high pressures and temperatures, *Physical Review B*, *53*(13), 8296–8309, doi:10.1103/PhysRevB.53.8296.

Weidner, D. J., L. Li, M. Davis, and J. Chen (2004), Effect of plasticity on elastic modulus measurements, *Geophysical Research Letters*, *31*(L06621), doi:10.1029/2003GL019090.

Wenk, H., S. Matthies, R. J. Hemley, H. Mao, and J. Shu (2000), The plastic deformation of iron at pressures of the Earth's inner core, *Nature*, *405*, 1044–1047, doi:10.1038/35016558.

Wenk, H. R., T. Takeshita, R. Jeanloz, and G. C. Johnson (1988), Development of texture and elastic anisotropy during deformation of hcp metals, *Geophysical Research Letters*, *15*(1), 76–79, doi:10.1029/GL015i001p00076.

Wicks, J. K., J. M. Jackson, and W. Sturhahn (2010), Very low sound velocities in iron-rich (Mg,Fe)O: Implications for the core-mantle boundary region, *Geophysical Research Letters*, *37*(15), 1–5, doi:10.1029/2010GL043689.

Wicks, J. K., J. M. Jackson, W. Sturhahn, and D. Zhang (2017), Sound velocity and density of magnesiowüstites: Implications for ultralow-velocity zone topography, *Geophysical Research Letters*, *44*, 2148–2158, doi:10.1002/2016GL071225.

Wood, B. J. (1993), Carbon in the core, *Earth and Planetary Science Letters*, *117*(3-4), 593–607, doi:10.1016/0012-821X(93)90105-I.

Wood, B. J., J. Li, and A. Shahar (2013), Carbon in the core: Its influence on the properties of core and mantle, *Reviews in Mineralogy and Geochemistry*, *75*(1), 231–250, doi:10.2138/rmg.2013.75.8.

Yamazaki, D., E. Ito, T. Yoshino, A. Yoneda, X. Guo, B. Zhang, W. Sun, A. Shimojuku, N. Tsujino, T. Kunimoto, Y. Higo, and K. I. Funakoshi (2012), $P - V - T$ equation of state for ϵ-iron up to 80 GPa and 1900

K using the Kawai-type high pressure apparatus equipped with sintered diamond anvils, *Geophysical Research Letters*, *39*(20), 1–6, doi:10.1029/2012GL053540.

Yu, X., J. Zhang, Y. Zhang, L. Wang, and Y. Zhao (2012), Comparative studies of yield strength and elastic compressibility between nanocrystalline and bulk cobalt, *Journal of Applied Physics*, *111*, 113,506, doi:10.1063/1.4724338.

Zarkevich, N. A., and D. D. Johnson (2015), Coexistence pressure for a martensitic transformation from theory and experiment: Revisiting the bcc-hcp transition of iron under pressure, *Physical Review B*, *91*, 174,104, doi:10.1103/PhysRevB.91.174104.

Zarochentsev, E. V., E. P. Troitskaya, and V. V. Chabanenko (2004), Elastic constants of noble-gas crystals under pressure and the Cauchy relations, *Physics of the Solid State*, *46*(2), 249–253, doi:10.1134/1.1649419.

Zha, C. S., H. K. Mao, and R. J. Hemley (2004), Elasticity of dense helium, *Physical Review B*, *70*, 174,107, doi:10.1103/PhysRevB.70.174107.

Zhang, D., J. M. Jackson, J. Zhao, W. Sturhahn, E. E. Alp, M. Y. Hu, T. S. Toellner, C. A. Murphy, and V. B. Prakapenka (2016), Temperature of Earth's core constrained from melting of Fe and $Fe_{0.9}Ni_{0.1}$ at high pressures, *Earth and Planetary Science Letters*, *447*, 72–83, doi:10.1016/j.epsl.2016.04.026.

Zhang, J., and F. Guyot (1999), Thermal equation of state of iron and $Fe_{0.91}Si_{0.09}$, *Physics and Chemistry of Minerals*, *26*(3), 206–211, doi:10.1007/s002690050178.

Zhang, Y., T. Sekine, H. He, Y. Yu, F. Liu, and M. Zhang (2014), Shock compression of Fe-Ni-Si system to 280 GPa: Implications for the composition of the Earth's outer core, *Geophysical Research Letters*, *41*, 4554–4559, doi:10.1002/2014GL060670.

Zhang, Y. G., and Q. Z. Yin (2012), Carbon and other light element contents in the Earth's core based on first-principles molecular dynamics, *Proceedings of the National Academy of Sciences of the United States of America*, *109*(48), 19,579–19,583, doi:10.1073/pnas.1203826109.

Zhao, J., and N. L. Ross (2015), Non-hydrostatic behavior of KBr as a pressure medium in diamond anvil cells up to 5.63 GPa, *Journal of Physics: Condensed Matter*, *27*(18), 185,402, doi:10.1088/0953-8984/27/18/185402.

A p p e n d i x A

QUANTITIES DERIVED FROM X-RAY DIFFRACTION DATA FOR EQUATION OF STATE AND ANISOTROPY ANALYSIS

Table A.1: bcc-$Fe_{0.91}Ni_{0.09}$ x-ray diffraction data[a]

$Fe_{0.91}Ni_{0.09}$ sample				W pressure calibrant				Pressure	σ_P
a (Å)	σ_a	Volume (Å^3)	σ_V	a (Å)	σ_a	Volume (Å^3)	σ_V	(GPa)	
FeNi-Run#1									
2.8700	0.0003	23.640	0.008					0	
2.8622	0.0005	23.448	0.011	3.1612	0.0002	31.590	0.007	1.1	0.1
2.8471	0.0006	23.079	0.016	3.1520	0.0002	31.315	0.007	3.8	0.1
2.8348	0.0005	22.781	0.011	3.1451	0.0002	31.110	0.006	6.0	0.1
2.8266	0.0004	22.584	0.010	3.1392	0.0002	30.935	0.007	7.9	0.1
2.8138	0.0004	22.278	0.010	3.1314	0.0005	30.705	0.014	10.4	0.2
2.8044	0.0004	22.056	0.009	3.1252	0.0003	30.523	0.008	12.5	0.1
2.7943	0.0057	21.818	0.134	3.1174	0.0006	30.295	0.018	15.2	0.2
FeNi-Run#2									
2.8603	0.0002	23.401	0.006	3.1601	0.0002	31.557	0.005	1.4	0.1
2.8548	0.0002	23.266	0.006	3.1566	0.0002	31.453	0.007	2.4	0.1
2.8377	0.0002	22.851	0.006	3.1464	0.0001	31.149	0.002	5.6	0.1
2.8231	0.0002	22.500	0.006	3.1375	0.0002	30.885	0.005	8.4	0.1
2.8080	0.0002	22.141	0.006	3.1273	0.0001	30.585	0.004	11.8	0.1
2.8028	0.0002	22.018	0.006	3.1235	0.0001	30.474	0.004	13.1	0.1

[a]See chapter 2.2 for a detailed description of uncertainty calculations.

Table A.2: hcp-$Fe_{0.91}Ni_{0.09}$ XRD data[a] (5 pages long)

$Fe_{0.91}Ni_{0.09}$ sample								W pressure calibrant				Pressure	σ_P[b]
a (Å)	σ_a	c (Å)	σ_c	Volume (Å^3)	σ_V	c/a	$\sigma_{c/a}$	a (Å)	σ_a	Volume (Å^3)	σ_V	(GPa)	
FeNi-Run#1													
2.4602	0.0011	3.9703	0.0040	20.811	0.028	1.6138	0.0018	3.1174	0.0006	30.295	0.018	15.2	0.2
2.4483	0.0010	3.9426	0.0026	20.466	0.021	1.6103	0.0012	3.1056	0.0011	29.953	0.032	19.5	0.4
2.4297	0.0009	3.9103	0.0024	19.992	0.019	1.6094	0.0012	3.0899	0.0010	29.501	0.028	25.5	0.4
2.4162	0.0011	3.8872	0.0030	19.653	0.023	1.6088	0.0014	3.0783	0.0008	29.170	0.023	30.2	0.3
2.4045	0.0011	3.8666	0.0030	19.360	0.023	1.6081	0.0015	3.0689	0.0009	28.903	0.026	34.2	0.4
2.3939	0.0011	3.8471	0.0033	19.093	0.024	1.6070	0.0016	3.0572	0.0006	28.574	0.017	39.3	0.3
2.3846	0.0011	3.8317	0.0030	18.869	0.023	1.6069	0.0015	3.0475	0.0009	28.303	0.025	43.8	0.4
2.3702	0.0010	3.8071	0.0029	18.522	0.021	1.6062	0.0014	3.0332	0.0010	27.906	0.028	50.7	0.5
2.3585	0.0009	3.7871	0.0024	18.244	0.018	1.6057	0.0012	3.0207	0.0009	27.563	0.026	57.0	0.5
2.3465	0.0005	3.7692	0.0015	17.973	0.011	1.6063	0.0007	3.0058	0.0036	27.157	0.097	64.9	2.0
2.3331	0.0006	3.7493	0.0017	17.675	0.012	1.6070	0.0008	2.9926	0.0015	26.801	0.041	72.4	0.9
2.3289	0.0006	3.7421	0.0017	17.577	0.011	1.6068	0.0008	2.9876	0.0021	26.667	0.056	75.3	1.2
2.3227	0.0005	3.7307	0.0014	17.430	0.010	1.6062	0.0007	2.9809	0.0023	26.488	0.062	79.3	1.4
2.3180	0.0005	3.7230	0.0016	17.324	0.011	1.6061	0.0008	2.9749	0.0026	26.328	0.070	82.9	1.6
2.3149	0.0007	3.7167	0.0020	17.249	0.014	1.6056	0.0010	2.9714	0.0007	26.235	0.019	85.1	0.5
2.3081	0.0004	3.7062	0.0013	17.099	0.009	1.6057	0.0006	2.9626	0.0033	26.003	0.087	90.7	2.2
2.3045	0.0005	3.7006	0.0015	17.020	0.010	1.6058	0.0008	2.9589	0.0011	25.905	0.030	93.1	0.8
2.2943	0.0009	3.6833	0.0025	16.791	0.017	1.6054	0.0013	2.9479	0.0008	25.618	0.020	100.5	0.5
2.2934	0.0008	3.6821	0.0022	16.772	0.015	1.6055	0.0011	2.9468	0.0007	25.589	0.019	101.2	0.5
2.2888	0.0007	3.6743	0.0021	16.669	0.014	1.6053	0.0010	2.9425	0.0009	25.477	0.024	104.2	0.6

[a]See chapter 2.2 for a detailed description of uncertainty calculations.

[b]The pressure uncertainties for data points above 1 Mbar were rounded to the nearest GPa in the main body of the thesis.

$Fe_{0.91}Ni_{0.09}$ sample								W pressure calibrant				Pressure	σ_P
a (Å)	σ_a	c (Å)	σ_c	Volume (Å^3)	σ_V	c/a	$\sigma_{c/a}$	a (Å)	σ_a	Volume (Å^3)	σ_V	(GPa)	
2.4640	0.0009	3.9647	0.0093	20.846	0.051	1.6091	0.0038	3.1179	0.0004	30.310	0.012	15.1	0.1
FeNi-Run#2													
2.4616	0.0007	3.9610	0.0063	20.786	0.035	1.6091	0.0026	3.1155	0.0005	30.240	0.015	15.9	0.2
2.4568	0.0008	3.9537	0.0084	20.667	0.046	1.6093	0.0035	3.1120	0.0009	30.138	0.025	17.2	0.3
2.4521	0.0005	3.9461	0.0014	20.548	0.011	1.6093	0.0006	3.1078	0.0010	30.016	0.029	18.7	0.4
2.4479	0.0004	3.9394	0.0014	20.443	0.010	1.6093	0.0006	3.1043	0.0011	29.915	0.033	20.0	0.4
2.4392	0.0005	3.9241	0.0014	20.219	0.011	1.6088	0.0007	3.0974	0.0004	29.716	0.011	22.6	0.2
2.4353	0.0004	3.9175	0.0013	20.121	0.010	1.6086	0.0006	3.0934	0.0006	29.601	0.018	24.1	0.2
2.4267	0.0005	3.9026	0.0014	19.903	0.011	1.6082	0.0007	3.0858	0.0009	29.383	0.027	27.2	0.4
2.4248	0.0004	3.8995	0.0013	19.856	0.010	1.6082	0.0006	3.0833	0.0013	29.312	0.038	28.2	0.5
2.4215	0.0005	3.8930	0.0014	19.769	0.011	1.6077	0.0007	3.0805	0.0007	29.232	0.019	29.3	0.3
2.4181	0.0004	3.8881	0.0014	19.689	0.010	1.6079	0.0006	3.0771	0.0010	29.136	0.027	30.7	0.4
2.4154	0.0004	3.8833	0.0013	19.620	0.009	1.6077	0.0006	3.0745	0.0009	29.062	0.025	31.8	0.4
2.4120	0.0004	3.8770	0.0012	19.534	0.009	1.6074	0.0006	3.0709	0.0007	28.960	0.020	33.3	0.3
2.4080	0.0004	3.8705	0.0013	19.436	0.009	1.6074	0.0006	3.0666	0.0008	28.838	0.022	35.2	0.3
2.4025	0.0004	3.8614	0.0013	19.302	0.009	1.6072	0.0006	3.0612	0.0007	28.686	0.021	37.5	0.3
2.3913	0.0004	3.8425	0.0012	19.029	0.008	1.6069	0.0006	3.0506	0.0008	28.389	0.022	42.3	0.4
2.3819	0.0003	3.8267	0.0010	18.802	0.007	1.6066	0.0005	3.0406	0.0008	28.111	0.022	47.1	0.4
2.3730	0.0003	3.8124	0.0010	18.592	0.007	1.6066	0.0005	3.0320	0.0007	27.873	0.020	51.3	0.4
2.3649	0.0003	3.8000	0.0010	18.405	0.007	1.6068	0.0005	3.0242	0.0007	27.659	0.019	55.2	0.4
2.3567	0.0003	3.7865	0.0010	18.213	0.007	1.6067	0.0005	3.0155	0.0008	27.421	0.021	59.7	0.4
2.3503	0.0003	3.7752	0.0010	18.060	0.007	1.6063	0.0005	3.0089	0.0007	27.241	0.018	63.3	0.4
2.3438	0.0003	3.7658	0.0011	17.916	0.007	1.6067	0.0005	3.0015	0.0008	27.041	0.021	67.3	0.4
2.3364	0.0003	3.7527	0.0010	17.741	0.007	1.6062	0.0005	2.9933	0.0007	26.820	0.020	72.0	0.4
2.3312	0.0003	3.7445	0.0010	17.623	0.007	1.6063	0.0005	2.9868	0.0008	26.645	0.022	75.8	0.5

$Fe_{0.91}Ni_{0.09}$ sample								W pressure calibrant				Pressure	σ_P
a (Å)	σ_a	c (Å)	σ_c	Volume (Å^3)	σ_V	c/a	$\sigma_{c/a}$	a (Å)	σ_a	Volume (Å^3)	σ_V	(GPa)	
2.3226	0.0003	3.7302	0.0010	17.427	0.007	1.6060	0.0005	2.9772	0.0009	26.389	0.024	81.5	0.6
2.3154	0.0004	3.7153	0.0012	17.250	0.009	1.6046	0.0006	2.9680	0.0008	26.145	0.022	87.3	0.5
2.3074	0.0005	3.7016	0.0014	17.067	0.010	1.6042	0.0007	2.9585	0.0008	25.895	0.022	93.4	0.5
2.2933	0.0005	3.6778	0.0015	16.751	0.011	1.6037	0.0008	2.9424	0.0009	25.474	0.025	104.3	0.7
FeNi-Run#3													
2.4642	0.0006	3.9637	0.0016	20.844	0.013	1.6085	0.0008	3.1191	0.0030	30.345	0.087	14.6	1.1
2.4606	0.0005	3.9621	0.0013	20.775	0.011	1.6102	0.0006	3.1171	0.0024	30.287	0.071	15.3	0.9
2.4504	0.0005	3.9461	0.0015	20.520	0.011	1.6104	0.0007	3.1083	0.0029	30.031	0.083	18.5	1.1
2.4485	0.0005	3.9427	0.0015	20.470	0.011	1.6103	0.0007	3.1073	0.0032	30.002	0.092	18.9	1.2
2.4451	0.0005	3.9371	0.0016	20.385	0.012	1.6102	0.0007	3.1031	0.0036	29.88	0.11	20.4	1.4
2.4333	0.0005	3.9168	0.0015	20.084	0.011	1.6097	0.0007	3.0929	0.0016	29.587	0.046	24.3	0.6
2.4300	0.0005	3.9115	0.0016	20.003	0.012	1.6097	0.0007	3.0908	0.0024	29.527	0.068	25.2	0.9
2.4274	0.0005	3.9076	0.0017	19.940	0.012	1.6098	0.0008	3.0884	0.0017	29.458	0.049	26.1	0.7
2.4172	0.0005	3.8922	0.0016	19.695	0.012	1.6102	0.0007	3.0787	0.0016	29.181	0.047	30.1	0.7
2.4158	0.0005	3.8898	0.0016	19.660	0.011	1.6101	0.0007	3.0779	0.0014	29.158	0.039	30.4	0.6
2.4146	0.0005	3.8877	0.0016	19.630	0.011	1.6101	0.0007	3.0768	0.0017	29.127	0.049	30.8	0.7
2.4129	0.0005	3.8852	0.0016	19.589	0.011	1.6102	0.0007	3.0747	0.0017	29.068	0.048	31.7	0.7
2.4106	0.0005	3.8816	0.0016	19.534	0.011	1.6102	0.0007	3.0729	0.0023	29.017	0.065	32.5	1.0
2.4068	0.0005	3.8757	0.0016	19.443	0.012	1.6103	0.0008	3.0687	0.0030	28.898	0.084	34.3	1.3
2.3990	0.0004	3.8607	0.0016	19.242	0.011	1.6093	0.0007	3.0629	0.0023	28.734	0.066	36.8	1.0
2.3940	0.0004	3.8532	0.0016	19.125	0.010	1.6095	0.0007	3.0577	0.0020	28.588	0.057	39.1	0.9
2.3873	0.0004	3.8431	0.0015	18.968	0.010	1.6098	0.0007	3.0500	0.0019	28.373	0.052	42.6	0.9
2.3815	0.0005	3.8334	0.0016	18.829	0.011	1.6097	0.0007	3.0437	0.0039	28.20	0.11	45.6	1.9
2.3754	0.0005	3.8235	0.0016	18.684	0.011	1.6096	0.0007	3.0389	0.0046	28.06	0.13	47.9	2.2
2.3721	0.0005	3.8187	0.0016	18.609	0.010	1.6098	0.0007	3.0356	0.0021	27.973	0.059	49.5	1.1

$Fe_{0.91}Ni_{0.09}$ sample								W pressure calibrant				Pressure	σ_P
a (Å)	σ_a	c (Å)	σ_c	Volume (Å^3)	σ_V	c/a	$\sigma_{c/a}$	a (Å)	σ_a	Volume (Å^3)	σ_V	(GPa)	
2.3698	0.0006	3.8156	0.0021	18.557	0.014	1.6101	0.0010	3.0341	0.0033	27.931	0.091	50.2	1.6
2.3628	0.0004	3.7987	0.0013	18.366	0.009	1.6077	0.0006	3.0263	0.0019	27.716	0.053	54.1	1.0
2.3613	0.0004	3.7964	0.0013	18.332	0.009	1.6078	0.0006	3.0247	0.0029	27.672	0.080	54.9	1.5
2.3587	0.0004	3.7920	0.0013	18.270	0.009	1.6077	0.0006	3.0221	0.0021	27.601	0.057	56.3	1.1
2.3538	0.0004	3.7840	0.0014	18.156	0.009	1.6076	0.0007	3.0182	0.0024	27.494	0.065	58.3	1.3
2.3486	0.0004	3.7760	0.0015	18.038	0.009	1.6078	0.0007	3.0115	0.0039	27.31	0.11	61.8	2.1
2.3437	0.0004	3.7680	0.0015	17.924	0.009	1.6077	0.0007	3.0066	0.0036	27.179	0.098	64.5	2.0
2.3382	0.0004	3.7585	0.0014	17.795	0.009	1.6074	0.0007	3.0007	0.0027	27.019	0.074	67.8	1.5
2.3290	0.0004	3.7442	0.0015	17.588	0.009	1.6076	0.0007	2.9886	0.0016	26.693	0.042	74.7	0.9
2.3230	0.0004	3.7331	0.0013	17.446	0.008	1.6070	0.0006	2.9820	0.0018	26.517	0.049	78.6	1.1
2.3198	0.0004	3.7278	0.0014	17.373	0.008	1.6069	0.0006	2.9785	0.0027	26.424	0.071	80.7	1.6
2.3164	0.0004	3.7225	0.0014	17.298	0.009	1.6070	0.0006	2.9744	0.0032	26.315	0.085	83.3	2.0
2.3116	0.0004	3.7149	0.0014	17.191	0.008	1.6071	0.0007	2.9682	0.0015	26.150	0.039	87.1	0.9
2.3080	0.0004	3.7093	0.0014	17.112	0.009	1.6071	0.0007	2.9626	0.0019	26.003	0.050	90.7	1.2
2.3032	0.0004	3.7021	0.0013	17.008	0.008	1.6074	0.0006	2.9566	0.0020	25.845	0.054	94.6	1.4
2.3006	0.0004	3.6979	0.0013	16.950	0.008	1.6074	0.0006	2.9536	0.0020	25.766	0.053	96.6	1.4
2.2954	0.0003	3.6888	0.0013	16.832	0.008	1.6070	0.0006	2.9488	0.0020	25.641	0.052	99.9	1.4
2.2937	0.0003	3.6860	0.0013	16.794	0.008	1.6070	0.0006	2.9465	0.0020	25.581	0.052	101.4	1.4
2.2915	0.0003	3.6820	0.0013	16.744	0.008	1.6068	0.0006	2.9439	0.0021	25.513	0.055	103.2	1.5
2.2890	0.0003	3.6778	0.0013	16.688	0.008	1.6067	0.0006	2.9410	0.0022	25.438	0.056	105.2	1.5
2.2866	0.0003	3.6738	0.0013	16.635	0.008	1.6067	0.0006	2.9382	0.0021	25.366	0.054	107.2	1.5
2.2850	0.0003	3.6708	0.0013	16.598	0.008	1.6065	0.0006	2.9361	0.0023	25.311	0.059	108.7	1.6
2.2817	0.0003	3.6653	0.0013	16.526	0.008	1.6064	0.0006	2.9320	0.0028	25.205	0.072	111.6	2.0
2.2789	0.0003	3.6604	0.0014	16.463	0.008	1.6062	0.0007	2.9285	0.0031	25.115	0.080	114.2	2.3
2.2758	0.0003	3.6554	0.0014	16.396	0.008	1.6062	0.0007	2.9253	0.0019	25.033	0.049	116.6	1.4

$Fe_{0.91}Ni_{0.09}$ sample								W pressure calibrant				Pressure	σ_P
a (Å)	σ_a	c (Å)	σ_c	Volume (Å^3)	σ_V	c/a	$\sigma_{c/a}$	a (Å)	σ_a	Volume (Å^3)	σ_V	(GPa)	
2.2733	0.0003	3.6508	0.0014	16.339	0.008	1.6059	0.0006	2.9221	0.0020	24.951	0.051	118.9	1.5
2.2703	0.0003	3.6457	0.0014	16.273	0.008	1.6058	0.0006	2.9183	0.0019	24.854	0.048	121.8	1.4
2.2678	0.0003	3.6413	0.0014	16.218	0.008	1.6057	0.0007	2.9151	0.0018	24.772	0.047	124.3	1.4
2.2649	0.0003	3.6362	0.0014	16.154	0.008	1.6055	0.0007	2.9113	0.0020	24.675	0.051	127.2	1.6
2.2618	0.0003	3.6311	0.0014	16.087	0.008	1.6054	0.0007	2.9075	0.0021	24.579	0.054	130.2	1.7
2.2594	0.0003	3.6271	0.0014	16.035	0.008	1.6053	0.0007	2.9045	0.0022	24.503	0.056	132.6	1.8
2.2568	0.0003	3.6227	0.0014	15.979	0.008	1.6052	0.0007	2.9013	0.0023	24.422	0.059	135.1	1.9
2.2538	0.0003	3.6177	0.0014	15.915	0.008	1.6052	0.0007	2.8973	0.0025	24.321	0.064	138.4	2.1
2.2510	0.0003	3.6130	0.0014	15.854	0.008	1.6051	0.0007	2.8937	0.0029	24.230	0.073	141.4	2.4
2.2486	0.0004	3.6089	0.0014	15.803	0.008	1.6050	0.0007	2.8908	0.0031	24.158	0.078	143.8	2.6
2.2461	0.0004	3.6051	0.0014	15.751	0.008	1.6050	0.0007	2.8878	0.0033	24.082	0.083	146.3	2.8
2.2437	0.0003	3.6007	0.0014	15.698	0.008	1.6048	0.0007	2.8847	0.0033	24.005	0.082	149.0	2.8
2.2415	0.0004	3.5974	0.0014	15.653	0.008	1.6049	0.0007	2.8820	0.0033	23.938	0.082	151.3	2.9
2.2395	0.0004	3.5941	0.0014	15.611	0.008	1.6049	0.0007	2.8795	0.0036	23.875	0.089	153.5	3.2
2.2372	0.0004	3.5902	0.0014	15.562	0.008	1.6048	0.0007	2.8768	0.0038	23.808	0.094	155.9	3.4
2.2352	0.0004	3.5869	0.0015	15.520	0.008	1.6047	0.0007	2.8744	0.0040	23.75	0.10	158.0	3.6
2.2330	0.0004	3.5835	0.0015	15.474	0.008	1.6048	0.0007	2.8717	0.0045	23.68	0.11	160.4	4.1
2.2308	0.0004	3.5798	0.0014	15.428	0.008	1.6047	0.0007	2.8691	0.0049	23.62	0.12	162.8	4.5
2.2286	0.0004	3.5762	0.0014	15.382	0.008	1.6047	0.0007	2.8664	0.0021	23.551	0.051	165.2	1.9
2.2281	0.0003	3.5754	0.0014	15.372	0.008	1.6047	0.0007	2.8658	0.0021	23.536	0.051	165.8	1.9
2.2271	0.0003	3.5738	0.0014	15.351	0.008	1.6047	0.0007	2.8645	0.0020	23.504	0.050	167.0	1.9
2.2266	0.0003	3.5730	0.0014	15.341	0.008	1.6047	0.0007	2.8641	0.0020	23.494	0.049	167.4	1.8

Table A.3: bcc-$Fe_{0.8}Ni_{0.1}Si_{0.1}$ x-ray diffraction data[a]

$Fe_{0.8}Ni_{0.1}Si_{0.1}$ sample				W pressure calibrant				Pressure	σ_P
a (Å)	σ_a	Volume (Å^3)	σ_V	a (Å)	σ_a	Volume (Å^3)	σ_V	(GPa)	
FeNiSi-Run#1									
2.8597	0.0004	23.386	0.009					0	
2.8515	0.0003	23.186	0.008	3.1603	0.0002	31.563	0.006	1.3	0.1
2.8390	0.0007	22.882	0.018	3.1527	0.0008	31.336	0.025	3.6	0.3
2.8234	0.0003	22.507	0.008	3.1421	0.0020	31.021	0.060	6.9	0.6
2.8070	0.0003	22.117	0.008	3.1316	0.0005	30.711	0.014	10.4	0.2
2.7974	0.0003	21.891	0.008	3.1262	0.0008	30.553	0.023	12.2	0.3
2.7829	0.0004	21.552	0.010	3.1168	0.0008	30.278	0.025	15.4	0.3
2.7735	0.0003	21.335	0.008	3.1077	0.0011	30.014	0.031	18.7	0.4
2.7647	0.0027	21.132	0.062	3.0999	0.0011	29.788	0.033	21.6	0.4

[a]See chapter 2.2 for a detailed description of uncertainty calculations.

Table A.4: hcp-$Fe_{0.8}Ni_{0.1}Si_{0.1}$ XRD data[a] (4 pages long)

$Fe_{0.8}Ni_{0.1}Si_{0.1}$ sample								W pressure calibrant				Pressure	σ_P[b]
a (Å)	σ_a	c (Å)	σ_c	Volume (Å^3)	σ_V	c/a	$\sigma_{c/a}$	a (Å)	σ_a	Volume (Å^3)	σ_V	(GPa)	
FeNiSi-Run#1													
2.4422	0.0004	3.9363	0.0034	20.332	0.019	1.6118	0.0014	3.0999	0.0011	29.788	0.033	21.6	0.4
2.4333	0.0003	3.9246	0.0008	20.124	0.007	1.6129	0.0004	3.0925	0.0004	29.575	0.012	24.5	0.2
2.4242	0.0003	3.9118	0.0009	19.909	0.007	1.6136	0.0004	3.0852	0.0007	29.366	0.019	27.4	0.3
2.4139	0.0003	3.8952	0.0009	19.656	0.007	1.6137	0.0004	3.0741	0.0006	29.051	0.018	32.0	0.3
2.4043	0.0003	3.8771	0.0009	19.410	0.007	1.6126	0.0004	3.0658	0.0006	28.816	0.017	35.5	0.3
2.3952	0.0003	3.8622	0.0008	19.189	0.006	1.6125	0.0004	3.0569	0.0006	28.566	0.017	39.5	0.3
2.3891	0.0003	3.8513	0.0008	19.037	0.006	1.6120	0.0004	3.0502	0.0010	28.378	0.029	42.5	0.5
2.3810	0.0003	3.8385	0.0008	18.846	0.006	1.6121	0.0004	3.0430	0.0006	28.178	0.017	45.9	0.3
2.3734	0.0003	3.8262	0.0008	18.666	0.006	1.6121	0.0004	3.0364	0.0009	27.995	0.025	49.1	0.5
2.3644	0.0003	3.8093	0.0008	18.442	0.006	1.6111	0.0004	3.0275	0.0017	27.749	0.045	53.5	0.8
2.3580	0.0003	3.7999	0.0009	18.297	0.006	1.6115	0.0004	3.0197	0.0007	27.535	0.020	57.5	0.4
2.3514	0.0003	3.7899	0.0009	18.147	0.006	1.6118	0.0004	3.0121	0.0007	27.328	0.020	61.5	0.4
2.3447	0.0003	3.7787	0.0008	17.991	0.006	1.6116	0.0004	3.0049	0.0008	27.133	0.021	65.4	0.4
2.3395	0.0003	3.7697	0.0008	17.868	0.006	1.6113	0.0004	3.0000	0.0011	27.000	0.029	68.2	0.6
2.3340	0.0003	3.7606	0.0008	17.741	0.006	1.6112	0.0004	2.9951	0.0008	26.868	0.020	70.9	0.4
2.3279	0.0003	3.7490	0.0008	17.594	0.006	1.6105	0.0004	2.9889	0.0010	26.701	0.028	74.5	0.6
2.3237	0.0003	3.7420	0.0008	17.498	0.006	1.6104	0.0004	2.9846	0.0014	26.586	0.038	77.1	0.8
2.3193	0.0003	3.7371	0.0008	17.409	0.006	1.6113	0.0004	2.9775	0.0021	26.397	0.055	81.4	1.3
2.3144	0.0003	3.7286	0.0008	17.296	0.005	1.6110	0.0004	2.9726	0.0011	26.267	0.030	84.4	0.7
2.3087	0.0003	3.7196	0.0008	17.170	0.005	1.6111	0.0004	2.9666	0.0008	26.108	0.020	88.1	0.5

[a]See chapter 2.2 for a detailed description of uncertainty calculations.

[b]The pressure uncertainties for data points above 1 Mbar were rounded to the nearest GPa in the main body of the thesis.

$Fe_{0.8}Ni_{0.1}Si_{0.1}$ sample								W pressure calibrant				Pressure	σ_P
a (Å)	σ_a	c (Å)	σ_c	Volume (Å^3)	σ_V	c/a	$\sigma_{c/a}$	a (Å)	σ_a	Volume (Å^3)	σ_V	(GPa)	
FeNiSi-Run#2													
2.4128	0.0016	3.8949	0.0047	19.637	0.035	1.6143	0.0022	3.0749	0.0010	29.073	0.030	31.6	0.4
2.4129	0.0007	3.8932	0.0021	19.630	0.015	1.6135	0.0010	3.0741	0.0013	29.051	0.036	32.0	0.5
2.4126	0.0006	3.8926	0.0021	19.622	0.015	1.6134	0.0010	3.0736	0.0010	29.036	0.028	32.2	0.4
2.4114	0.0007	3.8906	0.0022	19.592	0.015	1.6134	0.0010	3.0735	0.0010	29.034	0.029	32.2	0.4
2.4102	0.0007	3.8892	0.0022	19.566	0.016	1.6136	0.0010	3.0712	0.0012	28.968	0.034	33.2	0.5
2.4092	0.0008	3.8877	0.0022	19.542	0.017	1.6137	0.0011	3.0702	0.0012	28.940	0.035	33.6	0.5
2.4068	0.0008	3.8832	0.0023	19.481	0.017	1.6134	0.0011	3.0686	0.0010	28.895	0.029	34.3	0.4
2.4046	0.0008	3.8798	0.0023	19.428	0.017	1.6135	0.0011	3.0670	0.0011	28.850	0.030	35.0	0.5
2.4046	0.0012	3.8798	0.0035	19.428	0.027	1.6135	0.0017	3.0649	0.0010	28.790	0.029	35.9	0.5
2.3979	0.0006	3.8679	0.0020	19.261	0.014	1.6130	0.0010	3.0608	0.0012	28.675	0.033	37.7	0.5
2.3949	0.0006	3.8632	0.0021	19.189	0.014	1.6131	0.0010	3.0585	0.0012	28.611	0.035	38.7	0.6
2.3932	0.0006	3.8613	0.0022	19.152	0.015	1.6134	0.0010	3.0571	0.0012	28.571	0.034	39.4	0.6
2.3907	0.0008	3.8591	0.0024	19.101	0.017	1.6142	0.0011	3.0548	0.0014	28.507	0.039	40.4	0.6
2.3866	0.0008	3.8560	0.0022	19.021	0.016	1.6157	0.0011	3.0511	0.0013	28.403	0.035	42.1	0.6
2.3844	0.0009	3.8539	0.0025	18.975	0.018	1.6163	0.0012	3.0480	0.0014	28.317	0.040	43.6	0.7
2.3788	0.0006	3.8397	0.0020	18.817	0.014	1.6141	0.0010	3.0421	0.0010	28.153	0.027	46.3	0.5
2.3749	0.0008	3.8372	0.0024	18.743	0.017	1.6157	0.0011	3.0387	0.0013	28.058	0.037	48.0	0.6
2.3696	0.0011	3.8336	0.0033	18.642	0.023	1.6178	0.0016	3.0357	0.0013	27.975	0.036	49.4	0.6
2.3663	0.0014	3.8307	0.0048	18.576	0.032	1.6189	0.0022	3.0322	0.0013	27.879	0.036	51.2	0.6
2.3607	0.0012	3.8190	0.0035	18.432	0.025	1.6177	0.0017	3.0253	0.0014	27.689	0.039	54.6	0.7
2.3592	0.0013	3.8169	0.0044	18.398	0.030	1.6179	0.0021	3.0224	0.0011	27.609	0.029	56.1	0.5
2.3519	0.0007	3.7946	0.0023	18.178	0.015	1.6134	0.0011	3.0160	0.0009	27.434	0.026	59.5	0.5
2.3497	0.0006	3.7927	0.0020	18.134	0.013	1.6141	0.0009	3.0135	0.0010	27.366	0.027	60.8	0.5
2.3482	0.0020	3.7789	0.0094	18.045	0.054	1.6093	0.0042	3.0095	0.0009	27.257	0.025	62.9	0.5

$Fe_{0.8}Ni_{0.1}Si_{0.1}$ sample								W pressure calibrant				Pressure	σ_P
a (Å)	σ_a	c (Å)	σ_c	Volume (Å^3)	σ_V	c/a	$\sigma_{c/a}$	a (Å)	σ_a	Volume (Å^3)	σ_V	(GPa)	
FeNiSi-Run#2 cont.													
2.3420	0.0007	3.7778	0.0024	17.945	0.016	1.6131	0.0011	3.0041	0.0016	27.111	0.043	65.9	0.9
2.3394	0.0007	3.7733	0.0021	17.884	0.015	1.6129	0.0010	3.0018	0.0014	27.049	0.037	67.2	0.8
2.3351	0.0007	3.7662	0.0024	17.785	0.016	1.6129	0.0012	2.9974	0.0012	26.930	0.034	69.6	0.7
2.3311	0.0007	3.7584	0.0025	17.687	0.016	1.6123	0.0012	2.9915	0.0012	26.771	0.031	73.0	0.7
2.3291	0.0007	3.7550	0.0024	17.641	0.015	1.6122	0.0011	2.9895	0.0010	26.717	0.027	74.2	0.6
2.3243	0.0007	3.7473	0.0022	17.532	0.015	1.6122	0.0011	2.9844	0.0009	26.581	0.025	77.2	0.6
2.3196	0.0007	3.7400	0.0025	17.427	0.016	1.6123	0.0012	2.9796	0.0009	26.453	0.025	80.1	0.6
2.3153	0.0009	3.7332	0.0029	17.331	0.019	1.6124	0.0014	2.9751	0.0009	26.333	0.023	82.8	0.5
2.3109	0.0010	3.7258	0.0033	17.231	0.021	1.6123	0.0016	2.9703	0.0007	26.206	0.019	85.8	0.5
2.3055	0.0010	3.7164	0.0037	17.107	0.023	1.6120	0.0017	2.9638	0.0007	26.034	0.018	89.9	0.4
2.3009	0.0012	3.7086	0.0045	17.003	0.027	1.6118	0.0021	2.9577	0.0010	25.874	0.027	93.9	0.7
2.2976	0.0016	3.7011	0.0067	16.920	0.039	1.6109	0.0031	2.9512	0.0011	25.704	0.030	98.2	0.8
2.2950	0.0005	3.6985	0.0018	16.870	0.011	1.6115	0.0009	2.9476	0.0014	25.610	0.037	100.7	1.0
2.2916	0.0005	3.6916	0.0017	16.789	0.011	1.6109	0.0008	2.9440	0.0015	25.516	0.039	103.2	1.0
2.2855	0.0005	3.6824	0.0018	16.658	0.011	1.6112	0.0009	2.9383	0.0012	25.368	0.032	107.1	0.9
2.2798	0.0006	3.6731	0.0020	16.533	0.012	1.6112	0.0010	2.9327	0.0011	25.223	0.030	111.1	0.8
2.2744	0.0006	3.6634	0.0021	16.412	0.013	1.6107	0.0010	2.9285	0.0012	25.115	0.032	114.2	0.9
2.2705	0.0006	3.6563	0.0020	16.324	0.012	1.6104	0.0010	2.9238	0.0011	24.994	0.027	117.7	0.8
2.2669	0.0006	3.6504	0.0021	16.246	0.013	1.6103	0.0010	2.9191	0.0012	24.874	0.031	121.2	0.9
2.2633	0.0007	3.6437	0.0025	16.164	0.015	1.6099	0.0012	2.9135	0.0013	24.731	0.034	125.5	1.0
2.2602	0.0009	3.6372	0.0033	16.091	0.020	1.6092	0.0016	2.9096	0.0016	24.632	0.040	128.5	1.2
2.2567	0.0012	3.6294	0.0045	16.007	0.026	1.6083	0.0022	2.9044	0.0023	24.500	0.058	132.7	1.8
2.2524	0.0006	3.6249	0.0022	15.926	0.013	1.6094	0.0011	2.8974	0.0012	24.323	0.029	138.3	0.9
2.2502	0.0007	3.6206	0.0024	15.876	0.014	1.6090	0.0012	2.8937	0.0011	24.230	0.027	141.4	0.9

$Fe_{0.8}Ni_{0.1}Si_{0.1}$ sample								W pressure calibrant				Pressure	σ_P
a (Å)	σ_a	c (Å)	σ_c	Volume (Å^3)	σ_V	c/a	$\sigma_{c/a}$	a (Å)	σ_a	Volume (Å^3)	σ_V	(GPa)	
FeNiSi-Run#2 cont.													
2.2474	0.0008	3.6143	0.0028	15.809	0.017	1.6082	0.0014	2.8882	0.0010	24.092	0.026	146.0	0.9
2.2427	0.0009	3.6037	0.0034	15.697	0.019	1.6069	0.0016	2.8822	0.0011	23.943	0.026	151.1	0.9
2.2404	0.0010	3.5997	0.0036	15.648	0.021	1.6067	0.0017	2.8791	0.0010	23.865	0.026	153.9	0.9
2.2379	0.0010	3.5962	0.0037	15.598	0.021	1.6070	0.0018	2.8757	0.0010	23.781	0.026	156.8	0.9
2.2354	0.0010	3.5934	0.0038	15.551	0.021	1.6075	0.0018	2.8725	0.0011	23.702	0.026	159.7	1.0
2.2330	0.0010	3.5907	0.0037	15.506	0.021	1.6080	0.0018	2.8699	0.0011	23.637	0.027	162.0	1.0
2.2306	0.0010	3.5878	0.0037	15.460	0.021	1.6084	0.0018	2.8670	0.0012	23.566	0.029	164.7	1.1
2.2282	0.0010	3.5851	0.0038	15.415	0.022	1.6090	0.0019	2.8638	0.0012	23.487	0.029	167.6	1.1
2.2258	0.0011	3.5829	0.0040	15.372	0.023	1.6097	0.0020	2.8612	0.0012	23.423	0.030	170.1	1.1
2.2235	0.0011	3.5811	0.0041	15.333	0.023	1.6106	0.0020	2.8587	0.0012	23.362	0.030	172.4	1.2
2.2214	0.0011	3.5793	0.0042	15.296	0.023	1.6113	0.0020	2.8564	0.0013	23.305	0.031	174.6	1.2